# Process dynamics and structure formation in continuous spray fluidized bed processes

**Dissertation**

zur Erlangung des akademischen Grades

**Doktoringenieur**

**(Dr.-Ing.)**

von     M. Sc. Martin Schmidt

geb. am 05.08.1986 in Stendal

genehmigt durch die Fakultät für Verfahrens- und Systemtechnik

der Otto-von-Guericke Universität Magdeburg

Promotionskommission:     Prof. Dr.-Ing. habil. Kai Sundmacher (Vorsitz)

Prof. Dr.-Ing. habil. Evangelos Tsotsas (Gutachter)

Prof. Dr.-Ing. Andreas Bück (Gutachter)

Prof. Dr.-Ing. habil. Dr. h.c. Achim Kienle (Gutachter)

eingereicht am 31.05.2018

Promotionskolloquium am: 15.10.2018

# Abstract

Spray fluidized bed layering granulation (SFBLG) and spray fluidized bed agglomeration (SFBA) processes are used to produce particulate solids. Especially powders and granules in the chemical, food, and pharmaceutical industry are produced by spray fluidized bed processes (SFBP). These particulate products usually show, among other properties, good flowability, low dustiness, low residual moisture contents, and long shelf lives. Some particular products are: fertilizers, instant food powders (soups, cocoa, coffee, etc.), food and feed additives (proteins, granulated greens, fats or blood), granules for tablet pressing, and protective coatings for pills and tablets.

Simulation studies regarding continuous SFBLG have predicted the occurrence of oscillations in the particle size distribution (PSD). Oscillations in the PSD can be harmful to the operation of a process and the resulting product quality. Oscillations in the bed mass and product mass flow rate may occur, as well as product may be produced outside of the particle size requirements of the customer. Besides the described simulations, a systematic experimental study of the phenomenon of PSD oscillations during continuous SFBLG has only been published in the frame of this dissertation. The dissertation presents a systematical, experimental investigation of particle formation and process behavior during continuous SFBLG with internal seed particle formation for crystalline material, and during continuous SFBA for partly amorphous material.

Continuous SFBLG processes exhibited self-sustained oscillations in the PSD for moderate drying conditions and internal classifying product discharge. For external classifying product discharge, oscillations in the PSD were observed for humid process conditions. Vice versa, steady state continuous SFBLG processes with internal separation were realized for humid process conditions. Steady state processes for external separation were reached for intense drying. The different process behavior was attributed to different amounts of seed particles produced in the fluidized bed. For the experiments reaching the steady state, larger average granule growth rates were determined for an external classifying product discharge, compared to the experiments with internal classifying product discharge. Additionally, humid process conditions resulted in porous and rough granules, whereas intense drying produced relatively dense and smooth granules. Thus, in addition to process dynamics, the investigated drying and process conditions also determined the product quality.

The continuous SFBA experiments with partly amorphous material always reached a steady state. No oscillations in the PSD were observed. Even after a sudden, unwanted reduction of the average agglomerate size during process breaks, the system always returned to the steady state after restart. For internal separation and relatively high nuclei mass flow rates, also high average agglomerate growth rates were observed. The experiments with external separation

had to be conducted with considerably smaller nuclei feed mass flow rates. Thus, also the product mass flow rates were lower than in the internal classifying case, resulting in reduced average agglomerate growth rates. Additionally, comminution of oversize and feedback of fine material increased the average residence time for the product particles, which also reduced the average growth rate. Changes in agglomerate structure were not observed for varied nuclei mass flow rate, classifying air velocity and mill power level.

# Kurzzusammenfassung

Wirbelschicht-Sprühgranulation (WSSG) und Wirbelschicht-Sprühagglomeration (WSSA) sind Prozesse zur Herstellung von partikulären Feststoffen. Besonders Pulver und Granulate der chemischen, pharmazeutischen und Lebensmittelindustrie werden durch Wirbelschicht-Sprühprozesse hergestellt. Diese partikulären Produkte weisen typische Eigenschaften auf, z.B. gute Fließfähigkeit, geringe Staubentwicklung, geringe Restfeuchte und gute Haltbarkeit. Als Beispielprodukte seien genannt: Düngemittel, Instantpulver der Lebensmittelindustrie (Suppen, Kakao, Kaffee, etc.), Zusätze für Lebensmittel und Tierfutter (Proteine, granulierte Futtermittel, Fette oder Blut), Granulate für das Tablettenpressen, sowie Pillen und Tabletten mit Schutzschichten.

Simulationsstudien kontinuierlicher WSSG Prozesse haben das Auftreten von Oszillationen der Partikelgrößenverteilung (PGV) vorhergesagt. Oszillationen der PGV können sich nachteilig auf den Betrieb eines Prozesses und die Produktqualität auswirken. Es können Oszillationen der Bettmasse und des Produktmassestroms auftreten, und Produkt außerhalb der Partikelgrößenspezifikation des Kunden kann auftreten. Neben den erwähnten Simulationen wurde eine systematische experimentelle Untersuchung von Oszillationen der PGV während der kontinuierlichen WSSG bisher nur im Rahmen dieser Dissertation durchgeführt und veröffentlicht. Die vorliegende Dissertation präsentiert eine systematische, experimentelle Untersuchung von Partikelbildungsprozessen für kontinuierliche WSSG mit interner Keimbildung für kristallines Material, sowie für kontinuierliche WSSA mit teilamorphem Material.

Kontinuierliche WSSG Prozesse zeigten selbsterhaltende Oszillationen der PGV für moderate Trocknungsbedingungen und intern klassierenden Produktaustrag. Für den extern klassierenden Produktaustrag wurden Oszillationen der PGV für feuchte Prozessbedingungen beobachtet. Umgekehrt wurde der stationäre Zustand für kontinuierliche WSSG mit interner Klassierung für feuchte Prozessbedingungen, und für externe Klassierung bei starker Trocknung erreicht. Das unterschiedliche Prozessverhalten wurde auf unterschiedliche interne Keimbildung bei unterschiedlichen Trocknungsbedingungen zurückgeführt. Bei den Experimenten, die den stationären Zustand erreichten, wurden höhere mittlere Wachstumsraten für externe Klassierung als für interne Klassierung bestimmt. Zusätzlich resultierten feuchte Prozessbedingungen in porösen und rauen Granulaten, wohingegen trockene Versuchsbedingungen das Entstehen von dichten und glatten Partikeln begünstigten. Folglich beeinflussten die untersuchten Trocknungs- und Prozessbedingungen nicht nur die Prozessdynamik, sondern bestimmten auch die Produktqualität.

Die Versuche zur kontinuierlichen WSSA mit teilamorphem Material erreichten den stationären Zustand für alle Parameterkonfigurationen. Es wurden keine Oszillationen der

PGV beobachtet. Selbst nach plötzlicher, unerwünschter Verringerung der mittleren Partikelgröße im Wirbelbett durch Prozessunterbrechungen, wurde der stationäre Zustand nach Wiederaufnahme des Experiments erneut erreicht. Für die Versuche mit interner Klassierung wurden relativ hohe Keimzugabemasseströme gewählt, und somit folglich hohe mittlere Wachstumsgeschwindigkeiten der Agglomerate erreicht. Die Versuche mit externer Klassierung mussten mit reduzierten Keimzugabemasseströmen durchgeführt werden. Folglich waren auch die Produktmasseströme, und somit die mittleren Wachstumsraten der Agglomerate, niedriger als bei den Versuchen mit interner Klassierung. Zusätzlich erhöhten die Zerkleinerung von Überkorn sowie die Rückführung des Unterkorns die mittlere Verweilzeit der Partikel in der Wirbelschicht für externe Klassierung, was ebenfalls die mittlere Wachstumsrate reduzierte. Änderungen der Agglomeratstruktur wurden für variierten Keimmassestrom, variierte Klassiergeschwindigkeit und Mühlenleistung nicht beobachtet.

# Content

# Nomenclature

## Symbols

| | | |
|---|---|---|
| $A$ | cross-sectional area | [m$^2$] |
| $a_w$ | water activity | [-] |
| $Ar$ | Archimedes number | [-] |
| $B$ | birth term | [m$^{-1}$·s$^{-1}$] |
| $c$ | Gordon and Taylor constant | [-] |
| $c_{dg}$ | drag coefficient | [-] |
| $C_1$, $C_2$, $C_3$ | Magnus constants | [-, -, °C] |
| $CoV$ | coefficient of variation (forwards defined) | [-] |
| $CoV_{ba}$ | coefficient of variation (backwards defined) | [-] |
| $d$ | diameter (mainly: particle size/diameter) | [m] |
| $d_{1,3}$ | average particle diameter | [m] |
| $D$ | death term | [m$^{-1}$·s$^{-1}$] |
| $DF$ | drain factor | [-] |
| $D_f$ | fractal dimension | [-] |
| $e$ | error/deviation | [-] |
| $E$ | vaporization efficiency | [-] |
| $EE'$ | environmental equivalency factor (modified) | [-] |
| $F$ | force | [N] |
| $g$ | gravitational acceleration | [m·s$^{-2}$] |
| $G$ | growth rate | [m·s$^{-1}$] |
| $h$ | height | [m] |
| $H$ | Heavyside function | [-] |
| $i$ | control variable | [-] |
| $j$ | control variable | [-] |
| $k$ | number of a moment (integer) | [-] |
| $K$ | constant | [-] |
| $l$ | control variable | [-] |

| | | |
|---|---|---|
| $L$ | constant | [-] |
| $m$ | number of samples for averaging | [-] |
| $M$ | mass | [kg] |
| $\dot{M}$ | mass flow rate | [kg·s$^{-1}$] |
| $n$ | number density distribution | [m$^{-1}$] |
| $\dot{n}$ | number density distribution flow rate | [m$^{-1}$·s$^{-1}$] |
| $N$ | total number | [-] |
| $o$ | mass fraction of spray solution forming overspray | [-] |
| $p$ | pressure | [Pa] |
| $P$ | percentage of max. power | [%] |
| $\Delta p$ | pressure drop | [Pa] |
| $q_r$ | normalized particle size distribution density regarding quantity $r$ | [m$^{-1}$] |
| $Q_r$ | normalized particle size distribution regarding quantity $r$ | [-] |
| $r$ | type of quantity (0: number, 1: length, 2: area, 3: volume) | [-] |
| $rH$ | relative humidity | [%] |
| $R$ | average granule roughness | [m] |
| $R_a$ | arithmetic mean roughness | [m] |
| $Re$ | Reynolds number | [-] |
| $s$ | distance | [m] or [px] |
| $S$ | surface area | [m$^2$] |
| $t$ | process time | [s] |
| $T$ | temperature | [°C] |
| $T_g$ | glass transition temperature | [°C] |
| $u$ | velocity | [m·s$^{-1}$] |
| $v$ | particle volume | [m$^3$] |
| $V$ | volume | [m$^3$] |
| $x$ | mass fraction | [-] |
| $X$ | absolute moisture content per dry sample | [kg·kg$^{-1}$] |
| $Y$ | absolute moisture content per dry gas | [kg·kg$^{-1}$] |
| $z$ | height coordinate | [m] |

# Greek symbols

| | | |
|---|---|---|
| $\beta$ | agglomeration kinetics | [-] |
| $\kappa$ | separation function | [-] |
| $\mu_k$ | $k^{th}$ normalized statistic moment of a size distribution | [m$^k$] |
| $v$ | kinematic viscosity | [m$^2 \cdot$s$^{-1}$] |
| $\Pi$ | drying potential | [-] |
| $\rho$ | density | [kg$\cdot$m$^{-3}$] |
| $\sigma$ | standard deviation | variable |
| $\tau$ | average residence time of a particle in the fluidized bed | [s] |
| $\Psi$ | porosity (void fraction) of particle or bulk | [-] |

# Subscripts

| | |
|---|---|
| 0 | first value or starting value |
| av | average |
| b | buoyancy |
| ba | backwards in process time |
| bed | bed |
| box | box |
| bulk | bulk |
| class | classifying air |
| d | droplet |
| dg | drag |
| dry | sample holder + dry particles |
| e | elutriation |
| em | empirical |
| Ext | experiments with external separation |
| g | gas |
| gr | gravity |
| i | control variable |
| Int | experiments with internal separation |
| in | at inlet |
| k | number of a moment (integer) |

| | |
|---|---|
| m | measurement |
| $\dot{M}$ | mass flow rate |
| max | maximum value |
| mf | minimum fluidization (starting point of fluidization) |
| mill | mill |
| NaB | sodium benzoate |
| noz | nozzle |
| nuc | nuclei (new primary particles for agglomeration) |
| o | oversize |
| out | at outlet |
| p | particle |
| prac | in practice |
| prod | product |
| r | type of quantity (number, length, area, volume) |
| rec | recycled |
| s | pure solid |
| sam | samples |
| sat | at saturation |
| seed | seed particle |
| sep | separation |
| sh | sample holder |
| ss | steady state |
| t | total |
| th | theoretical |
| tube | classifying tube |
| u | undersize |
| w | water |
| wet | sample holder + wet particles |

# Abbreviations

2-D       –    two dimensional

3-D       –    three dimensional

API       –    active pharmaceutical ingredient

ca.       –    circa

CCD       –    charge-coupled device

CFD       –    computational fluid dynamics

CT        –    computed tomography

DE        –    dextrose equivalent

DEM       –    discrete element method

EE        –    environmental equivalency factor

Exp       –    experiment

HPMC      –    hydroxypropyl methylcellulose

IR        –    infrared

μ-CT      –    micro-computed tomography

MC        –    Monte Carlo

NaB       –    sodium benzoate ($C_7H_5NaO_2$)

PBE(s)    –    population balance equation(s)

PC        –    personal computer

PCS       –    process control system

PGV       –    Partikelgrößenverteilung

PSD       –    particle size distribution

SEM       –    scanning electron microscope/microscopy

SFBA      –    spray fluidized bed agglomeration

SFBC      –    spray fluidized bed coating

SFBLG     –    spray fluidized bed layering granulation

SFBP      –    spray fluidized bed process(es)

var.      –    varied

WSSA      –    Wirbelschicht-Sprühagglomeration

WSSG      –    Wirbelschicht-Sprühgranulation

# 1 Introduction

## 1.1 Motivation and scope

More than 75% of all processed materials include a particulate form during their production cycle (Merkus, 2009). Thus, specialized particles have to be produced for many applications and consumer demands. Particulate products of the daily life are, for example, instant soup powders, instant coffee, milk powder, cocoa, cornflakes, or detergents. In the solid dosage form, these products are easier to transport, easier to handle and more durable, compared to the liquid or paste-like states in preceding process steps. Besides the food industry, special particles are also produced for the chemical and pharmaceutical industries. Typical particulate products there are fertilizers, pharmaceutical pills and tablets, and catalytic or filter granules. Further applications of special particles can be decorative granules, pellets made from greens as animal feed, or fuel pellets made from combustible organic matter like wood.

For this wide range of particulate products a lot of particle properties are the key factors to be considered during production. The most important factor usually is the particle size. First of all, the smaller a particle gets, the larger are the inter-particulate forces in relation to the weight of the particles. Thus, the flowability for small particles is usually worse than for large particles, due to the sticking of the particles, complicating material handling. For fertilizer, which is applied to a field, larger particle sizes may be helpful, as the fertilizer particles take a longer time to dissolve, providing nutrition to the plants over a certain time interval. Thus, fertilizer has to be applied less often, saving work time. Small particles with a size below 100 µm are named dust. Dust may become airborne and can have multiple unwanted effects. If the material is toxic, inhalation of its dust may be harmful. If the material is combustible, certain concentrations of dust in the air pose the risk of dust explosions. Additionally, material taken away by air represents a material loss, directly diminishing profit. Thus, adjusting the correct particle size is a key aspect of producing particulate products.

Next to particle size, the particle moisture content is the second most important parameter. Especially perishable products like herbs or milk are usually dried to increase their shelf life. A good example is milk powder, which is more durable than milk itself. It can be re-hydrated to a milk-like liquid, containing most of the original nutrients. From an economic point of view, the moisture content should also not be too low. Within the legal constraints especially of the food industry, the maximum moisture content which is not harming the shelf life is usually wanted. Thus, a maximum mass of product is produced from a given input of educts, increasing the profit margin. Consequently, during the production of particulate solids, the moisture content has to exactly meet the customer demands.

An additional particle property is the particle porosity. Especially for instant powders like soup or coffee powder, the particle porosity determines the dissolution rate during re-hydration. Open and porous particles may dissolve faster, as the solvent (in most cases water) can migrate easily into the particle structure. In terms of coating of core materials like drugs, porous or dense coating shells lead to fast or slow release rates, respectively. Thus, depending on the application of the respective drug, the release rate can be controlled by the thickness and the porosity of the coating layer. Additionally, the particle porosity directly determines the particle, and thus, the bulk density of a product. The denser a product, the more material can be packed in the same unit, reducing the necessary material for the production of the packaging. The bulk density also affects the transport of the product. A product with low bulk density needs more space and thus, more transportation vehicles to get to its destination, which is increasing the transportation costs.

Besides the particle porosity, also the particle surface structure is an important morphological aspect in particle technology. Rough particles may show bad flowability due to mechanical inter-locking of the particles, hindering their movement. Additionally, rough surfaces can enhance friability, which leads to unwanted dust formation.

Particulate products can be produced by numerous processes. If the educt already is a solid, the product can be manufactured mechanically, for example by crushing, milling and sieving. An agglomeration step can further improve product quality aspects like particle size or instant properties by gluing together the already existing solids to larger clusters. If the solid educts need to be processed, or if the educts are solid-containing liquids like solutions, suspensions or melts, thermal and chemical processes like evaporation, granulation, phase transition, crystallization or precipitation are necessary to generate particles. This dissertation focusses on agglomeration and granulation processes. Agglomeration processes can be dry or wet. Dry agglomeration can be achieved by mechanical compression, like tablet pressing, or thermal treatment like sintering. For wet agglomeration, a binding liquid is applied to an agitated bed of particles. The liquid bridges enhance inter-particle forces, leading to cluster formation of the particles, the so-called agglomerates. Granulation is the phase transition of solid-containing liquids to the solid, particulate form. Wet agglomeration and granulation processes need a form of mechanical or pneumatic agitation of the particles. The necessary movement can be provided, for example, by a mixer, a rotating drum or a fluidized bed.

Agglomeration and granulation processes can be conducted in batch or continuous mode. When a product is developed, this is usually done in batch mode. Batch processes are versatile, easy to control, and have defined end points in time, resulting in defined product properties. But if larger quantities of products are needed, transition to continuous production can be useful. There are then no down times between the single batches, improving productivity. A special challenge may though be posed by process dynamics. Especially during the start-up period, transient process behavior is to be expected, resulting in changing product quality. But if the steady state is reached, a continuous process produces large volumes with uniform product quality. But continuous particle formation processes are though still less common in several sectors of industry than batch processes. Further investigation of the process behavior is necessary to change this fact. In particular, it is

necessary to know the dynamics of a process, to determine, for example, if the process will reach a steady state, and, thus, can be used for industrial purposes.

In this dissertation, continuous spray fluidized bed layering granulation (SFBLG) and spray fluidized bed agglomeration (SFBA) were investigated. In both processes, a liquid is sprayed onto fluidized particles. For SFBLG, the solids in the spray solution and the particles at the start of the process consist of the same solid material. Here, the goal is a phase transition of the dissolved solid into the particulate state. For SFBA, usually a liquid binder is sprayed onto fluidized particles to form larger particle clusters. Both processes are explained in more detail in Section 2.2.

Simulation studies showed that for continuous SFBLG oscillations in the particle size distribution (PSD) may occur. This is potentially harmful to a production process, as oscillations in the particle size may lead to product outside of the size specification, reducing the productivity of the process. Additionally, changing particle sizes may lead to changing bed masses and variable product mass flow rates, which may interfere with following process steps. Thus, any form of oscillation in a continuous process is usually unwanted, as product quality might not be as constant as during steady state. The simulation results indicate that the above mentioned oscillations in particle size distribution occur for certain process parameter combinations. But an experimental proof has not yet been published, other than by the author of this thesis. Consequently, this dissertation presents a systematic experimental investigation of the process behavior and the resulting product quality for continuous SFBLG and SFBA.

The main goal of this dissertation was to link operating features like drying, fluidization, particle feed, and product withdrawal to the dynamics of continuous SFBLG and SFBA processes. Furthermore, the impact of operating parameters and process behavior on product quality aspects like particle size distribution, particle roughness and particle porosity was analyzed.

## 1.2 Outline

This thesis contains five main chapters. These are a detailed literature survey, presenting the state of the art, a chapter presenting the methods used to measure particle properties, and three chapters presenting the experimental results regarding continuous SFBLG with internal and external separation, and continuous SFBA with both types of product discharge.

In Chapter 2, the theoretical groundwork for understanding this dissertation is established, and previously published work in the field of spray fluidized bed processes (SFBP) is presented. This chapter starts with the definition and explanation of fluidization. Then, the particle formation in fluidized beds is described in detail, covering the underlying micro-processes, the application of SFBP, an explanation, how the structure of the product granules is formed, and a section about which particle properties are of special interest with respect to product quality. Then, special challenges regarding the continuous mode of SFBP are described. In the next section, typical modeling strategies regarding SFBP are summarized. The results of different simulation studies for SFBLG and SFBA, known from literature, are presented, and their relevance for the present dissertation is discussed.

Chapter 3 gives an overview of the methods used to measure product quality aspects of particulate solids. At first, the theory and measurement of particle size distributions (PSD) is explained. This also includes the presentation of a method to determine a steady state, based on the measurement of an average particle diameter over process time, and a separate method on the calculation of an average particle growth rate for a continuous process in steady state. Then, the measurement of the particle moisture content in the sense of a mass fraction of water is explained briefly. The following three sections focus on self-developed methods to measure product quality parameters like granule porosity, granule roughness and the fractal dimension of agglomerates, based on micro-computed tomography (μ-CT), scanning electron microscopy (SEM) and light microscopy.

Chapter 4 and 5 present the experimental results regarding continuous SFBLG with internal and external separation, respectively. A section on materials and methods is followed by the presentation and discussion of the results. Especially the process behavior, expressed by the temporal evolution of the PSD and the average particle diameter, and the particle morphology, represented by particle porosity and particle roughness, are shown and discussed. Additional consideration is given to the steady state experiments, where average particle growth rates are calculated. Furthermore, the results for continuous SFBLG with internal and external classifying product discharge are compared.

In Chapter 6 the results regarding process behavior and resulting particle structure for continuous SFBA with internal and external separation are presented. The agglomeration experiments were conducted with partly amorphous material, in a way that spraying of water was sufficient to generate sticky particles, allowing for agglomeration without the need for an additional binding agent. The process dynamics are evaluated on the basis of the temporal evolution of the PSD and the average particle diameter. Additionally, the agglomerate structure is quantified by the fractal dimension, being a measure for the compactness of an object. Average agglomerate growth rates are calculated for steady state experiments and the results for internal and external separation are compared.

Chapter 7 summarizes the main conclusions and gives an outlook for future research work.

# 2   State of the art

This chapter gives a detailed literature survey regarding particle formation in fluidized beds, and places the dissertation in the context of scientific research. Firstly, fluidization is explained. Then, the underlying mechanisms of spray fluidized bed processes (SFBP) and their applications are presented. Special problems and considerations for continuous SFBP are discussed, and product quality requirements for particles produced in fluidized beds are described. Additionally, general modeling concepts for spray fluidized bed layering granulation (SFBLG) and agglomeration (SFBA) are presented, and conclusions regarding governing process parameters are drawn. Considering all former theory sections, the chapter is completed by a formulation of the goals to be achieved by the dissertation.

## 2.1 Fluidized bed technology

If a fluid (gas or liquid) flows through a fixed bed of particles opposed to gravity, the particles will be fluidized when a certain fluid velocity (minimum fluidization velocity) is exceeded. The fluid enters the bed through a perforated plate, the distributor plate. Increasing fluid velocity changes the fluidization behavior from smooth fluidization over bubbling and turbulent fluidization to pneumatic transport (Fig. 2–1). Besides fluid parameters, particle properties strongly influence the fluidization behavior. Therefore, Geldart (1973) proposed a classification of particles regarding their size and density, resulting in similar fluidization behavior in a gas flow:

- Group A: Powders falling into this group have a density below 1400 kgm$^{-3}$ and a particle size of about 50–200 μm. Bed expansion at minimum fluidization velocity and prior to bubble formation is characteristic here. Particles are rapidly mixed during fluidization.
- Group B: Particles of this group are most common in fluidized bed processes. They have a density between 1400 and 4000 kgm$^{-3}$ and a particle size between 40 and 500 μm. For these materials, bubble formation starts right at or slightly above the minimum fluidization velocity.
- Group C: Cohesive powders with a particle size below 50 μm fall into this group. Regular fluidization is hardly possible, resulting in fluid channels forming in the fixed bed. Fluidization can be realized by mixing elements or vibration, breaking said channels and reducing the inter-particle cohesive forces.
- Group D: Large particles ($> 500$ μm) with high density (1000–5000 kgm$^{-3}$) belong into this group. For such particles, the gas bubbles during fluidization usually rise

slower than the other gas. If a large portion of the fluidizing gas is entering the bed at the center of the distributor plate, particles will spout, meaning they will follow circular trajectories (rise in the middle, sink down at the wall of the apparatus).

Main applications for fluidized beds in general are chemical processes like combustion, gasification, adsorption, gas and water cleaning, or catalytic reactions, and physical processes like heating or cooling of materials, drying, separation of different particle sizes or density fractions, mixing, and particle formation processes (Mörl et al., 2007). Whereas the chemical processes are partly conducted with liquids as fluidization fluids, the physical applications of fluidized bed technology mainly use gases as fluidization media. This dissertation deals with the physical process of particle formation with fluidization by air.
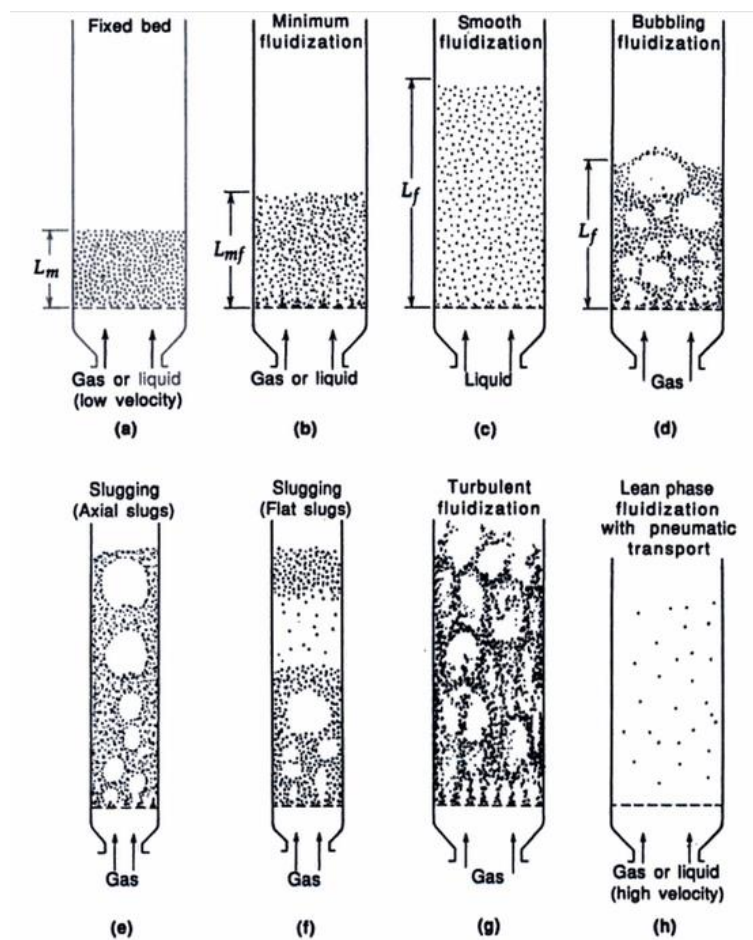


Fig. 2–1. Stages of fluidization for increasing fluid velocity (Kunii and Levenspiel, 1991).

To calculate the onset of fluidization, two dimensionless numbers are necessary. The Reynolds number *Re* is defined as follows:

$$Re = \frac{u_g \cdot d_p}{\nu_g},$$
(2–1)

with superficial gas velocity $u_g$, particle diameter $d_p$ and kinematic viscosity of the fluidizing gas $v_g$. The Archimedes number $Ar$ is calculated from:

$$Ar = \frac{g \cdot d_p^3 \cdot (\rho_p - \rho_g)}{v_g^2 \cdot \rho_g}, \tag{2–2}$$

with gravitational acceleration $g$, particle density $\rho_p$ and gas density $\rho_g$. The Reynolds number at onset of fluidization or minimum fluidization $Re_{mf}$ is derived from the Ergun equation (Ergun and Orning, 1949), describing the pressure drop in a fixed bed. For spherical particles $Re_{mf}$ is defined (Wirth, 2010):

$$Re_{mf} = 42.9(1 - \Psi_{mf})\left[\sqrt{1 + 3.1 \cdot 10^{-4} \frac{\Psi_{mf}^3}{(1 - \Psi_{mf})^2} Ar} - 1\right], \tag{2–3}$$

with bulk porosity at minimum fluidization $\Psi_{mf}$. The value of $\Psi_{mf}$ has to be determined experimentally or is estimated to 0.4 for a randomly packed bed of monodisperse spheres. Thus, the necessary gas velocity for minimal fluidization $u_{g,mf}$ of spheres of a given material is given with $Re_{mf}$ from Eq. 2–3 by:

$$u_{g,mf} = \frac{Re_{mf} \cdot v_g}{d_p}. \tag{2–4}$$

The maximum gas velocity of a fluidized bed is limited by the stationary sinking velocity of the particles. If the gas velocity exceeds the sinking velocity, particles are elutriated from the fluidized bed (pneumatic transport). The sinking velocity is derived from a force balance over a particle (Appendix A, p. 139). Thus, the Reynolds number at elutriation $Re_e$ is given by:

$$Re_e = \sqrt{\frac{4}{3}\frac{Ar}{c_{dg}}}, \tag{2–5}$$

with the drag coefficient $c_{dg}$, which is calculated as follows (Kaskas, 1970; quoted from Gahn and Mersmann, 1999):

$$c_{dg} = \frac{24}{Re_e} + \frac{4}{\sqrt{Re_e}} + 0.4. \tag{2–6}$$

Equation 2–5 has to be solved iteratively for the elutriation velocity:

$$u_{g,e} = \frac{Re_e \cdot \nu_g}{d_p}\,. \tag{2–7}$$

Consequently, successful fluidization is usually achieved for $u_{g,mf} < u_g < u_{g,e}$, depending on the Geldart group of the particles. For Group C particles, additional to an air velocity larger than $u_{g,mf}$, special measures to reduce the inter-particle forces, for example vibrations, have to be realized for successful fluidization.

## 2.2 Particle formation in fluidized beds

This section introduces the micro-processes occurring during particle formation in fluidized beds. The most common research fields, their main findings and their application in industrial processes are presented. Furthermore, quality aspects of particles produced in fluidized beds are discussed.

### 2.2.1 Mechanisms

In SFBP free-flowing particulate solids, so called granules, are produced. Three different sub-processes are distinguished (Fig. 2–2). For spray fluidized bed coating (SFBC) a liquid containing a different solid material than the particles is sprayed into the fluidized bed. The liquid wets the particles, is dried by heated fluidizing air, and leaves solid coating shells, usually protecting the core. If the spray liquid contains the same material as the particles, the resulting granules grow layer-wise, comparable to the coating process, which is called spray fluidized bed layering granulation (SFBLG). But here, the main goal is transferring the solid-containing liquid into a solid, granular state. When the spray liquid acts as a binder, gluing together the fluidized particles, the resulting process is named spray fluidized bed agglomeration (SFBA). Following, the occurring micro-processes during SFBP are discussed, separated according to the respective sub-process under consideration. A summary is given in Tab. 2–1.
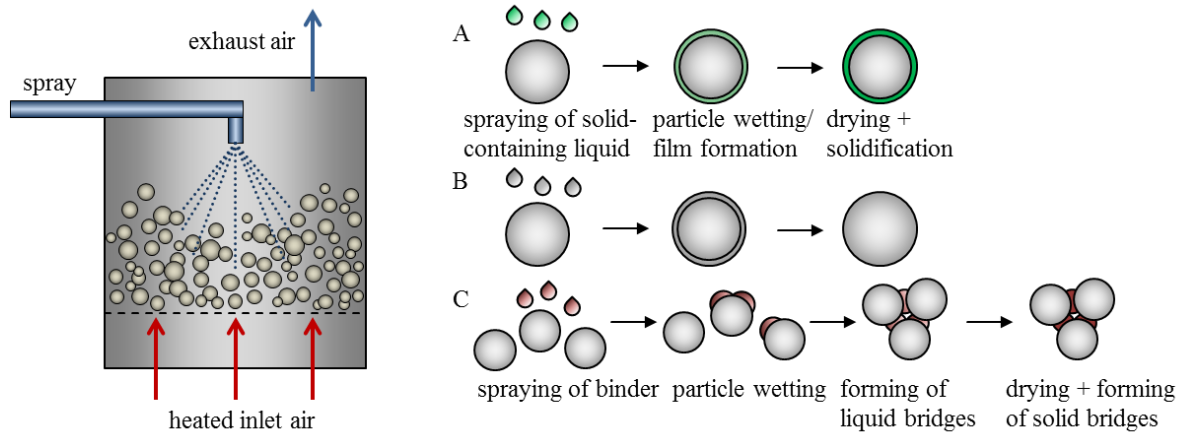
Fig. 2–2. Left: SFBP, right: sub-processes (A: coating, B: layering granulation, C: agglomeration).

*Agglomeration*

A large part of the groundwork regarding agglomeration of particles in general was laid by Rumpf (1958) and Schubert (1982). Inter-particle bonding mechanisms can be separated into five categories (Rumpf, 1958):

- *Solid bridges*: Particles bond via a solid connection. Typical processes using this mechanism are sintering, crystallization of a dissolved material, re-crystallization of a wetted, partly dissolved surface, or solidification of a molten material.

- *Interface forces*: Here, particles stick together in different ways. Liquid bridges, like those formed by a binder solution or a pure liquid, are formed, if the liquid-solid ratio is low. After drying, those liquid bridges are transformed to solid bridges. If more liquid is introduced to the particles, capillary forces become dominant in the agglomerates. If even more liquid is added in a way that the liquid droplets completely encapsulate the particles, the surface tension of the liquid is the dominant agglomeration mechanism.

- *Cohesive forces*: This type of agglomeration occurs, for example, for highly viscous liquid binders. Usually, those viscous binders dry or solidify over time, forming solid bridges. Additionally, adsorption layers may allow for agglomeration. These thin liquid layers (for water $< 30\,\text{Å}$) can fully transfer the molecular adhesion forces between the molecules, as no liquid meniscus is formed for such thicknesses. Usually at rough spots of the particles, the adsorption layers allow for bridge formation. By application of pressure, the contact areas are increased, realizing agglomeration. This mechanism is used, for example, for briquetting.

- *Attraction forces*: The commonly known attraction forces are Van der Waals forces and electro-static forces. The Van der Waals forces are a sum of repulsion and attraction forces, acting even at distances of $100\,\text{Å}$. Van der Waals forces are relatively low, but act without material contact. Other attraction forces are electro-static forces, which usually are evoked by friction through particle movement or comminution. Electro-static forces can be the initial bonding mechanisms, being

        replaced by the larger and more permanent liquid or solid bridges during the agglomeration process.

- *Positive locking*: For branched or chain-like particles, mechanical prevention of movement can be reached by positive locking. The particles can't move relative to each other anymore, thus forming agglomerates.

During SFBA, mainly the first three mechanisms of the list above occur. Liquid or viscous bridges are formed by the sprayed binder or by pure water. Agglomeration phenomena in fluidized beds by using binder solutions was investigated, among others, by Turton et al. (1998) and Iveson et al. (2001). During SFBA usually a dissolved or viscous binder is sprayed onto a fluidized bed of particles (primary particles). Porous particles are partly penetrated and partly covered by the binder and non-porous particles are only wetted by the binder. Upon particle contact on at least one wetted spot, particles will agglomerate, if the liquid is able to dissipate the kinetic energy of the involved particles. If the particles retain a part of their kinetic energy, rebound will occur (Ennis et al., 1991). After drying by the fluidizing air, the rather fragile liquid bridges connecting the particles become more durable solid bridges (Fig. 2–2, right, C). The resulting particles are called agglomerates. Depending on droplet size, nucleation, primary or secondary agglomeration occur (Tab. 2–1). Agglomeration with binder was also investigated by Hampel (2010). He presented batch SFBA experiments, laying the groundwork for the design of agglomeration experiments presented in this dissertation.

Especially with water based binders, water-soluble particles show slightly different agglomeration behavior (Palzer, 2011). Crystalline, water-soluble materials are partially dissolved, when sprayed onto with water. Particles can agglomerate at the liquefied spots. After drying and re-crystallization, solid bridges connect the particles. However, amorphous material, in which the molecules have no regular crystal lattice and free volume exists in between the molecules, will agglomerate differently. The sprayed water migrates into the free volume of the amorphous material and forms a cohesive, sticky patch on the particle, allowing for agglomeration. The particles may sinter together at these sticky spots and form viscous bridges. The materials undergo glass transition upon wetting. After drying, solid bridges remain, connecting the particles (Palzer, 2005, 2010; Avilés-Avilés et al., 2015). As most of the food powders in industry are water-soluble and crystalline, amorphous or a mixture of both (Palzer, 2009), the above mentioned mechanism is mainly applied in food industry to, for example, produce instant powders.

In practice, the glass transition temperature of the wetted material is of particular interest. Depending on the mass fraction of water absorbed $x_w$, the glass transition temperature $T_g$ can be calculated by the Gordon and Taylor equation (Gordon and Taylor, 1952), if the glass transition temperature of the pure solid $T_{g,s}$, the glass transition temperature of water $T_{g,w}$, and the Gordon and Taylor constant $c$ of the solid are known:

$$T_g = \frac{(1 - x_w) \cdot T_{g,s} + c \cdot x_w \cdot T_{g,w}}{(1 - x_w) + c \cdot x_w}. \qquad (2\text{–}8)$$
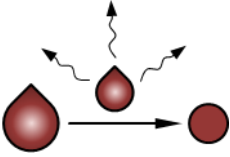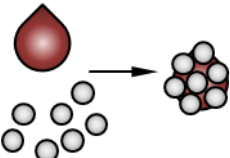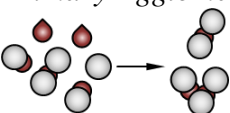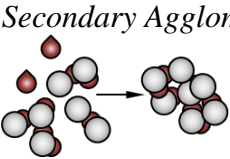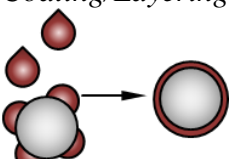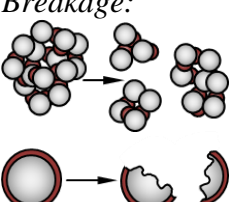
*Coating and layering granulation*

Coating and layering granulation are based on similar principles. The micro-processes during SFBC and SFBLG were investigated by numerous researchers (Uhlemann, 1990; Turton et al., 1998; Zank et al., 2001). If the dissolved solids in the sprayed liquid and the particles in the fluidized bed consist of the same material, the process is called layering granulation. If a different solid is sprayed, the particles are coated, forming a distinctive layer on the seed particles. If the sprayed droplets hit the fluidized particles (seed particles) and do not rebound, they will spread and eventually dry on the particle surface, leaving behind the solids, which form a layer around the particle. Thus, layer-wise growth of the particles is achieved. The resulting particles are called granules. Spray droplets drying prior to particle contact or rebounding from the particle surface may lead to dust formation by overspray (Tab. 2–1). The dust, which is formed by overspray, might be integrated into the granules by new droplets (Grünewald and Kind, 2011). But especially in coating processes overspray represents material loss, as the dust commonly is elutriated at the top of the fluidized bed. For layering granulation processes, dust formed by overspray may agglomerate and serve as new seed particles for the granulation, and thus, is not automatically lost material. Furthermore, agglomeration of seed particles is unwanted, especially in coating processes, as the resulting coating layers may be unevenly distributed and defective, and too large agglomerates may lead to de-fluidization of the whole bed.

A study regarding continuous coating was presented by Hampel (2015), investigating product quality and process behavior. Layering granulation, especially in batch mode, was investigated by Hoffmann (2016). He determined fundamental mechanisms of structure formation of the granules and described the process dynamics of batch layering granulation very well with his population balance model. The work of Hoffmann (2016) is the direct predecessor of this dissertation, laying the groundwork for the continuous SFBLG experiments presented here.

In most SFBP agglomeration and coating/layering may occur in parallel. For very large droplets, nucleation is the predominant process. For droplet sizes matching or smaller than the particle size, usually primary or secondary agglomeration takes place. If the droplets are small compared to the seed particle size, coating or layering is the pre-dominant process (Tab. 2–1). But in practice, droplets and particles possess a size distribution, resulting in mixed phenomena. The process parameters are chosen to either get agglomeration or coating/layering, but the respective other sub-process usually also occurs and is in most cases unwanted. Some researchers investigated the transition from layering to agglomeration. Hemati et al. (2003) reported for droplet sizes of 20–60 μm, that for particles larger than 300 μm layering usually is the dominant process. Below 300 μm, particles are more likely to agglomerate. Saleh et al. (2003) set this boundary at 200 μm, without mentioning the size of the droplets used for their experiments. Typical values for the granule growth rates of SFBP are given by Nienow (1995):

- Agglomeration: 1.7–17 μm·min$^{-1}$
- Layering granulation: <1.7 μm·min$^{-1}$
- Coating: <0.17 μm·min$^{-1}$

Tab. 2–1. Micro-processes during SFBP.

| Mechanism | Description | SFBA | SFBC | SFBLG |
|---|---|:---:|:---:|:---:|
| *Overspray:* | • partial droplet drying prior to particle contact <br> • missing droplet-particle adherence <br> • dust formation | ○ | − | + |
| *Nucleation:* | • $d_d \gg d_p$ <br> • wetting of powder/dust particles <br> • agglomeration to larger clusters | + | ○ | + |
| *Primary Agglomeration:* | • $d_d \approx d_p$ or $d_d < d_p$ <br> • wetting of primary particles and agglomerates <br> • agglomeration of a primary particle to an agglomerate or primary particle at wet spots <br> • drying, particle growth, repetition | ++ | − | + |
| *Secondary Agglomeration:* | • $d_d \approx d_p$ or $d_d > d_p$ <br> • wetting of agglomerates <br> • agglomeration to large clusters at wet spots <br> • drying, particle growth, repetition | ++ | ○ | ○ |
| *Coating/Layering:* | • $d_d \ll d_p$ <br> • spreading of droplets on seed particles <br> • drying/solidification <br> • repetition of wetting and drying <br> • drying, layer-wise particle growth, repetition | ○ | ++ | ++ |
| *Breakage:* | • impact of granule on wall or other granule <br> • agglomerates break into smaller clusters <br> • single particles break into fragments <br> • particle size reduction | + | ○ | ○ |
| *Attrition/Abrasion:* | • particle-wall or particle-particle contact <br> • formation of dust <br> • particle size reduction | + | − | + |

++ main effect, + occurring, − occurring, but unwanted, ○ negligible

Thus, agglomeration usually is the fastest process, as particles are simply glued together to achieve growth. In layering granulation, relatively high spray rates can be achieved with reasonable rates of agglomeration occurring in parallel. During coating, agglomerates are especially unwanted. To prevent excessive agglomeration, usually the spray rate is reduced to prevent the formation of liquid bridges during the process. Without liquid bridges, no durable solid bridges can be formed. But using low spray rates also reduces the growth rate, as also less solid material is sprayed. Consequently, SFBC processes usually have the smallest growth rates, compared to SFBA and SFBLG.

### 2.2.2 Applications

Previous work considering SFBP usually investigated their application for the production of defined industrial products. The following paragraph summarizes a few interesting applications for SFBP.

Goals of SFBA usually are the production of free-flowing powders, improvement of instant properties, or encapsulation of perishable materials, among others. SFBA is used to produce, for example, laundry powders (Boerefijn and Hounslow, 2005), fine chemicals like vitamin mixes (Palzer, 2011), pharmaceutical powders (Benelli et al., 2015), and food powders (Palzer, 2007) like soymilk powder (Jinapong et al., 2008) or encapsulated oils (Turchiuli et al., 2005). In SFBC the main goal is the protection of the core material. SFBC is applied, among others, for micro-encapsulation of bioactive compounds (Meiners, 2012) and anti-oxidants (Coronel-Aguilera and San Martín-González, 2015), for achieving controlled release rates of fertilizers (Donida and Rocha, 2007; Lan et al., 2011) or drugs (Tzika et al., 2003; Hacene et al., 2016), or the masking of tastes and odors (Teunou and Poncelet, 2002). SFBLG is mainly used to transfer a solid-containing liquid to the solid state. This is done mainly for fertilizers (Wang et al., 2013).

### 2.2.3 Product quality

The quality of a granular product is directly linked to its physical and chemical properties. During granulation, several properties are influenced and changed to produce the desired product. A key property is the particle size. Generally, larger particles are easier to handle, as they do not emit dust and flow easily, due to the low inter-particulate forces in relation to their weight forces. Particle morphology, such as particle porosity and surface structure, are also very important, as they affect various product quality aspects. Granules with rough surfaces are hard to handle, as the inter-particulate forces are enhanced due to larger and possibly interlocked contact areas of the particles. High porosity of granules or coating shells enhances the dissolution rate (Nakano and Yuasa, 2001), lowers the retarding capacity of the active ingredient and decreases the bulk density. The bulk density of granules is an important aspect in terms of logistics. High bulk densities mean smaller packaging for the same mass sold, reducing transportation costs.

Furthermore, the moisture content of the produced granules is of high importance. On the one hand, it influences the shelf life of degradable products, especially in the food and

pharmaceutical industry. On the other hand, from an economical point of view, granules should not be too dry, as the water in the product is sellable mass, as long as it is within the specifications dictated by the shelf life. Further minor quality aspects are the granule color, which could be important for advertisement, the durability in resisting mechanical stress to maintain an intact product, the friability to avoid dust formation during handling, etc.

SFBP feature some specific characteristics with regards to product quality. High mass and energy transfer rates allow for short process times or low process temperatures, enabling the handling of thermo-labile material. Good mixing of granules in the fluidized bed results in rather narrow particle size distributions in batch operation, which is especially important in the pharmaceutical industry, where product granules are supposed to have similar contents of the active pharmaceutical ingredient (API). Furthermore, the particle formation process during SFBC and SFBLG usually yields granules of high sphericity, enhancing product handling due to good flowability.

### 2.2.4 Structure formation

In SFBP, the process parameters determine the structure of the product particles. Structural properties are for instance the morphology of the particle surface, characterized for example by a surface roughness value. Also the inner structure of granules, for example the particle porosity is a key structural parameter. For agglomerates, especially the orientation of the primary particles in the agglomerate, defining a kind of agglomerate surface roughness, is a key factor. Previous work, regarding structure formation of particles in SFBP, is discussed in this section.

For SFBC processes, investigations regarding particle morphology have to be distinguished with respect to the type of sprayed liquid. If the coating liquid is containing a dissolved solid, especially the drying parameters control the structure formation of the product particles. An example for batch coating of $\gamma$-$Al_2O_3$ particles with a sodium benzoate solution ($x_{NaB} = 0.3$), which was conducted in the frame of this dissertation, is shown in Fig. 2–3. For larger temperatures and lower spray rates, the coating shell becomes denser and smoother. If the coating liquid contains suspended particles, the importance of the drying conditions is reduced, and parameters like composition of the suspension and atomizing pressure mainly determine the structure of the coating layer. A study regarding SFBC of $\gamma$-$Al_2O_3$ particles with a suspension made from limestone powder and hydroxypropyl methylcellulose (HPMC) as a binder was published by the author of this thesis (Schmidt et al., 2017b). Here, different drying conditions did not influence the coating shell morphology significantly (Fig. 2–4, top row). But with increased atomizing pressure of the spray nozzle and with decreased mass fraction of limestone and HPMC in the suspension, the coating shell became denser and smoother (Fig. 2–4, middle and bottom row). Consequently, the type of spray liquid (solution or suspension) determines the influencing process parameters for structure formation. To access structural parameters like roughness and porosity, different measurement systems are available. Image acquisition by, for example, light microscopy or scanning electron microscopy (SEM) followed by image analysis gives a visual impression of the particle surface and allows for the calculation of particle roughness, average layer thickness and

particle size. The methods are explained in detail in Chapter 3. The inner structure of coating shells and granules, namely the porosity, is a key product quality factor. To access the inner structure of granules in a non-destructive way, micro-computed tomography (μ-CT) is used. Sondej et al. (2015) described a method using μ-CT to determine the coating shell thickness distribution and average coating shell porosity for particles produced in batch SFBC.
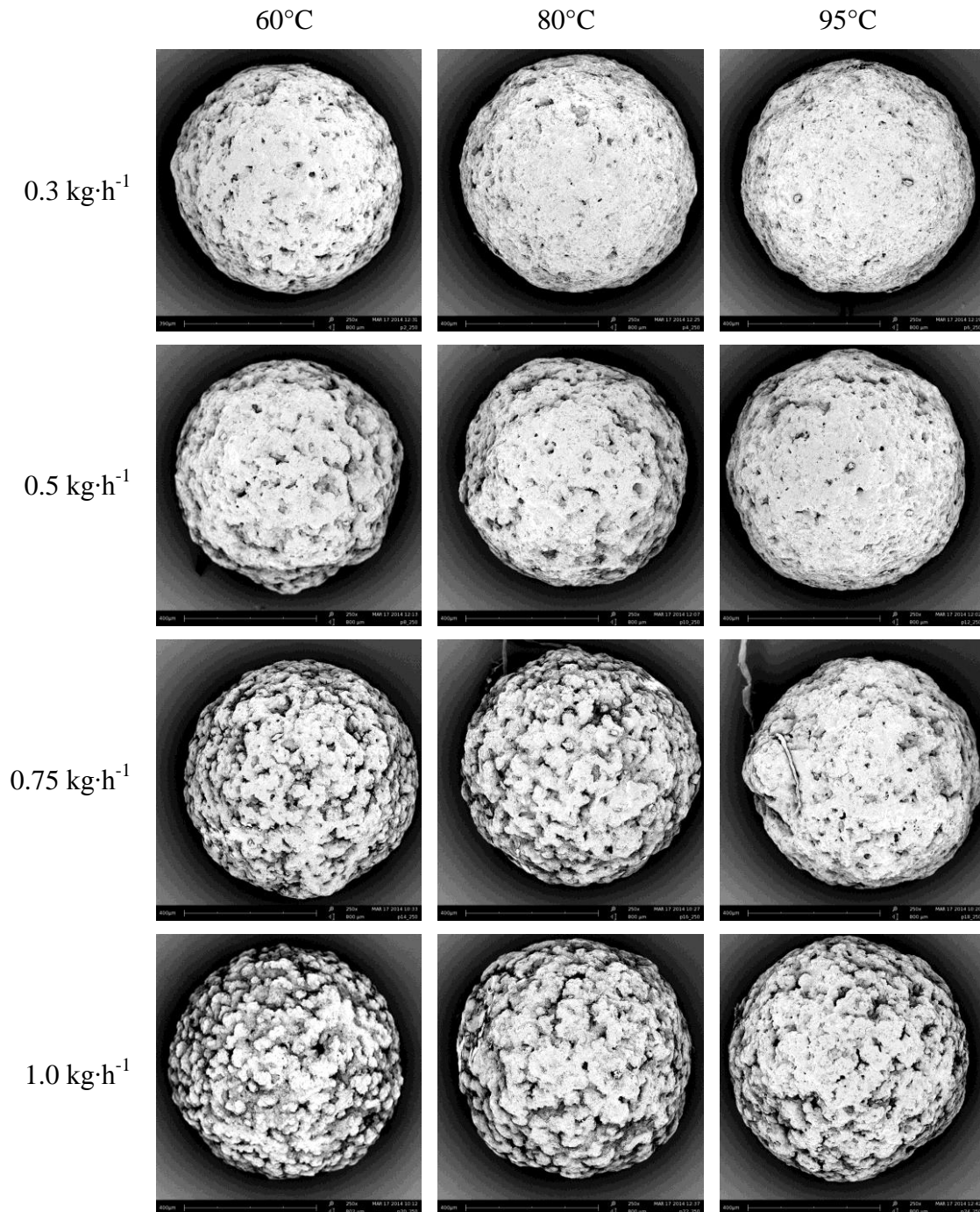


Fig. 2–3. SEM images of the typical shell morphology for batch SFBC of $\gamma$-$Al_2O_3$ particles with sodium benzoate solution at different inlet gas temperatures (columns) and different spray rates (rows).
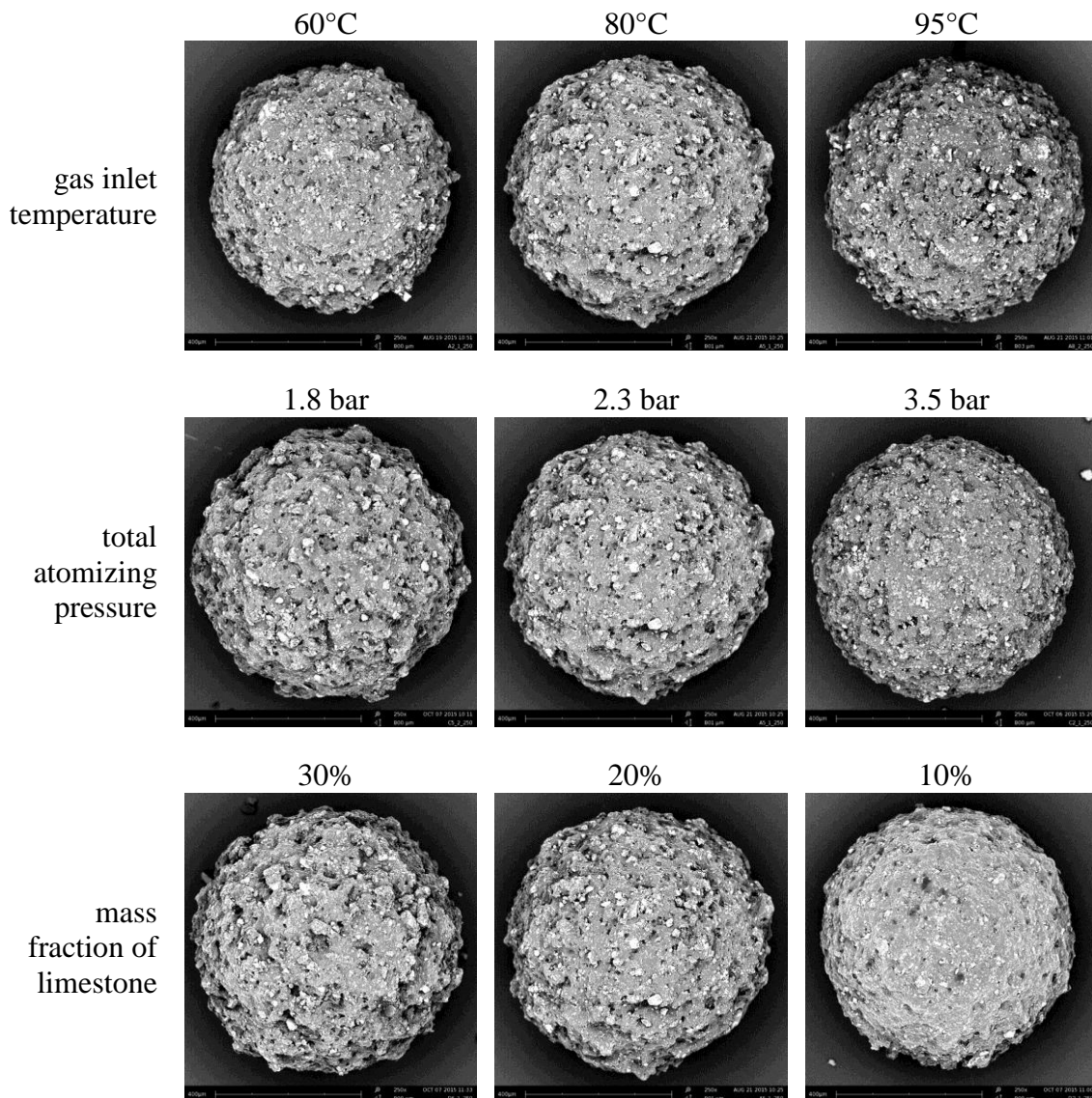
Fig. 2–4. SEM images of the typical shell morphology for batch SFBC of $\gamma$-Al$_2$O$_3$ particles with a suspension of limestone and HPMC at different inlet gas temperatures (top row), atomizing pressures (middle row) and mass fraction of limestone in the suspension (bottom row). The middle column shows the same particle from the reference experiment in all three rows (Schmidt et al., 2017b).

For SFBLG and SFBA the above described methods for evaluating particles produced by SFBC can be adapted. Microscope images and μ-CT measurements are commonly used to determine the granule roughness and porosity, respectively.

As stated above, for SFBC processes with aqueous solutions, the structure formation of the coating shell is mainly determined by the drying conditions. To summarize the influencing psychrometric parameters, Ebey (1987) introduced the Environmental Equivalency factor EE, which was adapted by Strong (2009):

$$EE' = \frac{Y_{sat} - Y_{in}}{Y_{out} - Y_{in}} = \frac{1}{E} \, , \qquad\qquad (2\text{--}9)$$

where $Y_{sat}$, $Y_{in}$ and $Y_{out}$ are the absolute moisture contents of the fluidizing gas at saturation, inlet and outlet, respectively, and $E$ is the vaporization efficiency, which was originally derived by Reiland et al. (1983). For a constant value of $EE'$, Strong (2009) claims that the resulting coating structure will be similar, regardless of the actual process parameters or the level of scale-up. The values of $EE'$ are in the range from unity (saturation) to infinity (no evaporation), which makes this factor mathematically impracticable. However, inverting $EE'$ yields the more practicable vaporization efficiency $E$, which ranges from zero (no evaporation) to unity (saturation). Rieck et al. (2015) use the drying potential $\Pi$ to describe their coating experiments. The drying potential describes the remaining capacity of the outlet fluidizing air to evaporate water. Thus, the drying potential is given by:

$$\Pi = 1 - E = 1 - \frac{1}{EE'} = \frac{Y_{sat} - Y_{out}}{Y_{sat} - Y_{in}} \, . \qquad\qquad (2\text{--}10)$$

The drying potential ranges from zero (completely saturated outlet air, no remaining drying capacity) to unity (completely dry air, full remaining drying capacity). Rieck et al. (2015) linked the drying potential to the coating shell porosity, which was measured via µ-CT. In their research, low drying potentials yielded porous coating shells and vice versa. This was attributed to the re-crystallization behavior of the dissolved salt (sodium benzoate). Humid process conditions, resulting in low drying potentials of the exhaust air, favored crystal growth upon drying. Slow drying of the coating solution led to the formation of large crystals, and thus, porous structures. However, dry process conditions led to fast drying of the coating solution. Thus, a lot of small crystalline nuclei were formed, which had little time to grow. This more precipitation-like solid formation led to denser coating shells (Rieck et al., 2015). Similar behavior was confirmed by the author of this thesis and was shown in Fig. 2–3.

In addition to process parameters, Link and Schlünder (1996) reported a dependency of the coating shell morphology on the porosity of the core material. Droplets were spreading better on a porous core material, resulting in a smoother and more uniform coating. Rieck et al. (2015) confirmed this observation, obtaining larger coating shell porosities for non-porous glass beads as core particles, compared to the porosity of the coating layer formed at similar process conditions on porous $\gamma$-Al$_2$O$_3$ particles. But contrary to Rieck et al. (2015), Link (1997) reported denser shells for coating with salt solutions for intense drying (high drying potential) and vice versa. But Link (1997) did single particle coating experiments with a time-separation of spraying and drying, neglecting the simultaneous drying and wetting present in a fluidized bed. Additionally, droplet deposition on the particles and accumulation of droplets on a particle will occur differently in a fluidized bed and a single particle experiment. Consequently, Link (1997) might have observed effects known from spray drying, where high temperatures (high drying potential) might lead to rupture of droplets during drying, resulting in rough and porous structures.

For SFBA with non-porous glass beads, Dadkhah and Tsotsas (2014) evaluated μ-CT images from agglomerates and reported high agglomerate porosity for high agglomeration rates (for example low gas temperature, high spray rate) and vice versa. For SFBA of partially amorphous maltodextrin Pashminehazar et al. (2016) reported open and fluffy agglomerates, but no relationship between process parameters and structure development was given.

## 2.3 Continuous particle formation in fluidized beds

For a continuous particle formation process, seed particle supply and product discharge have to be realized. The supply of new primary particles for continuous SFBA or new seed particles for SFBC is usually done externally. This means, material similar to the initial feed material in the fluidized bed is supplied to the granulator during the continuous process by, for example, a wheel sluice or a double pneumatic sluice gate. For SFBLG, seed particles may also be provided internally by overspray (Tab. 2–1). Internal seed particle supply simplifies the design of the granulator and the whole process, as seed particles do not have to be produced separately, for example, by spray drying. The product discharge is usually done in a classifying way to meet the respective necessary product particle size. Two basic principles for classifying discharge are used: Internal and external separation (Fig. 2–5). For internal separation, the classifying device, for example a classifying tube or zig-zag sifter, is directly connected to the fluidized bed. Particles are only discharged, if their sinking velocity exceeds the gas velocity in the tube. With increasing particle diameter during granulation, also the sinking velocity of the granules increases. The diameter, at which a particle's sinking velocity equals the gas velocity of the classifying air, is called separation diameter $d_{sep}$. It is calculated from Eqs. 2–5 and 2–7 to:

$$d_{sep} = \frac{3u_{class}^2 \rho_{class} c_{dg}}{4(\rho_p - \rho_{class})g}, \qquad (2\text{–}11)$$

with the velocity of the classifying air $u_{class}$ and density of the classifying air $\rho_{class}$. As the drag coefficient $c_{dg}$ depends on the Reynolds number (Eq. 2–6), which is dependent on the particle diameter (Eq. 2–1), $d_{sep}$ has to be calculated via iteration. Consequently, the product size range is controlled by the air velocity, and, thus, the air volume flow rate in the classifying tube.

In contrast, in case of external separation, particles are ideally discharged in a non-classifying way. Then, the discharged particles are fed, for example pneumatically, to a classifying device, for example a sieve, outside of the granulator. The particles are separated into oversize, undersize, and product fraction. The oversize fraction is milled and returned to the granulator alongside with the undersize fraction. The milled oversize particles serve as additional seed particles for the layering granulation process or additional primary particles and agglomeration partners during continuous SFBA. With external separation, the product size range is solely controlled by the mesh widths of the used sieves.

To prevent excessive filling or emptying of the granulator, the bed mass is usually kept constant. For external separation, the discharged particle mass flow rate is controlled by the discharge device. If a wheel sluice is used, the rotational speed of the sluice controls the mass flow rate of discharged particles. If, as shown in Fig. 2–5 B, material is discharged through a tube, an air volume flow controls the amount of discharged particles to keep the bed mass constant. In this case, a slight pre-classifying occurs before the material is finally separated by the external sieve. But this classifying effect of the discharge air is small compared to the effect of the sieve. In case of internal separation, it is rather difficult to maintain a constant bed mass. A controlled classifying air mass flow can be used to keep the bed mass constant, but this will directly change the size range of the product.
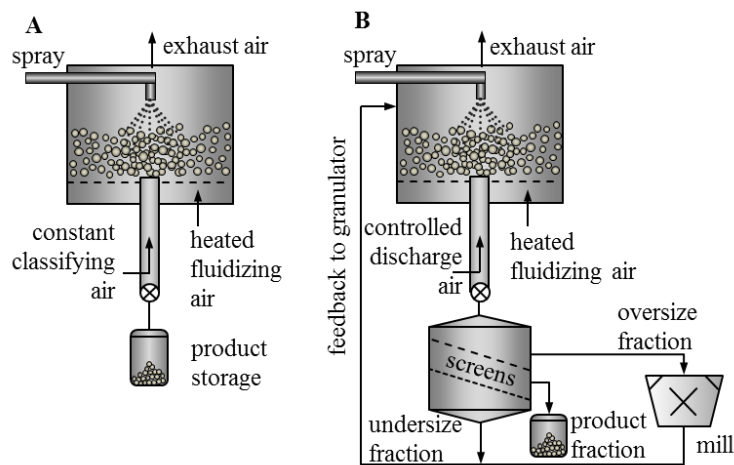


Fig. 2–5. Classifying product discharge. A: internal separation, B: external separation.

# 2.4 Modeling of continuous spray fluidized bed processes

This section gives an overview about modeling concepts for continuous SFBP known from literature. After introducing the basic modeling, the results of different simulation studies regarding process behavior, especially of SFBLG processes, are presented. Special consideration is given to the modeling of the process kinetics and their influence on process behavior. Important experimental parameters and their consideration in the presented studies are discussed. From the discussion, conclusions for the parameters to be investigated experimentally in this dissertation are drawn.

### 2.4.1 General modeling concepts

In SFBP, the interesting particle property is usually a distributed quantity. In most cases, this particle property is the distributed particle size. But also quantities like particle volume, particle temperature, or particle moisture content can be distributed. The most common approach to model distributed particle properties are population balance equations (PBE). A PBE can describe the temporal evolution of the number distribution density $n$, with respect to

internal coordinates like size, temperature or moisture content, and with respect to external coordinates in space (location/position). The concept of PBE has been applied to growth processes during crystallization (Randolph and Larson, 1971), SFBA (Hounslow et al., 1988) and SFBLG (Heinrich et al., 2002b). A good overview is given by Ramkrishna (2000).

Considering a fluidized bed as a well-mixed system (Burgschweiger and Tsotsas, 2002), the external coordinates are neglected and the PBE for a growth process, concerning a distributed particle size, reads:

$$\frac{\partial n}{\partial t} = -\frac{\partial (G \cdot n)}{\partial d} + B - D \, , \tag{2–12}$$

with the growth rate $G$, a birth term $B$ and a death term $D$. Depending on the type of growth process under consideration, the three terms take different forms (Sections 2.4.2 and 2.4.3).

In recent years, with advanced computational power and tools, coupled computational fluid dynamics (CFD) and discrete element methods (DEM) became more important in modeling fluidized bed systems. Actual growth processes are difficult to describe, but particle collisions and trajectories can be simulated well. For a pseudo 2-D fluidized bed, Jiang et al. (2017b) present a method to track particle movement and collisions. Also drying during SFBLG can be modeled using CFD methods (Li et al., 2012). Combining CFD-DEM with PBE, also structure formation can be accounted for. Nucleation in continuous SFBA was investigated (Li et al., 2013), agglomeration during spray drying (Jaskulski et al., 2015), and droplet deposition, residence time and particle collisions in SFBC (Jiang et al., 2017a), among others.

Not knowing the exact growth kinetics for SFBP, Monte Carlo (MC) methods can be applied for compensation. MC modeling for SFBP is a stochastic method, where a sequence of discrete micro-processes is applied to a finite set of particles (Rieck et al., 2016). Terrazas-Velarde et al. (2011) and Dernedde et al. (2012) showed the application of MC modeling to SFBA processes. For SFBA, the exact agglomeration kinetics is usually not known. Modeling the occurring micro-processes like binder droplet deposition, particle collision, etc. and implementing them in a Monte Carlo simulation enables the calculation of the agglomeration process. The agglomeration kinetics from the MC simulation can be used to improve PBE simulations. Additionally, Rieck et al. (2016) showed the application of the MC method to the simulation of a batch SFBC process. There, the growth kinetics is usually known, but the discrete modeling allows for the calculation of additional parameters like the coating shell thickness distribution, which are not accessible via PBE modeling.

### 2.4.2 Special considerations for SFBLG

Basic modeling of continuous SFBLG has already been done by Mörl et al. (1978) without the use of PBE. These authors introduced the idea of area-equivalent, spherical growth of the particles and used a simplified model, predicting the PSD of the product during steady-state operation of a continuous SFBLG process. The model was modified to account for newly

generated seed particles by overspray (Mörl, 1980). On this basis, Heinrich et al. (2002a) developed a PBE model describing continuous SFBLG using a similar growth term, but without considering overspray. Vreman et al. (2009) enhanced the understanding of the growth term by applying a modified growth rate considering the fraction of generated overspray $o$ to his PBE model of continuous SFBLG with internal separation. Thus, the growth term $G$ reads:

$$G = \frac{2 \cdot x_s \cdot \dot{M}_{spray} \cdot (1 - o)}{\rho_{part} \cdot S_{part,t}}, \tag{2–13}$$

with the mass fraction of solids in the spray $x_s$, the mass flow rate of the spray solution $\dot{M}_{spray}$, the particle density $\rho_{part}$, and the total surface area of all particles in the fluidized bed $S_{part,t}$. Following the understanding of Vreman et al. (2009), the mass fraction of overspray $o$ is variable, especially during the transient start-up period of a continuous SFBLG process. In top-spray configuration of the spray nozzle and for an empty bed, the whole sprayed mass contributes to overspray formation ($o = 1$). For a successively filling bed up to the nozzle height, $o$ is considered to decrease linearly. For bed heights larger than the nozzle height, the overspray fraction stays at a constant low level $o^*$ (Fig. 2–6). Following the understanding of Mörl (1980) and Vreman et al. (2009), the mass fraction of overspray directly contributes to dust formation serving as new seed particles for the layering process. These seed particles are accounted for in the birth term $B$.
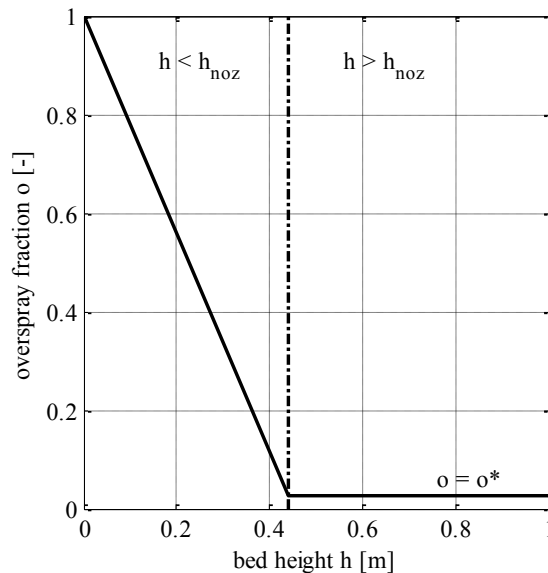


Fig. 2–6. Estimated overspray behavior during SFBLG.

In continuous layering granulation the death term $D$ denotes the number density distribution flow rate of the discharged particles $\dot{n}_{out}$. Depending on the choice of discharge (internal or external separation) different discharge functions are applied. In case of external separation,

particles are discharged non-classifying, which can be modeled with a drain factor *DF* (Bück et al., 2015):

$$D_{Ext} = \dot{n}_{out} = DF_{Ext}\dot{n}_{bed} \; . \tag{2–14}$$

The particles are then separated externally by two sieves with the separation functions for the oversize sieve $\kappa_o$ and the undersize sieve $\kappa_u$. The oversize particles are milled and recycled to the fluidized bed together with the undersize particles (Bück et al., 2015):

$$\dot{n}_{rec} = (1 - \kappa_o) \cdot (1 - \kappa_u) \cdot \dot{n}_{out} + \dot{n}_{mill} \; , \tag{2–15}$$

with the number density distribution flow rate of the recycled particles $\dot{n}_{rec}$ and of particles crushed in the mill $\dot{n}_{mill}$, which depends on the milling characteristics and the number density distribution flow rate of the oversize particles $\kappa_o \cdot \dot{n}_{out}$. The number density distribution flow rate of the product is given by:

$$\dot{n}_{prod} = (1 - \kappa_o) \cdot \kappa_u \cdot \dot{n}_{out} \; . \tag{2–16}$$

For continuous SFBLG with internal separation, *D* can be expressed by a drain factor and the Heaviside function *H* around the separation particle diameter $d_{sep}$ (Vreman et al., 2009):

$$D_{Int} = \dot{n}_{out} = DF_{Int}H(d - d_{sep}) \; . \tag{2–17}$$

Corresponding to the different types of product discharge, the according birth terms *B* are defined. For external separation, *B* includes potentially added external seed particles $\dot{n}_{seed,1}$, seed particles formed internally by overspray $\dot{n}_{seed,2}$, and the recycled particles from the sieve and mill $\dot{n}_{rec}$:

$$B_{Ext} = \dot{n}_{seed,1} + \dot{n}_{seed,2} + \dot{n}_{rec} \; . \tag{2–18}$$

In case of internal separation, no particles are recycled. The birth term then reads:

$$B_{Int} = \dot{n}_{seed,1} + \dot{n}_{seed,2} \; . \tag{2–19}$$

Some authors also include the idea of separate spraying and drying zones with continuous exchange between the zones in their modeling of SFBLG (Wnukowski and Setterwall, 1989;

Rieck et al., 2015). The additional mixing effect accounts for widening of the PSD during the process by dispersion.

For the presented way of modeling continuous SFBLG, special knowledge regarding the comminution in the mill, and the separation function of the sieves (external separation) or the separation function of the classifying tube (internal separation) are necessary. Especially the milling function usually has to be derived from experimental data, but is commonly approximated (Bück et al., 2015). The described models already allow for the consideration of key process parameters like mass fraction of solids in the spray $x_s$ (Eq. 2–13). Hoffmann (2016) has already accounted for the layer porosity during continuous SFBLG, influencing the particle density $\rho_{part}$ in $G$ (Eq. 2–13), by applying an empirical correlation. But the combined effect of parameters like drying conditions, droplet sizes, or possible agglomeration on process dynamics has not yet been considered for continuous SFBLG.

### 2.4.3 Special considerations for SFBA

For the modeling of SFBA processes by PBE, usually the particle volume is taken as internal coordinate to simplify the equations. In ideal agglomeration, the sprayed binder is only used to aggregate the primary particles, preserving the total particle volume in a batch process. Growth by layering is usually neglected, and thus $G = 0$. But birth and death terms are formulated more complexly by integro-differential equations. Considering two particles with the volumes $v_1$ and $v_2$-$v_1$, the volume of the resulting agglomerate is $v_2$ by the addition of the single volumes. The birth term $B$ then reads (Bück et al., 2016a):

$$B = B_{agg}(t, v_2) + \dot{n}_{nuc} + \dot{n}_{rec} , \qquad (2\text{–}20)$$

with the birth rate of agglomerates $B_{agg}$, the number density distribution flow rate of fed nuclei $\dot{n}_{nuc}$, and the number density distribution flow rate of the recycled particles $\dot{n}_{rec}$ (only for external separation; for internal separation $\dot{n}_{rec} = 0$). $B_{agg}$ is defined as follows:

$$B_{agg}(t, v_2) = \frac{1}{2} \int_{v_0}^{v_2} \beta(t, v_1, v_2 - v_1) n(t, v_1) n(t, v_2 - v_1) \mathrm{d}v_1 , \qquad (2\text{–}21)$$

with the agglomeration kinetics $\beta$, which is usually separated into a time-dependent part $\beta_0(t)$, the agglomeration frequency, and a volume dependent part $\beta^*(v_1, v_2\text{-}v_1)$, the agglomeration kernel, leading to the expression: $\beta(t, v_1, v_2\text{-}v_1) = \beta_0(t) \cdot \beta^*(v_1, v_2\text{-}v_1)$ (Bück et al., 2016a). The agglomeration frequency is usually fitted in the described models. The agglomeration kernel has to be determined empirically or is estimated by consideration of the flow-field or relevant micro-processes. An overview is given by Hampel (2010) and Hussain (2014).

The death term $D$ for continuous SFBA considers the reduction in a volume size class due to agglomeration of particles to a larger size class by $D_{agg}$ and the discharge of particles $\dot{n}_{out}$ (Bück et al., 2016a):

$$D = D_{agg}(t, v_2) + \dot{n}_{out} \, , \tag{2–22}$$

with $D_{agg}$:

$$D_{agg}(t, v_2) = \int_{v_0}^{\infty} \beta(t, v_1, v_2) n(t, v_1) n(t, v_2) \mathrm{d}v_1 \, . \tag{2–23}$$

The particle discharge $\dot{n}_{out}$ is modeled similarly to continuous SFBLG (Eqs. 2–14 and 2–17). The agglomeration kinetics can be extracted from experiments, but recent research is also able to nearly predict the agglomeration kinetics by means of Monte Carlo simulations (Terrazas-Velarde et al., 2011) or PBE simulations (Hussain et al., 2015).

### 2.4.4 Process dynamics

In this section, simulation results from literature are discussed, giving an impression of the process dynamics to be expected from continuous SFBLG and SFBA. The results mainly consider continuous SFBLG, as few studies were found regarding continuous SFBA.

Usually, in operation of continuous SFBP a steady state is wanted. This means, equilibrium between all particle mass flows and the sprayed solids has been established. Thus, the bed mass, particle size in the fluidized bed and product, product mass flow rate, growth rate, product moisture content, but also other process parameters like bed and outlet temperature, are constant over time. This steady state can only be achieved after the initial hold-up (bed mass of particles at the start) has been discharged and replaced by granules formed entirely by new seed particles (Heinrich et al., 2002a) during layering granulation or new primary particles during agglomeration.

The process behavior of continuous SFBLG has been widely investigated by simulations. Based on Mörl et al. (1978) and Mörl (1980), Heinrich et al. (2002a) developed a population balance model, which was able to predict the transient start-up period of a continuous SFBLG process and its final steady or unsteady state. They modelled internal and external separation, and simulated seed particle supply internally and externally. Heinrich et al. (2002a) predicted oscillations of the PSD in the fluidized bed for certain parameter regimes. But, they presented only one experiment with internal separation as validation for the entire model. A systematic experimental investigation was not given. Investigation of continuous SFBLG by means of simulations largely expanded from then on. Often, non-stationary process behavior is reported, resulting in, for example, oscillating PSD (Tab. 2–2).

Heinrich et al. (2003) reported self-sustained oscillations of the PSD for fine milling, and damped oscillations of the PSD for coarse milling in continuous SFBLG with external separation. Based on the findings of Heinrich et al. (2002a) and Heinrich et al. (2003), Drechsler et al. (2005) presented a comprehensive simulation study regarding continuous SFBLG with external separation. They confirmed the process behavior regarding milling, and additionally reported a stabilizing effect of seed particle formation by overspray. Using bifurcation and stability analysis, Radichkov et al. (2006) qualitatively identified stable and unstable operation regions for continuous SFBLG by using mass-based PBEs. Vreman et al. (2009) developed a PBE model for continuous SFBLG with internal separation, being able to describe oscillations of the PSD in a set of industrial data. In their understanding, the oscillations of the PSD resulted from bed height-dependent overspray generation, as described earlier (Fig. 2–6). For simulating the continuous SFBLG of urea, Cotabarren et al. (2010) also reported the occurrence of oscillations of the PSD, mainly depending on the operation of the sieves used for external separation. In their follow-up publication, Cotabarren et al. (2011) motivate the need for process control by their findings regarding the occurrence of unsteady operation regions for continuous SFBLG. Oscillations in the PSD were also reported from further simulation studies of the continuous SFBLG process (Dosta et al., 2010; Bück et al., 2011; Bertin et al., 2013). Based on the described simulation studies, control concepts were developed, to prevent unsteady process behavior or to return a SFBLG process to the steady state. Concepts to stabilize continuous SFBLG with internal separation (Palis et al., 2012), external separation (Palis and Kienle, 2012, 2014) and concerning both discharge types (Bück et al., 2015) were presented. Recent work on control concepts for continuous SFBLG processes also included the effect of zone formation (spray and drying zone) on process behavior (Dreyschultze et al., 2015; Bück et al., 2016b; Neugebauer et al., 2017). Applying a bifurcation analysis to a 2-zone PBE model, Dreyschultze et al. (2015) reported a reduction of the unsteady region for continuous SFBLG with external separation. Bück et al. (2016b) confirmed these findings and presented a stability regime map for different sizes of the spray zone. With internal separation, the influence of zone formation on process behavior was moderate (Neugebauer et al., 2017). But Neugebauer et al. (2017) reported a dependency of process stability on the volume flow rate of the sprayed liquid and the separation diameter of the discharged product based on their numerical investigation. They defined a stable parameter region, and a region, where self-sustained oscillations of the PSD occurred.

Tab. 2–2. Selection of publications focusing on/mentioning PSD oscillations for SFBLG.

| Year | Author | Comment |
|---|---|---|
| 1998 | Schütte et al. | German patent, only one set of experimental data for oscillating mean diameter, without further interpretation and explanation |
| 2002 | Heinrich et al. | presentation of a PBE model; report of slight oscillations in PSD in the start-up period in case of fine milling (external separation) |
| 2003 | Heinrich et al. | PBE model describing self-sustained PSD oscillations for fine milling during external separation |
| 2005 | Drechsler et al. | investigation of spray fluidized bed layering by simulation, description of oscillations of PSD by simulation |
| 2006 | Radichkov et al. | bifurcation and stability analysis, presentation of parameter regimes for PSD oscillations and steady-state operation |
| 2009 | Vreman et al. | presentation of one set of industrial data as a basis for simulations showing oscillations of PSD for internal separation |
| 2010 | Cotabarren et al. | simulations show oscillating PSD data |
| 2010 | Dosta et al. | description of PSD oscillations in simulation |
| 2011 | Bück et al. | description of oscillatory regimes in simulations |
| 2011 | Cotabarren et al. | PSD oscillations as an argument for the need of process control |
| 2012 | Palis and Kienle | application of feedback control to stabilize simulations featuring oscillating PSD for continuous SFBLG with external separation |
| 2012 | Palis et al. | stabilization of continuous SFBLG with internal separation |
| 2013 | Bertin et al. | PSD oscillations as an argument for the need of better models to describe spray fluidized bed layering |
| 2014 | Palis and Kienle | PSD oscillations shown and controlled for external separation |
| 2015 | Bück et al. | PSD oscillations as an argument for the need of feedback control in simulations for continuous SFBLG with internal and external separation |
| 2015 | Dreyschultze et al. | bifurcation analysis shows PSD oscillations for certain parameter regimes in case of continuous 2-zone SFBLG with external separation |
| 2016 | Bück et al. | stability analysis of continuous SFBLG with external separation and zone-formation showed oscillations in PSD |
| 2017 | Neugebauer et al. | stability analysis of continuous SFBLG with internal separation and zone-formation showed oscillations in PSD |

Experimental observation of oscillations in PSD is rarely found in literature. Schütte et al. (1998) and Vreman et al. (2009) each present one set of industrial data, featuring PSD oscillations. Hoffmann (2016) presents six continuous SFBLG experiments, thereof five conducted for 8–12 h and one conducted for 21 h of process time. He varies mass flow rate and inlet temperature of the fluidizing gas simultaneously, impeding the identification of clear influences of one process parameter on process stability. Due to the rather short process times for continuous SFBLG processes and the focus of his work on batch experiments and product quality, the experiments of Hoffmann (2016) served the experimental planning in this dissertation in terms of investigated parameter regimes. A systematic experimental study of SFBC has been presented by Hampel (2015). Here, the focus is on comparison between batch and continuous operation and the resulting product quality. The experiments presented by Hampel (2015) all reached the steady state within 10 h of process time, and no unusual process dynamics have been reported. A systematic experimental investigation of the process dynamics of continuous SFBLG was not yet presented.

Continuous SFBA has been modelled on the basis of the work of Hounslow (1990). He used population balance equations to predict the resulting product PSD. He did not investigate the process dynamics, as he only simulated the steady state behavior of the process. Boerefijn and Hounslow (2005) elaborate on SFBA in general and present only one set of experimental results to validate their model for continuous SFBA in steady state. Again, the transient starting behavior and possible unsteady states are not considered. In the work of Bück et al. (2016a) a simulation study of continuous SFBA is presented. They describe the occurrence of damped oscillations in PSD for certain agglomeration frequencies and diameters of milled oversize particles. But a systematic experimental study regarding SFBA, confirming the simulation studies, was not found in literature.

## 2.5 Goal of the thesis

To overcome the shortage of experimental data published so far, this dissertation investigates the process dynamics and the resulting product quality of continuous SFBLG and continuous SFBA by systematic experiments.

For continuous SFBLG parameter regimes leading, on the one hand, to oscillating PSD and, on the other hand, to steady state operation are identified. The effect of the variation of process parameters like gas temperature, gas mass flow rate and spray mass flow rate on the process behavior and product quality is investigated. Additionally, the effect of internal and external classifying product discharge on process dynamics and particle properties is examined. For experiments with internal classifying product discharge, also the classifying air velocity is varied. Accordingly, for experiments with external separation the power level of the mill is varied. In steady state experiments, the average granule growth rate is determined. The average particle size, the average surface roughness and the porosity of the product particles are defined as product quality aspects. Changes in process conditions are also linked to changes in product quality.

For continuous SFBA, an investigation similar to the continuous SFBLG experiments is conducted. Process dynamics are investigated with respect to nuclei feed mass flow rate and type of product discharge (internal or external classifying). According to the SFBLG experiments, for continuous SFBA with internal separation, the classifying velocity is also varied, and for external separation the mill power level is changed. The drying conditions remain constant for this experimental investigation, as even small changes in drying parameters jeopardize the ability of conducting the continuous SFBA experiments. Higher spray rates and lower temperatures lead to excessive lumping and de-fluidization. Reduced spray rates and increased temperatures nearly prevent the agglomeration process. For experiments in steady state the average agglomerate growth rate is calculated. Again, the effect of process conditions on product quality is investigated. The average product agglomerate size is measured, and product particles of all experiments are compared regarding their structure, using the concept of fractal dimension to describe the agglomerates' level of compactness.

# 3 Measurement methods

The following chapter describes in detail the used measurement systems and methods, as well as the evaluation of measured data to obtain product quality parameters. Product quality parameters under consideration are particle size distribution and average particle diameter, moisture content in the sense of mass fraction of water, and particle morphology, namely granule porosity, granule surface structure, and agglomerate structure.

## 3.1 Particle size distribution

### 3.1.1 Theory

In particle technology, the probability distribution of particle size in a particle population is of particular interest. A particle size distribution measures the fraction of particles smaller than a certain particle size in terms of a certain quantity. For a size distribution, this quantity is comparable to a geometric dimension, and denoted by the index $r$, that takes integer values from zero to three:

- 0: number
- 1: length
- 2: area
- 3: volume

Normally, number and volume-based distributions are used. Equation 3–1 gives a verbal definition of a normalized particle size distribution $Q_r$:

$$Q_r(d_i) = \frac{type\ r\ quantity\ of\ all\ particles\ with\ d < d_i}{total\ type\ r\ quantity\ of\ all\ particles} \ . \tag{3–1}$$

$Q_r$ is normalized with respect to the total type $r$ quantity (for example: total volume for $r = 3$), and, thus, takes values between zero and unity. The first derivative of the normalized distribution function results in the normalized distribution density $q_r$:

$$q_r(d) = \frac{dQ_r(d)}{dd} \ . \tag{3–2}$$

For a discrete measurement, the derivative has to be approximated by the difference quotient:

$$q_r(d_{m,i}) \approx \frac{Q_r(d_i) - Q_r(d_{i-1})}{d_i - d_{i-1}} .$$

(3–3)

A verbal definition of the normalized particle size distribution density $q_r$ is:

$$q_r(d_{m,i}) = \frac{particle\ fraction\ of\ type\ r\ quantity\ between\ d_i\ and\ d_{i-1}}{interval\ width\ d_i - d_{i-1}} .$$

(3–4)

An example of a particle size distribution and distribution density is given in Fig. 3–1. The particle size distribution density $q_r$ is always plotted over a mid-diameter $d_{m,i}$, characterizing the middle of each size class, which is defined by $d_i$ and $d_{i-1}$. The unit of a normalized particle size distribution density function is always mm$^{-1}$. For $r = 3$, the nominator of Eq. 3–4 is a volume fraction, and consequently has the unit 1. The denominator of a particle size distribution density is always a difference in mm.
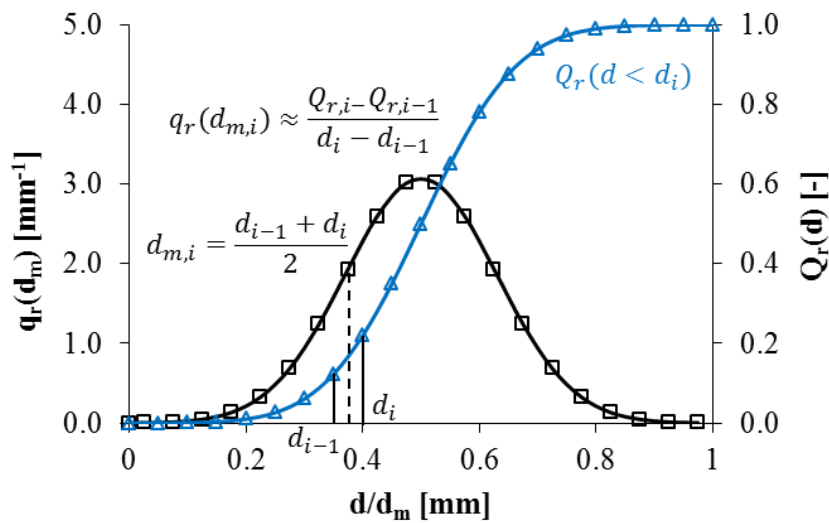


Fig. 3–1. Example of a particle size distribution density $q_r$ and a particle size distribution $Q_r$.

To further characterize particle size distribution densities, statistic moments are used. The $k^{th}$ normalized moment $\mu_{k,r}$ of a size distribution is defined as:

$$\mu_{k,r} = \int_{d_0}^{d_{max}} d^k q_r(d) \mathrm{d}d ,$$

(3–5)

and describes an expected value of the distribution. For $k = 1$ the mean particle size is calculated. For a discrete set of data, Eq. 3–5 becomes:

$$\mu_{k,r} \approx \sum_{i=1}^{N} d_{m,i}^{k} q_r(d_{m,i})(d_i - d_{i-1}) \ . \tag{3–6}$$

On the basis of moments, several mean particle diameters can be calculated. Following DIN ISO 9276-2, a mean particle diameter is calculated by:

$$d_{k,r} = \sqrt[k]{\mu_{k,r}} \ . \tag{3–7}$$

In this work, the weighted average particle size of the volume distribution density $q_3$, $d_{1,3}$, further named average particle size, is used to describe a distributed particle size by one characteristic value:

$$d_{1,3} = \mu_{1,3} \approx \sum_{i=1}^{N} d_{m,i} q_3(d_{m,i})(d_i - d_{i-1}) \ . \tag{3–8}$$

Furthermore, the standard deviation of a particle size distribution $\sigma_r$ is also calculated on the basis of statistic moments:

$$\sigma_r = \sqrt{\mu_{2,r} - \mu_{1,r}^2} \ . \tag{3–9}$$

For characterization purposes, different percentile diameters $d_{xy,r}$ are often used, defined as:

$$Q_r(d \leq d_{xy,r}) = xy \ \% \ . \tag{3–10}$$

Thus, at the median diameter $d_{50,3}$ of a volume based PSD, 50% of the particle volume belongs to particles smaller than or equal in particle size to $d_{50,3}$:

$$Q_3(d \leq d_{50,3}) = 50\% \ . \tag{3–11}$$

Percentile diameters can be commonly read directly from the measurement data by interpolation. But using only one percentile diameter as representation for a whole

distribution would neglect its shape. Thus, $d_{10,3}$ and $d_{90,3}$ are often stated to give an impression of the width of the distribution. However, using definitions of average particle diameters based on moments (Eq. 3–8) takes the complete distribution into account. In particle technology, the Sauter diameter:

$$d_{32} = \frac{\mu_{3,0}}{\mu_{2,0}}$$

(3–12)

is often used, which also considers the influence of the shape of the whole distribution. But for this dissertation, the $d_{1,3}$ was chosen as average particle diameter, due to its quantitative similarity to the $x_{50,3}$, which was initially used to interpret the results from this dissertation. A comparison of the different particle diameters for one set of experimental data is given in the appendix (Fig. B–1, p. 140).

### 3.1.2 Measurement

Particle size measurement was done with an optical system called Camsizer (Retsch Technology, Germany), Fig. 3–2 (left). The particles were fed to the measurement cameras by a vibration chute. The particles fell freely in front of the charge-coupled device (CCD) cameras, and their two dimensional projections were recorded. Different evaluation methods were possible (Fig. 3–2, right, adapted from: Retsch Technology, 2017). For this dissertation, the area-equivalent circle diameter was measured, because it considers all dimensions of a particle. By dividing all occurring diameters into classes, the normalized particle size distribution density $q_3$ was calculated by the measurement system. Applying Eq. 3–8, the average particle size $d_{1,3}$ was then calculated from the $q_3$ data.
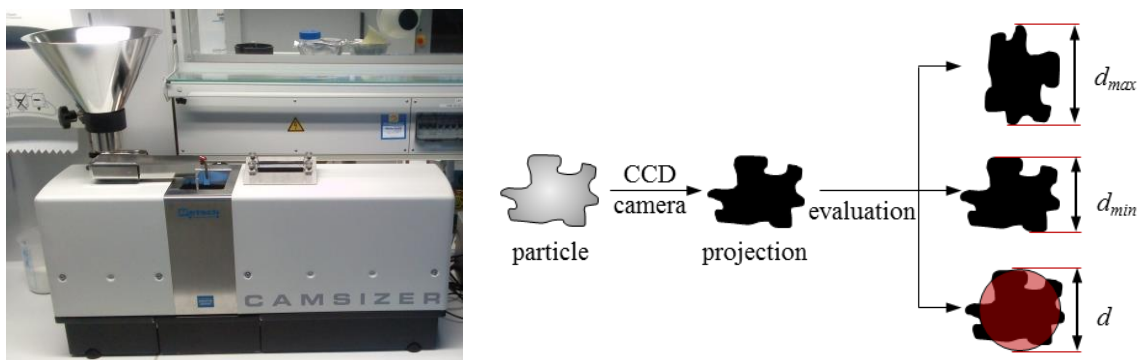


Fig. 3–2. Optical particle size measurement with a Camsizer (left). Measurement and evaluation (right, adapted from: Retsch Technology, 2017): $d_{max}$ = Feret diameter, $d_{min}$ – width of particle, $d$ – area equivalent circle diameter; $d_{min} < d < d_{max}$.

### 3.1.3 Steady state determination

To decide, if and when a continuous SFBLG or SFBA experiment reached the steady state, the temporal evolution of the average particle size $d_{1,3}$ was used. When $d_{1,3}$ was constant, the experiments were assumed to have reached steady state (example in Fig. 3–3, top). As experimental values often fluctuate, even in steady state, a criterion needed to be developed to decide, if and when $d_{1,3}$ could be considered constant. Occasionally, the experiments had to be interrupted to clean the spray nozzle, etc. Especially for the continuous SFBA experiments, process breaks led to steps in the graph of $d_{1,3}$. Consequently, the developed method needed to be able to recognize the onset of a steady state, as well as the interim terminations of the steady state due to process breaks.

In this work, the coefficient of variation $CoV$ was used to determine the onset and the termination of a steady state. To assess the onset of steady state, forward-averaging of $m$ values of $d_{1,3}$ was applied. First, for every value in the vector of $d_{1,3}$ (number of entries of the vector equals the number of samples taken during an experiment), except the last $m$-$1$ values, the average of $m$ values was calculated to form a new vector $d_{1,3,av}$. Each value $d_{1,3,av,j}$ was calculated as follows:

$$d_{1,3,av,j} = \frac{\sum_{i=j}^{j+m-1} d_{1,3,i}}{m} \qquad j = 1..l - (m - 1) \, , \tag{3–13}$$

with $l$ being the total number of values in $d_{1,3}$. An example from continuous SFBA with $m = 3$ is given in Fig. 3–3, top. For nearly all SFBA experiments, the steady states were determined for $m = 3$. For one experiment, $m = 6$ had to be used for the determination of steady state. For the continuous SFBLG experiments, the steady state was determined with $m = 4$, when samples from the product were used, and with $m = 16$, when samples from the bed were used.

In a second step, the sample standard deviation $\sigma_{sam,j}$ for each averaged set of $d_{1,3}$ was calculated by:

$$\sigma_{sam,j} = \sqrt{\frac{\sum_{i=j}^{j+m-1} \left( d_{1,3,i} - d_{1,3,av,j} \right)^2}{m - 1}} \, . \tag{3–14}$$

From Eqs. 3–13 and 3–14 the $CoV_j$ for each step of $m$ values of $d_{1,3}$ was calculated as follows:

$$CoV_j = \frac{\sigma_{sam,j}}{d_{1,3,av,j}} \, . \tag{3–15}$$

The onset of steady state was then defined, if the *CoV* was smaller than a critical value, which was set for each experimental series according to the process parameters. For SFBLG the critical value for *CoV* was 2-6%. For SFBA the critical value of *CoV* ranged from 1.6–12%. As agglomeration was the faster process, larger particle sizes and consequently larger fluctuations occurred. Thus, also the critical *CoV* value to determine the steady state had to be increased.

As stated above, for some experiments – especially the agglomeration experiments – process breaks led to temporary termination of the steady state. Upon restart, the experiments reached the steady state again after some time. Thus, the steady states were determined sequentially over the process time. The beginning of a steady state was determined as described above, with a forward definition of $d_{1,3,av}$ (Eq. 3–13). This means, for example calculating the first average value $d_{1,3,av,1}$ with $m = 3$ takes the values 1–3 from vector $d_{1,3}$ for calculation. The second average then is calculated from values 2–4, and so on. If the same definition was used to determine the endpoint of a steady state due to process breaks, the *CoV* would already vary too strongly *m-1* values before the steady was actually terminated. This was prevented by backwards-averaging of the average particle diameter to:

$$d_{1,3,av,ba,j} = \frac{\sum_{i=j-m+1}^{j} d_{1,3,i}}{m} \qquad j = m..l \,, \tag{3–16}$$

with *l* being the total number of values in $d_{1,3}$. This means, the calculation of an average value needs *m-1* predecessor values. For $m = 3$, the first average that can be calculated is $d_{1,3,av,ba,3}$ using the values 1–3 of vector $d_{1,3}$. With this definition, the $CoV_{ba}$ immediately changes when leaving the steady state. The $\sigma_{sam,ba}$ and $CoV_{ba}$ were calculated as described in Eqs. 3–14 and 3–15, exchanging $d_{1,3,av}$ for $d_{1,3,av,ba}$. Thus, the forward definition was used to find the onset of steady state, and the backward definition was used to determine the endpoint of a steady state. Onset and endpoint were determined using the same critical value for *CoV* and $CoV_{ba}$.

An example for $m = 3$ and the steady state criterion $CoV < 3\%$ is given in Fig. 3–3. The first steady state period is determined for $CoV < 3\%$ at 0.4 h (Fig. 3–3, bottom, first blue dot). The endpoint of this steady state period is found for $CoV_{ba} < 3\%$ at 3.0 h (last black square in the first steady state period). The next starting point (first blue dot in the second steady state period in Fig. 3–3, bottom) is found at 3.2 h, and the according endpoint (last black square) is found at 6.8 h. Comparing the steady state times to the graph of $d_{1,3}$ (Fig. 3–3, top) yields good visual agreement of the steady state determination. The presented method is limited by slow drifts in the average particle size, which are also recognized as steady states, depending on the critical value chosen for *CoV*. But the occurring drifts (compare Fig. 3–3, bottom: second steady state) were comparable small, and, thus, the method was applied.
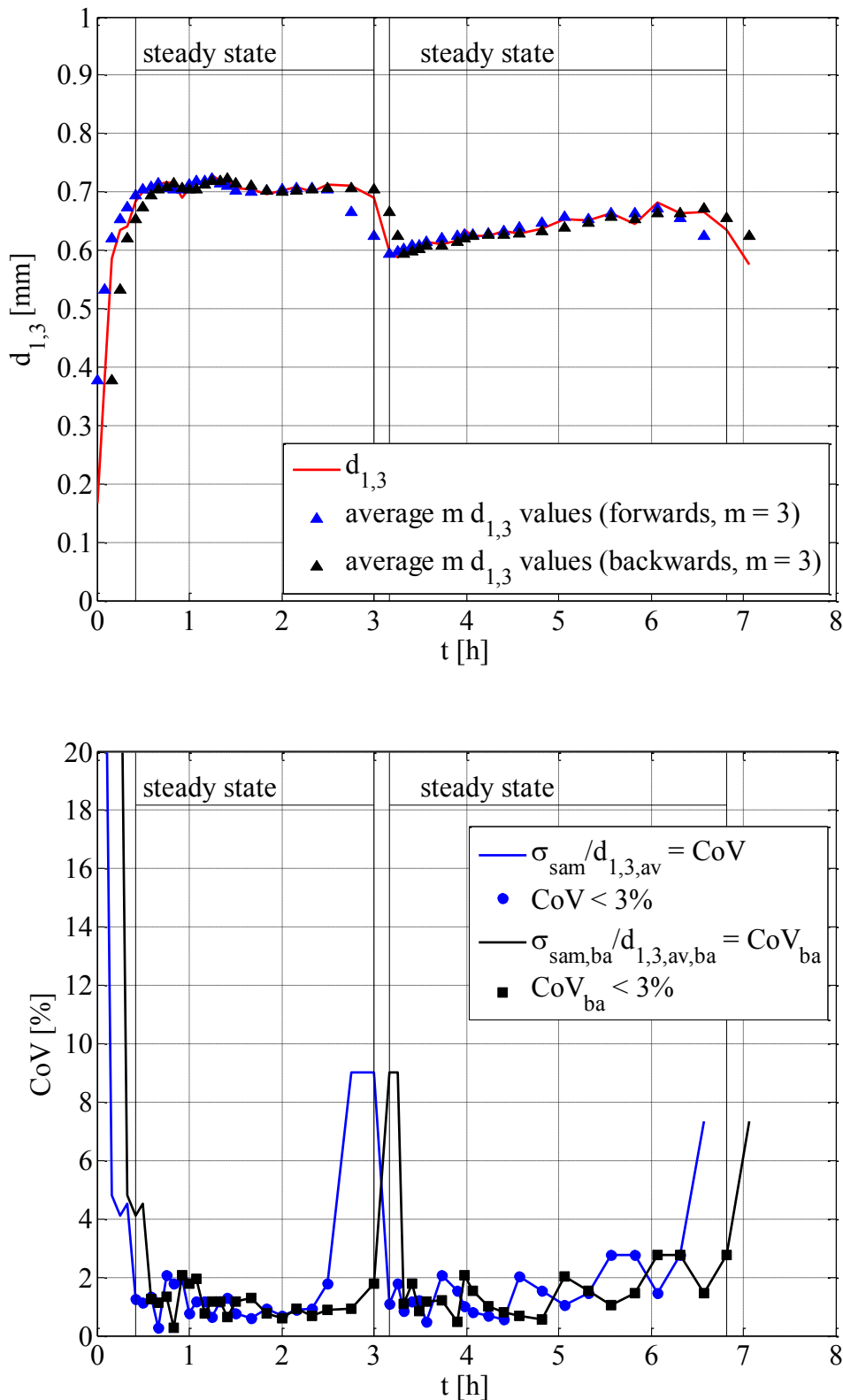
Fig. 3–3. Steady state determination based on an example (SFBA): Averaging of 3 values of $d_{1,3}$ (top). *CoV* and steady state determination (bottom). Onset of steady state for *CoV* < 3% (first blue dot in each steady state period). Endpoint of steady state for *CoV$_{ba}$* < 3% (last black square in each steady state period). Two steady state periods determined: 0.4–3 h and 3.2–6.8 h.

### 3.1.4 Average particle growth rate

In addition to the particle size, also the time and the rate in which the particles achieve their size are interesting. For continuous SFBP running in steady state, the average growth rate is defined by the difference in diameter from start to product discharge divided by the average particle residence time in the fluidized bed. The average residence time $\tau$ of particles is estimated as:

$$\tau = \frac{M_{bed,ss}}{\dot{M}_{prod,ss}},$$
(3–17)

with the average bed mass during steady state $M_{bed,ss}$ and the average product mass flow rate during steady state $\dot{M}_{prod,ss}$. The average particle growth rate in steady state $G_{av}$ is then calculated by the difference in particle size from start to product discharge, divided by the average residence time $\tau$:

$$G_{av} = \frac{d_{1,3,prod,ss} - d_{1,3,0}}{\tau}.$$
(3–18)

As the seed particles for layering granulation were formed internally, the starting size was defined as zero ($d_{1,3,start} = 0$) for the SFBLG experiments. For the SFBA experiments, the primary particle size was set for $d_{1,3,0}$. The growth rate $G_{av}$ is a rough estimate of the real growth rate in practice, as it includes averaging of the bed mass, the product mass flow rate and the particle sizes. Nevertheless, the average growth rate characterizes from an engineering point of view, how fast a process generates particles with the desired size.

### 3.1.5 Period time determination

For experiments with sustained oscillations in the PSD, the period times between the oscillations were determined (Fig. 3–4). Therefore, the maxima of the plot particle size $d_{1,3}$ over process time were located. The period times of oscillation were defined as the time between the maxima. For each experiment with sustained oscillations in the PSD, an average period time was calculated as the arithmetic mean of the determined period times.
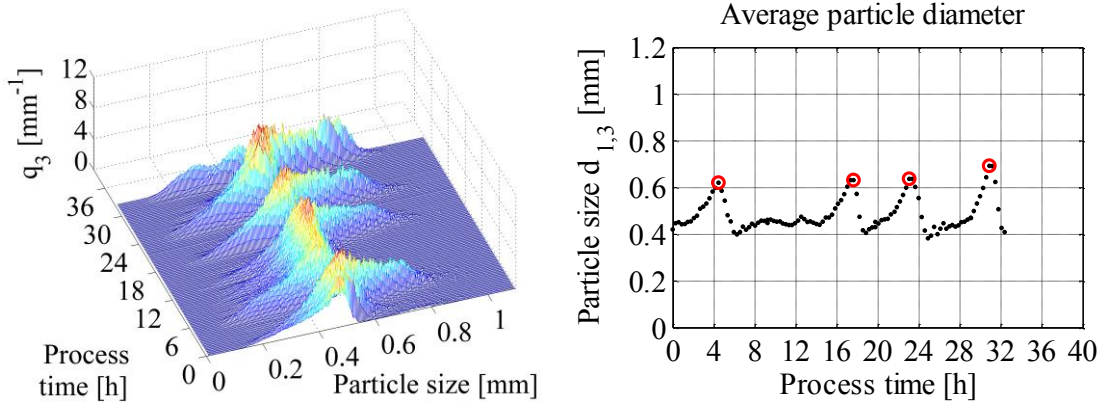
Fig. 3–4. Determination of period times for experiments with sustained oscillations in the PSD. Left: Exemplary temporal evolution of $q_3$. Right: $d_{1,3}$ over process time, maxima marked with ○.

## 3.2 Particle moisture content

The moisture content was determined by thermogravimetric analysis with a drying oven (Memmert GmbH, Germany, model: ULP 500) and an analytical balance (Sartorius AG, Germany, model: MC 1). At first, the mass of the empty sample holder was determined. Then, the wet sample was placed in the sample holder and the mass was measured again. After weighing, the sample was placed in the drying oven at 105°C. After 24 h the sample was sealed and cooled down. The mass of the cooled sample holder including the dry material was determined. The mass fraction of water (wet based) – here named moisture content – was calculated as follows:

$$x_w = \frac{M_{wet} - M_{dry}}{M_{wet} - M_{sh}},$$

(3–19)

with the mass of the sample holder including the wet and the dry particles, $M_{wet}$ and $M_{dry}$ respectively, and the mass of the empty sample holder $M_{sh}$. In general, several samples taken from the fluidized bed and the product were measured. The average mass fraction of water $x_{w,av}$ was calculated for bed and product samples separately as follows:

$$x_{w,av} = \frac{\sum x_{w,i}}{m},$$

(3–20)

with the number of samples $m$.

For the average moisture content of the particles in the fluidized bed, usually 5–15 samples were measured. The average mass fraction of water of the product particles was usually calculated from the measurements of 5–10 samples.

# 3.3 Granule porosity

The measurement of particle porosity was only done for granules obtained by SFBLG. The characterization of the morphology of agglomerates was performed by fractal dimension (Section 3.5). The particle porosity was measured via two methods. For several samples, the porosity was measured using micro-computed tomography (μ-CT). As this technique is very time consuming, an alternate method was used for the majority of the samples: The particles were weighed with a micro-balance and their size was measured with a scanning electron microscope (SEM). Knowing the true solid density of the particles (= solid density excluding pores, see: Section 3.6.3, p. 50), the porosity was calculated from particle volume and particle mass (Eq. 3–23).

### 3.3.1 Definitions

Two kinds of porosities are important in particle technology. The bulk porosity $\Psi_{bulk}$ denotes the fraction of the free volume between the particles in relation to the volume of the whole bulk. It is calculated as follows:

$$\Psi_{bulk} = 1 - \frac{V_{p,t}}{V_{bulk}}, \tag{3–21}$$

with the total particle volume $V_{p,t}$ and volume of the whole bulk $V_{bulk}$, including the spaces between the particles. In contrast, the particle porosity $\Psi_p$ gives the fraction of the free volume (pores) in relation to the total volume of a single particle. $\Psi_p$ is calculated as:

$$\Psi_p = 1 - \frac{V_s}{V_p}, \tag{3–22}$$

with the volume of a single particle $V_p$ and the volume of the pure solid $V_s$, excluding pores. Depending on the method, the volume of the solids in a single particle $V_s$, excluding the pores, is hard to measure. Here, the volume can be replaced by the particle mass $m_p$ and the true density of the solid material $\rho_s$:

$$\Psi_p = 1 - \frac{m_p}{\rho_s V_p} \, .$$

(3–23)

For this work, particle porosities were measured by micro-computed tomography (Section 3.3.2) and a mass-volume method (Section 3.3.3).

### 3.3.2 Measurement via μ-CT

To obtain the particle porosity, three particles from each sample under consideration were individually scanned using micro-computed tomography (μ-CT). Then, the resulting three porosity values were averaged. For the measurement, each particle was glued on a sample holder, and positioned in front of the X-ray source (Fig. 3–5). The intensity of the X-rays was measured behind the sample holder by a detector. Based on the intensity profile, a 2-D grayscale image of the particle and its surrounding was calculated. The sample holder was incrementally rotated up to 360° and each resulting image was saved. A 3-D model of the scanned particle was then reconstructed from the stack of 2-D images.
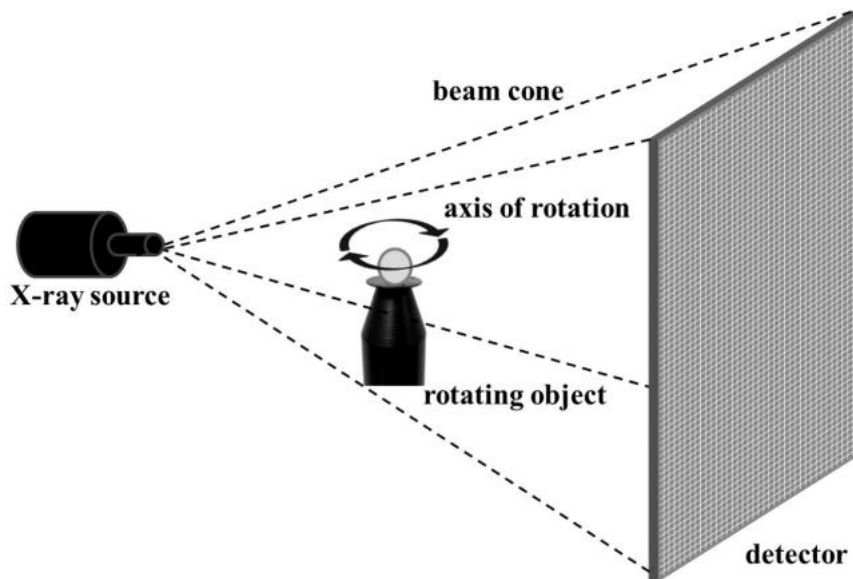
Fig. 3–5. General function of μ-CT (Sondej et al., 2015).

Before each measurement, the tomograph (ProCon X-ray GmbH, Germany, model: CT Procon alpha 2000) was warmed up and the X-ray source (filament) was adjusted. Then, the particle was placed on the sample holder and the measurement parameters (Tab. 3–1) were set. The measurement was controlled by the software Volex (Fraunhofer Institute for Integrated Circuits, Erlangen, Germany) and took four hours for each particle.

After the measurement, a separate reconstruction step was started, calculating the 3-D model of the scanned particle from the stack of 2-D images. From the 3-D model the particle porosity was obtained using the software MAVI (Fraunhofer Institute for Technical and

Industrial Mathematics, Kaiserslautern, Germany), following the evaluation steps described by Sondej et al. (2015). These steps include (Fig. 3–6):

(1) Cropping of the reconstructed model (particle + surrounding) to the size of the particle. To neglect overlapping of particle and sample holder, only the top half of each particle was investigated.

(2) Binarization of the gray-scale model. Here, a threshold gray value in the range from 1150 to 2047, allowing for a separation of the granule from the background, was set, assigning each voxel (3-D pixel) to either the solid or the void phase.

(3) Segmentation and removing of background noise.

(4) The volume of the remaining solid $V_s$ (top half of particle without pores) was measured by the software by counting the voxels.

(5) A closing algorithm was applied, giving the total volume $V_p$ of the top half of the particle (including pores). In this work, the ball element (size range 4–7) was used as a closing element. The respective size was chosen to achieve full closure of the particle surface.

(6) Using Eq. 3–22, the particle porosity was calculated.

Including warm-up of the tomograph, sample preparation, setting of parameters, measurement, reconstruction and evaluation of the images, the measurement of each particle took about 5–5.5 h. Three particles were scanned and evaluated individually for each sample under consideration. Due to this time demand, only one series of experiments (SFBLG with external separation and varied drying conditions, Tab. 5–5, p. 100) was investigated by μ-CT, and an alternate method to obtain the particle porosity (Section 3.3.3) was developed for all experiments.

Tab. 3–1. Measurement parameters for μ-CT.

| Parameter | Value |
|---|---|
| Exposure time | 3 s |
| Averaging | 3 images |
| Voltage | 45 kV |
| Current | 90 μA |
| Energy | 4.1 W |
| Position sample/detector | 675/0 mm |
| Number of projections (rotation increments) | 1200 (equals 0.3° increments) |
| Voxel (pixel in 3-D) size | 1.5 μm (edge length) |
| Measurement time | 4 h |
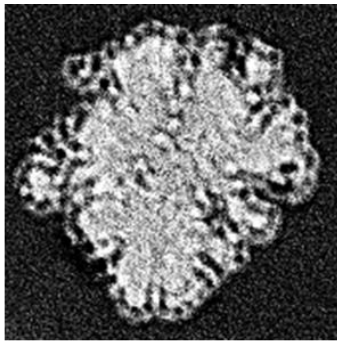
(1) Cropped gray-scale image, slice view

(2-4) Binarized and filtered image, pure solid volume in 3-D

(5) Image after closure, total particle volume in 3-D

Fig. 3–6. Steps to evaluate μ-CT measurements.

### 3.3.3 Measurement via mass and volume

Knowing the mass, total volume and true solid density of a particle, the particle porosity is calculated by Eq. 3–23. At first, the masses of 10 single particles per sample were determined with a micro scale (Sartorius AG, Germany, model: M2P, resolution: 1 μg). Each particle was weighed five times. All 10 particles were glued on a sample holder and prepared for scanning electron microscopy (SEM). Therefore, a conductive, 2 nm gold/palladium layer was applied to the particles by sputter coating. Then, the sample holder was placed in the microscope (Phenom World BV, Netherlands, model: G2 Pro). Gray-scale images of the particles were taken, considering following aspects:

- Ideally only one particle was visible per picture. If parts of other particles were in the picture, they had to be not in contact with the particle under consideration.
- The auto focus of the SEM was used for general focus and was then deactivated. The focus was shifted manually towards the edge of each particle, to allow for a better binarization and separation of particle and background later on.

The obtained images were then evaluated with the MatLab software (The MathWorks Inc., USA, version: R2014a). The following steps were executed during the evaluation of the SEM images (Fig. 3–7):

(1) Binarization of the gray-scale image. The edges of the particle are detected and a threshold gray value is set, separating the particle from the background.
(2) Dilation of the binarized image. Gaps in the particle perimeter are closed.
(3) Filling of the particle contour. Cropping of unwanted elements.
(4) The resulting area (particle projection area) is measured in number of pixels.
(5) Calculation of a diameter of a circle with the same area (in pixels).
(6) Applying scale from image (pixel to μm) to calculate particle circle diameter (in μm)
(7) Calculation of the volume of a sphere with this diameter.
(8) Calculation of particle porosity with Eq. 3–23.

Including particle weighing, sample preparation for SEM, SEM measurement, and evaluation in MatLab, the total measurement time of 10 particles per sample was approximately 2.5 h.

The average granule porosity $\Psi_{SEM,av}$ was then calculated by the arithmetic mean value of the $m = 10$ measurements:

$$\Psi_{SEM,av} = \frac{\sum_{i=1}^{m} \Psi_{p,i}}{m} \,.$$

(3–24)

The empirical standard deviation of the $m = 10$ measurements was then calculated:

$$\sigma_{em,\Psi} = \sqrt{\frac{\sum_{i=1}^{m}\left(\Psi_{SEM,i} - \Psi_{SEM,av}\right)^2}{m-1}} \,.$$
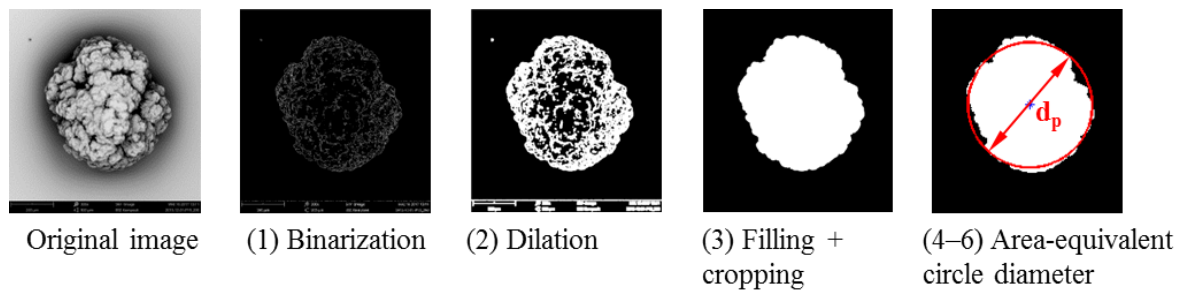
(3–25)



Fig. 3–7. Steps to obtain the particle diameter for volume and porosity calculation.

### 3.3.4 Comparison of the porosity measurement methods

The porosity calculation by measuring mass and volume resulted in more distinctive porosity values. For continuous SFBLG with internal separation, values in the range of 16.4–48.8% were measured (Tab. 4–6, p. 74), which were in qualitative accordance with the findings of Rieck et al. (2015). The values were slightly different, due to the dependency of the layer porosity on the core material, as reported by Rieck et al. (2015) for non-porous glass beads and porous γ-Al$_2$O$_3$ spheres. The findings regarding the porosity of sodium benzoate layers were also confirmed qualitatively for continuous SFBLG with external separation. The porosity values lay within the range of 17.8–28.7% (Tab. 5–5, p. 100).

The porosity measurement via μ-CT yielded values of 28.9–33.7% for continuous SFBLG with external separation (Tab. 5–5, p. 100). The values were indistinctive, regardless of the drying conditions. A dependency of the particle porosity on the drying potential (Eq. 2–10, p. 17), as described by Rieck et al. (2015) for coating with sodium benzoate solution, could not be observed for the values measured via μ-CT. But the surface structure of the particles, visualized by SEM images, agreed with the findings of Rieck et al. (2015). A possible source of error for this discrepancy is the resolution of the μ-CT. The pores in the center of a granule were rather small (Fig. 3–6, left), and possibly smaller than the minimal voxel size of the measurement system of 1 μm. If the pore sizes were smaller than the minimum resolution, the

measured voxels could not be assigned correctly to either the solid or the void phase. Hence, similar values for the granule porosity could be the result. Additionally, the measurement was conducted at a voxel size of 1.5 µm (Tab. 3–1), due to constraints in sample positioning, image contrast, and power level of the X-ray source. A specific reason, why the porosity values measured by µ-CT exceeded the values obtained by the mass-volume-method, could not be found.

The calculation of porosity, based on the measurement of volume and mass of a particle, has been considered to yield more reliable results for the particle porosity of sodium benzoate granules, than the measurement via µ-CT.

# 3.4 Granule roughness

The roughness of a granule influences its flow properties, dissolution kinetics, etc. This section presents a method how to assess the roughness of a granule from its 2-D projection.

## 3.4.1 Theory

The presented method is based on the understanding of roughness in mechanical engineering. The quality of the surface of machine elements is characterized, among others, by different roughness values, i.e. the arithmetic mean roughness $R_a$. The arithmetic mean roughness gives the mean of the absolute value of the deviation of points of the surface to a planar base line for a given measurement length $s_m$, and, thus, is always positive (Fig. 3–8):

$$R_a = \frac{1}{s_m} \int_0^{s_m} |z(x)|\,\mathrm{d}x \; . \tag{3–26}$$



Fig. 3–8. Definition of arithmetic mean roughness of a surface profile.
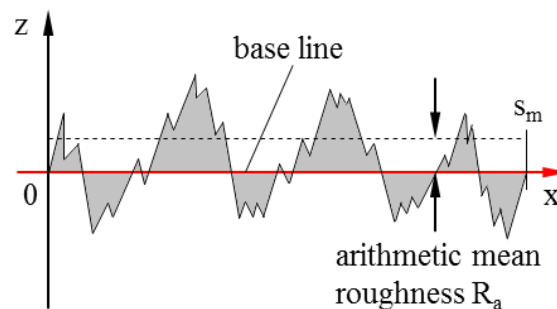
Adapting the concept of arithmetic mean roughness to irregular, spherical-like granules, requires the definition of a suitable base line. Accounting for the deviation of the granules' form from ideal spheres, in this work, an ellipse with the same normalized second central moment as the particle projection was defined, and served as base line for the roughness

calculation (Fig. 3–9). A description on how to operate with central moments in image analysis is given by Belkasim et al. (1991) and Flusser and Suk (1993). The average granule roughness $R$ was calculated as the average of the absolute value of the distance of all $m$ pixels of the perimeter $U_l$ to the base line $E$:

$$R = \frac{1}{m} \sum_{l=1}^{m} |\overline{U_l E}| \; .$$

(3–27)
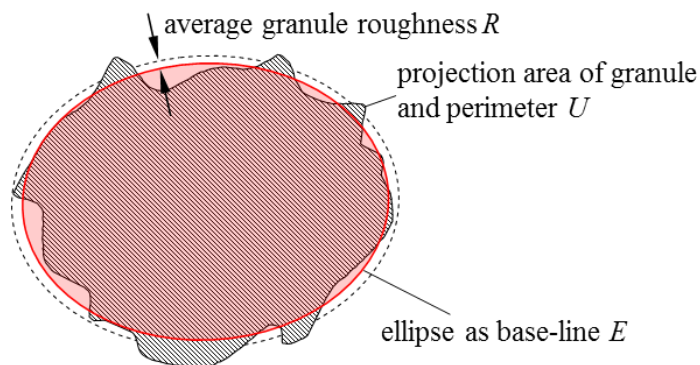


Fig. 3–9. Adaption of the arithmetic mean roughness concept to particle technology.

### 3.4.2 Measurement and data processing

The analysis of roughness was done with the same SEM images, which were taken for the porosity measurement (Section 3.3.3). The sample preparation and operation of the SEM was described in Section 3.3.3. The SEM images were then evaluated with the MatLab software (The MathWorks Inc., USA, version: R2014a). The following steps were executed to obtain the granule roughness (Fig. 3–10). Steps 1–4 are equal to the procedure of determining the granule porosity (Section 3.3.3):

(1) Binarization of gray-scale image. The edges of the particle are detected and a threshold gray value is set, separating the particle from the background.
(2) Dilation of the binarized image. Gaps in the particle perimeter are closed.
(3) Filling of the particle contour. Cropping of unwanted elements.
(4) The resulting area (particle projection area) is measured in number of pixels.
(5) Defining an ellipse with the same normalized second central moment as the projection of the granule.
(6) Calculation of the distance of perimeter and ellipse (in pixels).
(7) Application of the scale (pixel to µm) from the SEM image to obtain a roughness profile.
(8) Calculation of the averaged absolute value of the distance calculated in steps 6 and 7 as average granule roughness (in µm, Eq. 3–27).

| Original image | (1) Binarization | (2) Dilation | (3) Filling + cropping |



(4+5) Ellipse      (6+7+8)  Distance of perimeter to ellipse, calculation of R
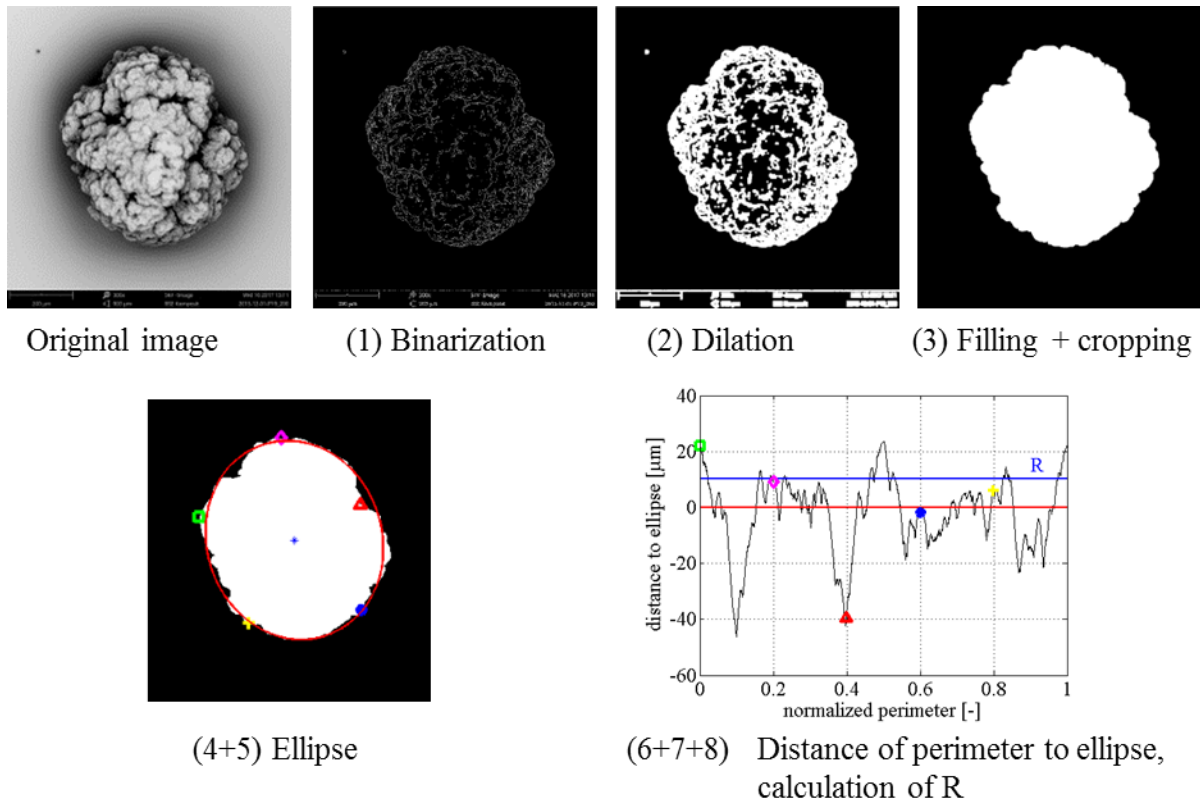
Fig. 3–10. Steps to obtain the roughness profile of a granule. The average roughness $R$ of the granule was calculated as the averaged absolute distance of perimeter and ellipse.

The roughness obtained by this method resembles the deviation of the granule from a smooth ellipsoid. Due to image resolution, the practicable minimal peak height detected was about 1 µm.

In total, the roughness of $m = 10$ particles per experiment was determined. The average roughness $R_{av}$ and empirical standard deviation $\sigma_{em,R}$ were calculated analogously to the values for the particle porosity from Eqs. 3–24 and 3–25, respectively, exchanging $\Psi_{SEM}$ by $R$.

## 3.5 Fractal dimension of agglomerates

### 3.5.1 Theory

The concept of fractal dimension was introduced by Mandelbrot (1983) to describe naturally occurring, irregular and fractured objects. A fractal is a fragmented or rough geometric shape, which is self-similar. This means, parts of the geometric shape are similarly formed like the original shape, and only reduced in size (Foroutan-pour et al., 1999). The fractal dimension $D_f$ quantifies the roughness of the shape under consideration. Compact structures tend to have higher values than open, porous ones. Different methods are available to empirically obtain $D_f$ from images. The $D_f$ value of a curve can be determined with the method of lines, where a

successively increasing number of horizontal lines intersects with the curve, and the original image is recreated by the intersections (Hyslip and Vallejo, 1997). For planar areas and 3-D objects, the box-counting method is usually used to obtain $D_f$ (Walsh and Watterson, 1993; Foroutan-pour et al., 1999). The box-counting method in this work is based on the description of Foroutan-pour et al. (1999).

Firstly, the image of the agglomerate under consideration has to be square. Then, a grid of square boxes is applied to the image, and all boxes intersecting the area of the agglomerate $N_{box}$ are counted (Fig. 3–11). This step is repeated for successively finer grids with the box size:

$$s_{box,i} = \frac{1}{2^{i-1}} \, s_{box,1} \, , \tag{3–28}$$

with the length/width of the square starting image $s_{box,1}$, and the number of calculation steps $i$. The number of boxes $N_{box}$ then is proportional to the box size $s_{box}$ to the power of $-D_f$ (Walsh and Watterson, 1993):

$$N_{box,i} \sim s_{box,i}^{-D_f} \, . \tag{3–29}$$

In a double logarithmic plot of $N_{box,i}$ over $s_{box,i}^{-1}$, the slope of the curve equals the fractal dimension $D_f$. In practice, the first two calculation steps ($i = 1, 2$) are neglected. For $i = 1$, the box size equals the size of the total squared image, and $N_{box,1}$ always equals unity. For $i = 2$, the grid applied to the image consists of four boxes. In most cases, $N_{box,2}$ then equals three or four. Due to the similarity of the results for $N_{box,1}$ and $N_{box,2}$, regardless of the agglomerate structure, these two calculation steps are neglected. Also Foroutan-pour et al. (1999) report 25% of the original image width as maximum box size (here: $i = 3$). Thus, the maximum box size for this investigation was set to $0.25 \cdot s_{box,1}$, which means the box counting method is started with $i = 3$. The minimum box size is limited by the image resolution. The smallest box must at least be one pixel wide, setting a theoretical limit. In this work, $i = 10$ was set as the limit for calculation steps, and thus the minimum box size was $512^{-1} \cdot s_{box,1}$ (Eq. 3–28). As the images generally have a starting width ($s_{box,1}$) of more than 1000 px, the minimum box size usually was 2–3 px.

The expected limits of a 2-D fractal dimension are unity and two. $D_f = 1$ is the theoretical limit for a line, and $D_f = 2$ is the limit for a full, regular area like a square or circle. Values in between indicate a roughness profile on the surface of the particle, or here: a rough perimeter. The closer $D_f$ gets to unity, the more open, irregular and rough is the particle under consideration. $D_f$ approaching the value two indicates a more compact and smoother surface structure.

Fig. 3–11. Box-counting method. Grids shown for $i = 3$ (left), $i = 4$ (middle), and $i = 5$ (right). Boxes intersecting the area of the agglomerate are counted (here: colored transparent red).

### 3.5.2 Measurement

For every sample, images of 10 agglomerates were taken by a light microscope (Olympus Corporation, Japan, model: SZX2-ILLD, lens: SDF PLAPO 1XPF). The white agglomerates were placed on black paper, and manually positioned below the lens. The reflected light was recorded by a digital camera, and the final image was saved manually on a measurement PC.

### 3.5.3 Data processing

The calculation of the fractal dimension $D_f$ from light microscope images was done with MatLab (The MathWorks Inc., USA, version: R2014a). Following steps were part of the algorithm (Fig. 3–12):

    (1) Converting the original image to a gray-scale image.
    (2) Binarization of the gray-scale image. The edges of the particle are detected and a threshold gray value is set, separating the particle from the background.
    (3) Dilation of the binarized image. Gaps in the particle perimeter are closed.
    (4) Filling of the particle contour. Cropping and squaring of image.
    (5) Applying a set of grids on the image and applying box counting method for $i = 3…10$.
    (6) Calculation of fractal dimension (Eq. 3–29).

In total, the fractal dimension of $m = 10$ agglomerates per experiment was determined. The average fractal dimension $D_{f,av}$ and empirical standard deviation $\sigma_{em,Df}$ were calculated analogously to the values for the particle porosity from Eqs. 3–24 and 3–25, respectively, exchanging $\Psi_{SEM}$ by $D_f$.

(1) Original image + converting to gray    (2) Binarization    (3) Dilation    (4) Filling, cropping + squaring

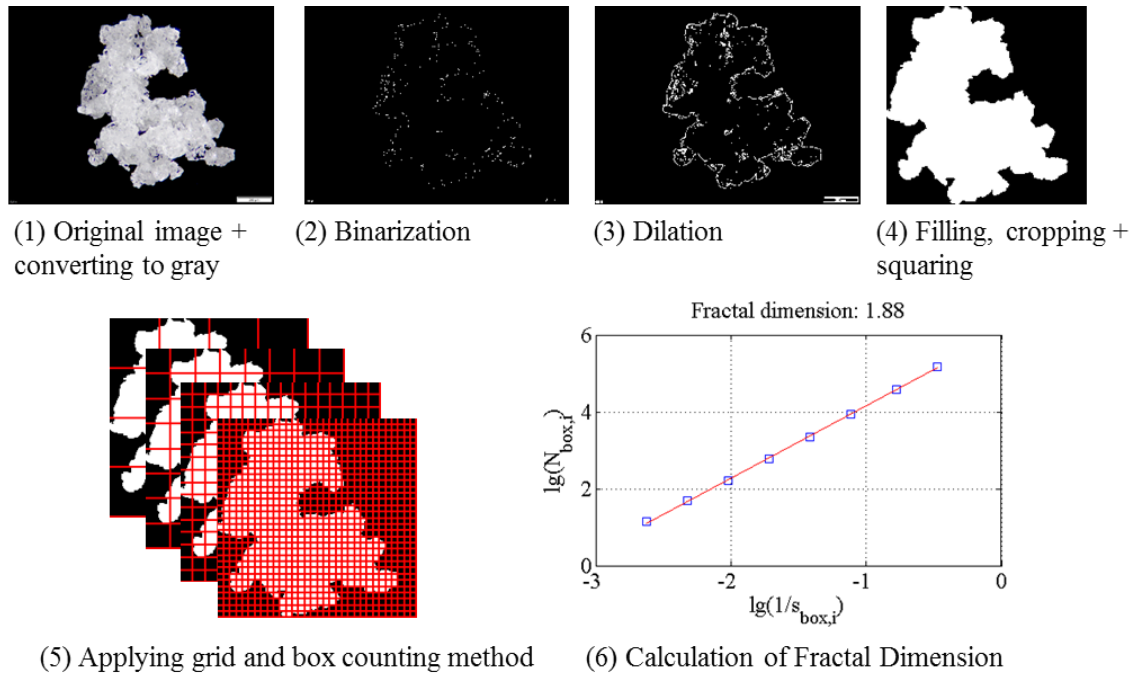(5) Applying grid and box counting method    (6) Calculation of Fractal Dimension

Fig. 3–12. Steps to obtain the fractal dimension of an agglomerate.

## 3.6 Further measurement techniques

This section covers measurement systems which are not directly connected to the product quality. The measurement of the gas moisture content during fluidized bed experiments via dew point meter and infrared-spectrometer is described. The gas moisture contents are necessary to characterize the conducted experiments psychrometrically. Additionally, a gas pycnometer for the measurement of true solid densities is presented. The measurement of the true solid density was necessary for the calculation of the porosity via mass and volume (Eq. 3–23, p. 39, and Section 3.3.3, p. 41).

### 3.6.1 Gas moisture content via dew point meter

A dew point meter (Michell Instruments GmbH, Germany, model: Optidew Vision) was used to determine the inlet gas moisture content during fluidized bed experiments. Its main component was a chilled mirror element. The measurement air was led over the mirror, and the reflection of a laser beam from the mirror was measured. When the mirror reached the dew point temperature of the measurement gas, water started condensing on the chilled mirror surface and the reflection signal of the laser beam was reduced (Michell Instruments, 2014).

Knowing the dew point temperature of the gas, which is a saturation temperature $T_{sat}$, the respective saturation vapor pressure $p_{sat}$ was calculated in mbar using a Magnus equation:

$$p_{sat} = C_1 e^{\left(\frac{C_2 T_{sat}}{C_3 + T_{sat}}\right)}, \tag{3-30}$$

with the constants $C_1$ = 6.11213, $C_2$ = 17.5043, $C_3$ = 241.3°C (valid for -30°C < $T_{sat}$ < 70°C, Laube and Höller, 1988). The saturation pressure was used to calculate the moisture content, in this case of the inlet gas, $Y_{in}$:

$$Y_{in} = 0.622 \frac{p_{sat}}{p_t - p_{sat}}, \tag{3-31}$$

with $p_t$ being the total pressure in the measurement device.

**3.6.2 Gas moisture content via infrared-spectrometer**

The outlet gas moisture content was measured with the infrared (IR) spectrometer NGA 2000 (Emerson Process Management Co., USA, type: MLT3 T – IR). The measurement was based on differences in absorption of infrared radiation. The type of gas was characterized by the gas-specific wavelengths of the absorption bands. The concentration of the component under consideration (here: water) was determined by the strength of absorption. A heat coil provided the necessary infrared radiation for the measurement (Fig. 3–13). The measurement system had two channels, supplied with similar amounts of infrared radiation from the same source. The reference channel measured the absorption bands of the original radiation. The measurement gas was led through the second channel, alongside with the infrared radiation. From the difference in the absorption intensity, the detector determined the amount of water present in the measurement gas, $Y_{out}$ (Emerson Process Management, 2008). Knowing both, the inlet (Section 3.6.1) and outlet absolute gas moisture content, the drying potential was calculated (Section 2.2.4, Eq. 2–10, p. 17).
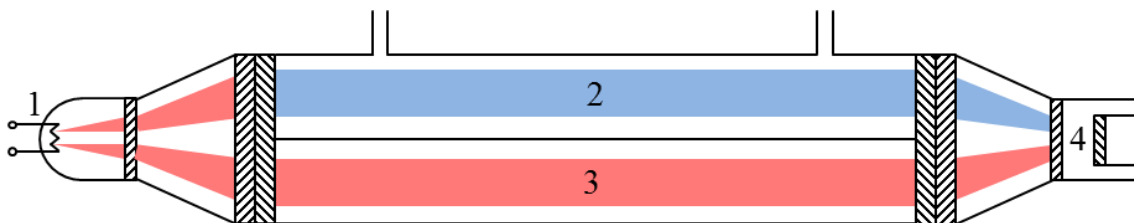


Fig. 3–13. Measurement setup of an IR. Main parts: (1) heat coil, (2) measurement channel, (3) reference channel, (4) detector and amplifier (adapted from Emerson Process Management, 2008).

### 3.6.3 Solid density via gas pycnometer

The true solid densities of several materials were measured with a gas pycnometer (Grabner Instruments, Austria, model: Minidens TCO). A gas pycnometer operates by detecting the shift in pressure caused by solid objects (Fig. 3–14). Therefore, the total volume of solids $V_{s,t}$ was filled in a sample holder with the volume $V_{sh}$. The sample holder was placed in a chamber with a known volume ($V_1$) at a known pressure ($p_1$). An integrated balance measured the mass of the solid particles $M_s$. In a second chamber of known volume $V_2$ the pressure was increased to $p_2$. After opening the connecting valve, an equilibrium pressure $p_3$ resulted, depending on the free and occupied volume in chamber 1. As the number of molecules did not change during this transition, following the law of ideal gases yielded (Webb, 2001):

$$p_1 \cdot \left(V_1 - V_{sh} - V_{s,t}\right) + p_2 \cdot V_2 = p_3 \cdot \left(V_1 - V_{sh} - V_{s,t} + V_2\right), \tag{3–32}$$

$$V_{s,t} = \frac{p_3 \cdot (V_1 + V_2) - p_1 \cdot (V_1 - V_{sh}) - p_2 \cdot V_2}{p_3 - p_1}. \tag{3–33}$$

Knowing the mass of the particles $M_s$, the true solid density was calculated:

$$\rho_s = \frac{M_s}{V_{s,t}}. \tag{3–34}$$

The calculations described above were carried out within the measurement system. Only the solid densities were recorded. In this work, all densities were measured in triplicate, and the average value was calculated.
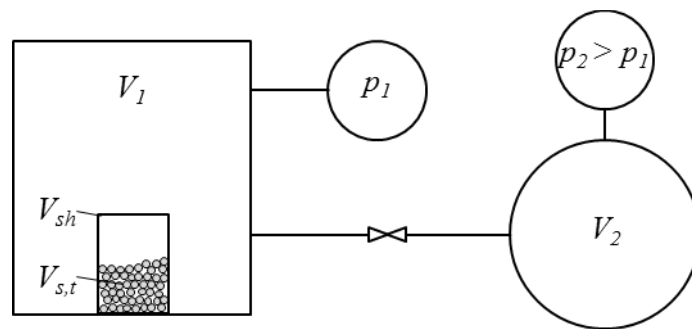


Fig. 3–14. Measurement principle of a gas pycnometer (adapted from Webb, 2001).

# 4 Continuous layering granulation with internal separation

This chapter is an extended version of Schmidt et al. (2015b). Here, the results regarding the process behavior and product quality during continuous SFBLG with internal separation are presented. Two series of experiments were conducted. In the first series, varying classifying velocity resulted in different bed hold ups, influencing the process dynamics, and the bed and product particle size. In the second series, the drying parameters (inlet gas temperature, spray mass flow rate, fluidizing gas mass flow rate) were varied to obtain different overspray, nucleation and drying behavior, which influenced the overall process behavior and the particle morphology.

## 4.1 Materials

All granulation experiments were conducted with sodium benzoate (Trigon Chemie GmbH, Germany, type: sodium benzoate SP, Food Grade, Kosher). Sodium benzoate is the sodium salt of benzoic acid ($C_7H_5NaO_2$). It is a white powder, mainly used as preservative, anti-microbial additive, fungicide, or flow additive in tableting. Its E- and CAS-number are 211 and 532-32-1, respectively (Trigon Chemie GmbH, 2014). The true solid density of 1475 kg·m$^{-3}$ was measured as described in Section 3.6.3 (p. 50).

For the continuous SFBLG experiments, a spray solution and an initial filling of the fluidized bed with granules had to be provided. The spray solution with a mass fraction of sodium benzoate $x_{NaB} \approx 0.3$ was prepared from the original sodium benzoate powder, sodium benzoate granules produced in former experiments, and tap water ($x_w \approx 0.7$). Granules from former experiments were also used as initial filling for the experiments. For the first series of experiments with varying classifying volume flow rate, the initial bed filling was prepared by sieving the granules by two screens (mesh width 100 µm and 600 µm) to the particle size fraction 100–600 µm, resulting in an average particle size of $d_{1,3,Series1} \approx 400$ µm (Section 3.1.1, Eq. 3–8, p. 31). For the second series with varying drying conditions, parameters were adjusted and the initial feed granules were sieved to the fraction 100–500 µm with two screens (mesh width: 100 µm and 500 µm), resulting in an average particle size of $d_{1,3,Series2} \approx 300$ µm. In both cases, the initial feed granules were characterized as Geldart Group B particles (Section 2.1, p. 5), and, thus, were easy to fluidize. In every diagram showing the temporal evolution of $q_3$ over process time (Section 4.4, p. 56; for example Fig. 4–2), the curve at $t = 0$ represents the PSD density of the initial feed granules.

Estimating a particle porosity $\Psi_p$ of 25%, and considering the particle porosity in the calculation of the particle density $\rho_p$ from the true solid density $\rho_s$ ($\rho_p = (1-\Psi_p)\cdot\rho_s$), the minimum fluidization velocity (Eq. 2–4) and elutriation velocity (Eq. 2–7) of sodium benzoate granules, depending on the particle diameter, are given in Tab. 4–1.

Tab. 4–1. Minimum fluidization velocity and elutriation velocity for sodium benzoate granules. Estimated $\Psi_p = 25\%$, $T_{gas,in}$: 130°C.

| $d_{1,3}$ [μm] | $u_{mf}$ [m·s$^{-1}$] | $u_{elu}$ [m·s$^{-1}$] |
|---|---|---|
| 100 | 0.004 | 0.22 |
| 500 | 0.09 | 2.31 |
| 600 | 0.12 | 2.79 |

## 4.2 Experimental setup

The experiments were conducted in a cylindrical, pilot-scale fluidized bed plant (Pergande Group, Germany, Fig. 4–1). The diameter of the fluidized bed was 300 mm. The particles were fluidized by heated ambient air. Two fans (Elektror airsystems GmbH, Germany, type: HRD65FU-100/7,5) allowed for control of mass flow rate and pressure inside the plant. Dust was separated from the outlet air by a cyclone and recirculated to the fluidized bed. After passing a bag filter, the fluidizing air was used again in closed loop. Waste moisture was removed from the air by a condenser at a controlled cooling temperature of 12°C. The dried air was heated and used again for fluidization. To prevent an accumulation of gas in the plant due to additional input of atomizing and classifying air, a small fraction of the process air was led out of the process through a purge valve. An external feed tank and screw pump (ALLWEILER GmbH, Germany, type: AEB 4H 12) supplied the two-fluid nozzle (Schlick, model 940, liquid orifice diameter: 0.8 mm), which was installed in top-spray configuration at a distance of 420 mm above the distributor plate of the fluidized bed, with the spray solution. Compressed air was used for atomization (air cap position: 2.5) creating droplets with a size of approximately 40 μm. The distributor plate was made from sintered metal and had a pore size of approximately 100 μm. The discharge of the granules was realized by the centered classifying tube at the bottom of the fluidized bed. Here, compressed air was used for separation, which was heated to prevent condensation in the tube and in the granulation chamber. The classifying tube had an inner diameter of 44 mm and a length to the entrance of the classifying air of 720 mm. For the first experimental series, the product particles were transported via pneumatic conveyer to the storage box. Due to excessive breakage and comminution in the conveyer, the setup was changed for the second series. There, the product particles directly fell into the product storage after leaving the classifier and the pneumatic sluice gate at the end of the classifying tube. In both cases, the product container was standing on a scale to measure the product mass $M_{prod}$ continuously.

The inlet and outlet gas temperature, the gas temperature in the bed, the temperature of the condenser, the inlet and outlet gas moisture content, the plant pressure, the pressure drop over the fluidized bed, the air and liquid pressure of the nozzle, all gas mass flow rates, the total spray mass flow rate and the product mass were measured and recorded in a process control system (PCS, Siemens AG, Germany, type: WinCC).



Fig. 4–1. Continuous SFBLG plant with internal separation setup.

# 4.3 Experimental plan

Two series of experiments were conducted. Every experiment in each series was started with the same material with similar particle size distributions. In the first series, the drying and fluidizing parameters were kept constant, and only the classifying air volume flow rate, and consequently the classifying air velocity, was changed to obtain different bed hold-ups during layering. By increasing the classifying air velocity, also the mean residence time of the particles in the fluidized bed increased, and, thus, the mean particle size grew. The goal here was to study in detail different overspray behavior with respect to different bed heights and its influence on the process behavior as described by Vreman et al. (2009). In the second series of experiments, the classifying air volume flow rate, and, thus the gas velocity and the separation diameter, were kept constant, and the spray mass flow rate, gas inlet temperature and fluidizing gas mass flow rate were changed. By varying drying conditions, different

53

overspray (Tab. 2–1, p. 12) behavior was realized. The influence of internal seed particle formation on the process behavior was thus investigated. For the second series, an experiment with high spray mass flow rate, medium gas inlet temperature and medium gas mass flow rate was chosen as a reference (Ref_Int), and its outcome was compared to the results of experiments in which these parameters were varied systematically, one at a time (Tab. 4–2). The temperature of the classifying air was kept constant at 100°C for all experiments. The spray solution was fed into the fluidized bed at ambient temperature (20°C). The liquid pressure was depending on the spray mass flow rate and was 1.6–1.9 bar. The atomizing air pressure was constant around at 2.6 bar. The mass fraction of sodium benzoate was subject to small differences between the experiments, as the solution had to be prepared anew after 2–3 experiments. Every experiment was conducted once. The separation particle size $d_{sep}$ in Tab. 4–2 was calculated using Eq. 2–11, estimating the particle porosity $\Psi_p = 25\%$ for the calculation of the particle density.

The process time of the experiments varied from 16 to 22 h. In each experiment a sample from the fluidized bed was taken after spraying 3 kg of solution. For the experiment with the lowest spraying mass flow rate (L1_Int), the samples were taken after 2 kg of solution were sprayed. This resulted in sampling times from 13 to 17 min, depending on the chosen parameters. Consequently, 55–80 bed samples were collected per experiment depending on process and sampling time. Every four bed samples, a sample from the discharged product was taken, resulting in 13–21 product samples per experiment. The total sample mass flow rate $\dot{M}_{sam}$ was equal to $\approx 0.1$ kg·h$^{-1}$. Following the experiments, the particle size distribution, the mass fraction of water of the particles, and the particle structure were measured and evaluated, as described in Chapter 3.

The bed mass for every experiment was measured and calculated by the pressure drop over the fluidized bed and the distributor plate. As the distributor plate was gradually clogged by the solids in the spray during the experiments, the pressure drop of the plate also gradually increased, which could not be accounted for in bed mass measurement. Thus, the bed mass value recorded by the PCS was unreliable. As a result thereof, the bed mass was obtained from a mass balance over the whole process, considering the average mass fraction of water $\bar{x}_w$ of starting, bed, and product material. Consequently, the bed mass balance was calculated a posteriori, after the measurement of the mass fraction of water from the bed and product samples (Section 3.2, p. 37). Knowing the initial bed mass at the start $M_{bed,0}$, the spray mass flow rate $\dot{M}_{spray}$, the product mass $M_{prod}$ and the mass of the taken samples $M_{sam}$, the bed mass depending on process time $t$ was calculated by:

$$M_{bed}(t) = \left[ M_{bed,0}\left(1 - x_{w,0}\right) + t\dot{M}_{spray}x_{NaB} - M_{prod}(t)\left(1 - x_{w,av,prod}\right) \right.$$
$$\left. - M_{sam}(t)(1 - x_{w,av,sam}) \right] / \left(1 - x_{w,av,ed}\right) , \tag{4–1}$$

with the mass fraction of sodium benzoate in the spray solution $x_{NaB}$.

Tab. 4–2. Overview of experimental parameters for continuous SFBLG with internal separation.

| Experiment | $T_{gas,in}$ [°C] | $\dot{M}_{gas,in}$ [kg·h⁻¹] | $u_{gas}$ [m·s⁻¹] | $\dot{M}_{spray}$ [kg·h⁻¹] | $x_{NaB}$ [-] | $M_{bed,0}$ [kg] | $u_{class}$ [m·s⁻¹] | $d_{sep}$ [µm] | |
|---|---|---|---|---|---|---|---|---|---|
| C1_Int | 120 | 350 | 1.6 | 12.76 | 0.32 | 6 | **2.8** | 594 | ⎫ |
| C2_Int | 120 | 350 | 1.6 | 12.96 | 0.29 | 6 | **3.3** | 716 | ⎬ series 1 |
| C3_Int | 120 | 350 | 1.6 | 12.73 | 0.29 | 6 | **4.0** | 889 | ⎭ |
| Ref_Int | **130** | **350** | **1.6** | **11.16** | 0.30 | 4 | 4.1 | 910 | ⎫ |
| L1_Int | 130 | 350 | 1.6 | **7.83** | 0.31 | 4 | 4.1 | 902 | ⎬ series 2 |
| L2_Int | 130 | 350 | 1.6 | **9.72** | 0.30 | 4 | 4.1 | 910 | ⎭ |
| T1_Int | **120** | 350 | 1.6 | 11.21 | 0.30 | 4 | 4.0 | 891 | |
| T2_Int | **140** | 350 | 1.6 | 11.18 | 0.30 | 4 | 3.8 | 835 | |
| A1_Int | 130 | **300** | **1.4** | 11.61 | 0.29 | 4 | 4.0 | 894 | |
| A2_Int | 130 | **400** | **1.8** | 11.48 | 0.29 | 4 | 3.8 | 845 | |

Experiment names and varied parameters (bold):

  C – Classifying air velocity

  L – Liquid mass flow rate

  T – Temperature

  A – Air mass flow rate

  Ref – Reference experiment

# 4.4 Results and discussion

This section presents and discusses the results from two experimental series regarding continuous SFBLG with internal separation. In the first series the classifying velocity for the product discharge was varied, and in the second series the drying conditions of the process were varied.

### 4.4.1 Influence of classifying air velocity on process behavior

In the first series, the influence of the classifying air velocity on the process behavior and product quality was investigated. Experiment C1_Int was conducted with a classifying air velocity of 2.8 m·s$^{-1}$. The PSD density and average particle diameter $d_{1,3}$ showed damped oscillations, which receded after about 10 h of process time (Fig. 4–2). Thus, the experiment was stationary regarding particle size, but the bed mass was still varying after 10 h.
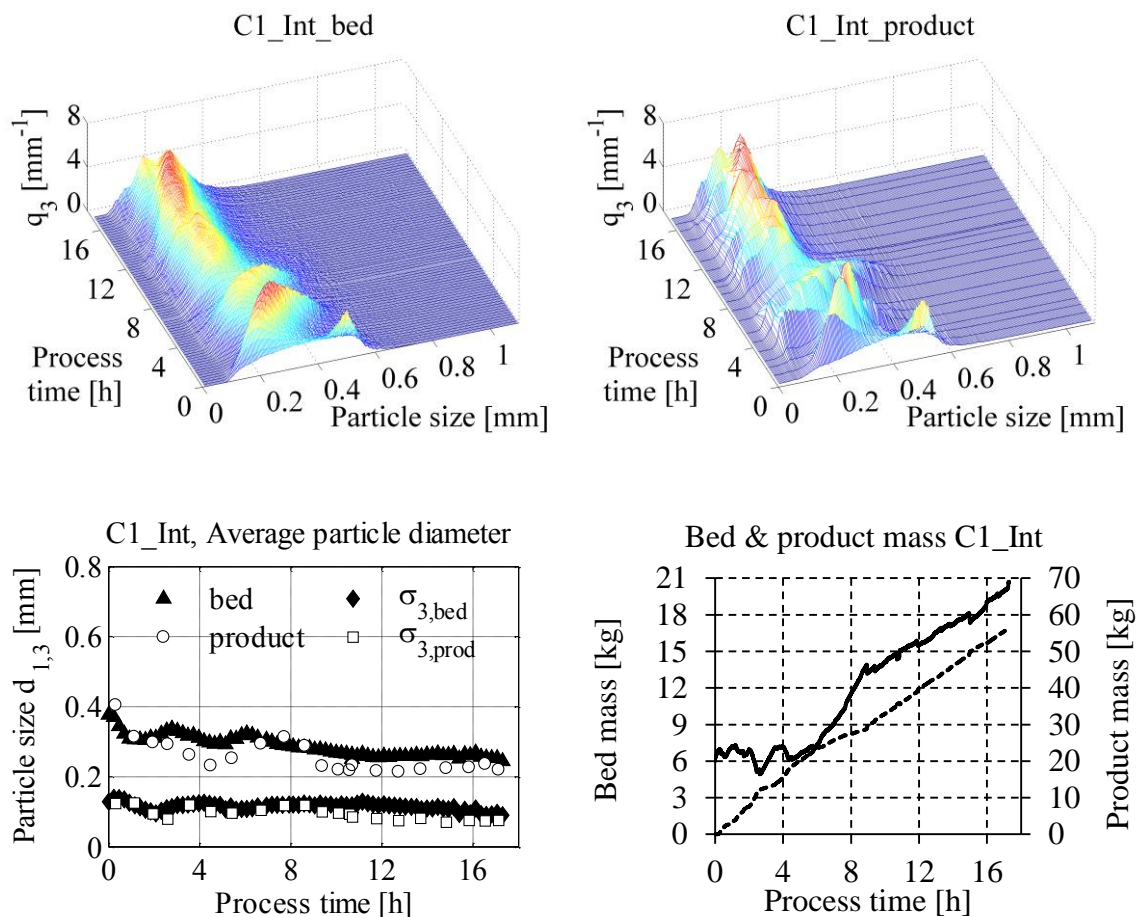


Fig. 4–2. SFBLG with internal separation and varied classifying velocity $u_{class}$, **C1_Int** (2.8 m·s$^{-1}$). Particle size distribution density in the bed (top left) and product (top right). Average particle diameter (bottom left) and bed and product masses (bottom right; solid line: bed, dashed line: product.
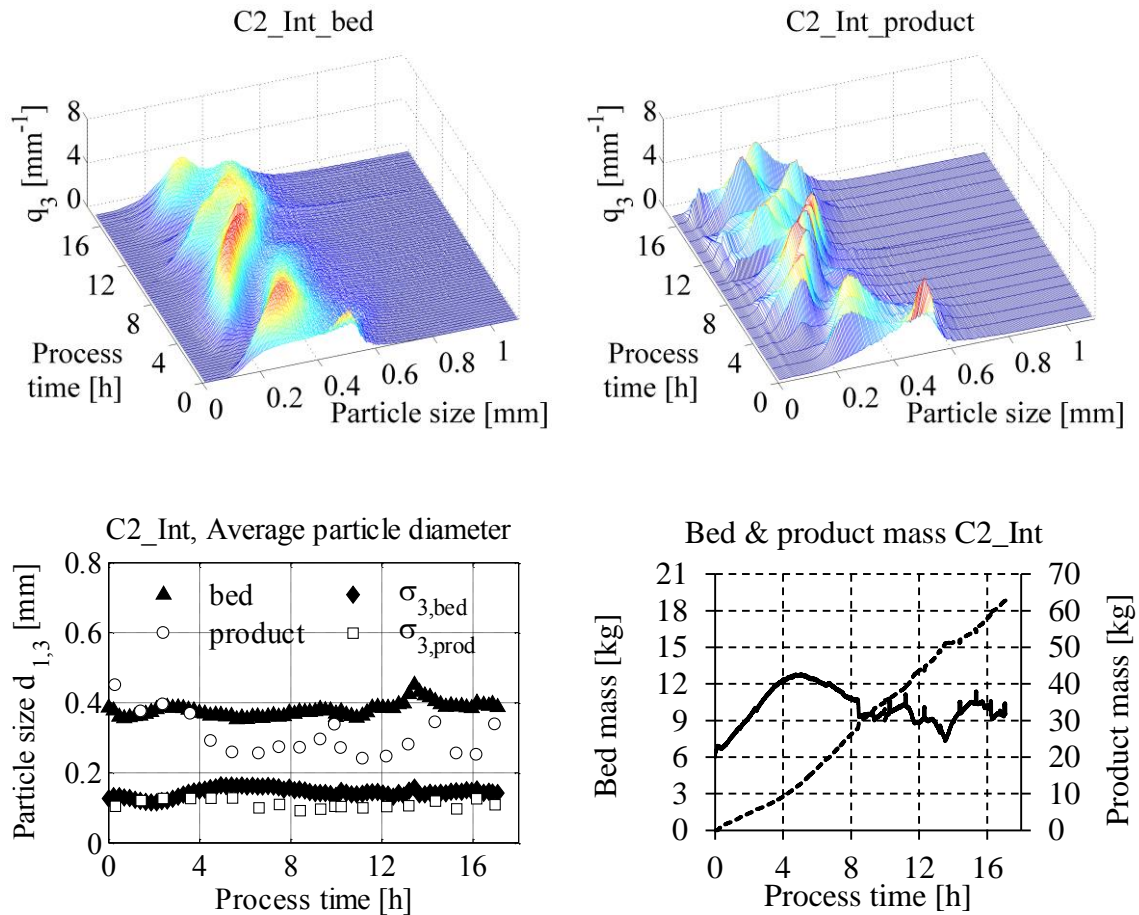
56

C2_Int_bed

C2_Int_product



C2_Int, Average particle diameter

Bed & product mass C2_Int



Fig. 4–3. SFBLG with internal separation and varied classifying velocity $u_{class}$, **C2_Int** (3.3 m·s⁻¹). Particle size distribution density in the bed (top left) and product (top right). Average particle diameter (bottom left) and bed and product masses (bottom right; solid line: bed, dashed line: product).

Increasing the classifying air velocity to 3.3 m·s⁻¹ in experiment C2_Int led to self-sustained oscillations in the PSD density (Fig. 4–3). The average diameter of bed and product particles, and also the bed mass, showed self-sustained oscillations. The experiment reached a limit cycle with an average period time of 5.4 h. The peak and period times (Section 3.1.5, p. 36) are summarized in Tab. 4–3.

Tab. 4–3. Period times for experiment C2_Int.

| Exp. | Parameter | Values [h] |
|---|---|---|
| C2_Int | peak times | 2.58; 9.29; 13.43 |
| | period times | 6.72; 4.14 |
| | average period time | 5.43 |

Consequences of these oscillations were, for example, bimodal particle size distribution densities leading to varying product particle sizes and mass flow rates. For an increased

classifying velocity of 4.0 m·s$^{-1}$ in experiment C3_Int, the PSD density showed damped oscillations again (Fig. 4–4). After about 8.0 h of process time, the average particle diameter $d_{1,3}$ was nearly stationary, indicating steady state operation.

Comparing all three experiments, the process behavior was controlled by the classifying air velocity. The dynamic process behavior changed from damped oscillatory, to sustained oscillatory, to damped oscillatory behavior in the considered parameter range of the classifying air velocity. This behavior is qualitatively explained by Vreman et al. (2009) and Fig. 2–6 (p. 21). A classifying air velocity of 2.8 m·s$^{-1}$ led to a small bed mass and bed height at the beginning of the experiment, due to fast product discharge. Consequently, a large fraction of the sprayed material is drying prior to contact with particles and forming dust (overspray, see Tab. 2–1, p. 12). This dust formed a high amount of new seed particles, stabilizing the process after 9 h of process time. The high amount of seed particles also led to the increasing bed mass later in the process. During the experiment with a classifying air velocity of 3.3 m·s$^{-1}$ varying fractions of overspray were formed. A large overspray fraction at the beginning led to a high amount of seed particles. The bed mass rose until about 4 h of process time, the overspray fraction was reduced, and the particles grew and were discharged. The increased amount of discharged particles led to a decreased bed mass and increased overspray fraction again. Thus, sustained oscillations in PSD density were observed. Contrary, for an increased classifying air velocity of 4.0 m·s$^{-1}$, the bed mass rose to or above nozzle height, leading to a constant, but low overspray fraction. Thus, the oscillations in PSD density were damped, and after 8.0 h of process time, at a level of around 17–18 kg bed mass, the process stabilized due to the constant amount of seed particles formed. So, the height dependent overspray generation assumed by Vreman et al. (2009) explained different process behavior for changing classifying air velocity for one specific set of drying and fluidizing parameters.

Neugebauer et al. (2017) presented a numerical stability analysis of continuous SFBLG with internal separation. The experimental results presented in this dissertation regarding process behavior of continuous SFBLG with internal separation and varied classifying air velocity, and, thus, varied separation diameter, are in qualitative agreement with the observations of Neugebauer et al. (2017). For small and large separation diameters, the simulations of Neugebauer et al. (2017) reached stable steady states. But for intermediate separation diameters, the simulations showed self-sustained oscillations in the PSD. This oscillatory behavior is in qualitative accordance with the experimental observations reported for experiment C2_Int, which was conducted with an intermediate separation diameter ($d_{sep} = 716$ µm, Tab. 4–2, p. 55).
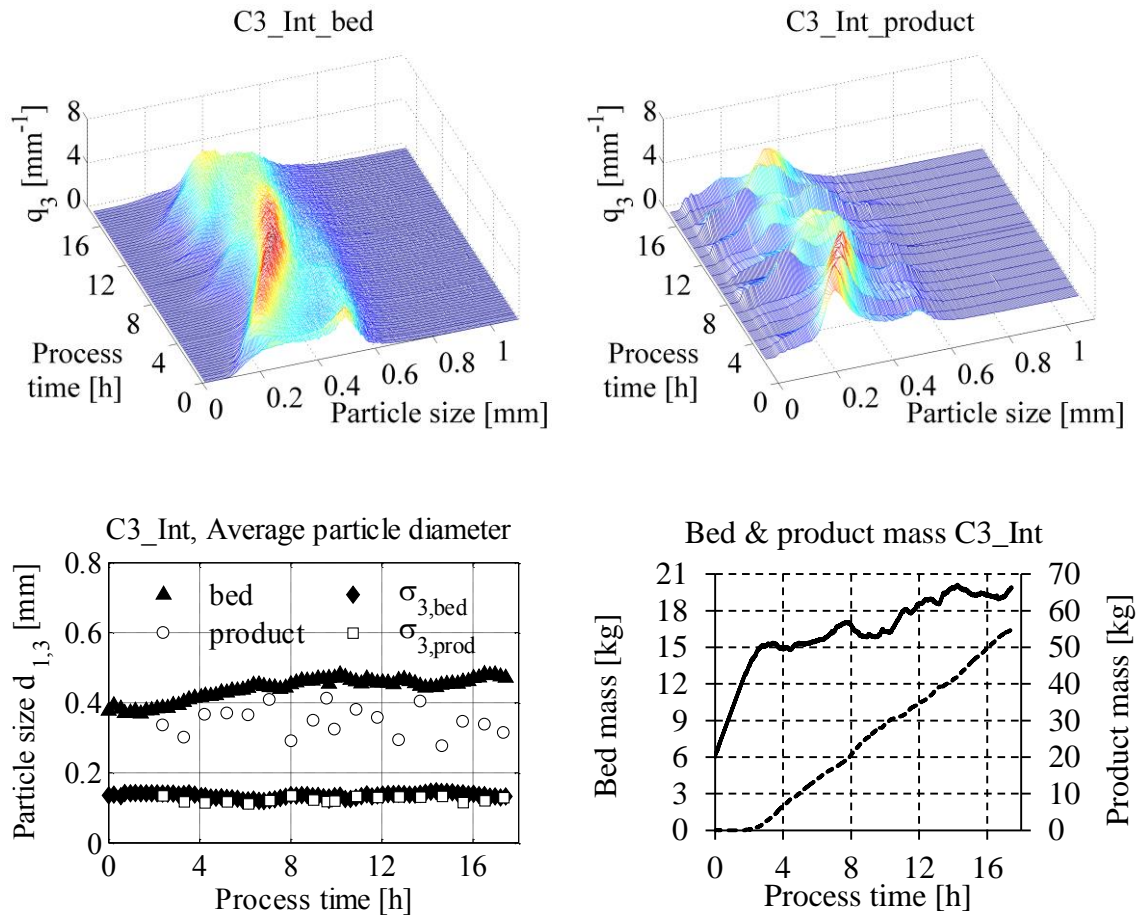
Fig. 4–4. SFBLG with internal separation and varied classifying velocity $u_{class}$, **C3_Int** (4.0 m·s$^{-1}$). Particle size distribution density in the bed (top left) and product (top right). Average particle diameter (bottom left) and bed and product masses (bottom right; solid line: bed, dashed line: product).

In general, the PSD density was shifted to the right, towards larger particle sizes for increased classifying air velocities. This was to be expected, as larger classifying velocities theoretically allowed for the discharge of particles with higher sinking velocities, and consequently, larger particle sizes. Thus, the particles stayed longer in the fluidized bed and grew to larger sizes. However, the PSD densities of product and bed were quite similar, contrary to expectations. No clear separation particle size was reached, at which particles were discharged. This was attributed to swarm hindering effects, meaning larger particles carried smaller particles alongside during product discharge, and to missing separation efficiency of the classifying tube, caused by missing length of the tube. The fact, that the average product particle size was smaller than the average bed particle size was caused by attrition in a pneumatic conveying system, transporting the product particles to the storage. This problem was amended in the second series, where the product directly fell into the storage box. The excessive product particle breakage for experiments C1_Int to C3_Int also complicated the evaluation of product quality.

### 4.4.2 Influence of classifying air velocity on product quality

As product particles were broken during discharge by the pneumatic conveyer, product quality was measured for samples taken from the fluidized bed. The drying conditions were maintained constant during the experiments, thus, the drying potential $\Pi$ (Eq. 2–10, p. 17) and product quality aspects like the surface roughness $R$ (Section 3.4, p. 43) and particle porosity $\Psi_{SEM}$ (Section 3.3, p. 38) were expected to be similar, which was proven by the measured values (Tab. 4–4; complete summary of all experiments with internal separation: Tab. 4–6, p. 74). SEM images of particles from this first series of experiments confirmed the similar, open, porous and rough structure (Fig. 4–5).

Tab. 4–4. Measured product quality values for continuous SFBLG with internal separation and varied classifying air velocities.

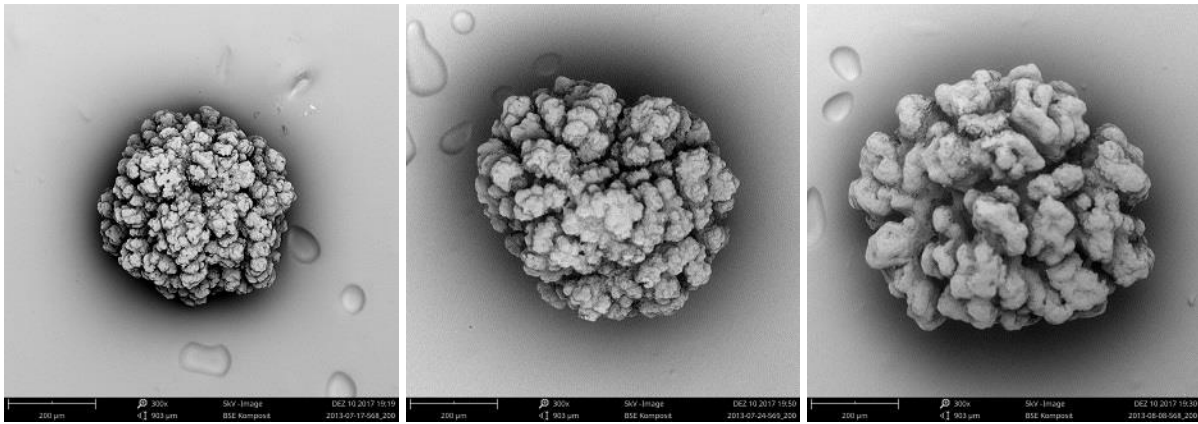| Exp. | $R_{av}$ [µm] | $\Psi_{SEM,av}$ [%] | $\Pi$ [%] |
|------|---------------|---------------------|-----------|
| C1_Int | 12.3 ± 3.3 | 41.5 ± 7.5 | 24.4 |
| C2_Int | 19.0 ± 5.7 | 48.8 ± 6.0 | 23.5 |
| C3_Int | 18.8 ± 3.8 | 41.4 ± 8.8 | 20.1 |



Fig. 4–5. SEM images from bed samples of continuous SFBLG experiments with internal separation and variation of classifying air velocity, C1_Int (left), C2_Int (middle), C3_Int.

### 4.4.3 Influence of drying conditions on process behavior

In the second series of experiments, the influence of the drying and fluidizing parameters on particle size and structure was investigated. At first, the results of the experiments with varied spray mass flow rate are presented. The lowest spray mass flow rate of 7.8 kg·h⁻¹ in experiment L1_Int yielded a nearly batch-like temporal evolution of the particle size distribution density (Fig. 4–6). A lack of new granulation seed particles in the particle size region of 0.1 to 0.2 mm was observed. Note, that occurring seed particles could not be formed solely by over-spray (droplet diameter: ~40 µm), but had to be agglomerates of dust formed

by overspray (see nucleation, Tab. 2–1, p. 12). Without these new seed particles the sprayed material was distributed on the existing granules which kept growing and were discharged until the fluidized bed was nearly empty. In this case (L1_Int) the fluidized bed was too empty to operate any further after approximately 20 h of process time.

Increasing the spray mass flow rate to 9.7 kg·h$^{-1}$ in experiment L2_Int only resulted in a slight change of the process behavior. The particles grew faster, and thus the process broke down even faster, in this case (L2_Int) after approximately 17 h (Fig. 4–7), due to the lack of seed particles in the size range from 0.1 to 0.2 mm. Two growth waves were distinguished in the temporal evolution of the PSD density. Due to the high growth rate, large particles were discharged even faster, and, thus, more spray was available for the smaller particles remaining in the fluidized bed, leading to the second wave observable from about 4 h of process time on. This wave did not originate from seed particles generated in the process, and so the temporal evolution of the PSD density of experiment L2_Int was still similar to a PSD density observable in a batch process.
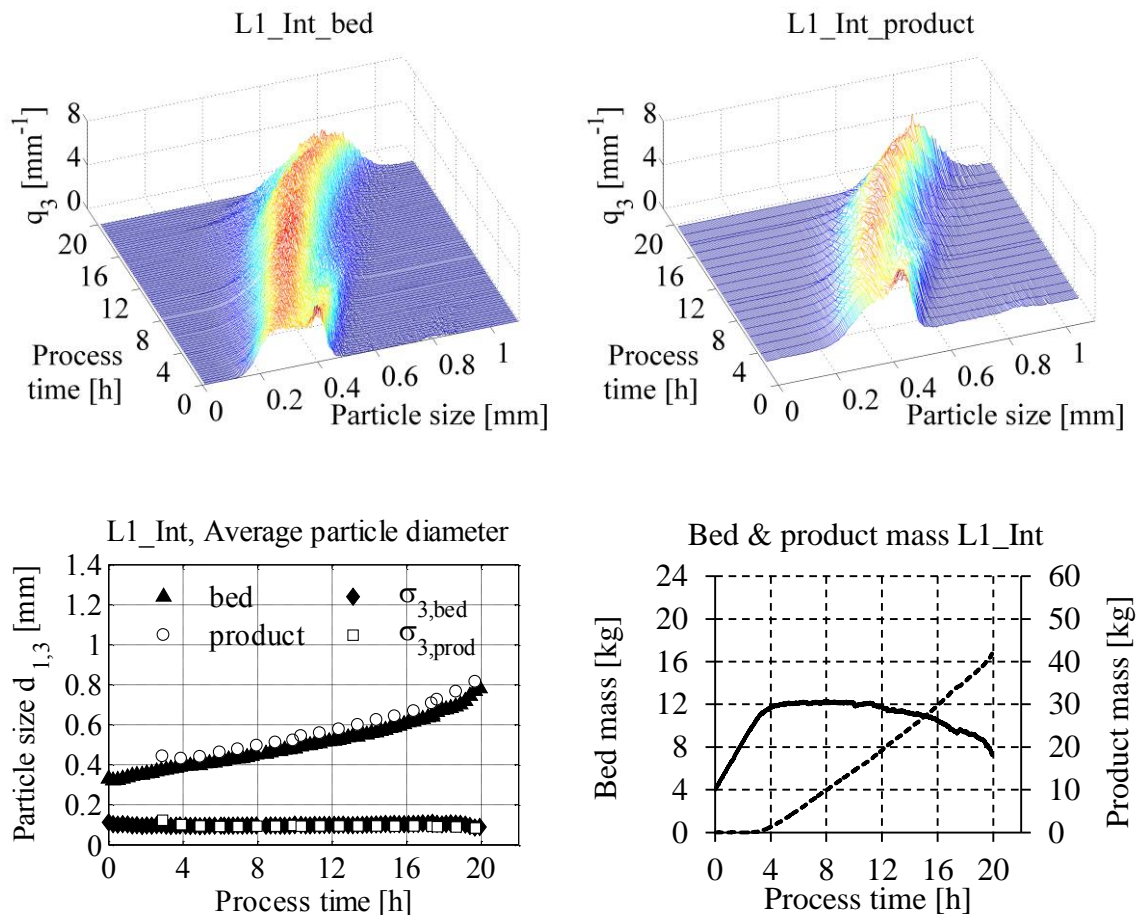


Fig. 4–6. SFBLG with internal separation and varied spray mass flow rate $\dot{M}_{spray}$, **L1_Int** (7.8 kg·h$^{-1}$). Particle size distribution density in the bed (top left) and product (top right). Average particle diameter (bottom left) and bed and product masses (bottom right; solid line: bed, dashed line: product).
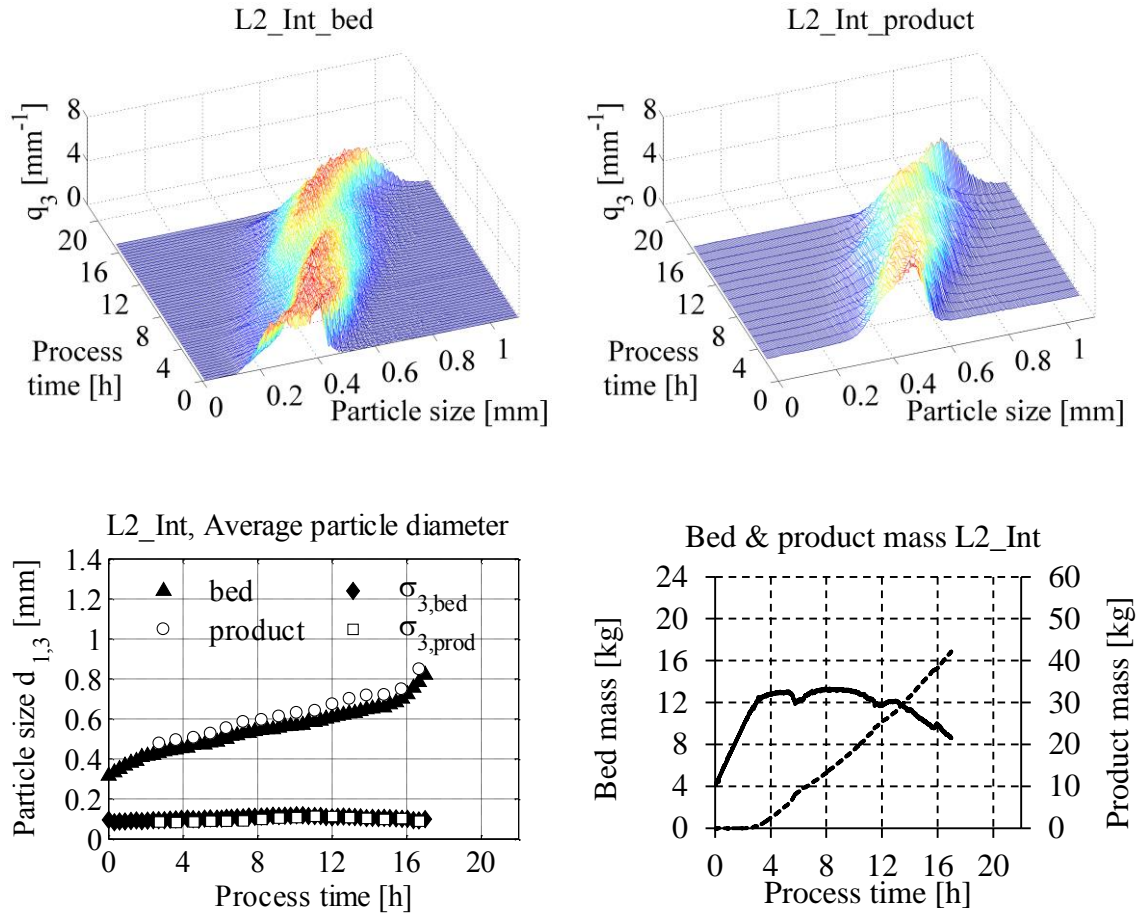
Fig. 4–7. SFBLG with internal separation and varied spray mass flow rate $\dot{M}_{spray}$, **L2_Int** (9.7 kg·h$^{-1}$). Particle size distribution density in the bed (top left) and product (top right). Average particle diameter (bottom left) and bed and product masses (bottom right; solid line: bed, dashed line: product).

Only at the highest spray mass flow rate of 11.2 kg·h$^{-1}$, in the reference experiment (Ref_Int), enough seed particles were produced to sustain the continuous process. But in this case the PSD density showed self-sustained oscillations over the whole process time investigated (Fig. 4–8). Three clear growth waves were identified in this experiment. After 20 h of process time, the start of a fourth wave was observed due to the peak at 0.2 mm, indicating self-sustaining oscillations also for longer process times. Thus, the process parameters of the reference experiment (Ref_Int) allowed for the conduction of a continuous process, but the process reached a limit cycle, featuring self-sustained oscillations of the PSD. As only two full growth waves were observed, only one period time between them could be determined. The period time of the oscillation was 10.66 h. The according peak times were 4.58 h and 15.24 h.

Higher spray mass flow rates could not be achieved due to interfering agglomeration that hindered the desired layering growth process. So this experiment was chosen as the reference for the following variation of fluidizing gas inlet temperature and mass flow rate. With increasing mass flow rate of the spray, the process behavior changed from unstable (empty

62

bed) to oscillatory due to the existence of sufficient seed particles in the particle size range of 0.1 to 0.2 mm.
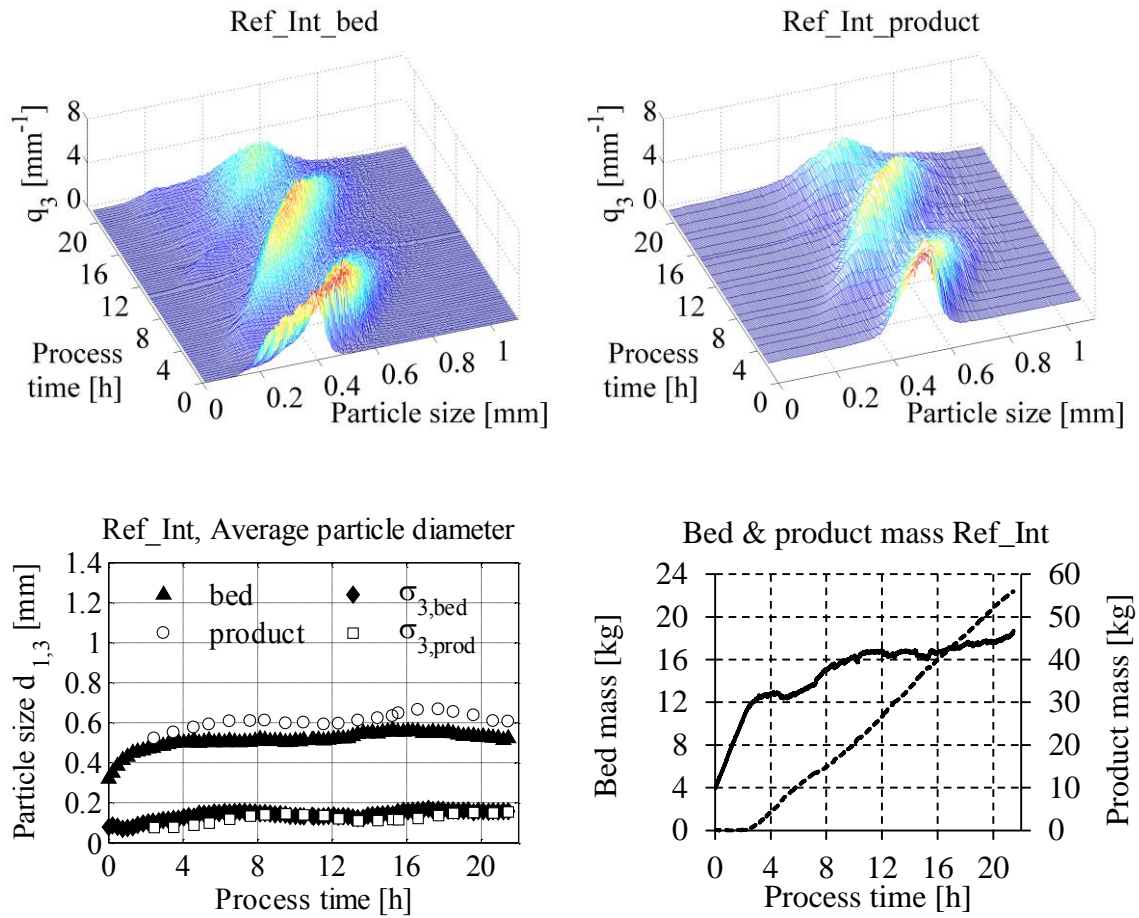


Fig. 4–8. SFBLG with internal separation, reference experiment **Ref_Int** ($\dot{M}_{spray}$ = 11.2 kg·h$^{-1}$, $T_{gas,in}$ = 130°C, $\dot{M}_{gas,in}$ = 350 kg·h$^{-1}$). Particle size distribution density in the bed (top left) and product (top right). Average particle diameter (bottom left) and bed and product masses (bottom right; solid line: bed, dashed line: product).
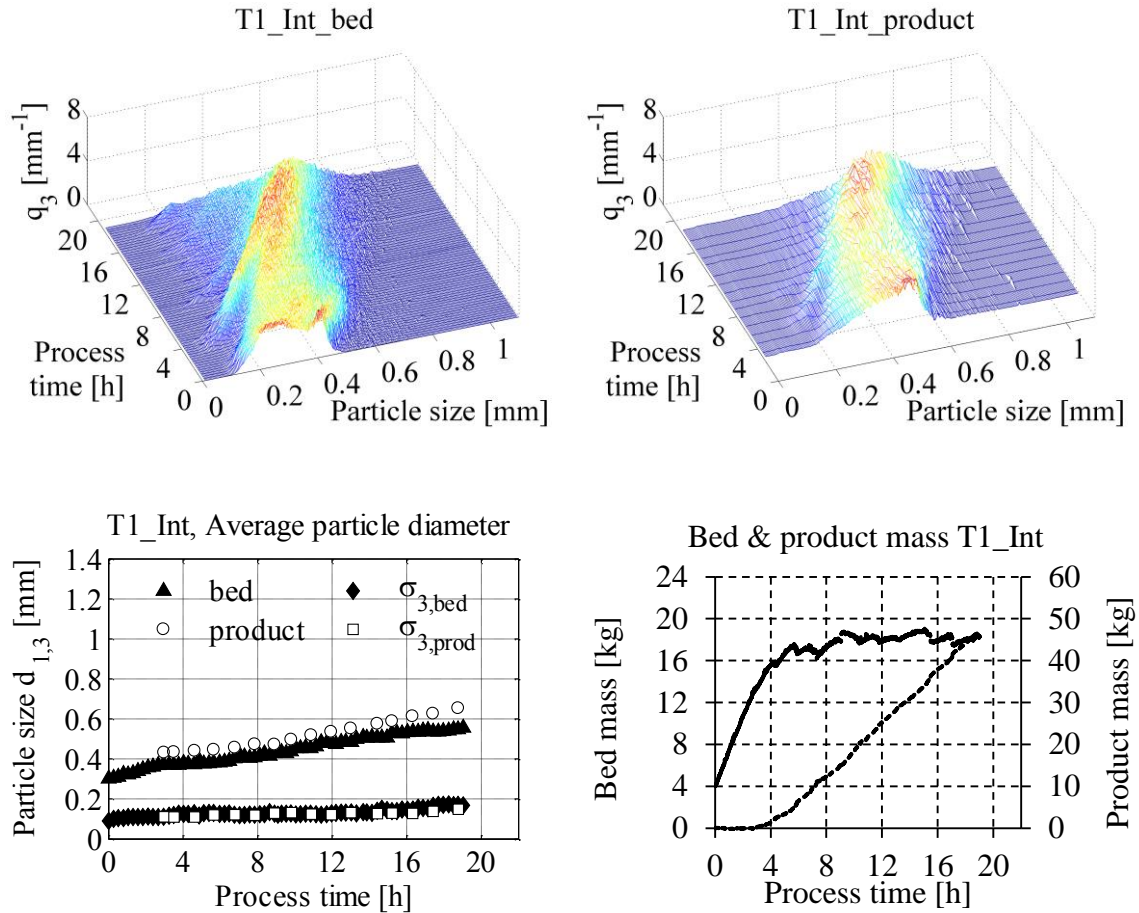
Fig. 4–9. SFBLG with internal separation and varied inlet temperature $T_{gas,in}$, **T1_Int** (120°C). Particle size distribution density in the bed (top left) and product (top right). Average particle diameter (bottom left) and bed and product masses (bottom right; solid line: bed, dashed line: product).

Reducing the fluidizing gas inlet temperature to 120°C in experiment T1_Int led to damped oscillatory behavior of the particle size distribution density (Fig. 4–9). A high amount of seed particles in the size range of 0.1 to 0.2 mm existed in the bed, leading to small growth waves merging with the main wave. New seed particles were formed (for example peak at 0.2 mm for 4 h process time) and grew into the size distribution originating from the initial condition. The high amount of formed seed particles dampened the oscillation of the particle size distribution. For long process times ($> 9.8$ h) the damped oscillation resulted in a nearly stationary evolution of the particle size distribution density, resulting in constant bed mass and product mass flow rate.

The experiment with a fluidizing gas inlet temperature of 130°C was already presented as the reference (Ref_Int, Fig. 4–8). Self-sustained oscillations of the particle size and three main growth waves were observed in the temporal evolution of the particle size distribution density.
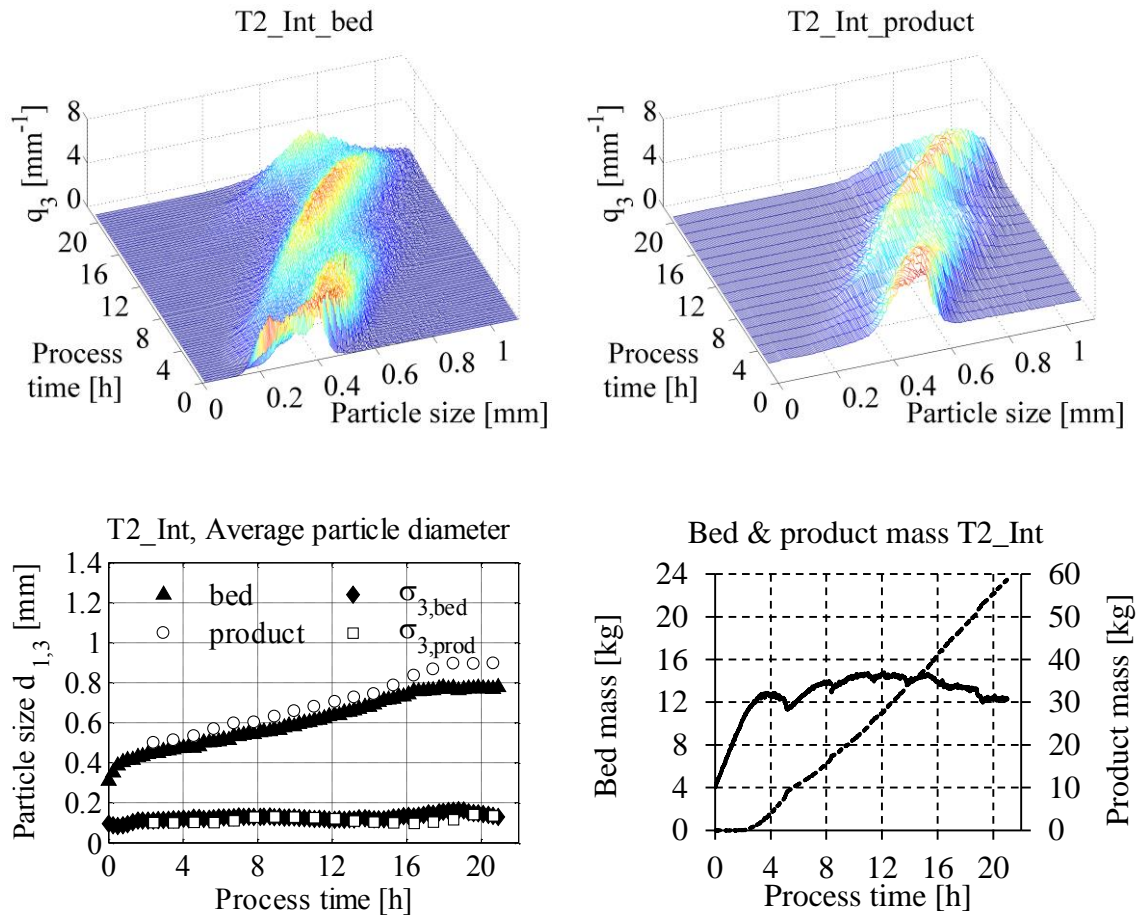
Fig. 4–10. SFBLG with internal separation and varied inlet temperature $T_{gas,in}$, **T2_Int** (140°C). Particle size distribution density in the bed (top left) and product (top right). Average particle diameter (bottom left) and bed and product masses (bottom right; solid line: bed, dashed line: product).

Further increase of the temperature to 140 °C in experiment T2_Int completely changed the process behavior (Fig. 4–10). The process was lacking seed particles (missing peaks around 0.1–0.2 mm) and, thus, the temporal evolution of the particle size distribution density showed less oscillations and a more batch-like shape. At the end of the experiment, after approximatley 22 h of process time, the bed mass was low but relatively constant, but the danger of emptying of the bed for longer process times existed. Three different growth waves were distinguishable, but the first two originated from the intitial starting particles, and the third one close to the end of the process also did not start from seed particle size (0.1–0.2 mm). Due to the increased discharge of large particles after about 16 h of process time, more spray was available for the growth of the smaller particle size fractions still remaining in the fluidized bed, leading to the observable growth wave at the end of the process. Comparing the three experiments with different fluidizing gas inlet temperature showed different behavior in overspray generation and seed particle formation. With increasing temperature, less seed particles were generated, leading to changing process behavior, stated as damped oscillatory, oscillatory, and possibly unstable for 120 °C, 130 °C and 140 °C, respectively.
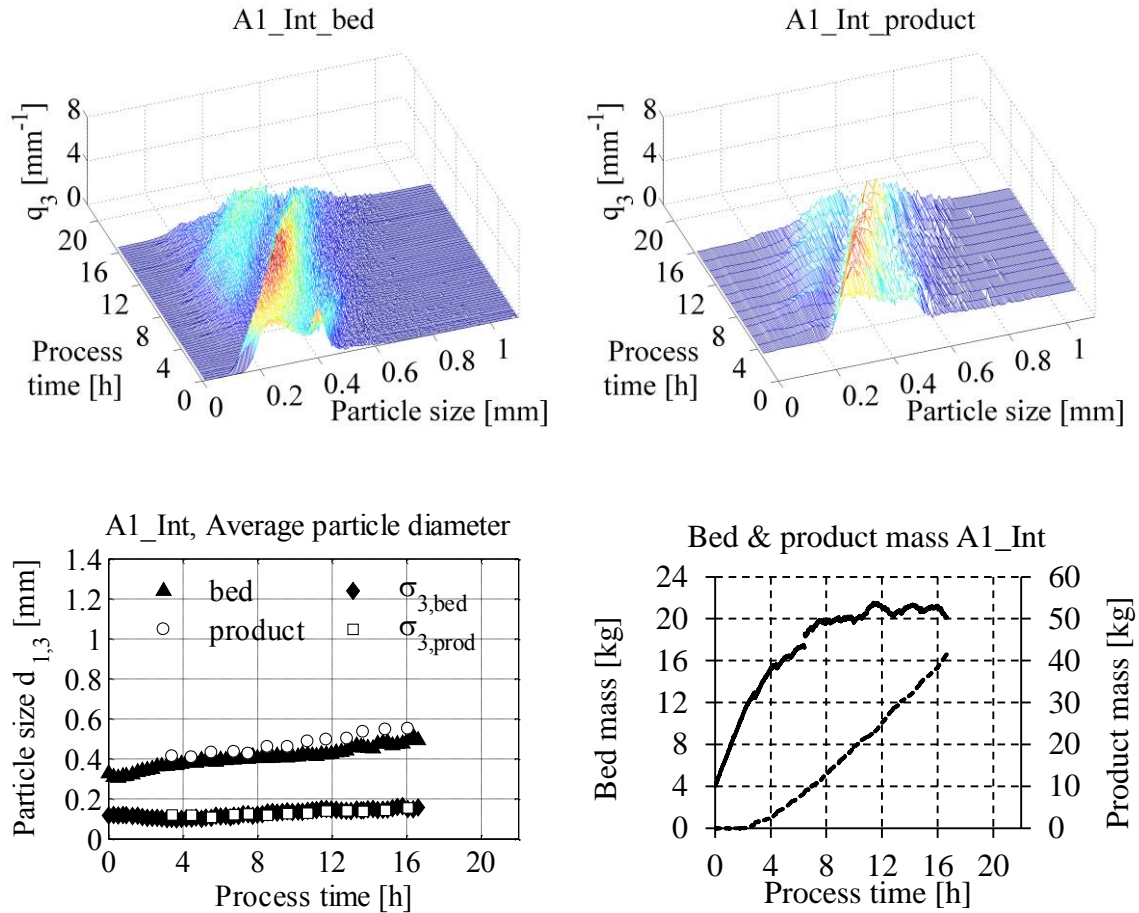
Fig. 4–11. SFBLG with internal separation and varied gas mass flow rate $\dot{M}_{gas,in}$, **A1_Int** (300 kg·h$^{-1}$). Particle size distribution density in the bed (top left) and product (top right). Average particle diameter (bottom left) and bed and product masses (bottom right; solid line: bed, dashed line: product).

The experiments with varied fluidizing gas mass flow rate yielded similar results to the experiments with varied fluidizing gas inlet temperature. For the lowest gas mass flow rate of 300 kg·h$^{-1}$ in experiment A1_Int (Fig. 4–11) a high amount of seed particle formation was observed leading to a damped oscillation of the PSD density. This was similar to the oscillations observed for the lowest fluidizing gas inlet temperature (T1_Int). After a process time of around 8.5 h, particle size and bed mass indicate a nearly steady state. The reference experiment with a fluidizing gas mass flow rate of 350 kg·h$^{-1}$ showed the strongly oscillating behavior already described above. Increasing the air mass flow rate to 400 kg·h$^{-1}$ led to an emptying of the fluidized bed after approximately 18 h of process time, and thus an unstable process (Fig. 4–12). Again no seed particles in the size range of 0.1 to 0.2 mm occured in the bed. The temporal evolution of the particle size distribution density was batch-like, since only one main growth wave was observed. In summary, with increasing fluidizing gas mass flow rate from 300 kg·h$^{-1}$ to 350 kg·h$^{-1}$ and 400 kg·h$^{-1}$ the process behavior changed from damped oscillatory to oscillatory to unstable, respectively. The dynamic behavior of all experiments with internal separation is summarized in Tab. 4–8 (p. 76).
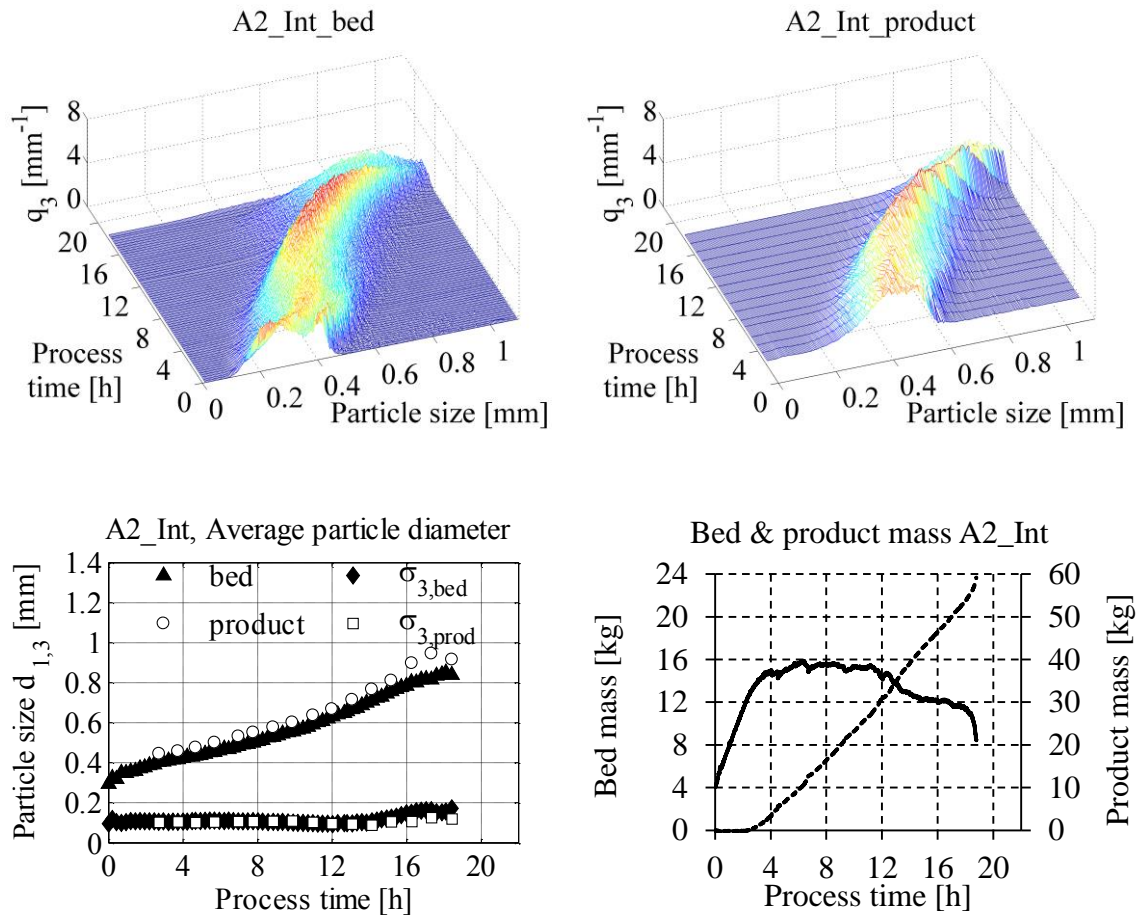
Fig. 4–12. SFBLG with internal separation and varied gas mass flow rate $\dot{M}_{gas,in}$, **A2_Int** (400 kg·h$^{-1}$). Particle size distribution density in the bed (top left) and product (top right). Average particle diameter (bottom left) and bed and product masses (bottom right; solid line: bed, dashed line: product).

The second series of experiments presented the effect of drying and fluidizing parameters on the formation of seed particles and thus the process behavior. The curves of the particle size distribution densities for all experiments started at a minimum particle size of approximately 0.1 mm. These particles could not have been formed by overspray solely (droplet size: ~40 μm, see Section 4.2, p. 52). The dust particles, which were formed by overspray, had to agglomerate before being large enough to stay in the fluidized bed and serve as seed particles. Grünewald et al. (2010) presented experimental nucleation studies for bottom-spray fluidized bed layering of limestone. In their work different overspray rates were linked to the drying parameters of the process. They did not consider the dust ($d < 0.15$ mm) formed by overspray to represent new seed particles for the granulation but agglomerates of this dust ($d \approx 0.15$ mm). Figure 4–13 shows the general idea behind their understanding of seed particle formation. Also Saleh et al. (2003) and Hemati et al. (2003) confirmed prevailing agglomeration for particles smaller than 0.2 mm and 0.3 mm, respectively, and layering growth for larger particles.

In the presented experiments, intense drying conditions, like small spray mass flow rates, high fluidizing gas inlet temperature and high fluidizing gas mass flow rate, led to missing seed

particles for the continuous layering growth process. With intense drying (L1_Int, L2_Int, T2_Int and A2_Int) presumably enough dust was formed by overspray, but the dust particles were too dry to form agglomerates, as proposed by Grünewald et al. (2010). The general mass fractions of water $x_w$ of particles in the fluidized bed and product are listed in Tab. 4–6 (p. 74). Consequently, agglomeration of dust particles ($< 40 \, \mu m$) to seed particle size (0.1–0.2 mm) was hardly possible. Additionally, a higher fluidizing air velocity, as used in experiments A2_Int and T2_Int (here only slightly increased), favored the discharge of dust particles and entrainment of spray droplets at the top of the fluidized bed. The dust reaching the cyclone was recycled, but possibly discharged from the fluidized bed again quickly. Thus, the seed particle formation was additionally reduced due to the lack of dust present in the fluidized bed.

Moderate drying conditions like higher spray mass flow rate (Ref_Int), lower fluidizing gas inlet temperature (T1_Int) and lower fluidizing gas mass flow rate (A1_Int) led to increased formation of seed particles. With these parameters, presumably less dust was generated through overspray, but the existing dust particles had a higher residual moisture (see mass fraction of water $x_w$ in Tab. 4–6, p. 74), due to the more moderate drying conditions. Thus the agglomeration of dust particles to seed particles was enhanced.

Moreover, with lower fluidizing gas mass flow rate (A1_Int) the dust was held more likely in the bed, also enhancing the formation of seed particles. A high generation of seed particles led to the described damped oscillatory behavior of the PSD density. Low seed particle formation resulted, on the other hand, in unstable processes due to the emptying of the bed and break-down of the process. Between these two limits for the drying conditions, self-sustained oscillations of the particle size were observed (Ref_Int), related to different behavior of seed particle generation during the process. Here agglomeration of the dust particles was possible, but the amount of dust was controlled by the changing bed height due to particle growth and discharge, as Vreman et al. (2009) described. This explanation also holds for the first series of experiments with varied classifying velocity, where agglomeration of the dust particles to seed particles was possible, and only the amount of dust in the bed was varied through different bed heights and, thus, different overspray rates. So in addition to the height dependency of the dust formation by overspray, the agglomeration of dust to seed particles, which depends on the residual moisture of the dust, has to be considered for a complete understanding of the process dynamics of continuous spray fluidized bed layering with internal separation and internal seed particle formation.
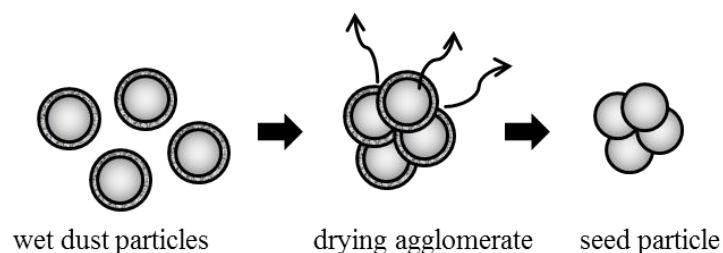


wet dust particles    drying agglomerate    seed particle

Fig. 4–13. Mechanism of seed particle production, following Grünewald et al. (2010).

### 4.4.4 Influence of drying conditions on product quality

As described in Section 2.2.4 (p. 14) a variation in drying conditions changed particle properties like porosity (Section 3.3, p. 38) and roughness (Section 3.4, p. 43). The measured values are summarized in Tab. 4–6 (p. 74), and the according SEM images are shown in Fig. 4–15. Intense drying ($\Pi > 47\%$) led to smooth and dense particles. Moderate drying ($\Pi \leq 47\%$) resulted in open, rough and porous structures. These changes in structure, depending on drying conditions, were in accordance with the findings of Rieck et al. (2015), describing different structure formation and shell porosity for SFBC processes with sodium benzoate. Drying of sodium benzoate solution is a crystallization process. Moderate drying conditions enhanced crystal growth. The liquid evaporated relatively slowly allowing for extended crystal growth. Thus large and porous structures were formed. Contrary, intense drying led to a more precipitation-like solidification of the sodium benzoate. Fast evaporation of the liquid resulted in fast super-saturation of the solution. Thus, many crystallization nuclei were formed on the particle surface, which had less time to grow, and thus a smoother and less porous surface was generated. For further discussion of this behavior see Rieck et al. (2015). A decreasing linear correlation, expressing the average particle porosity $\Psi_{SEM,av}$ over drying potential for continuous SFBLG experiments with internal separation, is shown in Fig. 4–14 (left). The correlation is in qualitative agreement with Rieck et al. (2015), but the exact values differ. Rieck et al. (2015) reported shell porosities for SFBC of $\gamma$-$Al_2O_3$ spheres with sodium benzoate in the range of 20–40%, which are comparable to the particle porosities presented here for SFBLG. But the correlation regarding the drying potential presented here differs slightly to the correlation given by Rieck et al. (2015). Main reason for this is the different core material in both experimental investigations.
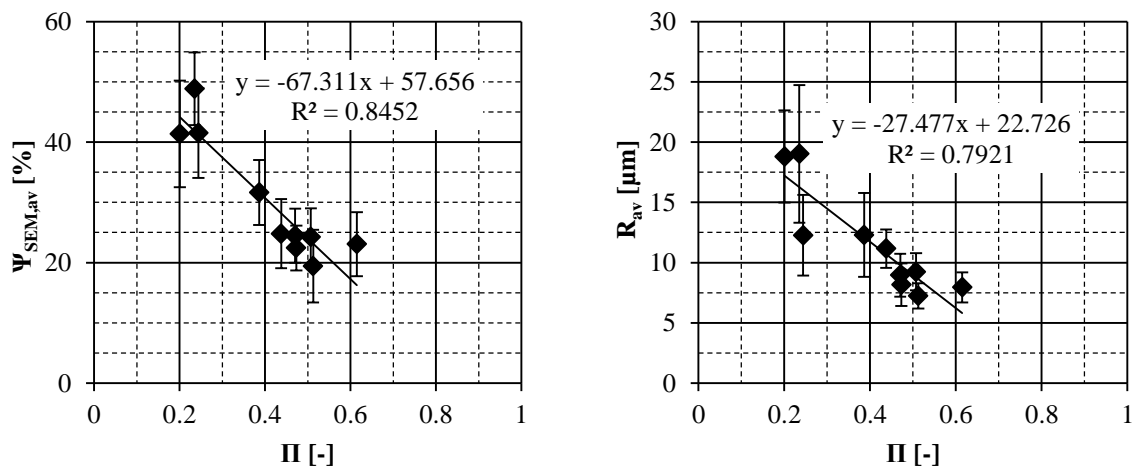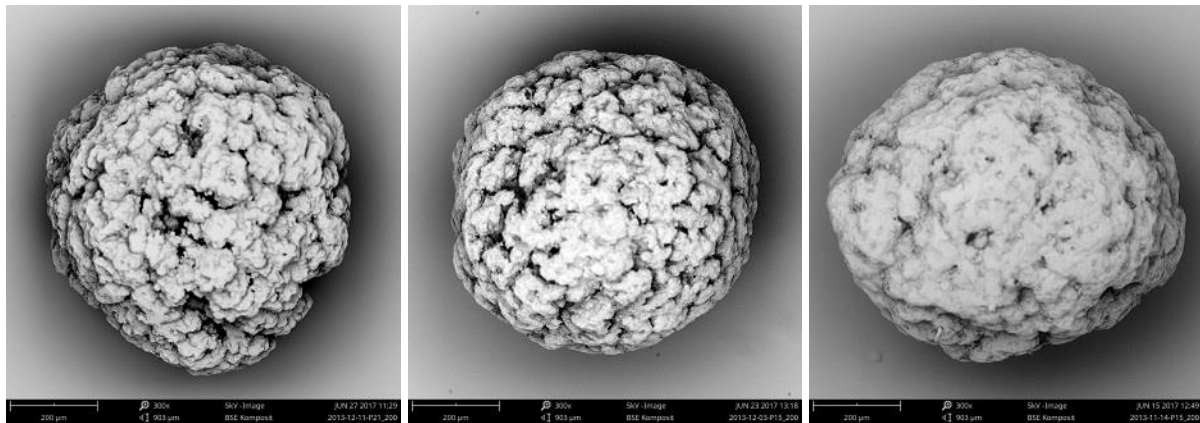


Fig. 4–14. Correlation between average particle porosity $\Psi_{SEM,av}$ and drying potential $\Pi$ (left), and average particle roughness $R_{av}$ and $\Pi$ (right) for continuous SFBLG with internal separation. Error bar: Standard deviation for 10 measurements.

Ref_Int: 11.2 kg·h$^{-1}$

$\Psi_{SEM, Ref} = 24.5\%$; $R_{Ref} = 9.0$ µm

L2_Int: 9.7 kg·h$^{-1}$

$\Psi_{SEM, L2} = 19.4\%$; $R_{L2} = 7.2$ µm

L1_Int: 7.8 kg·h$^{-1}$

$\Psi_{SEM, L1} = 23.1\%$; $R_{L1} = 7.9$ µm
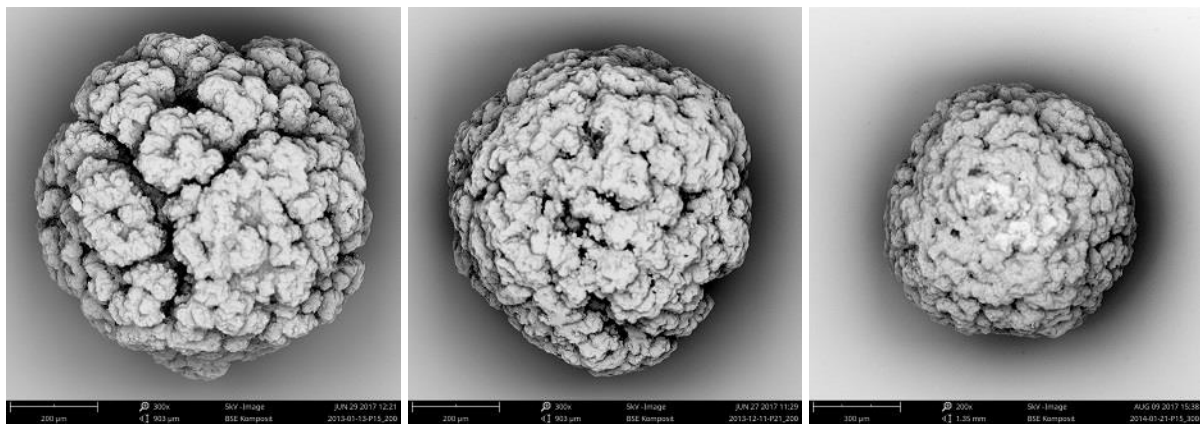
T1_Int: 120°C

$\Psi_{SEM, T1} = 24.8\%$; $R_{T1} = 11.2$ µm

Ref_Int: 130°C

$\Psi_{SEM, Ref} = 24.5\%$; $R_{Ref} = 9.0$ µm

T2_Int: 140°C

$\Psi_{SEM, T2} = 24.3\%$; $R_{T2} = 9.2$ µm
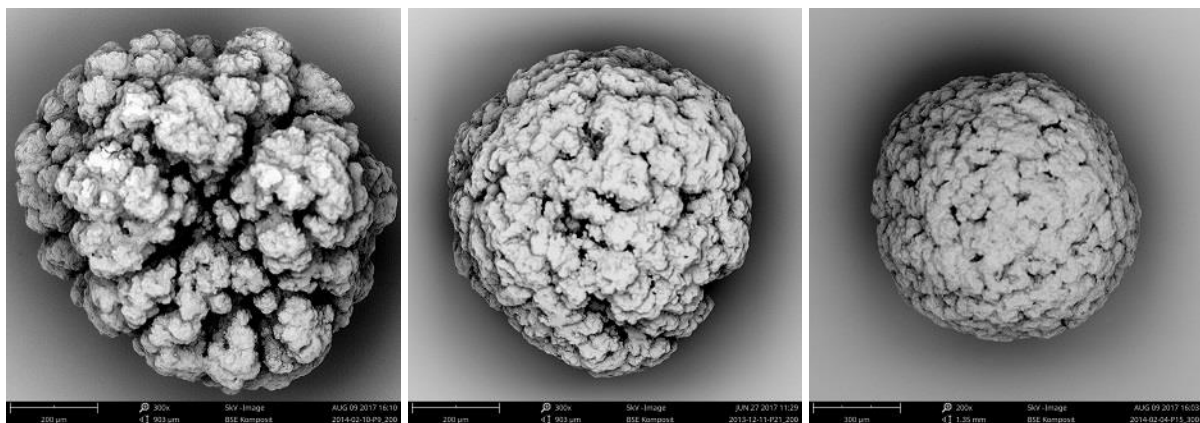
A1_Int: 300 kg·h$^{-1}$

$\Psi_{SEM, A1} = 31.6\%$; $R_{A1} = 12.3$ µm

Ref_Int: 350 kg·h$^{-1}$

$\Psi_{SEM, Ref} = 24.5\%$; $R_{Ref} = 9.0$ µm

A2_Int: 400 kg·h$^{-1}$

$\Psi_{SEM, A2} = 22.4\%$; $R_{A2} = 8.2$ µm

Fig. 4–15. SEM images from product samples of continuous SFBLG experiments with internal separation and variation of drying conditions.

70

The different structure formation due to different drying conditions also resulted in varying particle roughness. A decreasing linear correlation between the average particle roughness $R_{av}$ and the drying potential $\Pi$ is given in Fig. 4–14 (right). The particle porosity and roughness are correlating. Particles with a large roughness also were very porous, and vice versa. A linear correlation expressing this proportional trend is given in Fig. 4–16. In the investigated parameter region, $\Psi_{SEM,av}$ and $R_{av}$ depend linearly on $\Pi$ and on each other. Large particle roughness originated from large crystal structures of sodium benzoate, which also led to higher internal particle porosity. Consequently, the linear dependency of porosity and roughness was to be expected and is reasonable. The trends in particle porosity and roughness are also visible in the SEM images shown in Fig. 4–15. In each line, drying gets more intense from left to right, resulting in smoother and less porous granules.

Comparing the particles from series 1 (Fig. 4–5, p. 60) and series 2 (Fig. 4–15) indicates different particle structures. The higher spray mass flow rate and reduced fluidizing gas inlet temperature, and, thus, the reduced remaining drying potential of the exhaust air, led to very porous and rough particles in series 1, compared to the particles from series 2.
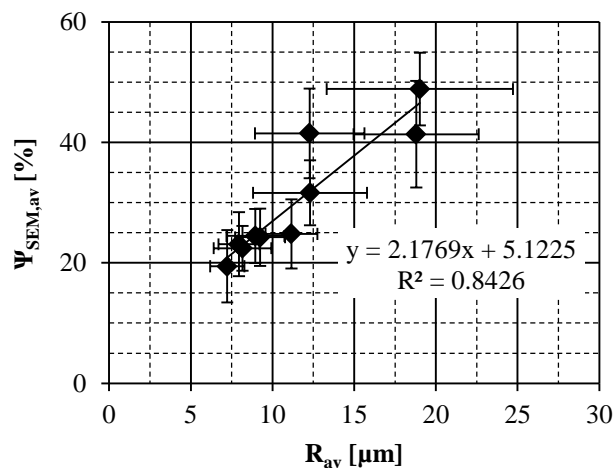


Fig. 4–16. Correlation between average particle porosity $\Psi_{SEM,av}$ and average particle roughness $R_{av}$ for continuous SFBLG with internal separation. Error bar: Standard deviation for 10 measurements.

### 4.4.5 Steady state considerations

All steady state data for experiments C1_Int, C3_Int, T1_Int and A1_Int is listed in Tab. 4–7. Unstable experiments and the experiment with self-sustained oscillations in the PSD are not considered here.

To determine the steady states for the first series of experiments, the values of the particle size $d_{1,3}$ of the bed samples were used, as product particles were partly broken. The steady states in average particle size were reached at 10.0 h and 8.0 h respectively (with $CoV < 2.0\%$ and $m = 16$, see Section 3.1.3, p. 33). The starting particle size was set to zero, as granules were formed completely by internal nucleation, and no external nuclei with a measureable size were added to the process. The steady state particle size in the bed was gained by averaging

71

$d_{1,3}$ in the steady state period. The obtained growth rates of 0.8–1.7 µm·min$^{-1}$ lie within the expected range of 0.17–1.7 µm·min$^{-1}$ (Section 2.2.1, p. 11).

The steady states for the second series of experiments were determined by successively averaging the particle diameters of each four ($m = 4$) product samples, and the following evaluation of $CoV$ (here: $CoV < 5\%$). As one product sample was taken in the time interval in which four bed samples were taken, averaging the particle size of four product samples ($m = 4$) equaled the averaging of particle sizes from 16 bed samples ($m = 16$), as described earlier for series 1. The temporal progression of an experiment, considering 16 bed samples or 4 product samples, was similar. The steady states for T1_Int and A1_Int were reached after 9.8 h and 8.5 h, respectively. Averaging the product particle size during steady state, the growth rates of 1.3–1.7 µm·min$^{-1}$ again lie within the expected range (Section 2.2.1, p. 11). Comparing the growth rates from series 1 and 2 to literature is difficult, as SFBLG in batch or continuous mode without external seed particles was scarcely found in literature, especially with similar material. Only Rieck et al. (2015) present data from batch SFBC experiments, where 0.5 kg of γ-Al$_2$O$_3$ were coated with 1 kg of sodium benzoate solution ($x_{NaB} = 0.3$). They achieved average growth rates of 1–3 µm·min$^{-1}$, which are comparable to the growth rates presented here.

For all four experiments, the product mass flow rate during steady state in practice never reached the theoretical maximum value of solids sprayed into the process (Tab. 4–5). The theoretical value of pure solids introduced into the fluidized bed $\dot{M}_{spray,s}$, is calculated by:

$$\dot{M}_{spray,s} = x_{NaB} \cdot \dot{M}_{spray} , \qquad (4\text{–}2)$$

with the mass fraction of sodium benzoate in the spray solution $x_{NaB}$ and the total spray mass flow rate $\dot{M}_{spray}$ (values in: Tab. 4–6). The product mass flow rate in practice $\dot{M}_{prod,prac}$ is the sum of the measured product mass flow rate in steady state $\dot{M}_{prod,ss}$ (values in: Tab. 4–7) and the average sample rate ($\dot{M}_{sam} \approx 0.1$ kg·h$^{-1}$):

$$\dot{M}_{prod,prac} = \dot{M}_{prod,ss} + \dot{M}_{sam} . \qquad (4\text{–}3)$$

Considering the average mass fraction of water of the product particles $\bar{x}_{w,prod}$ the product mass flow rate of pure solids $\dot{M}_{prod,s}$ is calculated by:

$$\dot{M}_{prod,s} = \left(1 - \bar{x}_{w,prod}\right) \cdot \left(\dot{M}_{prod,ss} + \dot{M}_{sam}\right) . \qquad (4\text{–}4)$$

The relative deviation in the mass flow rates $e_{\dot{M}}$ was then calculated:

$$e_{\dot{M}} = \frac{\dot{M}_{prod,s} - \dot{M}_{spray,s}}{\dot{M}_{spray,s}} . \qquad (4\text{–}5)$$

As stated above, the theoretical maximum of the product mass flow rate was never reached. The calculated values are summarized in Tab. 4–5. Dead zones in the whole plant, and accumulation of dust in the cyclone (sticking to the wall), were the reason for this discrepancy. Additionally, the bed masses were not entirely constant during the steady state of the average particle diameter, compensating varying product mass flow rates. Thus, the steady states described here were only reached from a practical point of view, but not if strictly holding to theory, as the solids inlet mass flow rate was higher than the solids output mass flow rate. The higher values for $e_{\dot{M}}$ for the experiments of the first series are attributed to losses in the pneumatic conveying system for product discharge. The pneumatic conveyer included a temporal storage, where the product was separated from the conveyer air by a filter. Parts of the product stuck to the filter and the walls of the temporal storage, and did not reach the product storage box.

Tab. 4–5. Deviation of the steady state product mass flow rate of pure solids $\dot{M}_{prod,s}$ from the theoretical maximum $\dot{M}_{prod,th}$.

| Exp. | $\dot{M}_{spray,s}$ [kg·h$^{-1}$] | $\dot{M}_{prod,s}$ [kg·h$^{-1}$] | $e_{\dot{M}}$ [%] |
|---|---|---|---|
| C1_Int | 4.08 | 3.24 | -20.5 |
| C3_Int | 3.69 | 3.29 | -11.0 |
| T1_Int | 3.36 | 3.23 | -3.9 |
| A1_Int | 3.37 | 3.32 | -1.3 |

Tab. 4–6. Overview of key process parameters and measured values for continuous SFBLG with internal separation.

| Exp | Parameters | | | | | | Measurement | | | | | | |
|---|---|---|---|---|---|---|---|---|---|---|---|---|---|
| | $T_{gas,in}$ [°C] | $\dot{M}_{gas,in}$ [kg·h⁻¹] | $u_{gas}$ [m·s⁻¹] | $\dot{M}_{spray}$ [kg·h⁻¹] | $x_{NaB}$ [-] | $u_{class}$ [m·s⁻¹] | $R_{av}$ [µm] | $Y_{SEM,av}$ [%] | $Y_{CT}$ [%] | $\Pi$ [%] | $x_{w,0}$ [%] | $x_{w,bed,av}$ [%] | $x_{w,prod,av}$ [%] |
| C1_Int | 120 | 350 | 1.6 | 12.76 | 0.32 | 2.8 | 12.3 ± 3.3 | 41.5 ± 7.5 | - | 24.4 | 0.7 | 4.0 | 3.2 |
| C2_Int | 120 | 350 | 1.6 | 12.96 | 0.29 | 3.3 | 19.0 ± 5.7 | 48.8 ± 6.0 | - | 23.5 | 0.6 | 5.0 | 5.3 |
| C3_Int | 120 | 350 | 1.6 | 12.73 | 0.29 | 4.0 | 18.8 ± 3.8 | 41.4 ± 8.8 | - | 20.1* | 2.3 | 4.5 | 8.6 |
| Ref_Int | 130 | 350 | 1.6 | 11.16 | 0.30 | 4.1 | 9.0 ± 1.8 | 24.5 ± 4.5 | - | 47.0 | 0.5 | 0.4 | 0.4 |
| L1_Int | 130 | 350 | 1.6 | 7.83 | 0.31 | 4.1 | 7.9 ± 1.3 | 23.1 ± 5.3 | - | 61.5 | 0.4 | 0.2 | 0.2 |
| L2_Int | 130 | 350 | 1.6 | 9.72 | 0.30 | 4.1 | 7.2 ± 1.0 | 19.4 ± 6.0 | - | 51.3 | 0.1 | 0.1 | 0.1 |
| T1_Int | 120 | 350 | 1.6 | 11.21 | 0.30 | 4.0 | 11.2 ± 1.6 | 24.8 ± 5.7 | - | 43.8 | 0.3 | 1.2 | 1.2 |
| T2_Int | 140 | 350 | 1.6 | 11.18 | 0.30 | 3.8 | 9.2 ± 1.5 | 24.3 ± 4.8 | - | 50.7 | 0.1 | 0.1 | 0.2 |
| A1_Int | 130 | 300 | 1.4 | 11.61 | 0.29 | 4.0 | 12.3 ± 3.5 | 31.6 ± 5.4 | - | 38.6 | 0.8 | 0.9 | 0.7 |
| A2_Int | 130 | 400 | 1.8 | 11.48 | 0.29 | 3.8 | 8.2 ± 1.8 | 22.4 ± 3.7 | - | 47.3 | 0.4 | 0.4 | 0.3 |

* The drying potential for C3_Int was calculated from a water balance, assuming complete evaporation. The measured value of $Y_{out}$, and thus, the calculated $\Pi$, was faulty.

Tab. 4–7. Steady state values for continuous SFBLG experiments with internal separation.

| Exp | From? | $m$ [-] | CoV < ? [%] | $t_{ss}$ [h] | $M_{bed,ss}$ [kg] | $\dot{M}_{prod,ss}$ [kg·h⁻¹] | $\tau$ [h] | $d_{1,3,0}$ [µm] | $d_{1,3,ss}$ [µm] | $G_{av}$ [µm·min⁻¹] |
|---|---|---|---|---|---|---|---|---|---|---|
| C1_Int | bed | 16 | 2 | 10.0–End | 17.02 | 3.25 | 5.23 | 0 | 261 | 0.8 |
| C3_Int | bed | 16 | 2 | 8.0–End | 18.22 | 3.49 | 5.22 | 0 | 461 | 1.5 |
| T1_Int | product | 4 | 5 | 9.8–End | 18.17 | 3.17 | 5.73 | 0 | 573 | 1.7 |
| A1_Int | product | 4 | 5 | 8.5–End | 20.67 | 3.25 | 6.37 | 0 | 505 | 1.3 |

# 4.5 Conclusions

The theoretically predicted oscillations of particle size distributions (Section 2.4.4, p. 24) were proven experimentally in this dissertation. For the first time, a systematic study, resulting in a reliable set of experimental data regarding continuous SFBLG with internal separation was conducted and published. The experimental findings are a valuable source for validation of future upcoming models of the continuous SFBLG process. The observed self-sustained oscillations in the PSD, which were dependent on the classifying, fluidizing and drying parameters, were linked to differences in seed particle generation. The observed process behavior for the investigated parameter region is summarized in Tab. 4–8. Knowledge of the observed process behavior will also improve process understanding in industry, where oscillations in the PSD are usually unwanted, and stable steady states are preferred to maintain constant product output and constant product quality.

For a single set of drying parameters with possible seed particle generation, the process behavior was influenced by the classifying air velocity as the experiments of series 1 showed. Changing bed hold-up influenced the overspray rate, as Vreman et al. (2009) predicted by simulations. A low classifying air velocity of 2.8 m·s$^{-1}$ (C1_Int) resulted in a low bed mass and bed height ($h_{bed} < h_{noz}$) at the beginning of the experiment, due to enhanced product discharge. Thus, a large fraction of the spray formed dust particles by overspray, which led to high seed particle production during the process. The high amount of seed particles overrode possible oscillations in the PSD, leading to damped oscillations and steady state operation after 10.0 h of process time. A high classifying air velocity of 4.0 m·s$^{-1}$ (C3_Int) led to a large bed mass and bed height ($h_{bed} > h_{noz}$), due to reduced product discharge from the beginning of the experiment. Thus, the overspray fraction was low, but constant. This also led to a constant production of seed particles, dampening the occurring oscillations in PSD for long process times. A classifying air velocity in between, here 3.3 m·s$^{-1}$ (C2_Int), led to varying bed mass and bed height. During particle growth, the bed height rose above nozzle height ($h_{bed} > h_{noz}$), reducing overspray but enhancing particle growth. When the large particles were discharged, the bed mass and height dropped relatively fast ($h_{bed} < h_{noz}$), temporarily increasing the overspray fraction. Thus, particle growth was slowed down, and a new growth wave was formed. During particle growth, the bed mass and bed height increased again, reducing overspray and enhancing particle growth, which led to the observed self-sustained oscillations in the PSD. The findings are in qualitative accordance with the numerical stability analysis from Neugebauer et al. (2017), who reported varying process behavior of their simulations, depending on the separation diameter and spray mass flow rate. For small and large separation diameters Neugebauer et al. (2017) observed stable steady states. But for intermediate separation diameters, they observed self-sustained oscillations in the PSD, comparable to the process behavior of experiment C2_Int.

Changing the set of drying conditions for a constant classifying air velocity also changed the process behavior drastically. Moderate drying parameters (T1_Int, A1_Int) led to high seed particle production. The high amount of seed particles resulted in damped oscillations of the PSD, leading to steady state operation. The dust formed by overspray had enough residual moisture to agglomerate to seed particle size (0.1–0.2 mm) and serve as new seeds for the

layering granulation process. Contrary, intense drying (L1_Int, L2_Int, T2_Int, A2_Int) resulted in unstable processes. The overspray generation was supposedly high, but the residual moisture of the dust particles was too low to agglomerate to seed particle size. Thus, the dust was carried out with the fluidizing air, and seed particles for the layering process were missing. Consequently, the existing particles grew, were discharged, and then the process collapsed due to a low bed mass. Drying conditions between those limits (Ref_Int) favored self-sustained oscillations of the PSD. Agglomeration of dust particles to seed particle size was possible, but a changing overspray fraction dependent on the bed mass and bed height resulted in a varying amount of seed particles, leading to self-sustained oscillations, as described in the paragraph above. This means the drying parameters control the process behavior and the product quality regarding particle size over time.

The particle structure was mainly governed by the drying conditions. Varying classifying air velocities did not affect particle roughness and porosity. Moderate drying ($\Pi < 47\%$) resulted in rough and porous granules. Intense drying ($\Pi > 47\%$) led to smooth and dense particles. The particle porosity decreased linearly with increasing drying potential, similarly to the effect described by Rieck et al. (2015) for SFBC with sodium benzoate. A linear correlation between particle porosity and particle roughness was observed, resulting from the crystallization behavior of sodium benzoate. Rough particles also were porous, and vice versa. Consequently, the process conditions for the production of large, smooth and dense particles (intense drying) are in contrast to good conditions for seed particle generation (moderate drying), which is needed in this setup to ensure the continuous process. Vice versa, controlling the drying and fluidizing parameters to ensure a process in steady state also changes the product quality. The classifying air velocity can additionally be used to control the particle size and process dynamics, while keeping a constant product structure.

Tab. 4–8. Process dynamics for continuous SFBLG with internal separation

| Experiment | Steady state? | Oscillating? | Unstable? |
|---|---|---|---|
| C1_Int | x | - | - |
| C2_Int | x | x | - |
| C3_Int | x | - | - |
| Ref_Int | x | x | - |
| L1_Int | - | - | x |
| L2_Int | - | - | x |
| T1_Int | x | - | - |
| T2_Int | - | - | x |
| A1_Int | x | - | - |
| A2_Int | - | - | x |

A next step would be designing a model, being able to describe the observed process behavior. This model needs to account for the agglomeration step of dust to seed particle size, as described by Grünewald et al. (2010). The idea, that dust particles directly serve as seed particles, as assumed in basic models by Mörl (1980) needs to be overcome. Based on such a model, controllers for stabilization of the observed oscillations in PSD could be developed. In general, steady state processes are preferable, as product mass flow rate and product particle size are constant, which in most cases is necessary in industry. This renders controllers important for certain parameter regimes of continuous SFBLG.

# 5 Continuous layering granulation with external separation

This chapter is an extended version of the publications Schmidt et al. (2015a) and Schmidt et al. (2017a). Here, the results of continuous SFBLG with external product separation regarding process dynamics and product quality are presented in two experimental series. In the first series, the influence of the power level of the mill, setting the mill rotation speed and defining the comminution of oversized particles, on process behavior was investigated. The second series determined the influence of drying conditions on product particle morphology and process dynamics.

## 5.1 Materials

The materials used for the experiments with external separation were similar to the materials used for the experiments with internal separation. The preparation of the materials and their properties have already been described in Section 4.1 (p. 51). Sodium benzoate in the size range of 0.1–0.5 mm, resulting in an average diameter of $d_{1,3} \approx 0.35$–0.4 mm, was used as initial filling for the fluidized bed. A sodium benzoate solution with a mass fraction of sodium benzoate of $x_{NaB} \approx 0.3$ was used as spray solution.

## 5.2 Experimental setup

The experimental setup shown in Fig. 5–1 is similar to the setup for internal separation (Section 4.2, p. 52). A cylindrical fluidized bed with a diameter of 300 mm was used in top-spray configuration. Differences only existed in the product discharge (Fig. 2–5, p. 19). Contrary to the setup with internal separation, where a constant classifying air velocity was chosen to obtain relatively constant product particle sizes, the air velocity in the discharge tube was controlled with the intention of maintaining a constant bed mass. Therefore, the bed mass was calculated from the pressure drop of the fluidized bed, including the distributor plate. As the distributor plate usually has a constant pressure drop for a constant fluidizing air mass flow rate, its pressure drop was subtracted from the total pressure drop to only account for the bed mass, at a given mass flow rate of fluidizing air. Due to constantly changing bed heights, bubble formation and pressure gradients in the fluidized bed, measurement of the pressure drop of the bed itself was not possible.

After discharging the material from the fluidized bed, the actual classification step was done externally from the fluidized bed, after a pneumatic conveyer had transported all discharged particles to a vibrating sieve (GKM Siebtechnik GmbH, Germany, type: KTS-V 450/2; mesh widths 0.5 mm and 0.7 mm). There, the particles were separated into oversize, product and undersize fraction. The product fraction was withdrawn from the process, and the oversize fraction was crushed by a rotor beater mill (Retsch Technology, Germany, type: SR 300) and fed back to the fluidized bed, alongside with the undersize fraction. Thus, especially during the startup period, the bed mass was not necessarily constant, as only the particle fraction in the size range of 0.5–0.7 mm was withdrawn, and an equilibrium of incoming solids (spray) and withdrawn solids (product) had yet to be established.
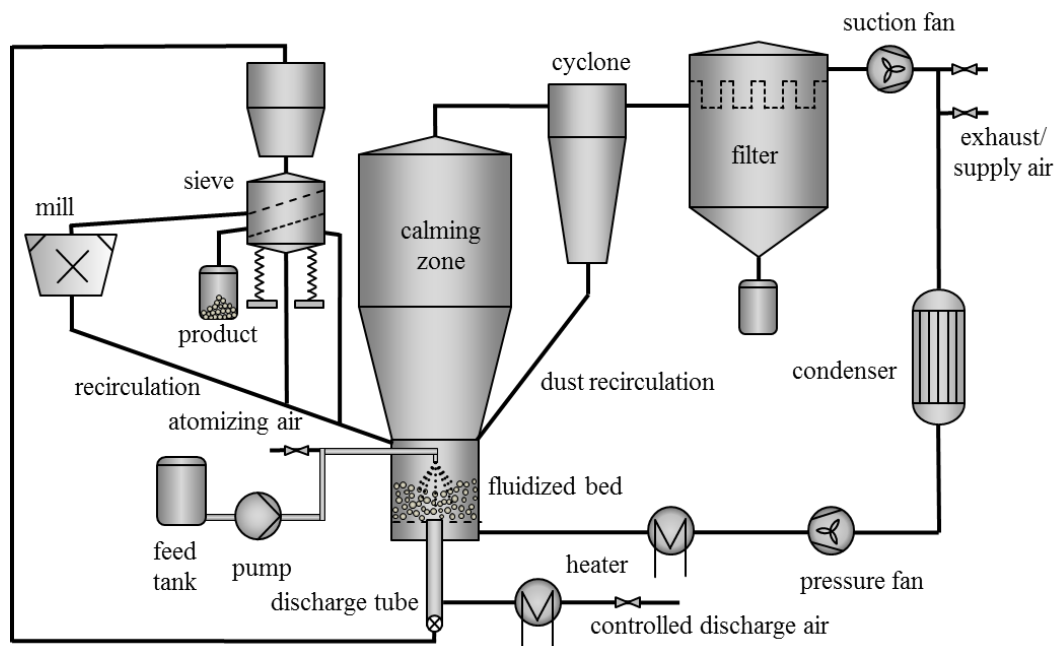


Fig. 5–1. Continuous SFBLG plant with external separation setup.

## 5.3 Experimental plan

Two experimental series were conducted (Tab. 5–1). In the first series, the influence of the comminution of oversized particles on the process behavior was investigated. Therefore, the power level of the mill was varied from 20% to 90%, 100% corresponding to the maximum number of revolution of the rotor of 8100 min$^{-1}$. As the engine's characteristic line was unknown, a clear allocation of power level and number of revolutions below 100% was not possible. All other process parameters were kept constant. In the second series, the influence of the drying conditions on the process behavior and product quality was investigated. Starting with a reference experiment, the inlet gas temperature, gas mass flow rate, and spray mass flow rate were increased and decreased, one parameter at a time.

Tab. 5–1. Overview of experimental parameters for continuous SFBLG with external separation.

| Experiment | $T_{gas,in}$ [°C] | $\dot{M}_{gas,in}$ [kg·h⁻¹] | $u_{gas}$ [m·s⁻¹] | $\dot{M}_{spray}$ [kg·h⁻¹] | $x_{NaB}$ [-] | $M_{bed,0}$ [kg] | $P_{mill}$ [%] | |
|---|---|---|---|---|---|---|---|---|
| M1_Ext | 130 | 350 | 1.6 | 9.77 | 0.30 | 4 | **20** | |
| M2_Ext | 130 | 350 | 1.6 | 9.79 | 0.30 | 4 | **50** | series 1 |
| M3_Ext | 130 | 350 | 1.6 | 10.05 | 0.30 | 4 | **80** | |
| M4_Ext | 130 | 350 | 1.6 | 9.87 | 0.30 | 4 | **90** | |
| Ref_Ext | **130** | **350** | **1.6** | **11.61** | 0.30 | 4 | 80 | |
| L1_Ext | 130 | 350 | 1.6 | **13.39** | 0.31 | 4 | 80 | |
| L2_Ext | 130 | 350 | 1.6 | **9.95** | 0.30 | 4 | 80 | |
| T1_Ext | **120** | 350 | 1.6 | 11.56 | 0.30 | 4 | 80 | series 2 |
| T2_Ext | **140** | 350 | 1.6 | 11.60 | 0.30 | 4 | 80 | |
| A1_Ext | 130 | **300** | **1.4** | 11.64 | 0.31 | 4 | 80 | |
| A2_Ext | 130 | **400** | **1.8** | 11.70 | 0.30 | 4 | 80 | |

Experiment names and varied parameters (bold):

M – Mill power level

L – Liquid mass flow rate

T – Temperature

A – Air mass flow rate

Ref – Reference experiment

A starting bed mass of 4 kg of sodium benzoate granules was filled into the fluidized bed. During heat-up, the classifying air temperature was set to 80°C. The classifying air velocity usually was set to 5.5 m·s$^{-1}$ at the start of each experiment. After 5–10 min the bed mass controller was started, controlling the classifying air velocity to maintain a constant bed mass. The spray solution was fed at ambient temperature (20°C), and, depending on the spray mass flow rate, a liquid pressure of 1.4–1.9 bar resulted. Atomization of the spray was done by compressed air at a nearly constant pressure of 2.5–2.7 bar. As described in Section 4.3 (p. 53), small fluctuations in the mass fraction of sodium benzoate in the spray liquid resulted from preparation of new spray solutions every 2–3 experiments. The mill power level was set to 80% for all experiments of series two. The mesh widths of the sieves for external separation were 0.5 and 0.7 mm for every experiment of both series.

Each experiment from the first series was conducted for 20–32 h. Every 4 kg of sprayed solution, a sample was taken from the fluidized bed. This resulted in a sampling time of 25 min and a total of 51–83 samples from the bed. A product sample was taken every 16 kg of sprayed solution, resulting in a sampling time of 100 min and a total of 12–20 samples from the product. The experiments from the second series were conducted for 34–39 h. Also every 4 kg of sprayed solution a sample was taken from the fluidized bed, resulting, depending on the spray mass flow rate, in a sampling time of 18–24 min and a total of 100–118 bed samples per experiment. The product samples were collected every 16 kg of spray solution, resulting in a sampling time of 72–96 min and a total of 25–29 product samples per experiment. The total sample mass flow rate was equal to $\dot{M}_{sam} \approx 0.1$ kg·h$^{-1}$. After each experiment, the samples were investigated offline as described in Chapter 3.

To maintain a constant bed mass, a controller was used. As described in Section 5.2, the bed mass was calculated from the total pressure drop over the distributor plate and the fluidized particles. A calibration curve was recorded in advance, accounting for the pressure drop of the distributor plate with empty fluidization chamber for the operating range of air velocities. Thus, theoretically, the bed mass could be monitored. In theory, the starting bed mass would be defined as set point for the bed mass controller. Then, throughout the process, the controller would adjust the volume flow rate of the discharge air to keep the bed mass constant. An increase in bed mass would be countered by a reduced volume flow rate of the classifying air, and vice versa, maintaining a constant bed mass. If, however, the discharged particles are not in the product size range (between the sieve mesh widths: 0.5 and 0.7 mm), they are fed back to the granulator, so that the bed mass in practice would not necessarily be held constant, and a large fraction of the particles would reside in the feedback cycle. Additionally, the distributor plate partly clogged during the experiments, as described for the experiments with internal separation (Section 4.3, p. 53). Thus, the pressure drop of the distributor plate gradually increased during the process, which could not be accounted for in the calibration curve that was measured for a clean distributor plate. Consequently, the calculated bed mass was higher than the actual bed mass. Thus, the bed mass controller would reduce the bed mass, although the actual bed mass did not increase, but only the pressure drop of the distributor plate. To account for that problem, the actual bed mass was calculated and checked by a mass balance during the experiment (Eq. 4–1, p. 54) with estimated values for the mass fraction of water of the bed and product particles. The set point of the controller was

then adjusted manually according to the mass balance, to maintain a relatively constant bed mass. But due to the mentioned problems with increased particle recycle, if the product size was not yet reached, and manual adjustment of the set point of the controller was needed, the bed mass could not be held entirely constant for most of the experiments. Some experiments would eventually reach a steady state bed mass, which was then maintained by the controller. But especially during the experiments with oscillations in the PSD, also changes in the bed mass were observed, which could not be completely amended by the controller. Nevertheless, experimental conclusions regarding the temporal evolution of the PSD are still valid.

# 5.4 Results and discussion

In this section the results regarding process dynamics and product quality for the continuous SFBLG experiments with external separation are presented and discussed. In the first series, the power level of the mill, crushing oversized particles, was varied. In the second series, different drying parameters resulted in different process behavior and product particle morphology.

### 5.4.1 Influence of mill speed on process behavior

This series investigated the influence of an increasing mill power level on the process behavior. For the power levels 20% and 50% in experiments M1_Ext and M2_Ext, respectively, the particle size distribution density in the fluidized bed exhibited self-sustained oscillating behavior (Fig. 5–2; Fig. 5–3). The average period times of the oscillations in the PSD density for M1_Ext and M2_Ext were 4.7 h and 8.6 h, respectively. The according peak times are summarized in Tab. 5–2.

Tab. 5–2. Period times for experiments M1_Ext and M2_Ext.

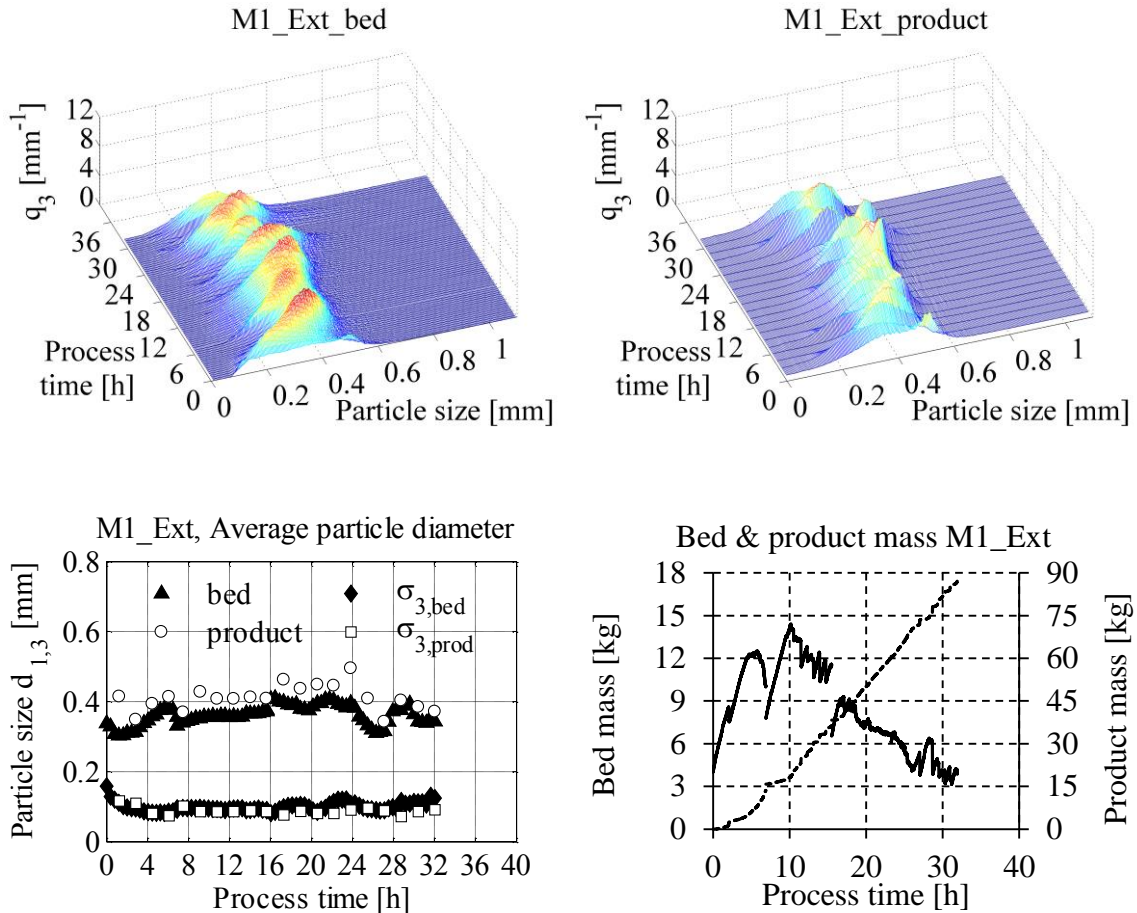| Exp. | Parameter | Values [h] |
| --- | --- | --- |
| M1_Ext | peak times | 6.07; 11.58; 16.46; 21.75; 23.82; 29.60 |
| | period times | 5.52; 4.88; 5.29; 2.07; 5.78 |
| | average period time | 4.71 |
| M2_Ext | peak times | 2.03; 11.33; 19.91; 27.78 |
| | period times | 9.30; 8.58; 7.87 |
| | average period time | 8.58 |

Fig. 5–2. SFBLG with external separation and varied mill power level $P_{mill}$, **M1_Ext** (20%). Particle size distribution density in the bed (top left) and product (top right). Average particle diameter (bottom left) and bed and product masses (bottom right; solid line: bed, dashed line: product).

The oscillations in size distribution for M1_Ext and M2_Ext also resulted in oscillating bed masses (Fig. 5–2 and Fig. 5–3, bottom right). Sudden drops in bed mass and sudden increases in product mass were caused by occasional process breaks, which were necessary to clean the nozzle or free the pneumatic conveyer from blockings, etc. After stopping the spray, and, thus, pausing the process time, product material in the tubes was discharged further, to reduce the danger of additional clogging in the tubes and the sieve. As the bed mass was calculated by a mass balance (Eq. 4–1), increases in the product mass directly reduced the bed mass. Consequently, the discharge during a process break was visible as a sudden decrease in bed mass after restarting the process. Increasing the mill power level to 80 and 90% in experiments M3_Ext and M4_Ext stabilized the process. In experiment M3_Ext damped oscillations of the particle size distribution were observed during the start-up period. The steady state was reached after approx. 6.5 h of process time, as shown in the graph of the average particle diameter $d_{1,3}$ and the bed mass (Fig. 5–4). Both lines are nearly constant or only oscillate in a narrow range. Similar behavior was observed for M4_Ext, where a nearly steady state was reached after about 2.9 h of process time. Particle size and bed mass varied only slightly after 2.9 h (Fig. 5–6).
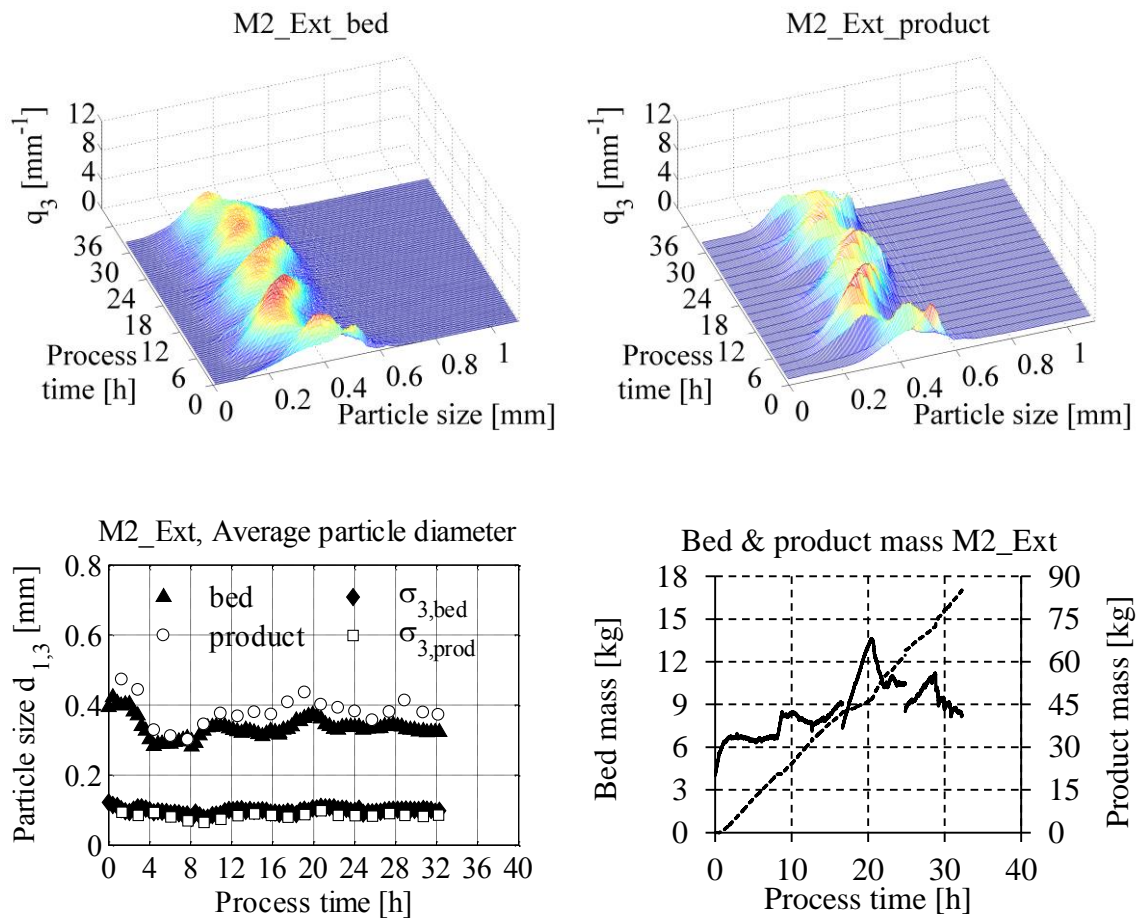
Fig. 5–3. SFBLG with external separation and varied mill power level $P_{mill}$, **M2_Ext** (50%). Particle size distribution density in the bed (top left) and product (top right). Average particle diameter (bottom left) and bed and product masses (bottom right; solid line: bed, dashed line: product).

The differences in process behavior were most likely caused by varying comminution behavior of the mill. Figure 5–5 shows the results of comminution tests, done with feed sodium benzoate granules in the size range of 0.3–1.2 mm, which was similar to the size range to be expected in the continuous SFBLG experiments. The black solid line marks the size distribution density of the feed material. For 20% and 40% mill power level nearly no size reduction of the material was observed. Starting with 60%, a minor size reduction was observed, followed by 80 and 100% resulting in a significant crushing of particles. The size of the crushed particles lay within seed particle size range (0.15–0.2 mm) for the continuous SFBLG process. Consequently, mill power levels of 60% and higher increased the amount of new seed particles for the granulation process. A higher amount of seed particles dampened the oscillations of the particle size distributions and led to steady state operation for experiments M3_Ext and M4_Ext.
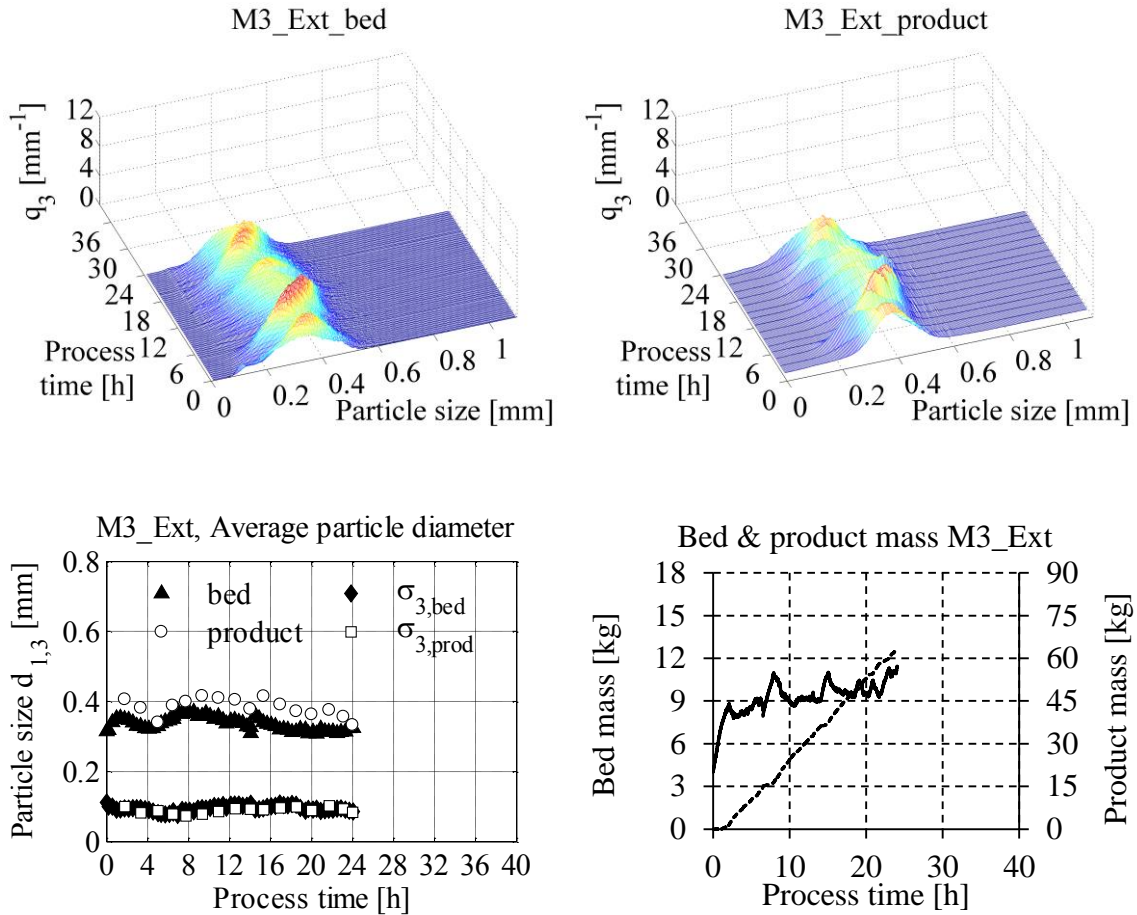
Fig. 5–4. SFBLG with external separation and varied mill power level $P_{mill}$, **M3_Ext** (80%). Particle size distribution density in the bed (top left) and product (top right). Average particle diameter (bottom left) and bed and product masses (bottom right; solid line: bed, dashed line: product).
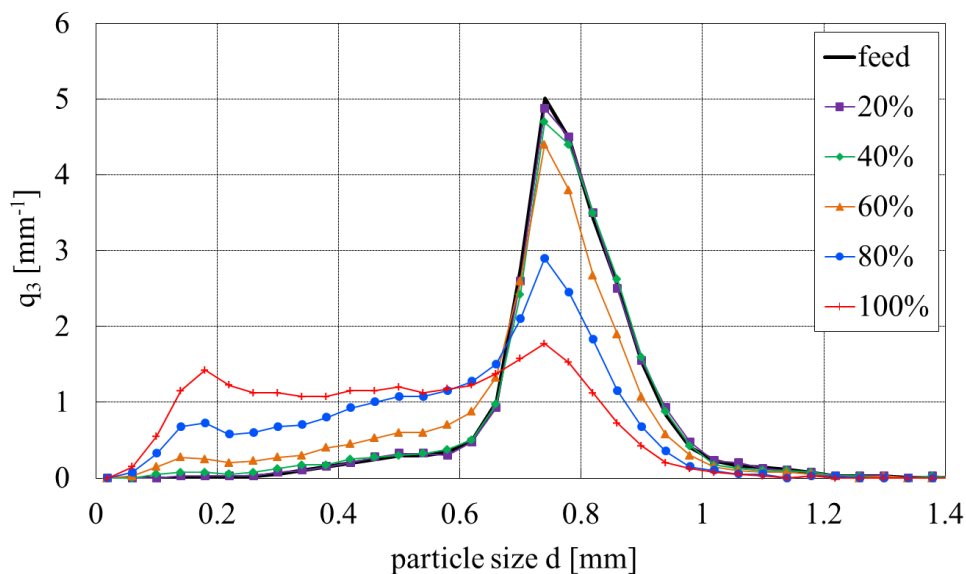


Fig. 5–5. Results from comminution tests with the mill. PSD densities of feed material and after crushing at different power levels.
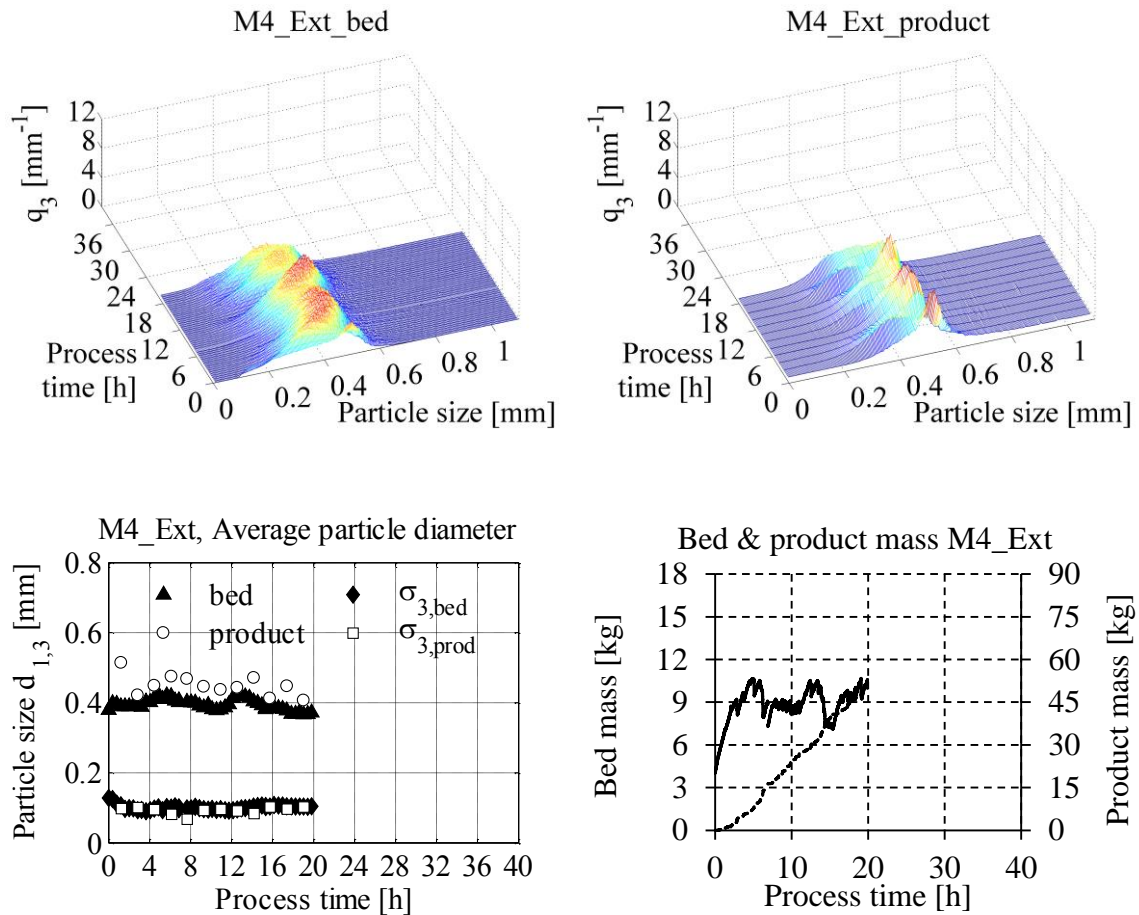
Fig. 5–6. SFBLG with external separation and varied mill power level $P_{mill}$, **M4_Ext** (90%). Particle size distribution density in the bed (top left) and product (top right). Average particle diameter (bottom left) and bed and product masses (bottom right; solid line: bed, dashed line: product).

The product PSD densities followed the evolution of the bed PSD densities. Ideally, the product particle size should lie within the size range of the sieves (0.5–0.7 mm, Section 5.2, p. 79). In fact, the average diameter of the product particles was slightly higher than the average bed particle diameter in all four experiments (Figs. 5–2 to Fig. 5–4 and 5–6, bottom left). But the fact that the average product diameter was lower than 0.5 mm in all experiments, inferred the discharge of undersized material. Local and temporal overloading of the sieve could result in undersize discharge, as the material would be discharged before having the possibility to fall though the meshes of the second sieve and be returned to the fluidized bed as undersize material. Thus, the spray mass flow rate for all experiments of the second series was increased to realize higher growth rates to prevent excessive undersize circulation and, thus, sieve overloading. Additionally, the stabilizing effect of seed particle production by crushing at mill power levels of 60% and higher resulted in a fixed mill speed of 80% for the second series of experiments, investigating the effect of drying conditions on the process behavior and product quality during continuous SFBLG with external separation.

### 5.4.2 Influence of mill speed on product quality

The drying potential and product quality aspects surface roughness and particle porosity for the experiments with varying mill power level are listed in Tab. 5–3 (complete summary of all experiments with external separation: Tab. 5–5, p. 100). Additionally, the product particle morphology is shown by means of SEM images (Fig. 5–7). No significant differences in roughness, porosity and surface morphology were observed. Thus, changing comminution behavior only influenced the amount of available seed particles, but not the structural properties. Similar drying conditions in all four experiments resulted in similar growth and, consequently, similar particle morphology.

Tab. 5–3. Measured product quality values for continuous SFBLG with external separation and varied classifying air velocities.

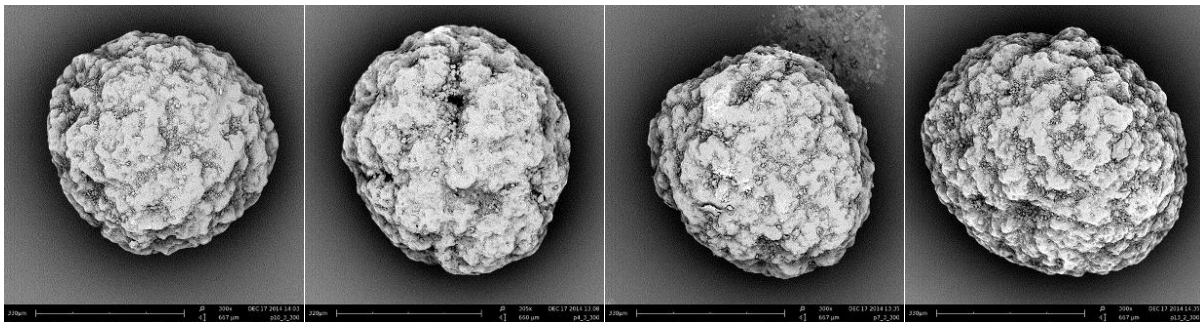| Exp. | $R_{av}$ [μm] | $\Psi_{SEM,av}$ [%] | $\Pi$ [%] |
|------|------|------|------|
| M1_Ext | 5.6 | 19.6 | 39.4 |
| M2_Ext | 6.1 | 19.7 | 28.9 |
| M3_Ext | 5.8 | 17.8 | 39.3 |
| M4_Ext | 6.1 | 20.6 | 40.2 |



Fig. 5–7. SEM images from product samples of continuous SFBLG experiments with external separation and variation of mill power level. From left to right: M1_Ext (20%), M2_Ext (50%), M3_Ext (80%), M4_Ext (90%).

### 5.4.3 Influence of drying conditions on process behavior

In this series the influence of the drying conditions on the process behavior and product quality was investigated. The experiment with medium spray mass flow rate, inlet gas temperature and gas mass flow rate was defined as the reference experiment (Ref_Ext). The PSD density and the average diameter of the bed and product particles reached a steady state after ca. 8.6 h of process time (Fig. 5–8). The bed mass could not be held constant and fluctuated during the whole experiment. Increasing the spray mass flow rate in experiment L1_Ext led to self-sustained oscillations of the PSD density and also of the average particle diameter (Fig. 5–9). The average period time of the oscillations was 8.8 h. The according peak times are summarized in Tab. 5–4 (p. 92). The amplitude of the oscillation of the average product particle size was reduced by the externally classifying sieves (mesh 0.5 and 0.7 mm). Also the bed mass was oscillating slightly.
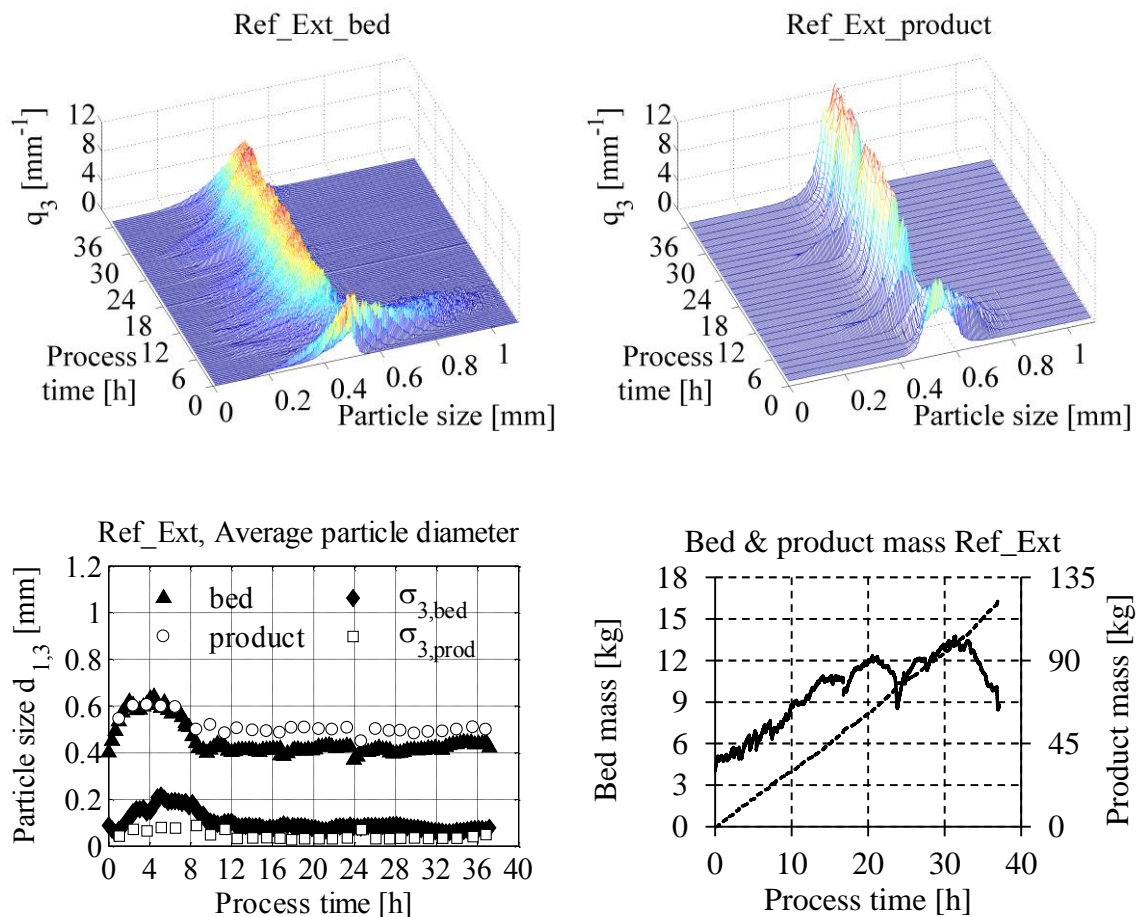


Fig. 5–8. SFBLG with external separation, reference experiment **Ref_Ext** ($\dot{M}_{spray} = 11.6$ kg·h$^{-1}$, $T_{gas,in} = 130°C$, $\dot{M}_{gas,in} = 350$ kg·h$^{-1}$). Particle size distribution density in the bed (top left) and product (top right). Average particle diameter (bottom left) and bed and product masses (bottom right; solid line: bed, dashed line: product).
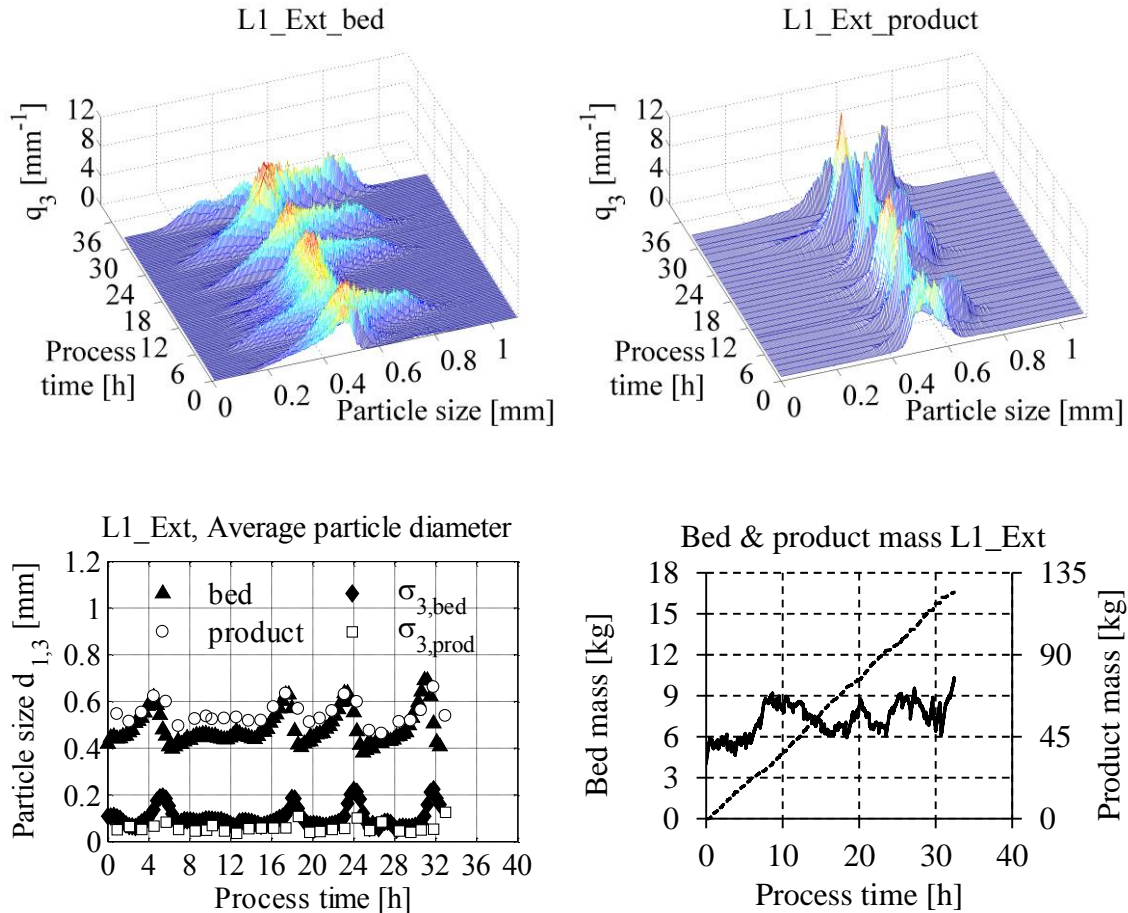
Fig. 5–9. SFBLG with external separation and varied spray mass flow rate $\dot{M}_{spray}$, **L1_Ext** (13.4 kg·h⁻¹). Particle size distribution density in the bed (top left) and product (top right). Average particle diameter (bottom left) and bed and product masses (bottom right; solid line: bed, dashed line: product).

Contrary, reducing the spray mass flow rate in experiment L2_Ext resulted in process behavior similar to the reference experiment. The particle size distribution density was stationary after about 15 h (Fig. 5–10). Nevertheless, the bed mass was still increasing slightly until 30 h of process time. Still, this time frame was taken to calculate the average growth rate of this experiment. After 30 h of process time, problems with the bed mass controller led to a sudden increase of the bed mass and finally to the termination of the process. Here, lower spray mass flow rates and, thus, drier process conditions stabilized the continuous layering granulation process.

Fig. 5–10. SFBLG with external separation and varied spray mass flow rate $\dot{M}_{spray}$, **L2_Ext** (10.0 kg·h$^{-1}$). Particle size distribution density in the bed (top left) and product (top right). Average particle diameter (bottom left) and bed and product masses (bottom right; solid line: bed, dashed line: product).
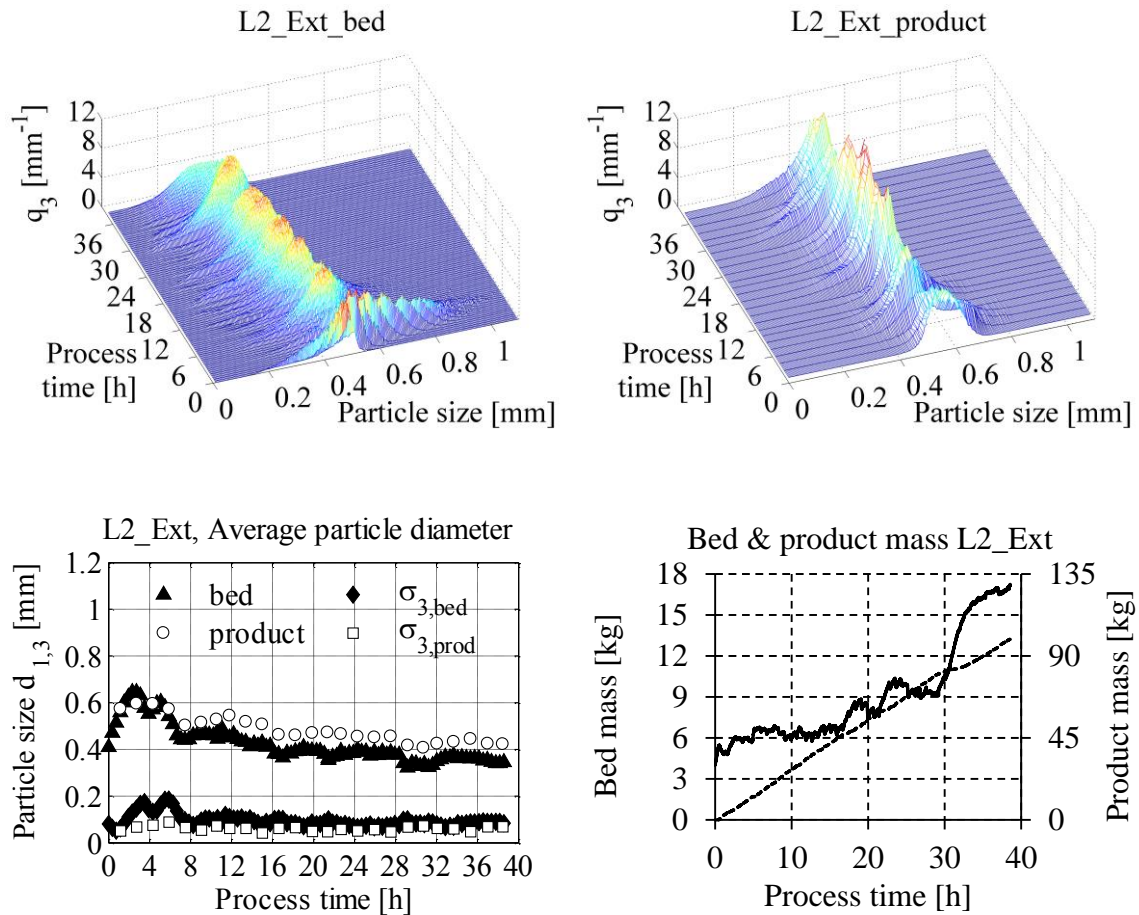
The influence of varying fluidizing gas inlet temperatures and gas mass flow rates were similar to the influence of varying spray mass flow rates. A decrease in inlet gas temperature in experiment T1_Ext resulted in more humid process conditions. The particle size distribution density showed self-sustained oscillations, also visible in the average particle diameter (Fig. 5–11). The average period time of the oscillations was 4.3 h (Tab. 5–4). The bed mass was quite constant, showing only small oscillations. Increased inlet gas temperature in experiment T2_Ext led to drier process conditions. The particle size distribution density was stationary after ca. 10.3 h of process time (Fig. 5–12). The bed mass did not reach a steady state, as the controller was not able to maintain a permanently constant bed mass. The steady state was considered to end at 26.5 h, as problems with the bed mass controller led to a drastically reduced bed mass, and consequently particles in the fluidized bed grew faster due to the higher availability of spray solution on less bed material.

Fig. 5–11. SFBLG with external separation and varied inlet temperature $T_{gas,in}$, **T1_Ext** (120°C). Particle size distribution density in the bed (top left) and product (top right). Average particle diameter (bottom left) and bed and product masses (bottom right; solid line: bed, dashed line: product).

Tab. 5–4. Period times for experiments L1_Ext, T1_Ext, and A1_Ext.

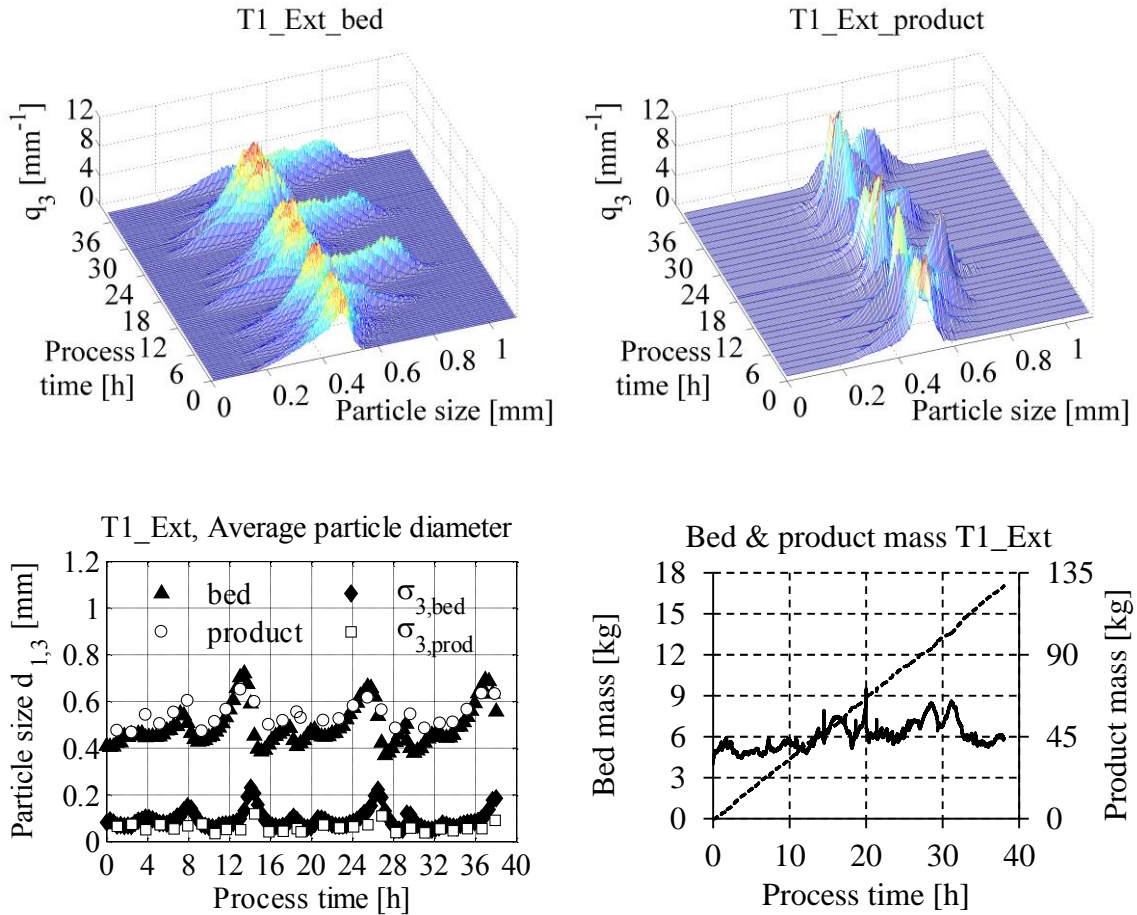| Exp. | Parameter | Values [h] |
|---|---|---|
| L1_Ext | peak times | 4.49; 17.66; 23.10; 30.90 |
| | period times | 13.17; 5.44; 7.80 |
| | average period time | 8.80 |
| T1_Ext | peak times | 2.43; 7.20; 13.44; 17.54; 19.95; 25.46; 29.25; 32.44; 36.95 |
| | period times | 4.78; 6.24; 4.10; 2.41; 5.51; 3.79; 3.19; 4.51 |
| | average period time | 4.32 |
| A1_Ext | peak times | 5.12; 8.55; 14.77; 22.99; 32.30 |
| | period times | 3.43; 6.22; 8.22; 9.31 |
| | average period time | 6.80 |
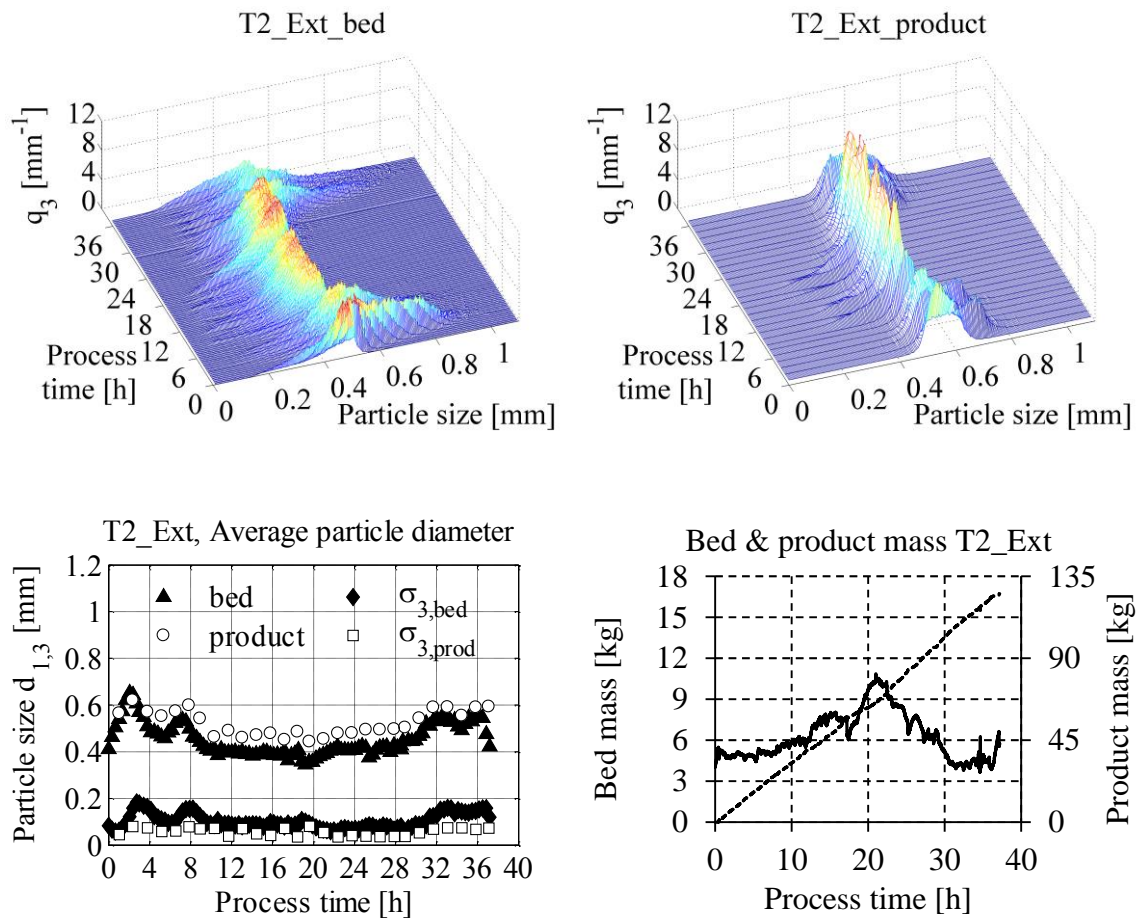
Fig. 5–12. SFBLG with external separation and varied inlet temperature $T_{gas,in}$, **T2_Ext** (140°C). Particle size distribution density in the bed (top left) and product (top right). Average particle diameter (bottom left) and bed and product masses (bottom right; solid line: bed, dashed line: product).

Compared to the reference experiment Ref_Ext a decrease in fluidizing gas mass flow rate in experiment A1_Ext led to self-sustained oscillations in the particle size distribution density and bed mass (Fig. 5–13). The average period time of the oscillations was 6.8 h (Tab. 5–4). Again, more humid process conditions de-stabilized the process. Contrary, an increased fluidizing gas mass flow rate in experiment A2_Ext resulted in similar process behavior to Ref_Ext. The process reached the steady state after ca. 18 h of process time, visible in the graph of the average particle diameter and the particle size distribution density (Fig. 5–14). The bed mass could not be stabilized.
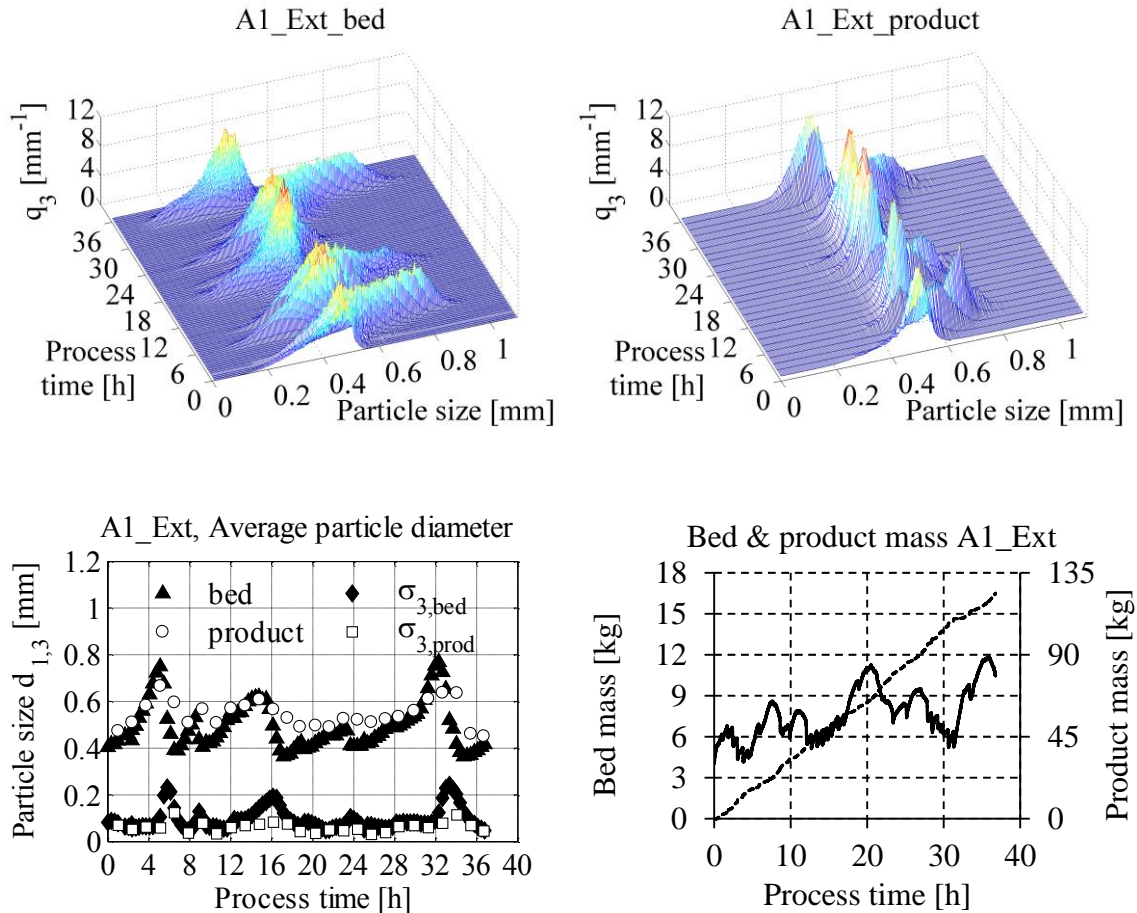
Fig. 5–13. SFBLG with external separation and varied gas mass flow rate $\dot{M}_{gas,in}$, **A1_Ext** (300 kg·h⁻¹). Particle size distribution density in the bed (top left) and product (top right). Average particle diameter (bottom left) and bed and product masses (bottom right; solid line: bed, dashed line: product).

The differences in process behavior for varying drying conditions resulted from differences in seed particle formation, as described in Section 4.4.3 (p. 67). For dry process conditions (low spray mass flow rate in L2_Ext, high inlet gas temperature in T2_Ext, high gas mass flow rate in A2_Ext), seed particle formation in the size range of 0.1 to 0.2 mm by agglomeration of dust formed by overspray (Fig. 4–13, p. 68) was hardly possible. Additionally, a high fluidizing gas mass flow rate also enhanced the elutriation of dust, which then was missing for seed particle formation in the fluidized bed. But the crushing of oversized particles by the mill generated a sufficient, relatively constant amount of particles in the size range of 0.1–0.2 mm (Fig. 5–5, p. 86), serving as seed particles. This way of seed particle formation was independent from a changing overspray amount, caused by changing bed masses, as described earlier in Section 2.4.1 (p. 19). Thus, seed particle generation solely by the mill had a stabilizing effect. However, humid process conditions (high spray mass flow rate in L1_Ext, low inlet gas temperature in T1_Ext, low gas mass flow rate in A1_Ext) allowed for the agglomeration of dust in the fluidized bed to seed particle size, as described for the experiments with internal separation in Section 4.4.3 (p. 67). Additionally, a low fluidizing gas mass flow rate enhanced dust retention in the fluidized bed, which then was available for

the aforementioned agglomeration step to seed particles. Thus, seed particle formation by agglomeration of dust was dependent on the amount of overspray and, thus, the bed mass/height (Fig. 2–6, p. 21), as described for the internal separation experiments (Section 4.4.3, p. 67). This varying seed particle formation in addition to the crushing of oversized particles led to temporarily high and low amounts of seed particles, resulting in the observed oscillations in the particle size distributions.
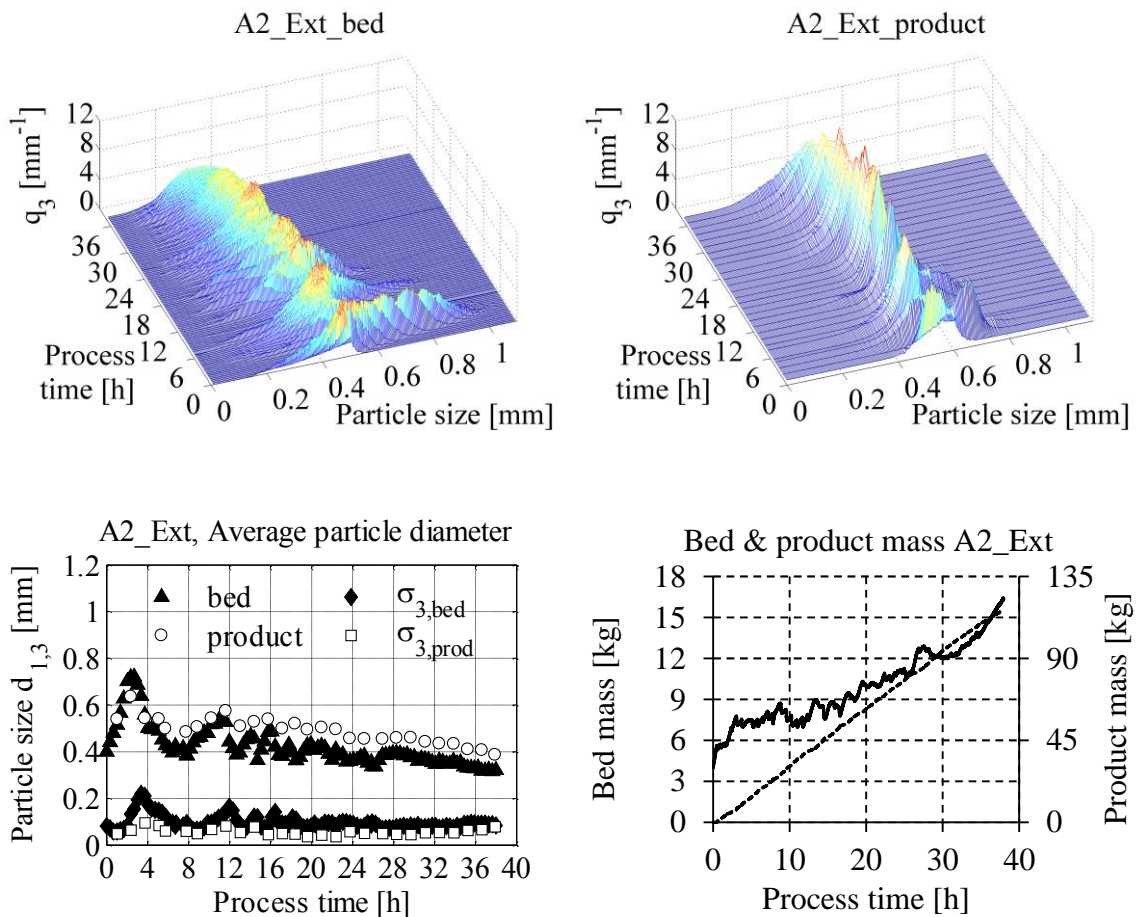


Fig. 5–14. SFBLG with external separation and varied gas mass flow rate $\dot{M}_{gas,in}$, **A2_Ext** (400 kg·h$^{-1}$). Particle size distribution density in the bed (top left) and product (top right). Average particle diameter (bottom left) and bed and product masses (bottom right; solid line: bed, dashed line: product).

The observed problems with the bed mass controller were caused by local clogging of the distributor plate. Thus, the pressure drop of the plate gradually increased by an unknown amount, which could not be accounted for in the bed mass calculation from the pressure drop (Section 5.2, p. 79). Consequently, the calculated bed mass increasingly deviated from the real bed mass during the process. Thus, manual adjustment of the set point of the controller was carried out during the experiments, resulting in the non-ideal bed mass graphs shown above. Nevertheless, the conclusions regarding the process behavior deduced from the evolution of the particle size distribution density are still valid. Additionally, even an ideal controller would not have been able to keep a constant bed mass, if the product particles were

not in product size range yet. This would only increase the amount of material in the feedback cycle, eventually being returned to the fluidized bed and increasing the bed mass one way or the other.

### 5.4.4 Influence of drying conditions on product quality

As initially described (Section 2.2.4, p. 14), the drying conditions determine the structure of water-soluble crystalline materials. Consequently, this was observed for the second series of continuous SFBLG with external separation (Fig. 5–17). Humid process conditions ($\Pi \leq 35\%$) resulted in rough and porous particles. Contrary, dry process conditions ($\Pi > 35\%$) resulted in the formation of smoother and denser granules. The according values are listed in Tab. 5–5 (p. 100). The differences in particle porosity $\Psi_{SEM,av}$ in relation to $\Pi$ were less distinct as for the internal separation experiments. This might be attributed to structure changes by excessive cycling of the material through pneumatic conveyer, sieve and mill, leading to attrition and unifying of the surface structure. A correlation of $\Psi_{SEM,av}$ in dependency of $\Pi$ is shown in Fig. 5–15 (left). In general, the decreasing linear trend is still visible, but less characteristic than for the internal classifying experiments.

The average particle roughness $R_{av}$ was also influenced by the drying conditions. For the sake of completeness, the linear correlation between $R_{av}$ and $\Pi$ is given in Fig. 5–15 (right). But as stated above, attrition during pneumatic conveying might have influenced particularly the particle roughness by equalizing the particle surface. Thus, differences in roughness between the experiments with varying $\Pi$ were less obvious, compared to the experiments with internal separation, where particles were discharged without a pneumatic conveyer. Having a closer look at the particle structure, the linear correlation between $\Psi_{SEM,av}$ and $R_{av}$ still holds true (Fig. 5–16). Large gaps and troughs in the particle surface lead to large particle roughness. But the gaps continue towards the center of the granule, increasing the particle porosity. Consequently, for the investigated crystalline material, particle porosity and roughness are proportional.

For the second series of experiments, the particle porosity was also measured via μ-CT (Section 3.3.2, p. 39). But the measured values for $\Psi_{CT}$ (Tab. 5–5, p. 100) lay within a very close range (28.9–33.7%), regardless of larger differences in $\Pi$ (28.2–40.1%). Differences in porosity of the granules could not be measured via μ-CT. In contrast, the porosity values determined via SEM and mass of the granules (Section 3.3.3, p. 41) were reasonable and showed the expected tendencies, as described above. A comparison of the results of both measurement techniques has already been given in Section 3.3.4 (p. 42).
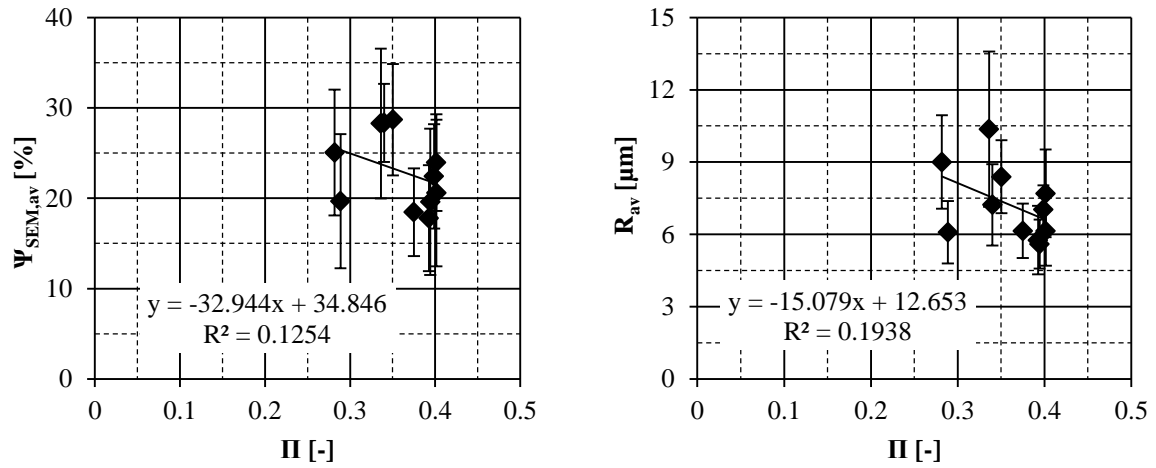
Fig. 5–15. Correlation between average particle porosity $\Psi_{SEM,av}$ and drying potential $\Pi$ (left), and average particle roughness $R_{av}$ and $\Pi$ (right) for continuous SFBLG with external separation. Error bar: Standard deviation for 10 measurements.
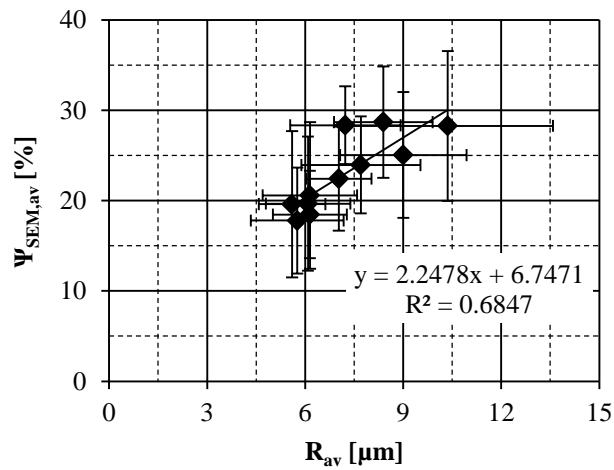


Fig. 5–16. Correlation between average particle porosity $\Psi_{SEM,av}$ and average particle roughness $R_{av}$ for continuous SFBLG with external separation. Error bar: Standard deviation for 10 measurements.
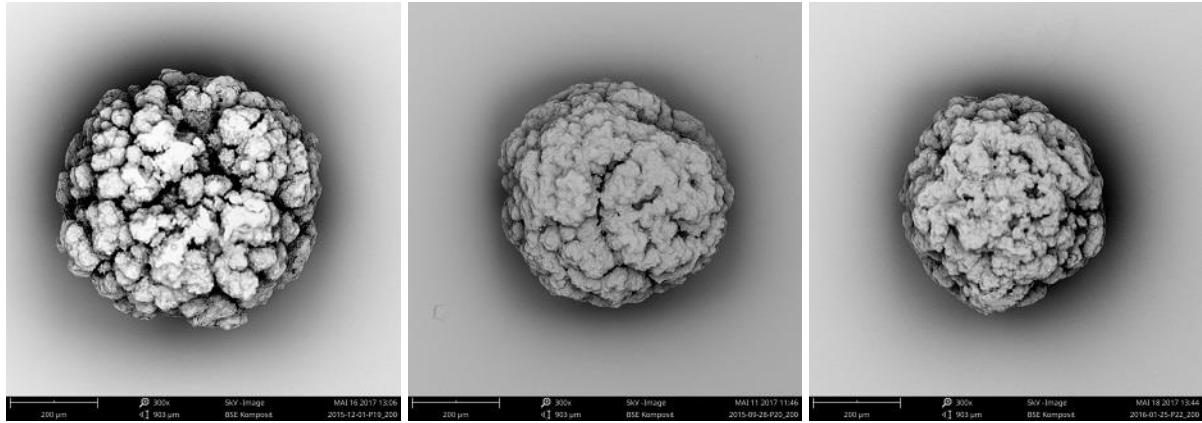
L1_Ext: 13.4 kg·h$^{-1}$

$\Psi_{SEM, L1} = 28.7\%$; $R_{L1} = 8.4$ μm

Ref_Ext: 11.6 kg·h$^{-1}$

$\Psi_{SEM, Ref} = 28.3\%$; $R_{Ref} = 7.2$ μm

L2_Ext: 10.0 kg·h$^{-1}$

$\Psi_{SEM, L2} = 18.5\%$; $R_{L2} = 6.1$ μm
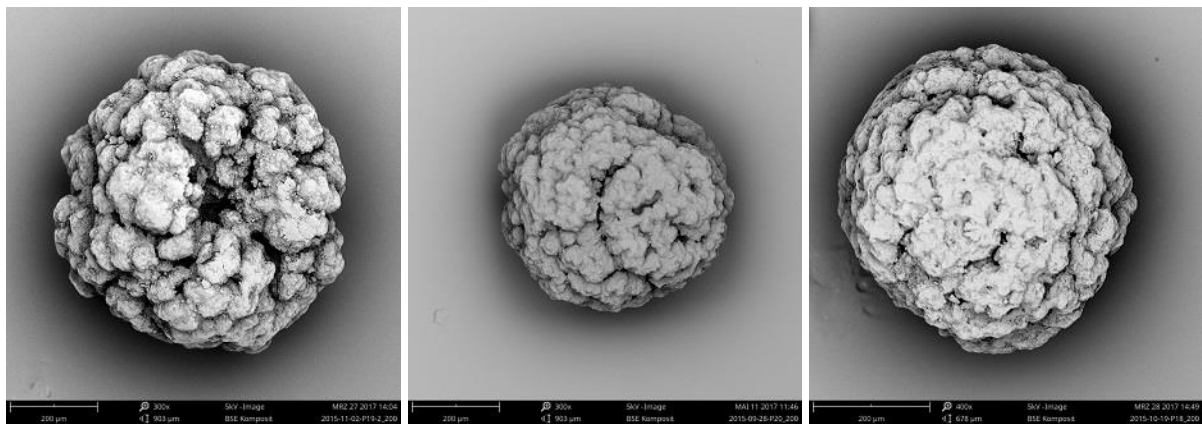
T1_Ext: 120°C

$\Psi_{SEM, T1} = 28.3\%$; $R_{T1} = 10.4$ μm

Ref_Ext: 130°C

$\Psi_{SEM, Ref} = 28.3\%$; $R_{Ref} = 7.2$ μm

T2_Ext: 140°C

$\Psi_{SEM, T2} = 22.4\%$; $R_{T2} = 7.0$ μm
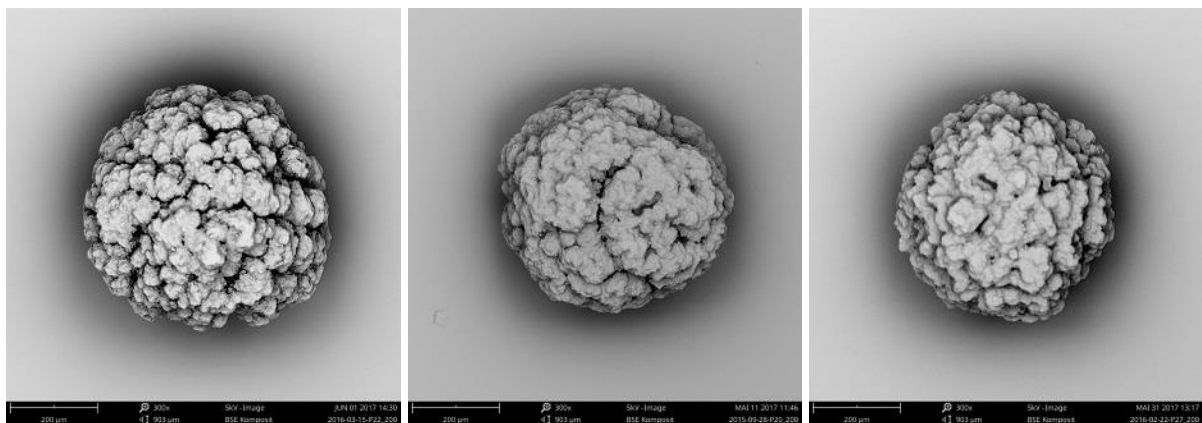
A1_Ext: 300 kg·h$^{-1}$

$\Psi_{SEM, A1} = 25.0\%$; $R_{A1} = 9.0$ μm

Ref_Ext: 350 kg·h$^{-1}$

$\Psi_{SEM, Ref} = 28.3\%$; $R_{Ref} = 7.2$ μm

A2_Ext: 400 kg·h$^{-1}$

$\Psi_{SEM, A2} = 23.9\%$; $R_{A2} = 7.7$ μm

Fig. 5–17. SEM images from product samples of continuous SFBLG experiments with external separation and variation of drying conditions.

### 5.4.5 Steady state considerations

All steady state data for experiments M3_Ext, M4_Ext, Ref_Ext, L2_Ext, T2_Ext and A2_Ext are listed in Tab. 5–6. For both series, the temporal evolution of the average particle diameter $d_{1,3}$ of the product samples was used for the determination of the steady state. The steady states were determined by successively averaging the particle diameters of each four ($m = 4$) product samples, and the following evaluation of $CoV$. For series 1 and 2 the criterion $CoV < 6\%$ was used. The average growth rates for both series were 1.9–3.2 $\mu m \cdot min^{-1}$, exceeding the expected range from Section 2.2.1 (p. 11). But the measured growth rates for continuous SFBLG with external separation were comparable to the growth rates calculated from the data provided by Rieck et al. (2015) for batch coating of gamma alumina oxide with sodium benzoate solution (compare Section 4.4.5, p. 71), being 1–3 $\mu m \cdot min^{-1}$.

The growth rates for external separation were considerably larger than the growth rates reported earlier for the experiments with internal separation. On the one hand, bed masses were lower in the external separation case, as the bed mass in each experiment was tried to be held constant. Consequently, more spray solution was available for the granules in the fluidized bed, increasing the average growth rate. On the other hand, in the internal separation case, for some experiments the average product particle size during steady state was 0.5 mm or higher, depending on the chosen classifying air velocity, increasing the residence time of the granules compared to the external separation setup, where particles were discharged at an average particle size during steady state below 0.5 mm. Consequently, the product mass flow rates for the external separation case were slightly higher, reducing the average residence time (Eq. 3–17, p. 36). Additionally, a lower bed mass also increased the probability of the granules to be discharged, possibly also reducing their residence time in the granulator, provided the particles had product size (0.5–0.7 mm). Thus, due to reduced average residence times, the average growth rates (Eq. 3–18, p. 36) for external separation exceeded the growth rates for internal separation in the parameter regime investigated.

Comparable to the experiments with internal separation, the product mass flow rate of pure solids $M_{prod,s}$ during steady state never reached the theoretical maximum value of the mass flow rate of solids in the spray. The values of the deviation in mass flow rates $e_M$ are listed in Tab. 5–7, and where calculated as described in Section 4.4.5 (Eqs. 4–2 to 4–5, p. 72). Again, dead zones in the plant, like possible accumulation of dust in the cyclone, and varying bed masses during steady state of the average particle diameter, influencing the product mass flow rate, were the reasons for this deviation. Thus, the steady states described here were only reached from a practical point of view, but not if strictly holding to theory. But the deviations in product mass flow rates were reasonable for the used fluidized bed plant.

Additionally, experiments M3_Ext and L2_Ext show good reproducibility. Both experiments were performed with similar process conditions and showed similar process behavior by reaching the steady state. The product quality (roughness, porosity, residual moisture) was also similar.

Tab. 5–5. Overview of key process parameters and measured values for continuous SFBLG with external separation.

| Exp | Parameters | | | | | | Measurement | | | | | | |
|---|---|---|---|---|---|---|---|---|---|---|---|---|---|
| | $T_{gas,in}$ [°C] | $\dot{M}_{gas,in}$ [kg·h$^{-1}$] | $u_{gas}$ [m·s$^{-1}$] | $\dot{M}_{spray}$ [kg·h$^{-1}$] | $x_{NaB}$ [-] | $P_{mill}$ [%] | $R_{av}$ [µm] | $\Psi_{SEM,av}$ [%] | $\Psi_{CT}$ [%] | $\Pi$ [%] | $x_{w,0}$ [%] | $x_{w,bed,av}$ [%] | $x_{w,prod,av}$ [%] |
| M1_Ext | 130 | 350 | 1.6 | 9.77 | 0.30 | 20 | 5.8 ± 1.4 | 17.8 ± 5.9 | - | 39.3 | 0.4 | 0.4 | 0.5 |
| M2_Ext | 130 | 350 | 1.6 | 9.79 | 0.30 | 50 | 5.6 ± 1.0 | 19.6 ± 8.1 | - | 39.4 | 0.1 | 0.2 | 0.3 |
| M3_Ext | 130 | 350 | 1.6 | 10.05 | 0.30 | 80 | 6.1 ± 1.4 | 20.6 ± 8.1 | - | 40.2 | 0.4 | 0.5 | 0.5 |
| M4_Ext | 130 | 350 | 1.6 | 9.95 | 0.30 | 90 | 6.1 ± 1.3 | 19.7 ± 7.4 | - | 28.9 | 0.1 | 0.2 | 0.2 |
| Ref_Ext | 130 | 350 | 1.6 | 11.61 | 0.30 | 80 | 7.2 ± 1.7 | 28.3 ± 4.3 | 32.5 | 34.0* | 0.1 | 0.4 | 0.3 |
| L1_Ext | 130 | 350 | 1.6 | 13.39 | 0.31 | 80 | 8.4 ± 1.5 | 28.7 ± 6.2 | 32.1 | 35.0 | 0.2 | 1.8 | 1.6 |
| L2_Ext | 130 | 350 | 1.6 | 9.95 | 0.30 | 80 | 6.1 ± 1.1 | 18.5 ± 4.8 | 30.6 | 37.5 | 0.3 | 0.3 | 0.3 |
| T1_Ext | 120 | 350 | 1.6 | 11.56 | 0.30 | 80 | 10.4 ± 3.2 | 28.3 ± 8.3 | 30.3 | 33.6 | 0.2 | 1.3 | 1.3 |
| T2_Ext | 140 | 350 | 1.6 | 11.60 | 0.30 | 80 | 7.0 ± 1.0 | 22.4 ± 5.8 | 28.9 | 39.9* | 0.3 | 0.4 | 0.4 |
| A1_Ext | 130 | 300 | 1.4 | 11.64 | 0.31 | 80 | 9.0 ± 1.9 | 25.0 ± 7.0 | 32.3 | 28.2 | 0.3 | 1.5 | 1.4 |
| A2_Ext | 130 | 400 | 1.8 | 11.70 | 0.30 | 80 | 7.7 ± 1.8 | 23.9 ± 5.4 | 33.7 | 40.1 | 0.3 | 0.3 | 0.2 |

* The drying potential for the experiments Ref_Ext and T2_Ext was calculated from a water balance, assuming complete evaporation of the sprayed water. The measured value of $Y_{out}$, and consequently the calculated drying potential, was faulty.

Tab. 5–6. Steady state values for continuous **SFBLG** experiments with external separation.

| Exp | From? | $m$ | $CoV < ?$ | $t_{ss}$ | $M_{bed,ss}$ | $\dot{M}_{prod,ss}$ | $\tau$ | $d_{1,3,0}$ | $d_{1,3,ss}$ | $G_{av}$ |
|---|---|---|---|---|---|---|---|---|---|---|
| | | [-] | [%] | [h] | [kg] | [kg·h$^{-1}$] | [h] | [µm] | [µm] | [µm·min$^{-1}$] |
| M3_Ext | product | 4 | 6 | 6.5–End | 9.73 | 2.85 | 3.41 | 0 | 385 | 1.9 |
| M4_Ext | product | 4 | 6 | 2.9–End | 9.16 | 2.83 | 3.23 | 0 | 443 | 2.3 |
| Ref_Ext | product | 4 | 6 | 8.6–End | 11.07 | 3.32 | 3.33 | 0 | 496 | 2.5 |
| L2_Ext | product | 4 | 6 | 15.0–30.0 | 8.72 | 2.68 | 3.25 | 0 | 456 | 2.3 |
| T2_Ext | product | 4 | 6 | 10.3–26.5 | 7.89 | 3.25 | 2.43 | 0 | 472 | 3.2 |
| A2_Ext | product | 4 | 6 | 10.3–End | 12.04 | 3.11 | 3.87 | 0 | 476 | 2.0 |

Tab. 5–7. Deviation of the steady state product mass flow rate of pure solids $\dot{M}_{prod,s}$ from the theoretical maximum $\dot{M}_{spray,s}$.

| Exp. | $\dot{M}_{spray,s}$ [kg·h$^{-1}$] | $\dot{M}_{prod,s}$ [kg·h$^{-1}$] | $e_{\dot{M}}$ [%] |
|---|---|---|---|
| M3_Ext | 3.02 | 2.94 | -2.5 |
| M4_Ext | 2.96 | 2.93 | -1.1 |
| Ref_Ext | 3.48 | 3.41 | -2.2 |
| L2_Ext | 2.99 | 2.78 | -7.0 |
| T2_Ext | 3.48 | 3.34 | -4.2 |
| A2_Ext | 3.51 | 3.20 | -8.8 |

## 5.5 Comparison: Internal and external separation

In this section the results from continuous SFBLG experiments with internal and external separation at varied drying conditions are compared. The different process behaviors are summarized in Tab. 5–8 (p. 105). Interpreting the results, three different cases are distinguished:

*1: Dry process conditions*

For low spray mass flow rates (L1_Int, L2_Int, L2_Ext), high fluidizing gas inlet temperatures (T2_int, T2_Ext), and high fluidizing gas mass flow rates (A2_Int, A2_Ext) open, porous, and rough granules were formed. If this structure is desired for continuous SFBLG processes, a setup with external classifying product discharge is recommended. For dry process conditions, the dust particles formed by overspray (d < 40 μm) were too dry to agglomerate to seed particle size (≈ 0.15 mm). Thus, an insufficient amount of seed particles was generated. With internal separation, the particles in the fluidized bed grew very large, as the sprayed solution was only distributed among the existing particles, because new seed particles were missing. Consequently, while the product discharge was running continuously, the fluidized bed emptied over time. The processes were unstable and not feasible. Switching to a setup with external separation stabilized the processes for otherwise the same process parameters. Still, not enough seed particles were formed by agglomeration of overspray. But particles from the fluidized bed, having grown beyond product particle size (here: > 0.7 mm) were separated from the product particles as oversized particles, crushed by the mill and fed back to the process. Thus, new seed particles were formed. Equilibrium between growth, seed particle formation, and product discharge was established and the processes reached the steady state for external separation. Additionally, the product particle size distribution was much narrower for external separation due to the sieves, limiting the product particle size.

*2: Humid process conditions*

For high spray mass flow rates (L1_Ext), low fluidizing gas inlet temperatures (T1_Int, T1_Ext), and low fluidizing gas mass flow rates (A1_Int, A1_Ext) relatively dense and smooth granules were formed. If this particle structure is required, the internal separation setup is recommended for product discharge. For humid process conditions most likely less overspray was formed than in the previous case. But the residual mass fraction of water of the particles in this case indicated that dust particles ($d < 40$ μm) were agglomerating to seed particle size ($\approx 0.1$–$0.2$ mm). More seed particles were formed, and in the internal separation case equilibrium between growth, seed particle formation, and product discharge was established. The processes were running in steady state (T1_Int, A1_Int). By switching to the external separation setup, additional seed particles were provided by comminution of oversized particles. The additional seed particles overrode the equilibrium, which was established in the internal separation case, and led to self-sustained oscillations of the particle size distribution. When particles in the fluidized bed reached product size (here: $0.5$–$0.7$ mm), not the whole bed was discharged immediately. Only particles hitting the opening of the discharge tube had the probability to be discharged from the fluidized bed. Thus, particles had the chance to grow larger than $0.5$ mm and even larger than $0.7$ mm. The discharge of large particles led to a temporarily increased supply of seed particles by crushing of oversized particles. After having been fed back to the granulator, the crushed particles reduced the growth rate of the remaining particles in the fluidized bed, as the sprayed mass of solution had to be distributed to a larger surface of particles. Then, the remaining large particles were discharged, leaving only the newly generated seed particles in the fluidized bed. Thus, a new "growth wave" emerged (compare 3D plots). The repetition of the effects described above resulted in the observed self-sustained oscillations. Additionally, the described changes in bed mass/height also resulted in changing overspray production, which enhanced the oscillatory behavior. For humid process conditions, internal separation led to steady state operation. But, depending on the separation efficiency of the classifying tube, the product particle size distribution was wider for the internal separation case. If this is no problem, the internal separation setup should be chosen.

*3: Moderate drying conditions*

For moderate drying parameters (Ref_Int, Ref_Ext) porosity and roughness of the granules lay between the values which were obtained in cases one and two. The seed particle formation by agglomeration of dust was possible. But varying amount of overspray led to self-sustained oscillation in the particle size distribution for the internal separation setup (Ref_Int). Switching to the external separation setup, while all other process parameters were held constant, led to steady state operation. The amount of the additionally formed seed particles by crushing of oversized particles possibly overrode the effect of a varying amount of overspray, stabilizing the process.

Comparing the steady states of both kinds of product separation, different average growth rates resulted. The average growth rates for the external separation setup were considerably larger than for the experiments with internal separation. The main reason was the amount of bed mass for each setup. For internal separation, a constant classifying air velocity was set. A

separate control of the bed mass was not possible, leading to rather high bed masses. For the external separation setup, the bed mass was held relatively constant. Smaller bed masses were realized, leading to smaller residence times (Eq. 3–17, p. 36). Smaller residence times resulted in higher growth rates (3–18, p. 36).

# 5.6 Conclusions

Like for the experimental setup with internal separation, the occurrence of theoretically predicted oscillations in particle size distribution (Section 2.4.4, p. 24) was proven experimentally. For the first time, a systematic experimental study of the process behavior of continuous SFBLG with external separation was conducted and published. The resulting data sets may be used for validation of future upcoming models and control concepts. The occurrence of self-sustained oscillations was linked to the seed particle production, which was influenced by the mill speed and the drying and fluidizing conditions. The process behavior is summarized in Tab. 5–8. Additionally, the experimental results for the setups with internal and external separation were compared. The findings of this dissertation may also improve process understanding in industry, where oscillations in the PSD usually need to be reduced, and stable steady states are preferred to obtain constant product outputs and constant product quality.

For a single set of drying conditions and varied mill power levels in the external separation setup, differences in process dynamics were observed. Higher mill power levels (M3_Ext, M4_Ext) led to stabilization of the experiments, compared to the experiments with oscillating PSD (M1_Ext, M2_Ext), as the amount of crushed particles in seed particle size (0.1–0.2 mm) was increased. However, the product particle structure was not significantly influenced by the mill power level.

Varying drying conditions influenced the product particle structure and the process behavior. During the dry experiments (L2_Ext, T2_Ext, A2_Ext) relatively smooth and dense granules were produced. All three experiments reached the steady state, which was only terminated by external effects like partial clogging of the discharge tube (A2_Ext) or problems with the bed mass controller (T2_Ext). During the experiment Ref_Ext slightly denser and less porous granules were produced, and the process still reached a steady state. In the more humid experiments (L1_Ext, T1_Ext, A1_Ext) rough and porous granules were formed. The temporal evolution of the PSD showed self-sustained oscillations. Temporarily occurring excessive amounts of seed particles from crushing of oversized particles were identified as the initial cause for the oscillations. The following changing bed masses/heights led to varying overspray production, which also enhanced the self-sustained oscillations in the PSD.

Comparing the setups for internal and external separation led to the following conclusions:

- For the production of dense and smooth granules at dry process conditions in steady state, continuous SFBLG with external separation is recommended. Additionally, the product particle size is well defined by the mesh widths of the screens used for external separation.

- For the production of more porous and rough granules at humid process conditions in steady state, continuous SFBLG with internal separation is recommended. Here, the width of the product particle size distribution is defined by the separation efficiency of the classifying tube and might be larger than for external separation.

Reproducibility of the experiments was shown by experiments M3_ext and L2_Ext, which gave similar results regarding process dynamics and product quality.

All continuous SFBLG experiments (Chapter 4 and 5) showed, that changes in process parameters severely changed the process dynamics from steady state to oscillatory or unstable, and vice versa. Additionally, product quality parameters like roughness and porosity were significantly changed. Even small changes in the spray mass flow rate of $\pm 1.7$ kg·h$^{-1}$ ($\approx 15\%$), in the fluidizing gas inlet temperature of 10 K ($\approx 8\%$), or in the fluidizing gas mass flow rate of 50 kg·h$^{-1}$ ($\approx 14\%$) significantly changed the process behavior. This calls for the development of control concepts for continuous SFBLG processes on the basis of improved models. The improved models need to account for agglomeration of dust to seed particles to be able to represent the changes in process behavior, which were observed. Also, improved understanding of the comminution behavior of the mill might enhance simulation results.

Tab. 5–8. Process behavior for continuous SFBLG with external separation.

| Experiment | Steady state? | Oscillating? | Unstable? | Comparison: Exp_Int |
|---|---|---|---|---|
| M1_Ext | x | x | - | - |
| M2_Ext | x | x | - | - |
| M3_Ext | x | - | - | - |
| M4_Ext | x | - | - | - |
| Ref_Ext | x | - | - | Ref_Int: oscillatory steady state |
| L1_Ext | x | x | - | -* |
| L2_Ext | x | - | - | L2_Int: unstable |
| T1_Ext | x | x | - | T1_Int: stable steady state |
| T2_Ext | x | - | - | T2_Int: unstable |
| A1_Ext | x | x | - | A1_Int: stable steady state |
| A2_Ext | x | - | - | A2_Int: unstable |

* Experiments L1_Int and L1_Ext were performed at different spray mass flow rates and, thus, not compared.

# 6   Continuous spray fluidized bed agglomeration

This chapter is focusing on process dynamics and structure formation during continuous SFBA processes. The agglomeration process was induced by spraying of water onto partly amorphous primary particles. No separate binder was dissolved in the water. Two series of experiments were conducted, switching between internal and external classifying product discharge. In the series with internal separation, the influence of nuclei mass flow rate and classifying air velocity on process dynamics and product structure was investigated. In the second series the product was discharged externally classifying, and the nuclei mass flow rate and the mill power level were varied.

## 6.1 Materials

The continuous SFBA experiments were performed with maltodextrin, a carbohydrate mixture usually used as food additive. Maltodextrin is a white, mostly odorless powder, which is produced by hydrolysis of starch and characterized by the DE (dextrose equivalent) value. Maltodextrins with a DE value above 20 are called dried glucose syrup. Maltodextrin is used, among others, as dispersing aid, fat replacer, flavor carrier, viscosifier or bulking agent. Often maltodextrins are an ingredient of baby foods, meat products, dry soups, confectionary, ketchup, sauces, and sport beverages (Descamps et al., 2013).

For this work, maltodextrin DE 12 (Roquette Frères, France, type: Glucidex$^®$ IT 12) was used. Depending on the production by spray drying, maltodextrins often are amorphous. The fast drying prevents the crystallization process and the material becomes amorphous. But during storage, the material may re-crystallize. Thus, maltodextrins are often partly amorphous and partly crystalline. Takeiti et al. (2010) investigated the fraction of crystalline material (crystallinity) in 12 maltodextrins, of which 11 had a crystallinity of 0.66–0.72, and one 0.8. To agglomerate amorphous materials like maltodextrin, they are usually heated above their glass transition temperature, at which their surface becomes sticky due to high mobility of their molecules. Amorphous materials have free volumes in their molecule structure, enabling them to absorb larger amounts of water than crystalline materials. This bound water plasticizes the amorphous solids, reducing their glass transition temperature (Palzer, 2005, 2009, 2010). Thus, humidified maltodextrin aggregates at gas temperatures below the glass transition temperature of the pure solid. In principle, the agglomeration mechanism has been explained earlier in Fig. 2–2C (p. 9). The particles are wetted by the sprayed water droplets. Where the droplets adhere to the maltodextrin particles, glass transition and local dissolution of the solid material takes place. Sticky spots at the particle surface are formed, at which viscous bridges between the primary particles can be formed upon particle contact.

Simultaneous drying during the process leads to re-solidification of the viscous bridges, as the glass transition temperature of the dry material exceeds the gas temperature present in the granulator, and the particles return to the solid, glassy state (Section 2.2.1, p. 8). Knowing the glass transition temperatures of the solid $T_{g,s}$ and of water $T_{g,w}$ and the Gordon and Taylor constant $c$ (Tab. 6–1), the glass transition temperature $T_g$ of the moistened material is calculated by the Gordon and Taylor equation (Eq. 2–8, p. 10). To approximate $T_g$ of the used maltodextrin DE 12, the values for maltodextrin DE 10 from Tab. 6–1 can be used.

Tab. 6–1. Glass transition temperatures and Gordon and Taylor constants for different dry maltodextrins and water.

| Material | $T_g$ [°C] | $c$ [-] |
|---|---|---|
| maltodextrin DE 5 | 188 [1] | 6.8 [2] |
| maltodextrin DE 10 | 160 [1] | 7.0 [2] |
| maltodextrin DE 20 | 141 [1] | 7.7 [2] |
| dried glucose syrup DE 36 | 100 [1] | - |
| water | -138 [3] | - |

[1] Roos and Karel (1991); [2] Palzer (2007); [3] Sugisaki et al. (1968)

For the experiments in this work, the maltodextrin was sieved to a defined particle size. Two screens (mesh widths 100 and 200 µm) were used for primary particle production. Oversized particles were crushed and sieved again. Dust below 100 µm was disposed of. The primary particle sizes for the two experimental series were:

- $d_{1,3,0,Int}$: 166–208 µm
- $d_{1,3,0,Ext}$: 173–351 µm.

As the experiments of series 2 with external separation were conducted later in time than the internal classifying experiments of series 1, slight agglomeration during storage of the sieved material may have led to the increased starting particle sizes for some experiments.

The true solid densities of different maltodextrins were measured (Section 3.6.3, p. 50):

- Maltodextrin DE 12: 1474 kg·m$^{-3}$
- Maltodextrin DE 6: 1407 kg·m$^{-3}$
- Dried glucose syrup DE 47: 1534 kg·m$^{-3}$.

Thus, the used maltodextrin DE 12 belonged to Geldart Group B (Section 2.1, p. 5).

# 6.2 Experimental setup

The continuous SFBA experiments were performed at the same plant as the continuous SFBLG experiments with internal (Section 4.2, p. 52) and external separation (Section 5.2, p. 79). Most of the configurations of the cylindrical fluidized bed with a diameter of 300 mm were similar. The respective setups are shown in Figs. 6–1 and 6–2. An external primary particle supply had to be realized for the agglomeration process. The primary particles were fed to a sluice by a vibration chute and fell into the fluidized bed. The screw pump from the granulation experiments had to be replaced by a peristaltic pump (Ismatec, Switzerland, type: MCP V5.10) to realize the lower spray mass flow rates, which were needed.
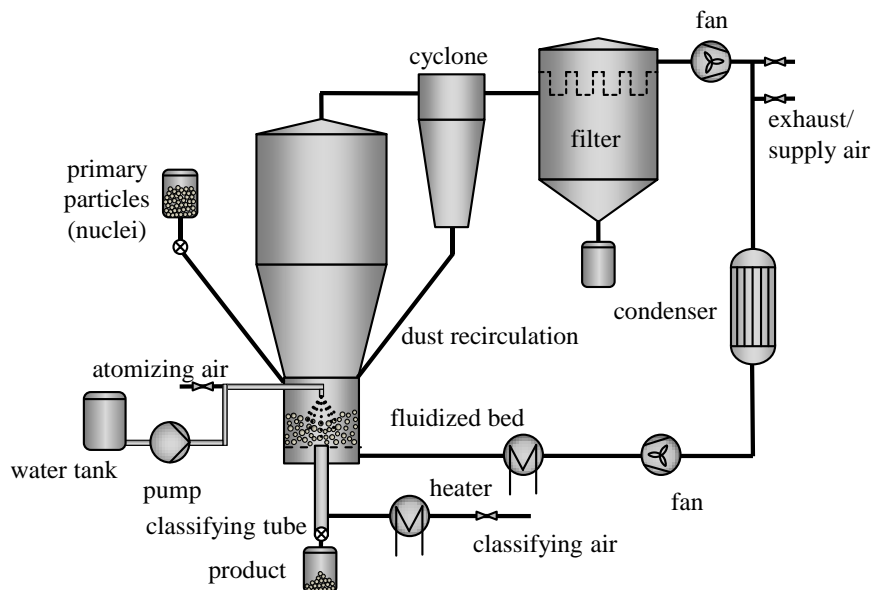


Fig. 6–1. Continuous SFBA plant with internal separation setup.
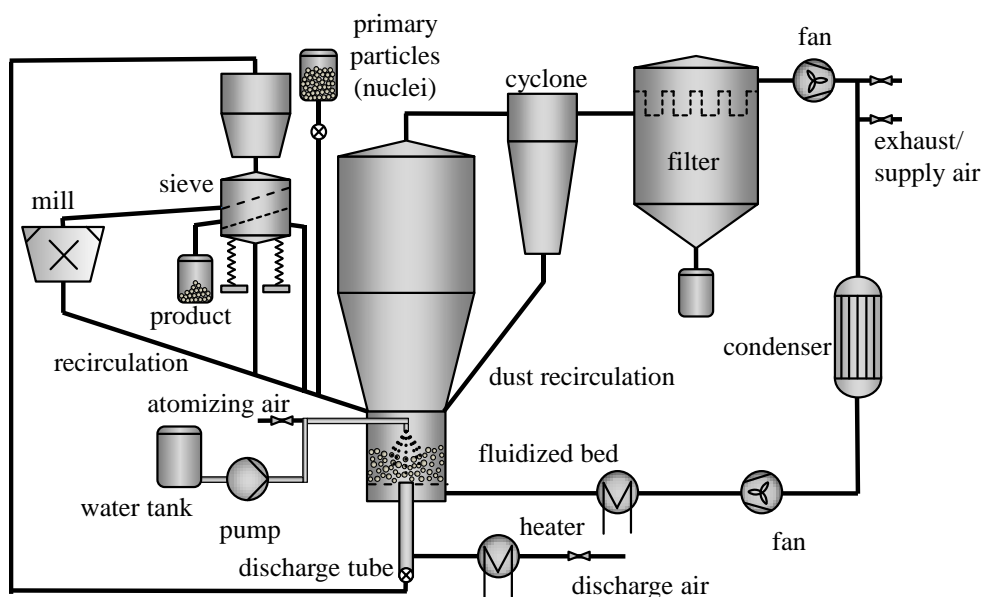


Fig. 6–2. Continuous SFBA plant with external separation setup.

## 6.3 Experimental plan

Two experimental series with different product separation were conducted. For the first series, the internal classifying setup was chosen. The classifying air velocity and nuclei mass flow rate were varied. The drying and fluidizing conditions were kept constant (Tab. 6–2, top half). During each experiment, the classifying air velocity was kept at a constant level. In the second series, the external classifying setup was investigated. Here, the nuclei mass flow rate and the mill power level were varied. The remaining process parameters were kept at a constant level (Tab. 6–2, bottom half). During the experiments with external separation, the volume flow rate of the discharge air was controlled manually to keep the bed mass nearly constant. The controller from the continuous SFBLG experiments with external separation was operating too slowly to adjust the discharge air volume flow rate correctly to maintain a constant bed mass for the fast agglomeration process. The temperature of the classifying air was set to 60°C for both experimental series.

Samples were taken from the fluidized bed and from the product throughout the experiments. After the start or restart of an experiment, samples from the fluidized bed were taken every 5 min, and samples from the product were taken every 15 min. During the process, the sampling times of bed and product were increased to 10 and 20 min, respectively. For longer, steady state periods, the sampling times were increased to 15 and 30 min, respectively. The samples taken from the fluidized bed had an average mass of ≈ 8 g, and the samples from the product had an average mass of ≈ 11 g. The total process time of each experiment was 7.5–8.5 h, resulting in 50–67 samples from the bed and 20–25 samples from the product for the internal separation setup, and 42–58 samples from the bed and 18–21 samples from the product for external separation.

During the experiments, the maltodextrin would eventually clog the nozzle, the discharge/classifying tube, the sieve, or the mill, if local over-wetting caused very sticky material. In these cases, the spray, heaters, nuclei supply, discharge, and consequently, the process time were stopped. After a short cooling period, the fluidizing gas was also stopped and the plant was opened to remedy the respective problem. Then, the fluidization air and the heaters were restarted. After a short heating time, the spray, nuclei supply and product discharge were also restarted, to continue the process. Thus, the process time is the time, during which the spray, the discharge, and the nuclei supply were operating. During the cooling and heating periods, some agglomerates broke, visible as a step in the particle size over process time diagrams in Section 6.4.

After each experiment, the samples were measured regarding the mass fraction of water, PSD, and particle structure (Chapter 3, p. 29). Also, the water tank, the nuclei storage, and the product storage were weighed before and after each experiment, to obtain the masses of sprayed water, fed nuclei and discharged product. Dividing the masses by the process time, the average spray mass flow rate, the average nuclei feed mass flow rate and the average product mass flow rate were calculated. The actual values of spray and nuclei feed mass flow rate are listed in Tab. 6–2.

Tab. 6–2. Overview of experimental parameters for continuous SFBA with internal and external separation.

| Experiment | $T_{gas,in}$ [°C] | $\dot{M}_{gas,in}$ [kg·h⁻¹] | $u_{gas}$ [m·s⁻¹] | $\dot{M}_{spray}$ [kg·h⁻¹] | $M_{bed,0}$ [kg] | $\dot{M}_{nuc}$ [kg·h⁻¹] | $u_{class}$ [m·s⁻¹] | $P_{mill}$ [%] | Sieves [mm] | |
|---|---|---|---|---|---|---|---|---|---|---|
| Ref_Int-A | 60 | 160 | 0.6 | 1.0 | 1.8 | **6.4** | **1.2** | - | - | |
| N1_Int-A | 60 | 160 | 0.6 | 1.4♦ | 1.8 | **3.6** | 0.9# | - | - | series 1 |
| N2_Int-A | 60 | 160 | 0.6 | 1.0 | 1.8 | **8.7** | 1.2 | - | - | |
| C1_Int-A | 60 | 160 | 0.6 | 1.0 | 1.8 | 6.7 | **1.0** | - | - | |
| C2_Int-A | 60 | 160 | 0.6 | 1.0 | 1.8 | 6.0 | **1.3** | - | - | |
| Ref_Ext-A | 60 | 160 | 0.6 | 1.0 | 1.8 | **3.4** | var.* | **60** | 0.5/1.0 | |
| N1_Ext-A | 60 | 160 | 0.6 | 1.0 | 1.8 | **2.5** | var.* | 60 | 0.5/1.0 | series 2 |
| N2_Ext-A | 60 | 160 | 0.6 | 1.0 | 1.8 | **4.0** | var.* | 60 | 0.5/1.0 | |
| M1_Ext-A | 60 | 160 | 0.6 | 1.0 | 1.8 | 3.2 | var.* | **40** | 0.5/1.0 | |
| M2_Ext-A | 60 | 160 | 0.6 | 0.9 | 1.8 | 3.5 | var.* | **80** | 0.5/1.0 | |

♦ The deviation to the reference experiment is probably a recording error of the mass of the water tank.

# This classifying air velocity was necessary to conduct the experiment and prevent excessive filling of the fluidized bed.

* var.: varied manually, to keep the bed mass constant

Experiment names and varied parameters (bold):

  N – Nuclei mass flow rate

  C – Classifying air velocity

  M – Mill power level

  Ref – Reference experiment

# 6.4 Results and discussion regarding process behavior

The results for both experimental series are summarized and discussed in this section. The investigation of the process behavior included the interpretation of the temporal evolution of particle size distribution density, average particle size over process time, evolution of bed and product mass, the steady state determination, and the calculation of the average agglomerate growth rate.

### 6.4.1 Internal separation

For continuous SFBA with internal separation, the reference experiment Ref_Int-A reached the steady state after 0.4 h (Tab. 6–3, p. 119). The relatively narrow particle size distribution density at the start of the experiment broadened quickly in the first 10 min (Fig. 6–3, left). The still visible but reduced peak around 0.2 mm during the experiment resulted from the continuous supply of primary particles to the process. The standard deviation of the PSD density of the bed particles more than tripled during the first 10 min (Fig. 6–4, top). The observed growth pattern is typical for a well-mixed agglomeration process. At the beginning, particles underwent mainly primary agglomeration. After a few clusters were formed, also secondary agglomeration took place, forming large agglomerates relatively fast. But during the process, primary particles, very large agglomerates, and small agglomerates formed by primary agglomeration, coexisted, resulting in the observed wide PSD, especially for $q_3$. After the first product was discharged (Fig. 6–3, right), the PSD density of the product particles stayed relatively constant. It was shifted towards larger particle sizes compared to the evolution of $q_3$ in the bed, and few primary particles were discharged. The fact, that also the product PSD density was very broad, indicated that the separation efficiency of the classifying tube was insufficient. Nevertheless, the average product particle size was larger than the average particle size in the bed (Fig. 6–4, top). As the temporal evolution of the PSD density showed similar behavior for all experiments with internal separation, only $q_3$ for Ref_Int-A is shown (Fig. 6–3). The remaining diagrams are placed in the appendix (Fig. C–1, p. 141 and Fig. C–2, p. 142).
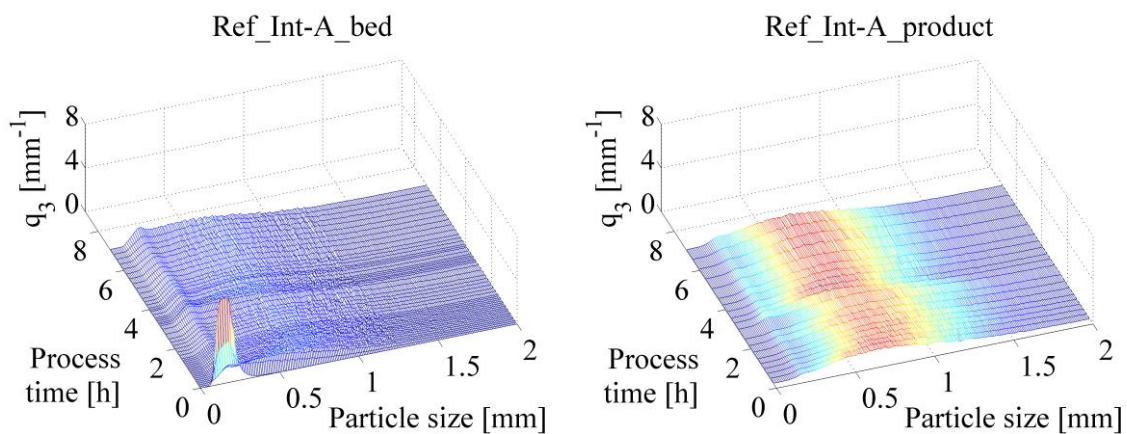


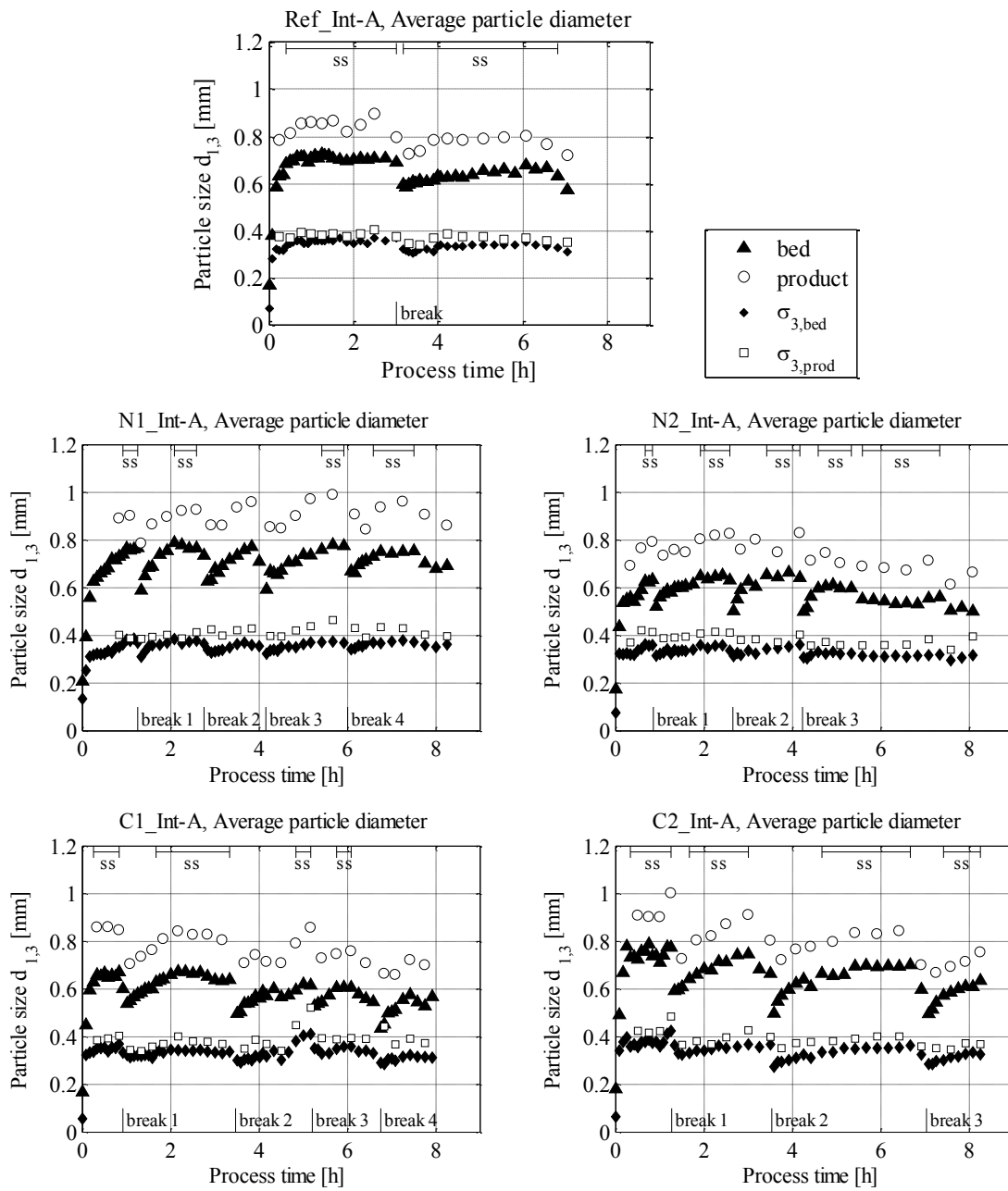Fig. 6–3. Particle size distribution densities $q_3$ for Ref_Int-Agg: Bed (left) and product (right).

Fig. 6–4. Average particle diameter $d_{1,3}$ for all continuous SFBA experiments with internal separation. Legend valid for all five plots, ss – steady state.
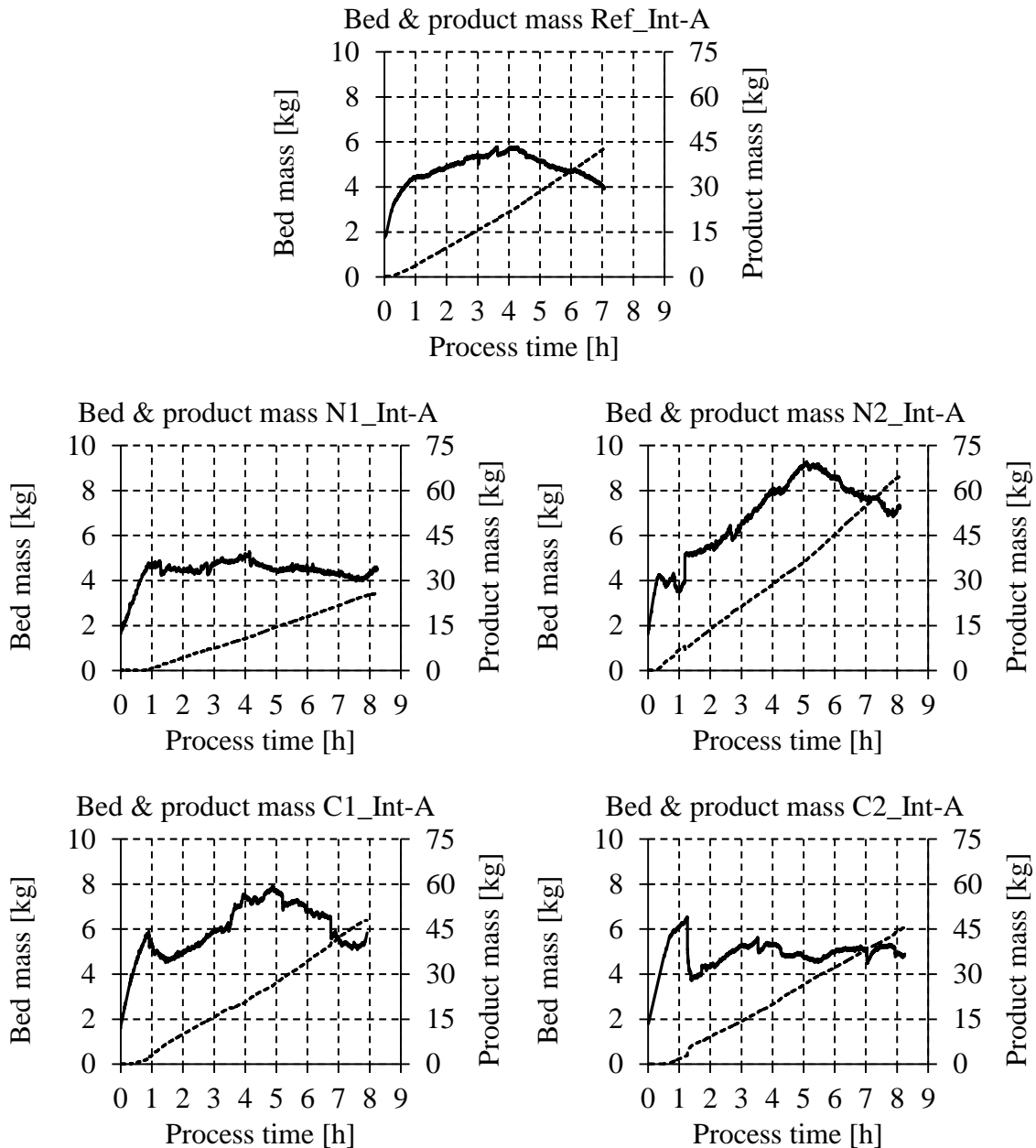
Fig. 6–5. Calculated bed (solid line) and product masses (dashed line) for continuous SFBA with internal separation.

The graphs of the average particle diameter $d_{1,3}$ for the bed particles over process time (Fig. 6–4) were used for steady state determination (Section 3.1.3, p. 33). The steady state values are listed in Tab. 6–3 (p. 119) and marked in Fig. 6–4 ("ss"). All experiments reached a steady state after 0.3–0.9 h. Clear differences in process behavior related to process parameters were not observed. Steps in the graphs resulted from breaks in the experiments, which were necessary to clean the clogged nozzle or discharge tube (Section 6.3). Usually, after a restart of the experiment, the steady state was reached again before the next break. The calculated bed masses were relatively steady for all experiments (Fig. 6–5). A low nuclei mass flow rate (N1_Int-A) led to a low bed mass and low product mass flow rate, and vice versa (N2_Int-A). But the low bed mass in N1_Int-A allowed for formation of relatively large

114

particles, compared to Ref_Int-A, as the sprayed water was distributed to less bed material. The high nuclei mass flow rate and consequently high bed mass in experiment N2_Int-A resulted in smaller agglomerates, compared to the experiments with lower nuclei mass flow rates, as the sprayed water needed to be distributed to more particles in the bed. But the resulting average residence time was lower for a high nuclei mass flow rate. Thus, large particles were formed during large residence times and vice versa, resulting in similar growth rates.

A clear influence of the classifying air velocity on the bed mass was not observed. The chosen parameter regime of $0.9$–$1.3$ m·s$^{-1}$ was too narrow to see an influence on the bed mass, product mass flow rate, product particle size, or growth rate. But outside of the chosen parameter regime the experiments were not feasible. The according average growth rates were calculated with the average particle size of the product in the determined intervals (Tab. 6–3, p. 119). All growth rates were similar, except for the reference experiment. There, only one break was necessary, and the whole process was continuously steady. Thus, a high product mass flow rate, and consequently a low residence time were realized, increasing the average growth rate. Additionally, the average product particle size was considerably large for the low residence time, due to the missing particle breakage during process breaks, also enhancing the growth rate.
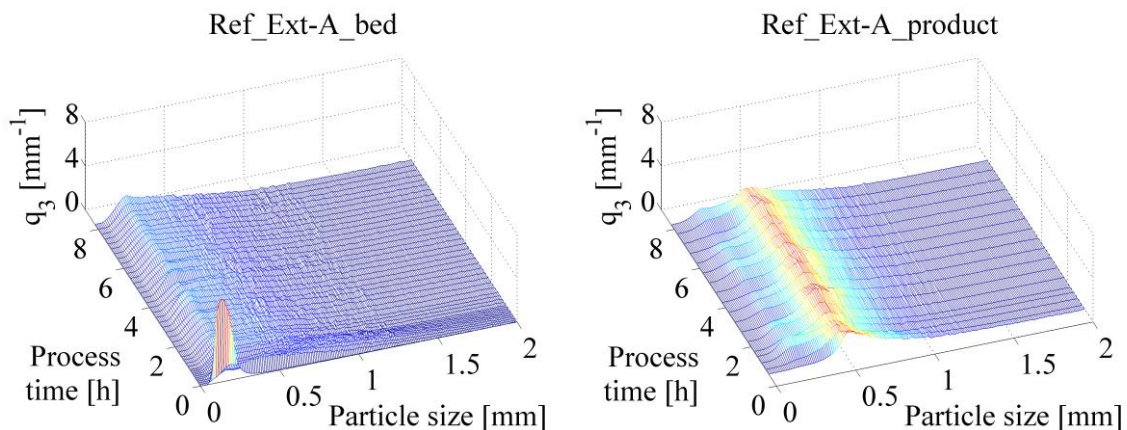


Fig. 6–6. Particle size distribution densities $q_3$ for Ref_Ext-Agg: Bed (left) and product (right).

## 6.4.2 External separation

For the continuous SFBA experiments with external separation, the temporal evolution of $q_3$ is shown for the reference experiment Ref_Ext-A (Fig. 6–6). The PSD density of the bed was very similar to the PSD densities of the experiments with internal separation, as process parameters like spray mass flow rate, fluidizing gas inlet temperature and fluidizing gas mass flow rate were similar. After 5 min the narrow starting PSD density broadened, as expected for an agglomeration process. But the PSD density of the product was narrower than for internal separation, as it was limited by the mesh widths of the screens (0.5 and 1 mm). It showed a clear peak around 0.5 mm. Particles smaller than 0.5 mm were formed by breakage during the discharge from the sieve, or were entrained by the larger product particles due to

swarm hindering effects or were sticking to the large particles. The PSD density also showed particles larger than 1 mm. Particles with, for example, a width of 1 mm and a length of 2–3 mm might still fit through the sieve. But the projections of the large and long particles, which were measured by Camsizer (Section 3.1.2, p. 32), consequently were subsequently assigned to area-equivalent circle diameters larger than 1 mm. Thus, particle sizes larger than 1 mm are visible in the PSD of the product. As the 3-D diagrams of $q_3$ were very similar for all experiments, they are only shown for bed and product particles of experiment Ref_Ext-A. The remaining diagrams are shifted to the appendix (Fig. C–3, p. 143, Fig. C–4, p. 144).
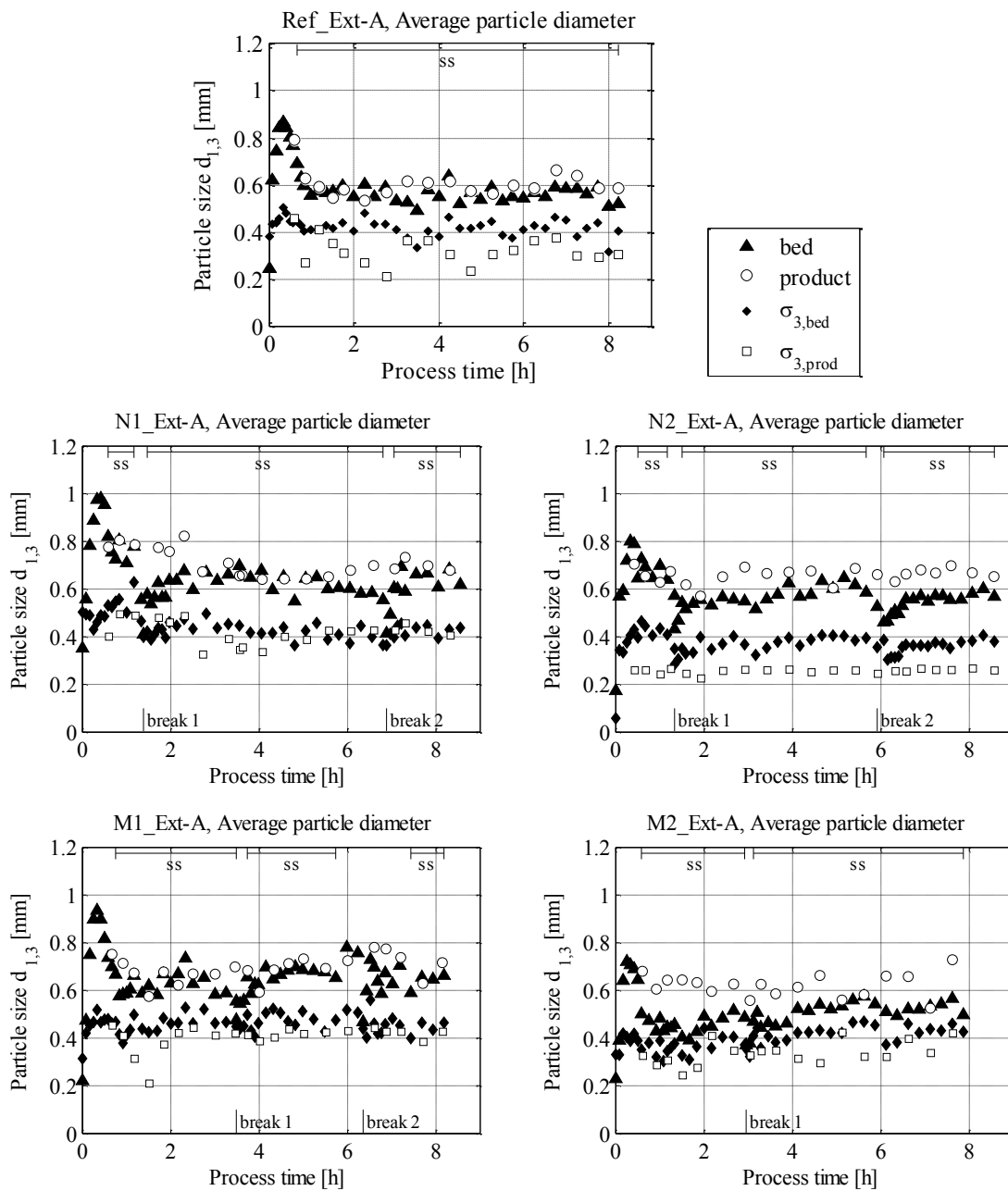


Fig. 6–7. Average particle diameter $d_{1,3}$ for all continuous SFBA experiments with external separation. Legend valid for all five plots, ss – steady state.

Bed & product mass Ref_Ext-A

Bed & product mass N1_Ext-A

Bed & product mass N2_Ext-A

Bed & product mass M1_Ext-A
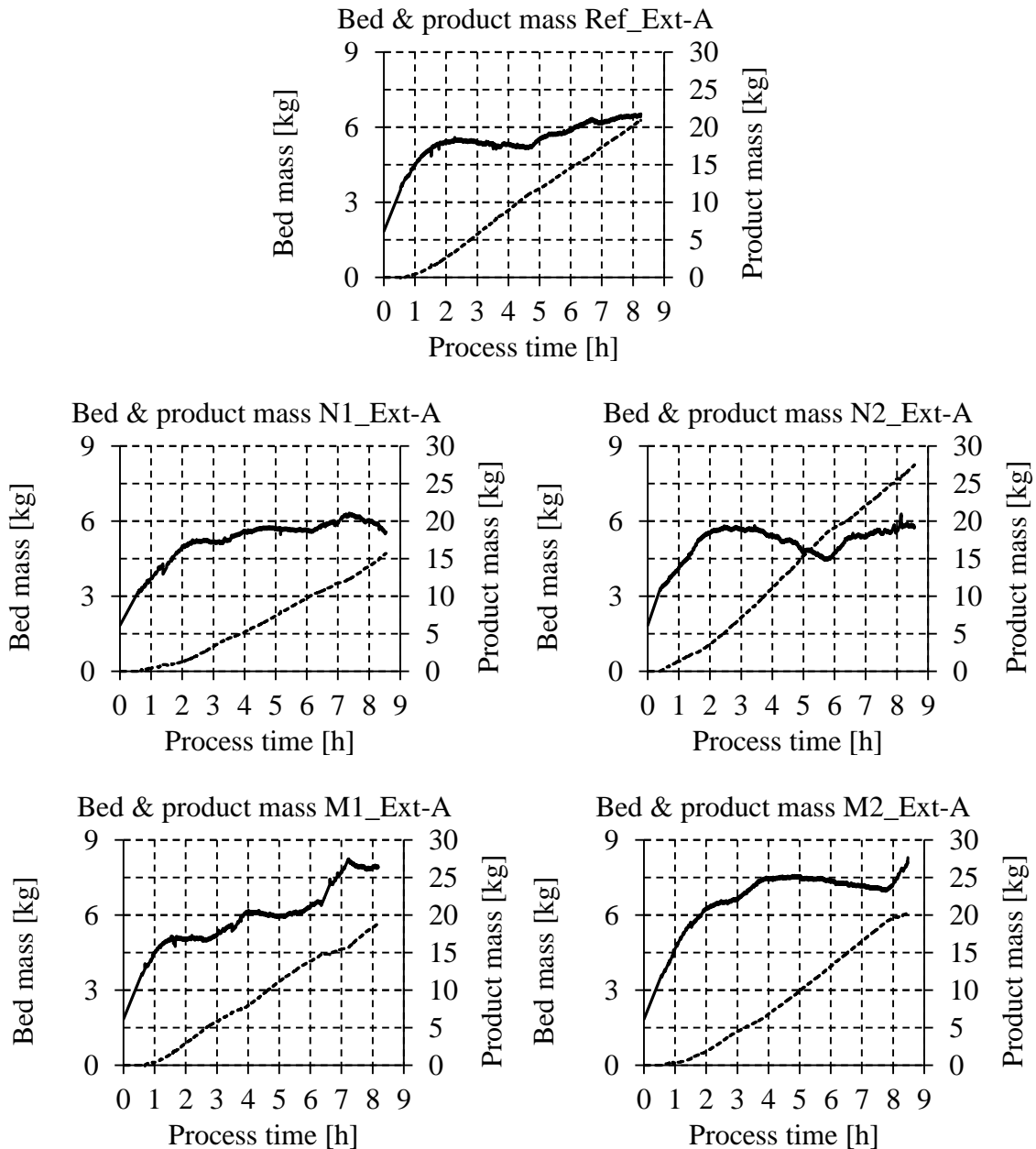
Bed & product mass M2_Ext-A

Fig. 6–8. Calculated bed (solid line) and product masses (dashed line) for continuous SFBA with external separation.

Again, the graphs of the average particle diameter $d_{1,3}$ of the bed particles (Fig. 6–7) were used for steady state determination (Section 3.1.3, p. 33). The steady state values are listed in Tab. 6–3 (p. 119). All experiments reached a steady state after 0.5–0.8 h. Steps in the graphs were attributed to process breaks, which were necessary to clean the nozzle and discharge tube from sticking lumps of maltodextrin. Usually, the steady state was then reached again before a possible next break. The product particle size was limited by the used screens, but generally the product particles were larger than the bed particles. Exceptions occurred at the start or restart of the experiments, when the product mass flow rate had not yet reached the steady state value. In these cases, particles might have had longer time for agglomeration, resulting in large particle sizes in the fluidized bed.

The comparison of the experiments with varied nuclei mass flow rate yielded the expected results (Tab. 6–3). A low nulcei mass flow rate in experiment N1_Ext-A resulted in a low steady state product mass flow rate. As particle growth ($d_{1,3,prod,ss}$ - $d_{1,3,0}$) and bed mass were similar to the values in Ref_Ext-A, the average growth rate during steady state was lower than for high nuclei mass flow rates. Contrary, for an increased nuclei mass flow rate in N2_Ext-A a higher product mass flow rate resulted. For a similar bed mass and larger particle growth, also a larger average growth rate resulted. The graphs of the bed mass were steady for all three experiments (Fig. 6–8).

For the experiments with a varied mill power level, similar nuclei mass flow rates were set, resulting in similar product mass flow rates during steady state. For a low power level in experiment M1_Ext-A, a smaller amount of oversized particles was crushed by the mill than in Ref_Ext-A and M2_Ext-A, resulting in an overall increased product particle size. Additionally, the steady state bed mass in experiment M1_Ext-A was similar to the bed mass of Ref_Ext-A and smaller than in M2_Ext-A, resulting in an increased average net growth rate of the particles. However, increasing the mill power level enhanced the comminution of oversized particles, and, thus, a larger amount of small particles was present in the fluidized bed. This resulted in a larger bed mass and higher residence time, ultimately causing a lower net growth rate. The steep rises in the bed masses towards the end for experiments M1_Ext-A and M2_Ext-A (Fig. 6–8) were attributed to problems with the discharge due to clogging of the discharge tube, leading to the termination of the processes.

Comparing internal and external classifying experiments, higher average agglomerate growth rates were reached for internal separation. Higher nuclei mass flow rates and thus higher product mass flow rates, as well as missing size reduction by a mill, reduced the average residence time of the agglomerates compared to the experiments with external separation, resulting in larger average growth rates.

Tab. 6–3. Steady state values for continuous SFBLG experiments with internal and external separation.

| Exp | determi-nation?* | m [-] | CoV < ? [%] | $t_{ss}$ [h] | $M_{bed,ss}$ [kg] | $\dot{M}_{prod,ss}$ [kg·h⁻¹] | $\tau$ [h] | $d_{1,3,0}$ [µm] | $d_{1,3,prod,ss}$ [µm] | $G_{av}$ [µm·min⁻¹] |
|---|---|---|---|---|---|---|---|---|---|---|
| Ref_Int-A | bed | 3 | 3.0 | 0.4–3.0; 3.2–6.8 | 4.9 | 6.4 | 0.8 | 166 | 812 | 13.9 |
| N1_Int-A | bed | 3 | 1.6 | 0.9–1.3; 2.1–2.6; 5.4–5.9; 6.6–7.5 | 4.4 | 3.7 | 1.2 | 208 | 940 | 10.3 |
| N2_Int-A | bed | 3 | 3.0 | 0.7–0.8; 1.9–2.6; 3.4–4.2; 4.6–5.3; 5.6–7.3 | 7.8 | 8.4 | 0.9 | 174 | 752 | 10.4 |
| C1_Int-A | bed | 3 | 2.5 | 0.3–0.8; 1.7–3.3; 4.8–5.2; 5.8–6.1 | 5.7 | 5.6 | 1.0 | 167 | 811 | 10.6 |
| C2_Int-A | bed | 3 | 3.3 | 0.3–1.3; 1.7–3.0; 4.7–6.7; 7.4–End | 5.0 | 5.3 | 0.9 | 181 | 840 | 11.7 |
| Ref_Ext-A | bed | 6 | 10.0 | 0.7–End | 5.6 | 2.9 | 1.9 | 244 | 592 | 3.0 |
| N1_Ext-A | bed | 3 | 10.0 | 0.6–1.2; 1.5–6.8; 7.1–End | 5.4 | 2.1 | 2.5 | 351 | 702 | 2.3 |
| N2_Ext-A | bed | 3 | 6.5 | 0.5–1.2; 1.5–5.7; 6.1–End | 5.3 | 3.5 | 1.5 | 173 | 652 | 5.4 |
| M1_Ext-A | bed | 3 | 8.4 | 0.8–3.5; 3.7–5.7; 7.4–End | 5.8 | 2.9 | 2.0 | 220 | 669 | 3.8 |
| M2_Ext-A | bed | 3 | 12.0 | 0.6–2.9; 3.1–End | 6.8 | 2.7 | 2.5 | 229 | 623 | 2.6 |

* Determination of steady state via bed samples. Growth rate calculation with product particle sizes, averaged in the steady state intervals

varied parameters internal separation ($\dot{M}_{nuc}$, $u_{class}$):

- Ref_Int-A (6.4 kg·h⁻¹, 1.2 m·s⁻¹), N1_Int-A (3.6 kg·h⁻¹, 0.9 m·s⁻¹), N2_Int-A (8.7 kg·h⁻¹, 1.2 m·s⁻¹), C1_Int-A (6.7 kg·h⁻¹, 1.0 m·s⁻¹), C2_Int-A (6.0 kg·h⁻¹, 1.3 m·s⁻¹)

varied parameters external separation ($\dot{M}_{nuc}$, $P_{mill}$):

- Ref_Ext-A (3.4 kg·h⁻¹, 60%), N1_Ext-A (2.5 kg·h⁻¹, 60%), N2_Ext-A (4.0 kg·h⁻¹, 60%), M1_Ext-A (3.2 kg·h⁻¹, 40%), M2_Ext-A (3.5 kg·h⁻¹, 80%)

# 6.5 Results and discussion regarding product quality

The concept of fractal dimension was used for structural description of the produced agglomerates (Section 3.5, p. 45). Images taken by a light microscope were evaluated with a MatLab algorithm, and the fractal dimension of each agglomerate was calculated. Ten agglomerates were evaluated per sample to calculate an average fractal dimension. Furthermore, the mass fraction of water was measured for ca. 10 bed and 10 product samples from each experiment, allowing for the calculation of an average mass fraction of water of the particles in the fluidized bed and in the product (Section 3.2, p. 37).

### 6.5.1 Internal separation

To get an impression of the structure of the agglomerates formed by binder-less continuous SFBA with internal separation, an image of one particle from each experiment with a $D_f$ close to the $D_{f,av}$ of the whole sample is shown in Fig. 6–9 for representation. The two dimensional images show relatively porous agglomerates. This corresponds to the value of $D_f$ around 1.85–1.86 (Tab. 6–4). For long chained, very open diesel soot agglomerates, Samson et al. (1987) reported $D_f$ values of 1.7–1.8, calculated also from 2-D projections. Thus, the measured values of $D_f = 1.85$–1.86 for the denser maltodextrin agglomerates seem reasonable. A study presenting $D_f$ values measured by 3-D μ-CT images has been published by Pashminehazar et al. (2016). But due to the 3-D method, the values for $D_f$ range up to three, not allowing for a direct comparison with values obtained from a 2-D method. However, the conclusions regarding the structure of maltodextrin agglomerates were similar. Thus, the structure of the agglomerates was described well by the concept of fractal dimension, even in 2-D. But the agglomerates produced during the continuous SFBA experiments with internal separation have a very similar structure. Changing the nuclei mass flow rate and the classifying air velocity did not alter the product structure in the parameter regime investigated. As the focus of this work was process behavior, and a working set of drying conditions was difficult to determine in the first place, only the process dynamics parameters nuclei mass flow rate and classifying air velocity were varied. Structural change might have occurred for a change in drying conditions, as observed by Dadkhah and Tsotsas (2014) for agglomerates made of glass beads and hydroxypropyl methyl cellulose. They reported denser agglomerates, and, thus, larger values of $D_f$, for small agglomeration rates, and vice versa. But due to the 3-D method and different material systems used, the values presented by Dadkhah and Tsotsas (2014) and the values presented in this dissertation are not comparable. Consequently, future studies focusing on continuous SFBA should also use a 3-D method to determine the agglomerate fractal dimension, to ensure comparability with Dadkhah and Tsotsas (2014) and Pashminehazar et al. (2016).

The mass fraction of water of the product agglomerates was higher than at the beginning of the experiments (Tab. 6–4). As the drying conditions were kept constant, the mass fractions of water for all experiments were similar. The additional water was stored in the amorphous matrix of the maltodextrin.

Ref_Int-A, $D_{f,1} = 1.859$ ($D_{f,av,1} = 1.857$)

N1_Int-A, $D_{f,2} = 1.846$ ($D_{f,av,2} = 1.857$)

N2_Int-A, $D_{f,3} = 1.853$ ($D_{f,av,3} = 1.854$)

C1_Int-A, $D_{f,4} = 1.844$ ($D_{f,av,4} = 1.855$)

C2_Int-A, $D_{f,5} = 1.850$ ($D_{f,av,5} = 1.854$)

Fig. 6–9. Light microscope images and calculated fractal dimension $D_f$ for particles from product samples of continuous SFBA with internal separation.

Tab. 6–4. Overview of key process parameters and measured structure and moisture values for continuous SFBA with internal and external separation.

| Exp | Parameters | | | Measurement | | | |
|---|---|---|---|---|---|---|---|
| | $\dot{M}_{nuc}$ | $u_{class}$ | $P_{mill}$ | $D_{f,av}$ | $x_{w,0}$ | $x_{w,bed,av}$ | $x_{w,prod,av}$ |
| | [kg·h$^{-1}$] | [m·s$^{-1}$] | [%] | [%] | [%] | [%] | [%] |
| Ref_Int-A | 6.4 | 1.2 | - | 1.857 ± 0.023 | 5.3 | 6.8 | 7.0 |
| N1_Int-A | 3.6 | 0.9 | - | 1.857 ± 0.033 | 5.6 | 6.9 | 7.1 |
| N2_Int-A | 8.7 | 1.2 | - | 1.854 ± 0.018 | 5.8 | 7.0 | 6.7 |
| C1_Int-A | 6.7 | 1.0 | - | 1.855 ± 0.025 | 6.7 | 5.5 | 7.6 |
| C2_Int-A | 6.0 | 1.3 | - | 1.854 ± 0.019 | 4.9 | 6.4 | 6.1 |
| Ref_Ext-A | 3.4 | - | 60 | 1.846 ± 0.018 | 5.4 | 7.3 | 7.6 |
| N1_Ext-A | 2.5 | - | 60 | 1.862 ± 0.017 | 5.9 | 7.5 | 7.8 |
| N2_Ext-A | 4.0 | - | 60 | 1.855 ± 0.021 | 5.5 | 7.1 | 7.5 |
| M1_Ext-A | 3.2 | - | 40 | 1.842 ± 0.031 | 5.3 | 7.2 | 7.7 |
| M2_Ext-A | 3.5 | - | 80 | 1.849 ± 0.040 | 5.2 | 6.7 | 7.3 |

## 6.5.2 External separation

All findings reported in the previous section also apply for continuous SFBA with external separation. The values for $D_f$ lay within a similar region of 1.84–1.86 (Tab. 6–4). The structure of the agglomerates formed in the experiments with external separation was similarly open and porous as the structure of the agglomerates from the experiments with internal separation, as shown in Fig. 6–10. The slightly larger span of the $D_f$ values might be attributed to the additional comminution step, partly destroying the already formed structures of the agglomerates in the fluidized bed. The proposed method was again able to represent the particle structure properly.

The mass fraction of water for the agglomerates from the external classifying experiments was again similar for all experiments, as the drying conditions remained similar (Tab. 6–4). But the mass fractions of water were overall larger than for the internal classifying experiments, due to the larger residence times of the agglomerates. A larger residence time meant longer exposition to the sprayed water, so that a higher mass fraction of water resulted in the product particles. Additionally, the mass fraction of water of product particles from the experiments with internal separation was slightly lower, due to additional drying effects in the classifying tube. The volume flow rate and, thus, the velocity of the classifying air were larger for the internal classifying experiments. For internal separation, volume flow rates of 123–156 L·min$^{-1}$ were used. For the experiments with external separation, the volume flow rate of the discharge air was controlled in the range of 83–109 L·min$^{-1}$.

Ref_Ext-A, $D_{f,6} = 1.859$ ($D_{f,av,6} = 1.846$)

N1_Ext-A, $D_{f,7} = 1.857$ ($D_{f,av,7} = 1.862$)



N2_Ext-A, $D_{f,8} = 1.856$ ($D_{f,av,8} = 1.855$)

M1_Ext-A, $D_{f,9} = 1.851$ ($D_{f,av,9} = 1.842$)



M2_Ext-A, $D_{f,10} = 1.855$ ($D_{f,av,10} = 1.849$)

Fig. 6–10. Light microscope images and calculated fractal dimension $D_f$ for particles from product samples of continuous SFBA with external separation.

# 6.6 Conclusions

All conducted continuous SFBA experiments reached the steady state after 15–55 min. Oscillations in the particle size distribution, as those presented for continuous SFBLG, were not observed for the investigated parameter regime. Oscillation-like steps in the graphs of average particle size or bed mass were induced by breaks, necessary to clean the nozzle, discharge tube or sieve and mill from sticky maltodextrin. But the steady state, that was reached before a break, was usually reached again after restart of each experiment.

The varied parameters mainly had an influence on the average growth rate of the agglomerates. For internal separation, relatively high growth rates of $> 10$ µm·min$^{-1}$ were reached. Reasons for the high growth rates were the missing size reduction by comminution, lower residence time due to missing feedback of fines, and the high product mass flow rates due to the high nuclei mass flow rates, leading to smaller residence times, compared to the experiments with external separation. For internal separation, changing nuclei mass flow rates resulted in similar growth rates. The influence of the classifying air velocity was small in the investigated parameter regime, but outside of this regime, the process was not feasible.

In the experiments with external separation, considerably smaller average growth rates of 2.3–5.4 µm·min$^{-1}$ were measured, compared to the experiments with internal separation. This was attributed to size reduction by comminution, feedback of fines and smaller product mass flow rates, induced by smaller nuclei mass flow rates. A clear advantage of external separation was the relatively constant average product particle size, determined by the sieves. Realizing constant product particle diameters, the influence of the process parameters on the average growth rate was clearly visible. A low nuclei mass flow rate resulted in a large residence time and a small average agglomerate growth rate. A high nuclei mass flow rate led to a lower average residence time and consequently to a larger average growth rate.

The mass fraction of water of the product agglomerates was similar for each type of separation, as the drying conditions were not altered during the experimental series. The mass fraction of water in the fluidized bed was similar for all experiments (5.5–7.5%). The mass fraction of water of the product for internal separation (6.1–7.6%) was slightly lower than for external separation (7.3–7.8%). The higher volume flow rate of classifying air, resulting in higher air velocities during internal separation experiments had a slight additional drying effect on the product, compared to the experiments with external separation. The average volume flow rate of classifying air lay within the range of 123–156 L·min$^{-1}$ for internal separation, and was controlled in the range of 83–109 L·min$^{-1}$ for external separation. During the experiments, the mass fraction of water of the product was considerably higher than the mass fraction of water of the primary particles. This was attributed to the spraying of water, which was partly integrated into the amorphous matrix of the maltodextrin.

The agglomerate structure visible from the light microscope images was similar for all experiments. Also the structural description by the fractal dimension yielded similar results (1.84–1.86). Consequently, the nuclei mass flow rate, classifying air velocity and mill power level did not influence the agglomerate structure.

# 7　Summary and outlook

Oscillations in the PSD for continuous SFBLG, which were predicted by simulations of various authors, have been proven by a systematical, experimental investigation (Chapters 4 and 5). The experimental proof of these oscillations is considered to be a main outcome of this dissertation. The underlying principles during continuous SFBLG regarding particle growth, overspray generation, seed particle formation, type of product discharge, feedback of undersize material, and structure formation on the granule surface were explained, discussed, and their various effects were shown in the different experimental series. A very interesting result is the fact, that even relatively small changes in process parameters ($\leq 15\%$) could completely change the process behavior from unstable (insufficient seed particles) to a limit cycle (self-sustained oscillation) or steady state, and vice versa. Thus, parameter selection for continuous SFBLG processes regarding particle size and structure also has to take into account process dynamics. Concluding from the presented experiments, recommendations for the production of granules via continuous SFBLG with solutions and internal seed particle production were derived as follows:

- Open, porous and rough granules of crystalline materials are formed for humid process conditions. Steady state production of porous granules is realized by internal classifying product discharge. Depending on the separation efficiency of the classifier, relatively wide product PSD may result.
- Dense and smooth crystalline granules are produced at dry process conditions. Steady state production of these granules is possible by using an external classifying product discharge. Additionally, the product PSD is limited by the sieves, used for external separation, and can be considerably narrower than for internal separation.

Understanding the occurrence of the described oscillations in PSD is helpful to conduct processes in steady state. In the rare case that oscillations in PSD are wanted, for example to produce two different particle sizes of the same material in one plant, better understanding of the oscillation also supports maintaining them. The process behavior of continuous SFBLG with suspensions cannot be deduced from this dissertation, as overspray and layer formation are mere drying, and no crystallization processes. Thus, the seed particle production, which is a key factor for process behavior, works differently. Consequently, further research is necessary in this area.

For product quality aspects, like particle surface roughness and particle porosity, decreasing linear correlations in terms of drying potential were developed. For dry processes, particle porosity and roughness were low, and vice versa. Additionally, porosity and roughness were linearly proportional to each other. For porous particles, rough particle surfaces were measured, and vice versa.

Additionally, different average granule growth rates were observed for the different product discharge setups. For the experiments with internal separation, no bed mass control was applied, leading to large bed masses, and, thus, relatively large average residence times (5.2–6.4 h). For the investigated parameter regimes, the average granule growth rate during steady state for internal separation lay within the range of 0.8–1.7 $\mu m \cdot min^{-1}$. In the experiments with the external classifying setup, it was attempted to hold the bed mass at a constant lower level, compared to the experiments with internal separation. Thus, smaller average residence times (2.4–3.8 h) and larger average granule growth rates (1.9–3.2 $\mu m \cdot min^{-1}$) resulted.

Concerning continuous SFBA of partly amorphous food powder (Chapter 6), all experiments reached the steady state, regardless of the chosen parameters. Even after process breaks, where size reduction took place due to missing spray and additional drying during the cooling and re-heating periods, the system returned to its steady state after restart. Oscillations in the PSD were not observed for the investigated parameter regime. Additionally, the nuclei mass flow rate, classifying air velocity and mill power level did not influence the agglomerate structure in the investigated parameter region.

Large average agglomerate growth rates ($> 10\ \mu m \cdot min^{-1}$) were observed for internal separation with relatively high nuclei mass flow rates, compared to the external classifying experiments (2.3–5.4 $\mu m \cdot min^{-1}$). Main reason for this effect were the different residence times for internal (0.8–1.2 h) and external (1.9–2.5 h) separation, resulting from the different nuclei feed mass flow rates. The different trends regarding average growth rates depending on the type of product separation for SFBLG and SFBA were the result from different seed particle/nuclei supply concepts. For SFBLG the seed particles were formed internally, and their amount solely depended on the other process parameters. For SFBA, external supply of nuclei was necessary. Thus, the nuclei mass flow rate was adjustable and represented an additional parameter to influence process behavior, apart from the rest of the process conditions.

Besides the experimental findings, also the methods described in Chapter 3 may find application in future work:

- A method for obtaining the granule surface roughness was presented, which might be applied to future granulation studies.
- An alternative method to porosity measurement via $\mu$-CT was presented by weighing single particles and consecutive evaluation of their 2-D SEM images to attain an approximated particle volume.
- The method and criterion of using the value of the *CoV*, which were derived for the determination of an experimental steady state, might be used in future investigations of continuous particle growth processes.
- A guideline is given, on how to calculate the average growth rate of a process, using the previously determined steady state values.

- The method of determining the 2-D fractal dimension from light microscope images for comparison of different agglomerate structures may be used in future work, when a relatively quick investigation of the agglomerate structure is needed. But if longer measurement times are tolerable, a 3-D method (for example by μ-CT) to determine the fractal dimension might be more suitable.

Future work in the field of continuous SFBLG processes should include the improvement of the existing models for the description of particle growth in fluidized beds by considering the agglomeration of dust to seed particle size, before the new particles take part in the layering process. Based on the improved models, existing control concepts (Palis and Kienle, 2012; Bück et al., 2015; Bück et al., 2016c) can be applied for stabilization of the continuous SFBLG process. Additionally, further experimental investigations should regard continuous SFBLG with suspensions, as overspray, drying and seed particle production work differently for suspensions.

Further work in the field of continuous SFBA is currently being done, for example by Du et al. (2018) and Strenzke et al. (2018). Both authors further investigate the continuous agglomeration process with binder in different fluidized bed setups. Their aim also is the improvement of existing models describing the agglomerate growth, with the ultimate goal of controlling this process.

# 8 References

AVILÉS-AVILÉS, C., DUMOULIN, E., TURCHIULI, C., 2015. Fluidised bed agglomeration of particles with different glass transition temperatures. *Powder Technology* 270, 445–452. 10.1016/j.powtec.2014.03.026.

BELKASIM, S.O., SHRIDHAR, M., AHMADI, M., 1991. Pattern recognition with moment invariants: A comparative study and new results. *Pattern Recognition* 24 (12), 1117–1138.

BENELLI, L., CORTÉS-ROJAS, D.F., SOUZA, C.R.F., OLIVEIRA, W.P., 2015. Fluid bed drying and agglomeration of phytopharmaceutical compositions. *Powder Technology* 273, 145–153. 10.1016/j.powtec.2014.12.022.

BERTIN, D.E., COTABARREN, I., PIÑA, J., BUCALÁ, V., 2013. Granule size distribution for a multi-chamber fluidized-bed melt granulator: Modeling and validation using process measurement data. *Chemical Engineering Science* 104, 319–329. 10.1016/j.ces.2013.08.012.

BOEREFIJN, R., HOUNSLOW, M.J., 2005. Studies of fluid bed granulation in an industrial R&D context. *Chemical Engineering Science* 60 (14), 3879–3890. 10.1016/j.ces.2005.02.021.

BÜCK, A., PEGLOW, M., TSOTSAS, E., MANGOLD, M., KIENLE, A., 2011. Model-based measurement of particle size distributions in layering granulation processes. *AIChE J.* 57 (4), 929–941. 10.1002/aic.12314.

BÜCK, A., PALIS, S., TSOTSAS, E., 2015. Model-based control of particle properties in fluidised bed spray granulation. *Powder Technology* 270, 575–583. 10.1016/j.powtec.2014.07.023.

BÜCK, A., WEGNER, M., NEUGEBAUER, C., PALIS, S., TSOTSAS, E., 2016a. Bifurcation analysis of process stability of continuous fluidized bed agglomeration with external product classification, in: Kravanja, Z., Bogataj, M. (Eds.)*, 26th European Symposium on Computer Aided Process Engineering*: *Part A*, vol. 38. Elsevier Science, Amsterdam, Netherlands, pp. 1881–1886.

BÜCK, A., NEUGEBAUER, C., MEYER, K., PALIS, S., DIEZ, E., KIENLE, A., HEINRICH, S., TSOTSAS, E., 2016b. Influence of operation parameters on process stability in continuous fluidised bed layering with external product classification. *Powder Technology* 300, 37–45. 10.1016/j.powtec.2016.03.019.

BÜCK, A., DÜRR, R., SCHMIDT, M., TSOTSAS, E., 2016c. Model predictive control of continuous layering granulation in fluidised beds with internal product classification. *Journal of Process Control* 45, 65–75. 10.1016/j.jprocont.2016.07.003.

## 8 References

BURGSCHWEIGER, J., TSOTSAS, E., 2002. Experimental investigation and modelling of continuous fluidized bed drying under steady-state and dynamic conditions. *Chemical Engineering Science* 57 (24), 5021–5038. 10.1016/S0009-2509(02)00424-4.

CORONEL-AGUILERA, C.P., SAN MARTÍN-GONZÁLEZ, M.F., 2015. Encapsulation of spray dried β-carotene emulsion by fluidized bed coating technology. *LWT - Food Science and Technology* 62 (1), 187–193. 10.1016/j.lwt.2014.12.036.

COTABARREN, I.M., BERTÍN, D., ROMAGNOLI, J., BUCALÁ, V., PIÑA, J., 2010. Dynamic simulation and optimization of a urea granulation circuit. *Ind. Eng. Chem. Res.* 49 (14), 6630–6640. 10.1021/ie901885x.

COTABARREN, I.M., BERTÍN, D., PIÑA, J., BUCALÁ, V., 2011. Analysis of optimal control problems and plant debottlenecking for urea granulation circuits. *Ind. Eng. Chem. Res.* 50 (21), 11996–12010. 10.1021/ie200043z.

DADKHAH, M., TSOTSAS, E., 2014. Influence of process variables on internal particle structure in spray fluidized bed agglomeration. *Powder Technology* 258, 165–173. 10.1016/j.powtec.2014.03.005.

DERNEDDE, M., PEGLOW, M., TSOTSAS, E., 2012. A novel, structure-tracking Monte Carlo algorithm for spray fluidized bed agglomeration. *AIChE J.* 58 (10), 3016–3029. 10.1002/aic.13709.

DESCAMPS, N., PALZER, S., ROOS, Y.H., FITZPATRICK, J.J., 2013. Glass transition and flowability/caking behaviour of maltodextrin DE 21. *Journal of Food Engineering* 119 (4), 809–813. 10.1016/j.jfoodeng.2013.06.045.

DONIDA, M.W., ROCHA, S.C.S., 2007. Coating of urea with an aqueous polymeric suspension in a two-dimensional spouted bed. *Drying Technology* 20 (3), 685–704. 10.1081/DRT-120002824.

DOSTA, M., HEINRICH, S., WERTHER, J., 2010. Fluidized bed spray granulation: Analysis of the system behaviour by means of dynamic flowsheet simulation. *Powder Technology* 204 (1), 71–82. 10.1016/j.powtec.2010.07.018.

DRECHSLER, J., PEGLOW, M., HEINRICH, S., IHLOW, M., MÖRL, L., 2005. Investigating the dynamic behaviour of fluidized bed spray granulation processes applying numerical simulation tools. *Chemical Engineering Science* 60 (14), 3817–3833. 10.1016/j.ces.2005.02.010.

DREYSCHULTZE, C., NEUGEBAUER, C., PALIS, S., BÜCK, A., TSOTSAS, E., HEINRICH, S., KIENLE, A., 2015. Influence of zone formation on stability of continuous fluidized bed layering granulation with external product classification. *Particuology* 23, 1–7. 10.1016/j.partic.2015.02.004.

DU, J., BÜCK, A., TSOTSAS, E., 2018. Investigation of spray agglomeration process in continuously operated horizontal fluidized bed, In: *Proceedings of 21st International Drying Symposium*, Valencia. 11.-14.09.2018, (in preparation).

EBEY, G.C., 1987. A thermodynamic model for aqueous film-coating. *Pharmaceutical Technology* 114, 40–50.

EMERSON PROCESS MANAGEMENT, 2008. *Instruction Manual - NGA 2000*. URL: <http://www.emerson.com/documents/automation/69952.pdf>. Accessed 10 November 2017.

ENNIS, B.J., TARDOS, G., PFEFFER, R., 1991. A microlevel-based characterization of granulation phenomena. *Powder Technology* 65, 257–272.

ERGUN, S., ORNING, A.A., 1949. Fluid flow through randomly packed columns and fluidized beds. *Industrial and Engineering Chemistry* 41, 1179–1184.

FLUSSER, J., SUK, T., 1993. Pattern recognition by affine moment invariants. *Pattern Recognition* 26 (1), 167–174. 10.1016/0031-3203(93)90098-H.

FOROUTAN-POUR, K., DUTILLEUL, P., SMITH, D.L., 1999. Advances in the implementation of the box-counting method of fractal dimension estimation. *Applied Mathematics and Computation* 105 (2-3), 195–210. 10.1016/S0096-3003(98)10096-6.

GAHN, C., MERSMANN, A., 1999. Brittle fracture in crystallization processes Part 2. Growth of fragments and scale-up of suspension crystallizers. *Chemical Engineering Science* 54 (9), 1283–1292. 10.1016/S0009-2509(98)00452-7.

GELDART, D., 1973. Types of gas fluidization. *Powder Technology* 7, 285–292.

GORDON, M., TAYLOR, J.S., 1952. Ideal copolymers and the second-order transitions of synthetic rubbers. Part 1. Non-crystalline copolymers. *Journal of Applied Chemistry* 2, 493–500.

GRÜNEWALD, G., WESTHOFF, B., KIND, M., 2010. Fluidized bed spray granulation: Nucleation studies with steady-state experiments. *Drying Technology* 28 (3), 349–360. 10.1080/07373931003641495.

GRÜNEWALD, G., KIND, M., 2011. Traceruntersuchungen zum Granulatwachstum durch Staubeinbindung bei der Wirbelschicht-Sprühgranulation. *Chemie Ingenieur Technik* 83 (5), 618–625. 10.1002/cite.201000140.

HACENE, Y.C., SINGH, A., VAN DEN MOOTER, G., 2016. Drug loaded and ethylcellulose coated mesoporous silica for controlled drug release prepared using a pilot scale fluid bed system. *International Journal of Pharmaceutics* 506 (1-2), 138–147. 10.1016/j.ijpharm.2016.04.047.

HAMPEL, N.A., 2015. Diskontinuierliches und kontinuierliches Pelletcoating im Wurster-Wirbelschichtprozess. *Dissertation*, Otto von Guericke University, Magdeburg.

HAMPEL, R., 2010. Beitrag zur Analyse von kinetischen Einflüssen auf die Wirbelschicht-Sprühagglomeration. *Dissertation*, Otto von Guericke University, Magdeburg.

HEINRICH, S., PEGLOW, M., IHLOW, M., HENNEBERG, M., MÖRL, L., 2002a. Analysis of the start-up process in continuous fluidized bed spray granulation by population balance modelling. *Chemical Engineering Science* 57 (20), 4369–4390. 10.1016/S0009-2509(02)00352-4.

HEINRICH, S., PEGLOW, M., MÖRL, L., 2002b. Unsteady and steady-state particle size distributions in batch and continuous fluidized bed granulation systems. *Chemical Engineering Journal* 86 (1-2), 223–231. 10.1016/S1385-8947(01)00293-5.

HEINRICH, S., PEGLOW, M., IHLOW, M., MÖRL, L., 2003. Particle population modeling in fluidized bed-spray granulation: Analysis of the steady state and unsteady behavior. *Powder Technology* 130 (1-3), 154–161. 10.1016/S0032-5910(02)00259-0.

HEMATI, M., CHERIF, R., SALEH, K., PONT, V., 2003. Fluidized bed coating and granulation: Influence of process-related variables and physicochemical properties on the growth kinetics. *Powder Technology* 130 (1-3), 18–34. 10.1016/S0032-5910(02)00221-8.

HOFFMANN, T., 2016. Experimentelle Untersuchungen des Einflusses von verschiedenen Prozessparametern auf das Partikelwachstum bei der Wirbelschicht-Sprühgranulation. *Dissertation*, Otto von Guericke University, Magdeburg.

HOUNSLOW, M.J., RYALL, R.L., MARSHALL, V.R., 1988. A discretized population balance for nucleation, growth, and aggregation. *AIChE J.* 34 (11), 1821–1832. 10.1002/aic.690341108.

HOUNSLOW, M.J., 1990. A discretized population balance for continuous systems at steady state. *AIChE J.* 36 (1), 106–116. 10.1002/aic.690360113.

HUSSAIN, M., 2014. Micro-Macro Transition from Discrete Modeling to Population Balances in Spray Fluidized Bed Agglomeration. *Dissertation*, Otto von Guericke University, Magdeburg.

HUSSAIN, M., KUMAR, J., TSOTSAS, E., 2015. A new framework for population balance modeling of spray fluidized bed agglomeration. *Particuology* 19, 141–154. 10.1016/j.partic.2014.06.005.

HYSLIP, J.P., VALLEJO, L.E., 1997. Fractal analysis of the roughness and size distribution of granular materials. *Engineering Geology* 48 (3-4), 231–244. 10.1016/S0013-7952(97)00046-X.

IVESON, S.M., LITSTER, J.D., HAPGOOD, K., ENNIS, B.J., 2001. Nucleation, growth and breakage phenomena in agitated wet granulation processes: A review. *Powder Technology* 117 (1-2), 3–39. 10.1016/S0032-5910(01)00313-8.

JASKULSKI, M., WAWRZYNIAK, P., ZBICIŃSKI, I., 2015. CFD model of particle agglomeration in spray drying. *Drying Technology* 33 (15-16), 1971–1980. 10.1080/07373937.2015.1081605.

JIANG, Z., BÜCK, A., TSOTSAS, E., 2017a. CFD–DEM study of residence time, droplet deposition, and collision velocity for a binary particle mixture in a Wurster fluidized bed coater. *Drying Technology* 36 (6), 638–650. 10.1080/07373937.2017.1319852.

JIANG, Z., HAGEMEIER, T., BÜCK, A., TSOTSAS, E., 2017b. Experimental measurements of particle collision dynamics in a pseudo-2D gas-solid fluidized bed. *Chemical Engineering Science* 167, 297–316. 10.1016/j.ces.2017.04.024.

JINAPONG, N., SUPHANTHARIKA, M., JAMNONG, P., 2008. Production of instant soymilk powders by ultrafiltration, spray drying and fluidized bed agglomeration. *Journal of Food Engineering* 84 (2), 194–205. 10.1016/j.jfoodeng.2007.04.032.

KASKAS, A.A., 1970. Schwarmgeschwindigkeiten in Mehrkornsuspensionen am Beispiel der Sedimentation. *Dissertation*, TU Berlin, Berlin.

KUNII, D., LEVENSPIEL, O., 1991. *Fluidization engineering,* Butterworth-Heinemann, Boston.

LAN, R., LIU, Y., WANG, G., WANG, T., KAN, C., JIN, Y., 2011. Experimental modeling of polymer latex spray coating for producing controlled-release urea. *Particuology* 9 (5), 510–516. 10.1016/j.partic.2011.01.004.

LAUBE, M., HÖLLER, H., 1988. Thermodynamics of water vapor, in: Fischer, G. (Ed.)*, Landoldt-Börnstein*: *Numerical Data and Funtional Relationships in Science and Technology*, Group V: Geophysics and Space Research, Volume 4: Meteorology, Subvolume b: Physical and Chemical Properties of the Air. Springer, Berlin.

LINK, K.C., SCHLÜNDER, E.-U., 1996. A new method for the characterisation of the wettability of powders. *Chem. Eng. Technol.* 19 (5), 432–437. 10.1002/ceat.270190508.

LINK, K.C., 1997. Wirbelschicht-Sprühgranulation: Untersuchung der Granulatbildung an einer frei schwebenden Einzelpartikel. *Dissertation*, University of Karlsruhe, Karlsruhe, Published in: Fortschritt-Berichte VDI, Reihe 3, VDI Verlag, Düsseldorf.

LI, Z., KESSEL, J., GRÜNEWALD, G., KIND, M., 2012. CFD simulation on drying and dust integration in fluidized bed spray granulation. *Drying Technology* 30 (10), 1088–1098. 10.1080/07373937.2012.685672.

LI, Z., KESSEL, J., GRÜNEWALD, G., KIND, M., 2013. Coupled CFD-PBE simulation of nucleation in fluidized bed spray granulation. *Drying Technology* 31 (15), 1888–1896. 10.1080/07373937.2013.840649.

MANDELBROT, B.B., 1983. *The fractal geometry of nature,* W. H. Freeman and Company, New York.

MEINERS, J.A., 2012. Fluid bed microencapsulation and other coating methods for food ingredient and nutraceutical bioactive compounds, in: McClements, D.J., Garti, N. (Eds.)*, Encapsulation technologies and delivery systems for food ingredients and nutraceuticals*. Woodhead Pub, Philadelphia, Pa, pp. 151–176.

MERKUS, H.G., 2009. *Particle size measurements: Fundamentals, practice, quality.,* Springer Science+Business Media B.V., Dordrecht.

MICHELL INSTRUMENTS, 2014. *Optidew Vision - Datasheet*. URL: <http://www.michell.com/us/documents/Optidew_vision_97144_US_Datasheet-V6.pdf>. Accessed 10 November 2017.

MÖRL, L., MITTELSTRAß, M., SACHSE, J., 1978. Berechnung der Verteilungsspektren von Feststoffgranulatteilchen in Wirbelschichtapparaten mit klassierendem Abzug. *Chem. Techn.* 30 (5), 242–245.

MÖRL, L., 1980. Granulatwachstum bei der Wirbelschichtgranulationstrocknung unter Berücksichtigung sich neu bildender Granulatkeime. *Wiss. Z. Techn. Hochsch. Magdeburg* 24, 13–19.

MÖRL, L., HEINRICH, S., PEGLOW, M., 2007. Fluidized bed spray granulation, in: Salman, A.D., Hounslow, M.J., Seville, J.P.K. (Eds.)*, Granulation*. Elsevier B.V., pp. 21–188.

NAKANO, T., YUASA, H., 2001. Suppression of agglomeration in fluidized bed coating. Part 4: Effects of sodium citrate concentration on the suppression of particle agglomeration and the physical properties of HPMC film. *International Journal of Pharmaceutics* 215 (1-2), 3–12. 10.1016/S0378-5173(00)00620-7.

NEUGEBAUER, C., PALIS, S., BÜCK, A., TSOTSAS, E., HEINRICH, S., KIENLE, A., 2017. A dynamic two-zone model of continuous fluidized bed layering granulation with internal product classification. *Particuology* 31, 8–14. 10.1016/j.partic.2016.07.001.

NIENOW, A.W., 1995. Fluidised bed granulation and coating: Applications to materials, agriculture and biotechnology. *Chemical Engineering Communications* 139 (1), 233–253. 10.1080/00986449508936406.

PALIS, S., BÜCK, A., KIENLE, A., 2012. Low order controller design for continuous fluidized bed spray granulatiovn with internal product classification by robust control methods. *IFAC Proceedings Volumes* 45 (13), 701–706. 10.3182/20120620-3-DK-2025.00177.

PALIS, S., KIENLE, A., 2012. Stabilization of continuous fluidized bed spray granulation with external product classification. *Chemical Engineering Science* 70, 200–209. 10.1016/j.ces.2011.08.026.

PALIS, S., KIENLE, A., 2014. Discrepancy based control of particulate processes. *Journal of Process Control* 24 (3), 33–46. 10.1016/j.jprocont.2013.12.003.

PALZER, S., 2005. The effect of glass transition on the desired and undesired agglomeration of amorphous food powders. *Chemical Engineering Science* 60 (14), 3959–3968. 10.1016/j.ces.2005.02.015.

PALZER, S., 2007. Agglomeration of dehydrated consumer foods, in: Salman, A.D., Hounslow, M.J., Seville, J.P.K. (Eds.)*, Granulation*. Elsevier B.V., pp. 591–671.

PALZER, S., 2009. Influence of material properties on the agglomeration of water-soluble amorphous particles. *Powder Technology* 189 (2), 318–326. 10.1016/j.powtec.2008.04.034.

PALZER, S., 2010. The relation between material properties and supra-molecular structure of water-soluble food solids. *Trends in Food Science & Technology* 21 (1), 12–25. 10.1016/j.tifs.2009.08.005.

PALZER, S., 2011. Agglomeration of pharmaceutical, detergent, chemical and food powders: Similarities and differences of materials and processes. *Powder Technology* 206 (1-2), 2–17. 10.1016/j.powtec.2010.05.006.

PASHMINEHAZAR, R., KHARAGHANI, A., TSOTSAS, E., 2016. Three dimensional characterization of morphology and internal structure of soft material agglomerates

produced in spray fluidized bed by X-ray tomography. *Powder Technology* 300, 46–60. 10.1016/j.powtec.2016.03.053.

RADICHKOV, R., MÜLLER, T., KIENLE, A., HEINRICH, S., PEGLOW, M., MÖRL, L., 2006. A numerical bifurcation analysis of continuous fluidized bed spray granulation with external product classification. *Chemical Engineering and Processing* 45 (10), 826–837. 10.1016/j.cep.2006.02.003.

RAMKRISHNA, D., 2000. *Population balances. Theory and applications to particulate systems in engineering,* Acad. Press, New York.

RANDOLPH, A.D., LARSON, M.A., 1971. *Theory of Particulate Processes. Analysis and techniques of continuous crystallization,* Academic Press, Inc., New York.

REILAND, T.L., SEITZ, J.A., YEAGER, J.L., 1983. Aqueous film-coating vaporization efficiency. *Drug Development and Industrial Pharmacy* 9 (6), 945–958. 10.3109/03639048309042834.

RETSCH TECHNOLOGY, 2017. *Particle Analyzer CAMSIZER P4, Brochure.* URL: <https://www.retsch-technology.com/dltmp/www/53e4b554-3654-473b-9a08-636500000000-34672015b4f6/brochure_camsizerP4_en.pdf>. Accessed 19 March 2018.

RIECK, C., HOFFMANN, T., BÜCK, A., PEGLOW, M., TSOTSAS, E., 2015. Influence of drying conditions on layer porosity in fluidized bed spray granulation. *Powder Technology* 272, 120–131. 10.1016/j.powtec.2014.11.019.

RIECK, C., BÜCK, A., TSOTSAS, E., 2016. Monte Carlo modeling of fluidized bed coating and layering processes. *AIChE J.* 62 (8), 2670–2680. 10.1002/aic.15237.

ROOS, Y., KAREL, M., 1991. Phase transitions of mixtures of amorphous polysaccharides and sugars. *Biotechnol. Prog.* 7 (1), 49–53. 10.1021/bp00007a008.

RUMPF, H., 1958. Grundlagen und Methoden des Granulierens. *Chemie Ingenieur Technik* 30 (3), 144–158.

SALEH, K., STEINMETZ, D., HEMATI, M., 2003. Experimental study and modeling of fluidized bed coating and agglomeration. *Powder Technology* 130 (1-3), 116–123. 10.1016/S0032-5910(02)00254-1.

SAMSON, R.J., MULHOLLAND, G.W., GENTRY, J.W., 1987. Structural analysis of soot agglomerates. *Langmuir* 3 (2), 272–281. 10.1021/la00074a022.

SCHMIDT, M., RIECK, C., BÜCK, A., TSOTSAS, E., 2015a. Experimental investigation of process stability of continuous spray fluidized bed layering with external product separation. *Chemical Engineering Science* 137, 466–475. 10.1016/j.ces.2015.06.060.

SCHMIDT, M., BÜCK, A., TSOTSAS, E., 2015b. Experimental investigation of process stability of continuous spray fluidized bed layering with internal separation. *Chemical Engineering Science* 126, 55–66. 10.1016/j.ces.2014.11.057.

SCHMIDT, M., BÜCK, A., TSOTSAS, E., 2017a. Experimental investigation of the influence of drying conditions on process stability of continuous spray fluidized bed layering

granulation with external product separation. *Powder Technology* 320, 474–482. 10.1016/j.powtec.2017.07.012.

SCHMIDT, M., BÜCK, A., TSOTSAS, E., 2017b. Shell porosity in spray fluidized bed coating with suspensions. *Advanced Powder Technology* 28 (11), 2921–2928. 10.1016/j.apt.2017.08.020.

SCHUBERT, H., 1982. *Kapillarität in porösen Feststoffsystemen,* Springer, Berlin.

SCHÜTTE, R., RUHS, A., PELGRIMS, I., KLASEN, C.-J., KAISER, L., 1998. Verfahren zur Herstellung von Granulat mit periodisch oszillierender Korngrößenverteilung und Vorrichtung zu seiner Durchführung, Patent DE 19639579 C1.

SONDEJ, F., BÜCK, A., KOSLOWSKY, K., BACHMANN, P., JACOB, M., TSOTSAS, E., 2015. Investigation of coating layer morphology by micro-computed X-ray tomography. *Powder Technology* 273, 165–175. 10.1016/j.powtec.2014.12.050.

STRENZKE, G., GOLOVIN, I., WEGNER, M., PALIS, S., BÜCK, A., KIENLE, A., TSOTSAS, E., 2018. Influence of drying conditions on process properties and parameter identification for continuous fluidized bed spray agglomeration, In: *Proceedings of 21st International Drying Symposium*, Valencia. 11.-14.09.2018, (in preparation).

STRONG, J.C., 2009. Psychrometric analysis of the environmental equivalency factor for aqueous tablet coating. *AAPS PharmSciTech* 10 (1), 303–309. 10.1208/s12249-009-9204-7.

SUGISAKI, M., SUGA, H., SEKI, S., 1968. Calorimetric study of the glassy state. Part 4: Heat capacities of glassy water and cubic ice. *Bulletin of the Chemical Society of Japan* 41 (11), 2591–2599.

TAKEITI, C.Y., KIECKBUSCH, T.G., COLLARES-QUEIROZ, F.P., 2010. Morphological and physicochemical characterization of commercial maltodextrins with different degrees of dextrose-equivalent. *International Journal of Food Properties* 13 (2), 411–425. 10.1080/10942910802181024.

TERRAZAS-VELARDE, K., PEGLOW, M., TSOTSAS, E., 2011. Investigation of the kinetics of fluidized bed spray agglomeration based on stochastic methods. *AIChE J.* 57 (11), 3012–3026. 10.1002/aic.12506.

TEUNOU, E., PONCELET, D., 2002. Batch and continuous fluid bed coating: Review and state of the art. *Journal of Food Engineering* 53 (4), 325–340. 10.1016/S0260-8774(01)00173-X.

TRIGON CHEMIE GMBH, 2014. *Specifications: Sodium benzoate SP, Food Grade, Kosher*. URL: <http://www.trigon-chemie.com/products/46/CAS_532-32-1/1>. Accessed 15 November 2017.

TURCHIULI, C., FUCHS, M., BOHIN, M., CUVELIER, M.E., ORDONNAUD, C., PEYRAT-MAILLARD, M.N., DUMOULIN, E., 2005. Oil encapsulation by spray drying and fluidised bed agglomeration. *Innovative Food Science & Emerging Technologies* 6 (1), 29–35. 10.1016/j.ifset.2004.11.005.

TURTON, R., TARDOS, G.I., ENNIS, B.J., 1998. Fluidized bed coating and granulation, in: Yang, W.-C. (Ed.)*, Fluidization, solids handling and processing*: *Industrial applications*. Noyes Publications, Westwood, N.J, pp. 331–434.

TZIKA, M., ALEXANDRIDOU, S., KIPARISSIDES, C., 2003. Evaluation of the morphological and release characteristics of coated fertilizer granules produced in a Wurster fluidized bed. *Powder Technology* 132 (1), 16–24. 10.1016/S0032-5910(02)00345-5.

UHLEMANN, H., 1990. Kontinuierliche Wirbelschicht-Sprühgranulation. *Chemie Ingenieur Technik* 62 (10), 822–834. 10.1002/cite.330621010.

VREMAN, A.W., VAN LARE, C.E., HOUNSLOW, M.J., 2009. A basic population balance model for fluid bed spray granulation. *Chemical Engineering Science* 64 (21), 4389–4398. 10.1016/j.ces.2009.07.010.

WALSH, J.J., WATTERSON, J., 1993. Fractal analysis of fracture patterns using the standard box-counting technique: Valid and invalid methodologies. *Journal of Structural Geology* 15 (12), 1509–1512.

WANG, G., YANG, L., LAN, R., WANG, T., JIN, Y., 2013. Granulation by spray coating aqueous solution of ammonium sulfate to produce large spherical granules in a fluidized bed. *Particuology* 11 (5), 483–489. 10.1016/j.partic.2012.10.005.

WEBB, P.A., 2001. Volume and Density Determinations for Particle Technologists, Micromeritics Instrument Corp.

WIRTH, K.-E., 2010. Flow patterns and pressure drop in fluidized beds, in: Verein Deutscher Ingenieure (Ed.)*, VDI Heat Atlas*, 2nd ed. Springer, Berlin, pp. 1197–1206.

WNUKOWSKI, P., SETTERWALL, F., 1989. The coating of particles in a fluidized bed: Residence time distribution in a system of two coupled perfect mixers. *Chemical Engineering Science* 44 (3), 493–505.

ZANK, J., KIND, M., SCHLÜNDER, E.-U., 2001. Particle growth and droplet deposition in fluidised bed granulation. *Powder Technology* 120 (1-2), 76–81. 10.1016/S0032-5910(01)00350-3.

# Appendix

## A   Derivation of the elutriation velocity

A particle is elutriated, if the gas velocity overcomes the stationary sinking velocity. The latter is calculated from a force balance over a particle, where the gravitational force is in balance with the forces of flow resistance and buoyancy:
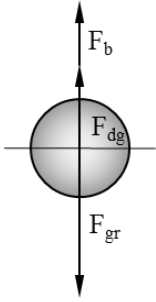


$$F_{gr} - F_b - F_{dg} = 0 \tag{A–1}$$

$$m_p g - m_g g - \frac{\rho_g}{2} u_e^2 A_p c_{dg} = 0 \tag{A–2}$$

$$g V_p (\rho_p - \rho_g) - \frac{\rho_g}{2} u_e^2 A_p c_{dg} = 0 \tag{A–3}$$

$$g \frac{\pi}{6} d_p^3 (\rho_p - \rho_g) - \frac{\rho_g}{2} u_e^2 \frac{\pi}{4} d_p^2 c_{dg} = 0 \qquad | \div v_g^2 \tag{A–4}$$

$$\frac{(\rho_p - \rho_g) g d_p^3}{6 v_g^2} = \frac{\rho_g u_e^2 d_p^2}{8 v_g^2} c_{dg} \qquad | \div \rho_g \; ; Re_e = \frac{u_e d_p}{v_g} ; Ar = \frac{g \cdot d_p^3 \cdot (\rho_p - \rho_g)}{v_g^2 \cdot \rho_g} \tag{A–5}$$

$$\frac{Ar}{6} = \frac{Re_e^2}{8} c_{dg} \tag{A–6}$$

Solving for $Re_e$ yields Eq. 2–5:

$$Re_e = \sqrt{\frac{4}{3} \frac{Ar}{c_{dg}}} \tag{A–7}$$

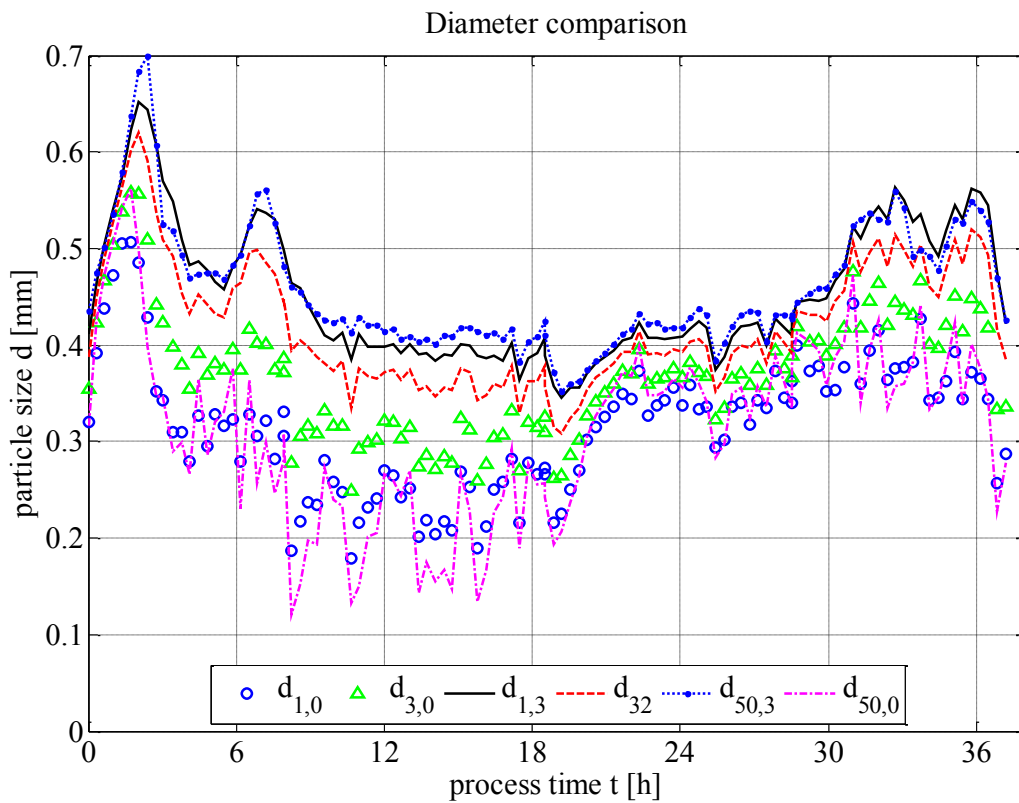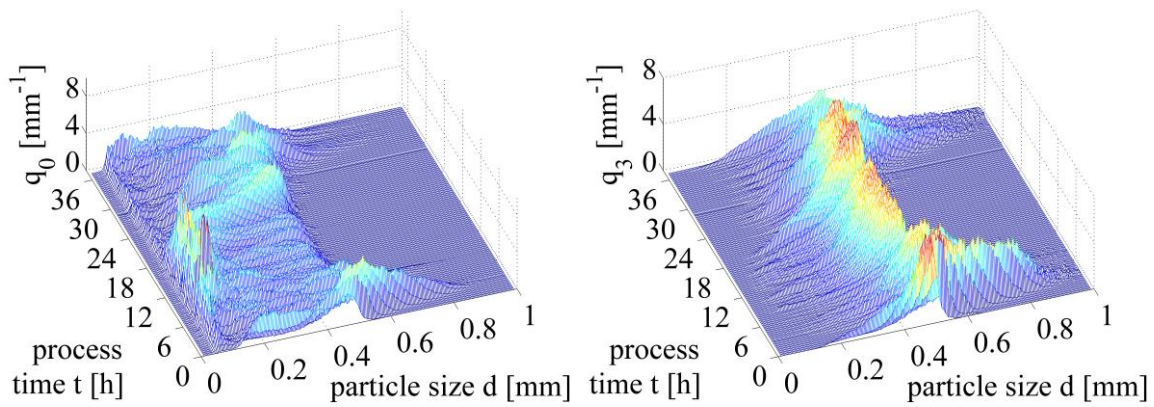# B   Comparison of characteristic particle diameters



Fig. B–1. Temporal evolution of an experimental PSD density ($q_0$: top left; $q_3$: top right) and different average/median diameters for each measured PSD density.

# C   Experimental data – Agglomeration
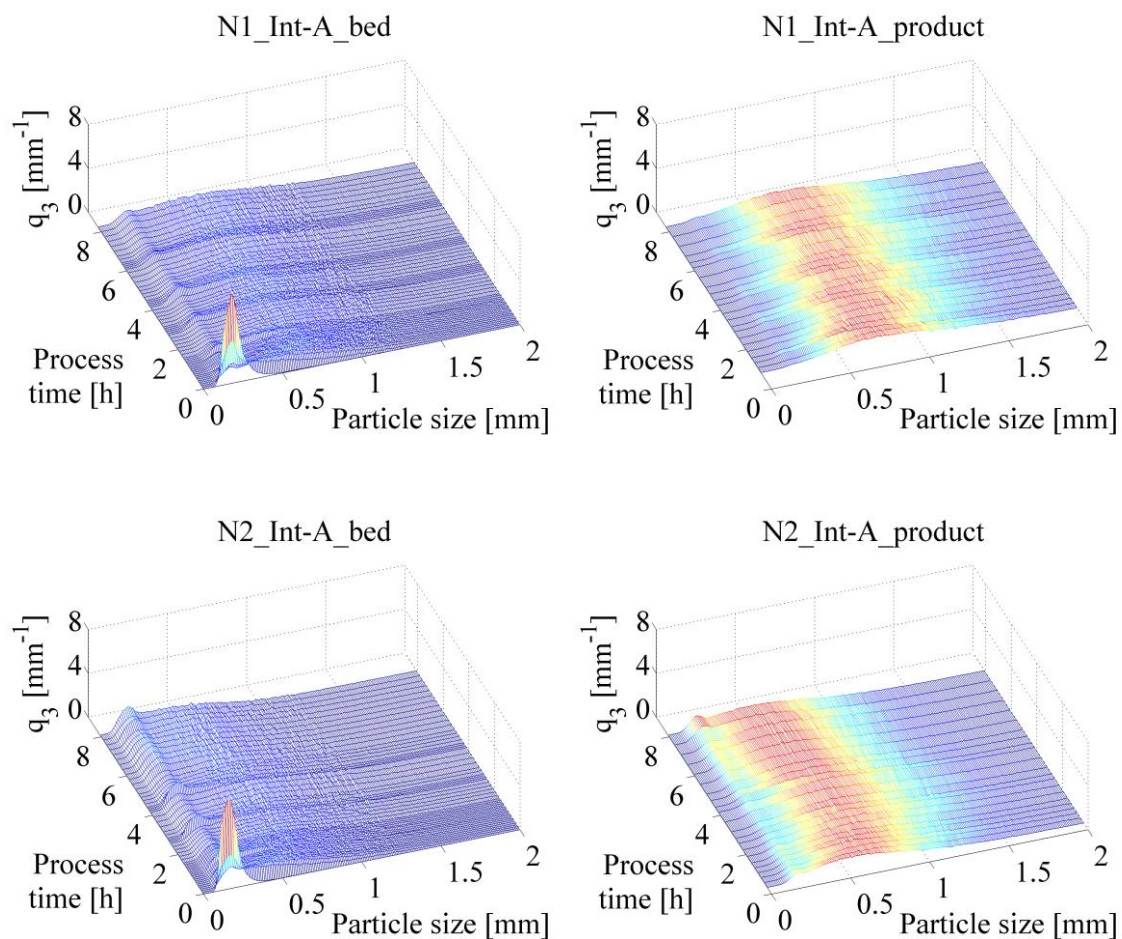
## C.1   3D PSD density for SFBA with internal separation



N1_Int-A_bed

N1_Int-A_product

N2_Int-A_bed

N2_Int-A_product

Fig. C–1. Temporal evolution of $q_3$ for the continuous SFBA experiments with internal separation and varied $\dot{M}_{nuc}$ (N1_Int-A: 3.6 kg·h$^{-1}$, N2_Int-A: 8.7 kg·h$^{-1}$).
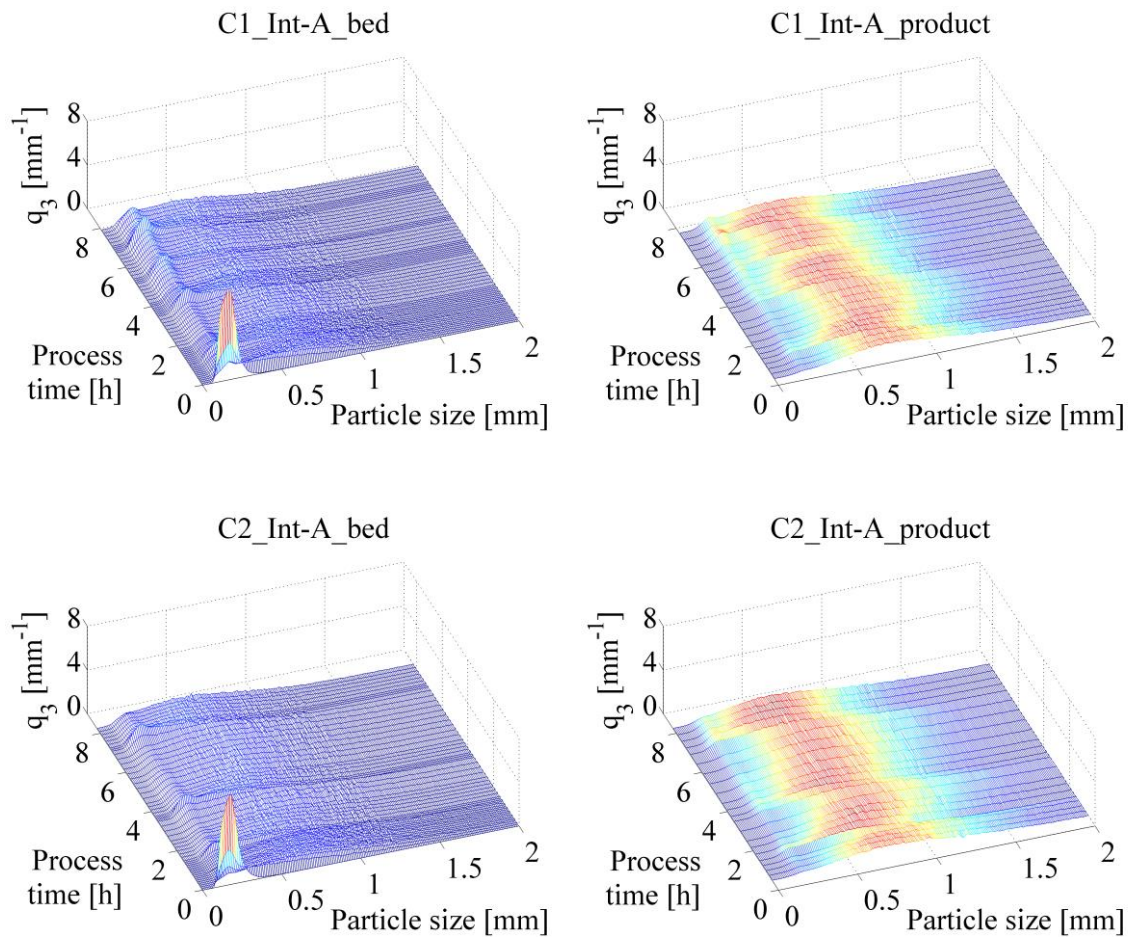
Fig. C–2. Temporal evolution of $q_3$ for the continuous SFBA experiments with internal separation and varied $u_{class}$ (C1_Int-A: 1.0 m·s$^{-1}$, C2_Int-A: 1.3 m·s$^{-1}$).
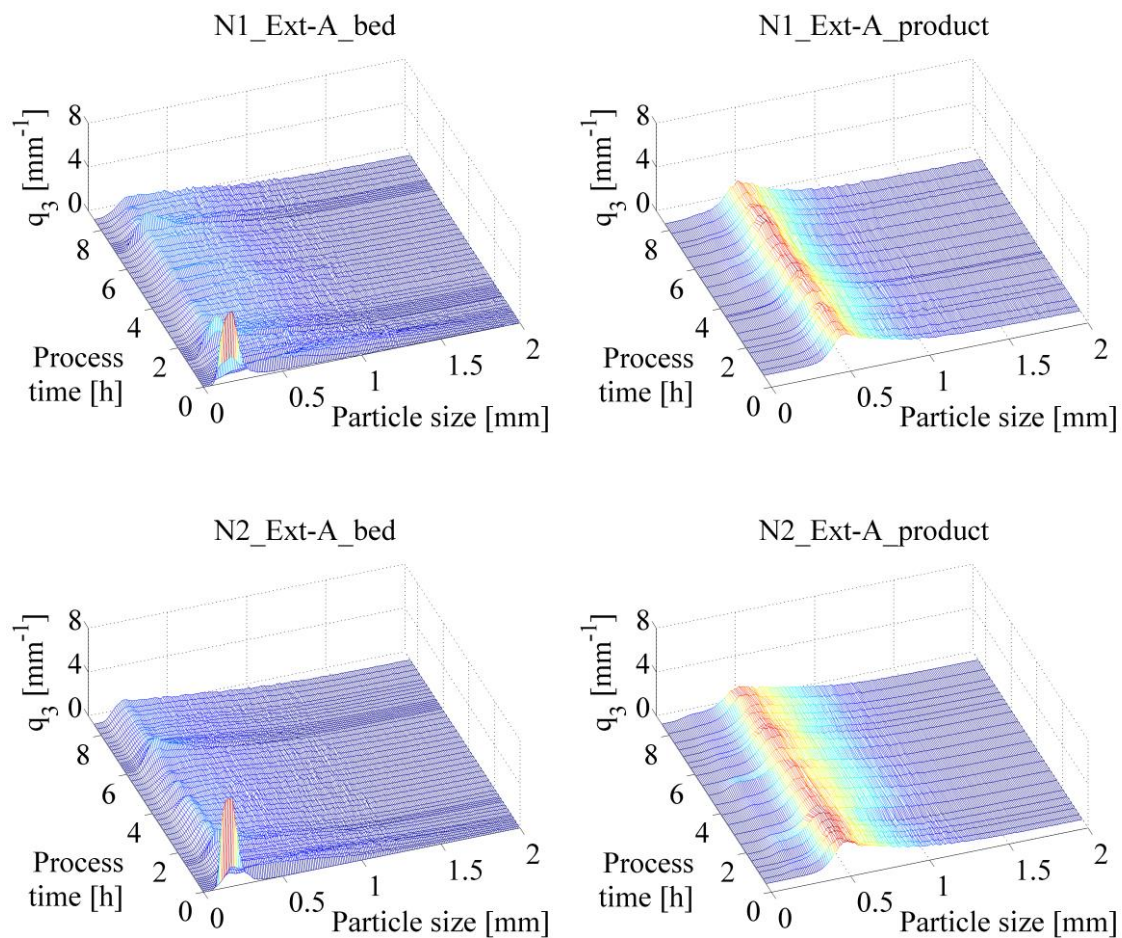
## C.2   3D PSD density for SFBA with external separation



Fig. C–3. Temporal evolution of $q_3$ for the continuous SFBA experiments with external separation and varied $\dot{M}_{nuc}$ (N1_Int-A: 2.5 kg·h$^{-1}$, N2_Int-A: 4.0 kg·h$^{-1}$).
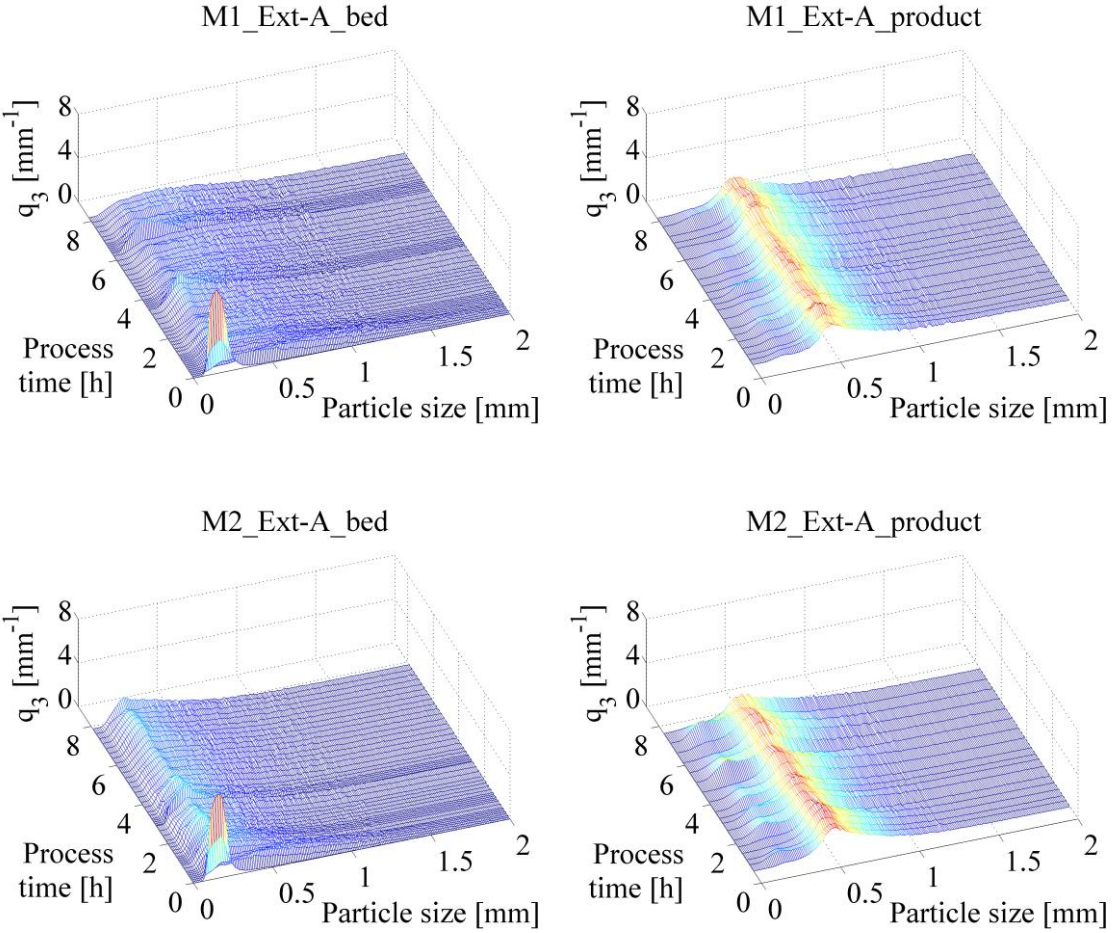
Fig. C–4. Temporal evolution of $q_3$ for the continuous SFBA experiments with external separation and varied $P_{mill}$ (M1_Int-A: 40%, M2_Int-A: 80%).

# Scientific contributions

## Publications

- Bück, A., Dürr, R., **Schmidt, M.**, Tsotsas, E., 2016. Model predictive control of continuous layering granulation in fluidised beds with internal product classification. *Journal of Process Control* 45, 65–75. DOI: 10.1016/j.jprocont.2016.07.003.

- Hoffmann, T., Rieck, C., **Schmidt, M.**, Bück, A., Peglow, M., Tsotsas, E., 2015. Prediction of shell porosities in continuous fluidized bed spray layering. *Drying Technology* 33 (13), 1662–1670. DOI: 10.1080/07373937.2015.1064943.

- Rieck, C., **Schmidt, M.**, Bück, A., Tsotsas, E., 2018. Monte Carlo modeling of binderless spray agglomeration in fluidized beds. *American Institute of Chemical Engineers Journal* 64 (10), 3582-3594. DOI: 10.1002/aic.16349.

- **Schmidt, M.**, Rieck, C., Bück, A., Tsotsas, E., 2015. Experimental investigation of process stability of continuous spray fluidized bed layering with external product separation. *Chemical Engineering Science* 137, 466–475. DOI: 10.1016/j.ces.2015.06.060.

- **Schmidt, M.**, Bück, A., Tsotsas, E., 2015. Experimental investigation of process stability of continuous spray fluidized bed layering with internal separation. *Chemical Engineering Science* 126, 55–66. DOI: 10.1016/j.ces.2014.11.057.

- **Schmidt, M.**, Bück, A., Tsotsas, E., 2017. Experimental investigation of the influence of drying conditions on process stability of continuous spray fluidized bed layering granulation with external product separation. *Powder Technology* 320, 474–482. 10.1016/j.powtec.2017.07.012.

- **Schmidt, M.**, Bück, A., Tsotsas, E., 2017. Shell porosity in spray fluidized bed coating with suspensions. *Advanced Powder Technology* 28 (11), 2921–2928. DOI: 10.1016/j.apt.2017.08.020.

## Conference proceedings

- **Schmidt, M.**, Bück, A., Tsotsas, E. Experimental investigation of continuous fluidized bed spray granulation with internal classification. *19$^{th}$ International Drying Symposium* (IDS 2014), 24.-27.08.2014, Lyon, France.

- **SCHMIDT, M.**, HOFFMANN, T., BÜCK, A., TSOTSAS, E. Experimental investigation of continuous fluidized bed spray granulation with internal classification. *7th World Congress on Particle Technology* (WCPT 7), 18.-21.05.2014, Beijing, China, in: Procedia Engineering 102 (2015), 565-574. DOI: 10.1016/j.proeng.2015.01.127.

- SONDEJ, F., RIECK, C., **SCHMIDT, M.**, BÜCK, A., TSOTSAS, E. Use of X-ray micro-computed tomography in pharmaceuticals and food industry. *6th Conference on Industrial Computed Tomography* (iCT 2016), Wels, Australia.

- **SCHMIDT, M.**, BÜCK, A., TSOTSAS, E. Spray fluidized bed agglomeration of amorphous food powders. *International Congress on Particle Technology* (PARTEC 2016), 19.-21.04.2016, Nuremberg, Germany.

- **SCHMIDT, M.**, BÜCK, A., TSOTSAS, E. Influence of drying conditions on spray fluidized bed agglomeration behavior of amorphous food powders. *20th International Drying Symposium* (IDS2016), 07.-10.08.2016, Gifu, Japan.

# Conference presentations

- Jahrestreffen der ProcessNet Fachgruppe Agglomeration und Schüttguttechnik, 11.03.2014, Magdeburg, Germany:
  "Experimentelle Untersuchung der kontinuierlichen Wirbelschicht-Sprühgranulation mit interner Klassierung"

- 19th International Drying Symposium (IDS 2014), 24.–27.08.2014, Lyon, France:
  "Experimental investigation of fluidized bed spray granulation with internal classification"

- 7th World Congress on Particle Technology (WCPT 7), 19.–22.05.2014, Beijing, China:
  "Experimental investigation of fluidized bed spray granulation with internal classification"

- International Congress on Particle Technology (PARTEC 2016), 19.–21.04.2016, Nuremberg, Germany:
  "Spray fluidized bed agglomeration of amorphous food powders"

- Jahrestreffen der ProcessNet Fachgruppen Agglomerations- und Schüttguttechnik, Grenzflächenbestimmte Systeme und Prozesse, Trocknungstechnik, Lebensmittel-verfahrenstechnik und Wärme- und Stoffübertragung, 13.–17.02.2017, Bruchsal, Germany:
  "Beeinflussung der Schichtporosität beim Wirbelschicht-Sprühcoating mit wässriger Kalksteinsuspension"

- Jahrestreffen der ProcessNet Fachgruppe Trocknungstechnik, 26.–28.02.2018, Merseburg, Germany:
  "Einfluss der Trocknungsbedingungen auf die kontinuierliche Wirbelschicht-Sprühgranulation mit interner und externer Klassierung"

# Conference posters

- Jahrestreffen der ProcessNet Fachgruppe Agglomeration und Schüttguttechnik, 16–17.03.2015, Magdeburg, Germany:
"Prozessstabilität der kontinuierlichen Wirbelschicht-Sprühgranulation mit externer Klassierung"

- 7th Granulation Workshop, 01.–03.07.2015, Sheffield, UK:
"Experimental investigation of process stability of continuous spray fluidized bed layering processes"

- Jahrestreffen der ProcessNet Fachgruppe Lebensmittelverfahrenstechnik, 10.–11.03.2016, Erlangen, Germany:
"Investigation of spray fluidized bed agglomeration of amorphous food powders"

- 20th International Drying Symposium (IDS 2016), 07.–09.08.2016, Gifu, Japan:
"Influence of drying conditions on spray fluidized bed agglomeration behavior of amorphous food powders"

- Jahrestreffen der ProcessNet Fachgruppen Agglomerations- und Schüttguttechnik, Grenzflächenbestimmte Systeme und Prozesse, Trocknungstechnik, Lebensmittel-verfahrenstechnik und Wärme- und Stoffübertragung, 13.–17.02.2017, Bruchsal, Germany:
"Experimentelle Untersuchung der Prozessdynamik der kontinuierlichen Wirbelschicht-Sprühagglomeration von Maltodextrin"

  "Nachträgliche Modifizierung der Struktur der Coatingschicht beim Wirbelschicht-Sprühcoating"

- 8th Granulation Workshop, 28.–30.06.2017, Sheffield, UK:
"Experimental investigation of process dynamics of continuous spray fluidized bed agglomeration of maltodextrin"

- 10th World Congress of Chemical Engineering (WCCE 2017), 01.–05.10.2017, Barcelona, Spain:
"Influencing shell porosity during spray fluidized bed coating with aqueous limestone suspension"

- Jahrestreffen der ProcessNet Fachgruppe Agglomeration und Schüttguttechnik, 13.–15.03.2018, Neuß. Germany:
"Vorstellung einer Methode zur Bestimmung der Rauheit von Granulaten"

- 21st International Drying Symposium (IDS 2018), 11.–14.09.2018, Valencia, Spain:
"Influence of drying conditions on continuous spray fluidized bed layering granulation with internal and external separation"

# Supervised student theses

- MARIYA STEFANOVA (B. Sc.), 03.06.–26.08.2013

  "Experimentelle Untersuchung der kontinuierlichen Wirbelschicht-Sprühgranulation mit intern klassierendem Austrag"

- JUN LU (M. Sc.), 04.12.2013–23.04.2014

  "Experimental investigation of continuous fluidized bed spray granulation with internal classification"

- YUXIANG ZHAO (M. Sc.), 31.01.–20.06.2014

  "Experimental investigation of the influence of the drying parameters on the particle structure during fluidized bed spray granulation"

- SAADI HASSAN MUFTI (M. Sc.), 27.10.2014–16.03.2015

  "Experimental investigation of continuous fluidized bed spray granulation with external classification"

- PATRICK WILL (B. Sc.), 23.02.–18.05.2015

  "Experimentelle Untersuchung der Batch-Wirbelschicht-Sprühagglomeration"

- SEBASTIAN GRAßHOFF (M. Sc.), 06.07.–23.11.2015

  "Experimentelle Untersuchung der binderlosen Batch-Wirbelschicht-Sprühagglomeration"

- MENGYANG RAO (M. Sc.), 28.09.2015–15.02.2016

  "Batch spray fluidized bed coating with limestone suspension"

- XINKUO CHEN (M. Sc.), 20.01.–08.06.2016

  "Experimental investigation of the influence of drying conditions on process stability of continuous spray fluidized bed granulation with external classification"

- AMOL VITHAL JADHAV (M. Sc.), 04.04.–22.08.2016

  "Upscaling of binder-less spray fluidized bed agglomeration"


- XINTONG MA (M. Sc.), 20.04.–07.09.2016

  "A posteriori modification of porous layers in fluidized beds"


- MENGTING HE (M. Sc.), 04.07.–21.11.2016

  "Experimental investigation of binder-less continuous spray fluidized bed agglomeration with internal product separation"


- SUDIP SAHA (M. Sc.), 12.10.2016–15.03.2017

  "Experimental investigation of continuous spray fluidized bed agglomeration of amorphous powder with external product separation"